APPLICATION OF LIQUID STATE NUCLEAR MAGNETIC RESONANCE TECHNIQUES FOR THE STUDY OF POROUS MATERIALS

Taylor Jake Rottreau

Doctor of Philosophy

Aston University

May, 2018

Aston University

APPLICATION OF LIQUID STATE NUCLEAR MAGNETIC RESONANCE TECHNIQUES FOR THE STUDY OF POROUS MATERIALS

Taylor Jake Rottreau

Doctor of Philosophy, 2018.

Thesis Summary

This thesis describes the work undertaken to develop and apply the liquid state NMR techniques of cryoporometry and diffusometry for the study of porous materials. Solid/liquid interfaces are at the heart of modern applied science. Understanding liquid dynamics, when located within a confining environment, such as a pore, is of utmost importance when expanding knowledge in this field. There are many novel solid/liquid systems that have yet to be studied; NMR offers the opportunity to probe these systems in their working states.

The technique of cryoporometry was initially implemented using a series of highly ordered controlled pore glasses with varying pore diameters. This preliminary work built the foundations for further application. However, one key drawback in the thermoporometry area is the lack of consensus on the two key parameters for converting melting point data into pore size distributions. This work offers values for both. NMR cryoporometry is also limited by the lack of suitable liquids that can not only probe a wide range of pore size, but can also match the chemistry of the solid being studied. Two novel cryoporometric liquids are introduced here; *t*-butanol and menthol, with the aim of reducing the significance of this limitation. The suitability of these liquids is then investigated further by analysing the change in porosity, with swelling, of polymer systems.

The physical and chemical behaviour of a confined liquid is often rate limiting in catalytic science. Diffusion NMR has been utilized for the first time to distinguish whether in-pore diffusion, or diffusion from the bulk media into a pore network, was the rate-limiting step for catalytic esterification over sulfonic acid silica analogues. Rate of reaction and liquid diffusion were found to be uncorrelated, discounting the former hypothesis.

NMR spectrometers have near ubiquitous use in materials research. The work detailed here should offer to make NMR cryoporometry a more widely used technique in the analysis of porous materials. The future design of porous materials, such as the optimisation of silica architectures for catalytic activities, will also be aided by the physiochemical insights obtained here from diffusion NMR.

Keywords: cryoporometry, diffusion, pore size distribution, mesoporous, silica.

List of Publications

1. **Rottreau, T. J.**, Parlett, C. M. A., Lee, A. F. and Evans, R. Diffusion NMR Characterization of Catalytic Silica Supports: A Tortuous Path. *J. Phys. Chem. C.,* **2017**, 121 (30), 16250-16256.
2. **Rottreau, T. J.**, Parlett, C. M. A., Lee, A. F. and Evans, R. NMR Cryoporometric Measurements of Porous Silica: A Method for the Determination of Melting Point Depression Parameters of Probe Liquids. *Micropor. Mesopor. Mat.,* **2018***,* 264, 265-271.
3. **Rottreau, T. J.**, Parlett, C. M. A., Lee, A. F. and Evans, R. Extending the Range of Liquids Available for NMR Cryoporometry Studies of Porous Materials. *Micropor. Mesopor. Mat.,* **2019**, 274, 198-202.
4. Patyukova, E., **Rottreau, T. J.,** Evans, R., Topham, P. D. and Greenhall, M. J. Hydrogen Bonding Aggregation in Acrylamide: Theory and Experiment. *Macromolecules.,* **2018,** 51, 7032-7043.

Acknowledgements

One thing for certain is that without the help, support and guidance from my supervisor, Dr. Rob Evans, this project wouldn't have been half as successful and enjoyable as it has been. One of the most hard-working, passionate and intelligent people I have ever had the pleasure to work with. You have been brilliant. I'm sure you will go on to great things in the future (unlike Reading F.C.), you truly deserve it. Thank you for everything.

A special mention goes out to Dr. Chris Parlett and Prof. Adam Lee. This project wouldn't have been possible without your contribution. It has been a pleasure to work with you both.

Financial support for the PhD studentship from the School of Engineering and Applied Science, Aston University, is gratefully acknowledged.

I am extremely grateful for the support and guidance from the CEAC community, none more so than Prof. Paul Topham and Prof. Brian Tighe. The caravan will never be forgotten! I'd also like to apologise one last time to Dr. Khalid Doudin, I'm still very sorry for breaking that transfer line….

My postgraduate office family, past and present. Anna, Chris, Christian, Georgie, Siân and Sim, in particular. We've shared a lot of laughter over the past three years. Thank you for your advice and for keeping me sane during stressful times.

Mom, Dad, Céline, Nan, Grandad and all of my close friends. Even though you still don't understand what I actually do (apart from you dad, obviously), your support has been brilliant. Thank you.

Lastly to Laura, the most important person in my life. I wouldn't have been able to get through these years of study if it wasn't for your constant support and encouragement. Thank you for being a calming influence in times of stress and for never failing to make me smile. This is for you.

Table of Contents

List of Abbreviations

BJH	Barrett-Joyner-Halenda
CPG	controlled pore glass
CPMG	Carr-Purcell-Meiboom-Gill
DMSO	dimethyl sulfoxide
DOSY	diffusion ordered spectroscopy
DSC	differential scanning calorimetry
DSTEBPGP_3S	double stimulated echo bipolar gradient pair sequence
DVB	divinylbenzene
HEA-HMAA	2-hydroxyethyl acrylate - *co* – n-hydroxymethyl acrylamide
IER	ion exchange resin
KIT-6	Korean institute of technology
MCM	Mobil composition of matter
MRI	magnetic resonance imaging
NLDFT	non-local density functional theory
NMR	nuclear magnetic resonance
OMCTS	octamethylcyclotetrasiloxane
PFG	pulsed field gradient
PFGSE	pulsed field gradient spin echo
PFGSTE	pulsed field gradient stimulated echo
PHPMA	poly(*N*-(2-hydroxypropyl) methacrylamide)
PROJECT	periodic refocusing of j modulation by coherence transfer
PSD	pore size distribution
RAFT	reversible addition fragmentation chain transfer
R.F	radiofrequency
SAC	strongly acidic cation exchange resin
SBA	strongly basic anion exchange resin
SBA-15/16	Santa-Barbara amorphous
STEBPGP_1S	stimulated echo bipolar gradient pair sequence
STEM	scanning transmission electron microscopy
TOF	turn over frequency
VT	variable temperature
WAC	weakly acidic cation exchange resin
WBA	weakly basic anion exchange resin
XRD	X-ray diffraction

List of Tables

List of Figures

CHAPTER 1

Introduction

1.1. Characterisation of Porous Materials

Porous materials have become an integral part of recent advances in modern science. Their applications span over many industries ranging from catalysis, to medicine, and even construction. Their importance arises from their existence as a diverse set of structures, designed and synthesised to impact upon behaviour of any species present within its matrix. The matrix itself is a solid structure embedded with pores. These pores can be very regular, ordered and interconnected, as they often are in man-made matrices such as catalytic silica. However they can also be very irregular and disordered, as often found with naturally occurring porous materials. Their structures can be defined and characterised by a number of properties. The key properties include pore size, tortuosity, pore shape, surface area and pore volume. One property that often determines its applicability in catalytic science is the pore size. The size of the pores can be separated into three categories; microporous, mesoporous and macroporous, with the mesoporous region being the key area in this study. In chemistry, a macropore is defined as a void which is greater than 50 nm in diameter. A micropore is defined as being less than 2 nm in diameter. Mesoporosity is found within these two regions.

Porosity is a measure of the amount of voids present in a material. The distribution in sizes of these voids is referred to the pore size distribution, and this provides a quantitative representation of the entire pore size range in a solid. The extent of pore space in a compound affects several critical aspects of fluid dynamics such as movement of liquids though the matrix and the transport and reaction of chemical species. This phenomena controls the function of these materials and affects their ability to perform effectively in important scientific fields, such as drug delivery. Therefore, it is essential to probe the exact range of pore sizes present. Several techniques can be used to measure the

distribution including gas porosimetry, thermoporometry and image analysis. The advantages and disadvantages of these techniques are explored throughout this work.

The geometry of a pore can also affect the liquid's migration through the matrix. The size and geometry of a pore is one of the determining factors which defines the ability of a molecule to penetrate the pores and interact with its surface. Once inside the porous matrix, the behaviour of the liquid is then determined by the tortuosity. In a very ordered system, a molecule can easily flow and diffuse through the matrix. However, if the system is very disordered, consisting of different sized pores which are connected via twisted channels, then the molecule is highly affected by, for example, any interaction with the pore walls. Structures with large surface areas and high pore volumes are commonly used in gas separation, medicine and catalysis due to their ability to enable easy accessibility to the active site responsible for the catalytic activity. As chemical reactions occur on the surfaces of porous materials, it is critical that substances, both reactants and products, are able to diffuse through the porous matrices to reach the active sites. An underlying understanding on the overall structure and geometry is key to determining how well a material, such as a catalyst, can perform.

Nuclear magnetic resonance (NMR) has been established as an important technique in understanding liquid behaviour within porous materials. NMR properties of liquids in the vicinity of solids will change from those of the bulk liquid, including changes in state, diffusion and relaxation. As a routinely implemented spectroscopic technique that measures how different nuclei behave when subjected to an external magnetic field, NMR is becoming increasingly important in modern science, especially due to the advances of the materials which can now be observed. The development of novel NMR pulse sequences, in particular, has enabled further investigation into the characteristics of sophisticated systems, such as porous materials. These techniques provide an insight into not only the properties of the liquids, but also the environment in which they are placed.

There are a variety of solid-state NMR methods that offer the capability to extensively study a solid system. Liquid-state NMR techniques, including cryoporometry and diffusometry, should also be considered as significant contributors to this study. This work aims to demonstrate this significance, with the overall aim of investigating novel liquid/solid systems, which are at the heart of modern applied chemistry, through liquid-state NMR analysis.

1.2. Thesis Structure

This thesis explores the application of liquid state NMR techniques to study the behaviour of various liquids confined within porous materials. **Chapter 2** initially introduces some of the basic fundamentals behind the NMR technique and eventually focuses on the two main branches of physio-chemical phenomena studied in this work; how the diffusion of liquids are affected by confining environments and phase transition of a species within a pore. **Chapter 3** demonstrates some of the experimental considerations that need to be made prior to acquiring good quality data. These include temperature calibrations, convection compensation and gradient correction. These parameters needed to be carefully considered in order to ensure that all data presented herein was to the highest degree of accuracy.

The NMR cryoporometry method is established, in **Chapter 4**, using a set of porous materials with known and highly ordered pore sizes. It was essential to develop a protocol for variable temperature experiments prior to applying the method to other materials. **Chapter 5** then describes the application of NMR cryoporometry to catalytic silica, with particular emphasis on a new method for determining the two key parameters, which are essential for converting melting point depression data into accurate pore size distributions. Good correlations with other pore size determination techniques, differential scanning calorimetry and nitrogen porosimetry, show the applicability of the NMR technique.

Chapter 6 delves into the issue that there is a relatively small number of commonly-used probe liquids, with the requirement to match the probe liquid to the chemistry of the material being studied. Two

new cryoporometric liquids are introduced, t-butanol and menthol, where the latter is used particularly to access larger pore sizes. Both alcohols, as well as established cryoporometric liquids, water and cyclohexane, are then used to examine both the *effective* porosity in a cross-liked polymer hydrogel and the porosity of a macroreticular ion exchange resin, as described in **Chapter 7**. Focus switches to the diffusion behaviour of liquids within catalytic silica, in **Chapter 8**, in order to understand why esterification rates of reaction are different for acids confined within two different types of cylindrical pores. **Chapter 9** then summarises the work contained herein and suggests potential avenues for future work.

CHAPTER 2

NMR Theory and Application

2.1. Nuclear Magnetic Resonance

The origins of nuclear magnetic resonance date back to the start of the 20th century when in 1925, Pauli introduced the Pauli Exclusion Principle [1]. The existence of a fourth quantum number was suggested by Pauli and his principle stated that no two electrons could occupy a state with the same values for the four quantum numbers. Inspired by the work of Pauli, the concept of spin angular momentum was developed by Uhlenbeck and Goudsmit who interpreted the fourth quantum number as electronic spin [2]. A quantitative theory of the Zeeman Effect, assuming the ratio between magnetic moment and angular momentum is twice the ratio of orbital revolution, was established. The theory was then advanced by Schrödinger and Heisenberg as they explored a novel formulation for quantum theory by combining both representations of Schrödinger's constant operators and time-evolving wave functions with Heisenberg's constant state-vectors and variable operators [3, 4]. This theory was first put into practice by Rabi when he demonstrated how nuclei could be induced to flip their orientation by application of an oscillating magnetic field. The field consisted of a molecular beam of lithium chloride molecules within a vacuum chamber; work for which he was later awarded the Nobel Prize in 1944 [5].

The first NMR experiments in condensed matter, water and paraffin, were independently conducted by the Bloch [6] and Purcell [7] research groups, respectively. Purcell's method consisted of measuring energy absorption whereas Bloch's approach involved recording the current generated from the rotation of a magnetization vector, a combination of both the quantum and classical approaches. In 1952, both Bloch and Purcell were jointly awarded the Nobel Prize for their findings and their development of a new method for nuclear magnetic precision measurements. Magnetic resonance

primarily belonged to the physics community until in the mid-fifties where the contributions of Packard and Arnold [8] into the phenomenon known as chemical shift, allowed for different types of protons to be distinguished based on their chemical environment. NMR was now becoming a broad research field.

The ability of NMR to elucidate the physical and chemical properties of a system meant that magnetic resonance found application in medical fields. The principles of magnetic resonance was used to obtain a non-invasive and non-destructive measurement for the distribution of nuclei. A linear set of gradients ordered in different directions yielded a multi-dimensional image of the signal which allowed for the acquisition of spatial and chemical information simultaneously – known as magnetic resonance imaging (MRI) [9]. Lauterbur's in vivo studies into the behaviour of malignant tumours led to the understanding that the proton signals of the tumours had significantly longer relaxation times than healthy tissues. Mansfield then used these findings to develop an MRI protocol known as echo-planar imaging, which allowed for the development of images at a much quicker pace [10]. These findings were made possible due to the research of Hahn into self-diffusion coefficients [11], the development of this theory by Carr and Purcell [12] and the incorporation of these effects into the Bloch Equations, leading to the formation of the Bloch-Torrey Equation [13].

Modern day developments in the field of magnetic resonance have enabled more complex systems, such as porous media, to be probed and investigated. Figure 2.1 is a schematic representation of a modern day NMR spectrometer. Developments of simple pulse sequences has allowed for a greater ability to exploit new systems and obtain new information. This chapter will explore the fundamentals behind the NMR techniques used throughout this work.

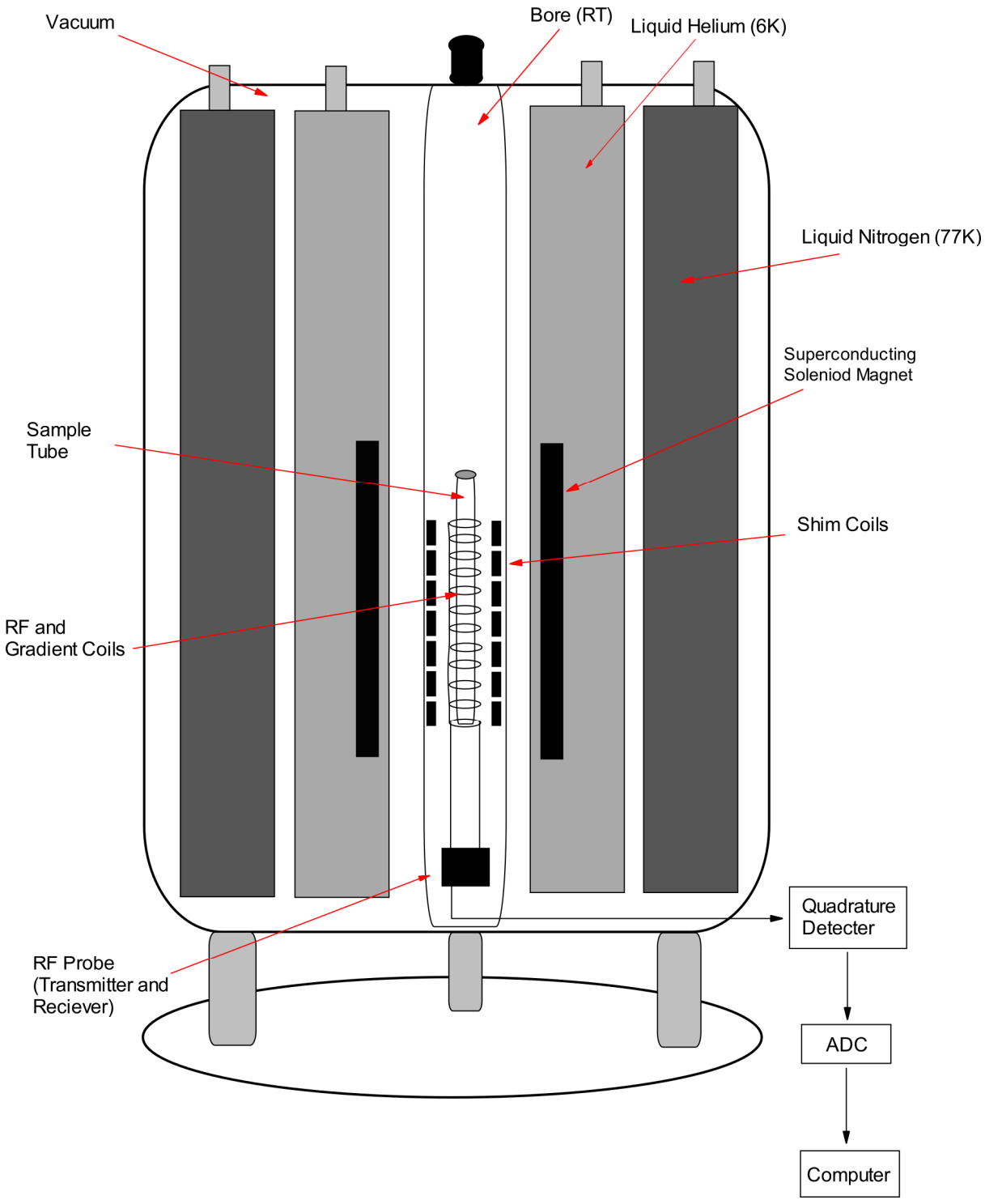

Figure 2.1. *Schematic representation of a modern day NMR spectrometer.*

2.2. Spin Physics

Nuclear magnetic resonance uses the principle that nuclei have an intrinsic angular momentum, known as spin. When subjected to a static magnetic field, B_o, the spin starts to precess at a rate that is dependent on the properties of the nuclei and the field itself. This rate is given by the Larmor equation

$$\omega = \gamma B_o \tag{2.1}$$

where γ is the gyromagnetic ratio of a given nuclei in units of rad s^{-1} T^{-1}. The gyromagnetic ratio is a constant for a given isotope of an element. The spinning nucleus possesses a magnetic moment, μ, and this is proportional to the gyromagnetic ratio, γ, the Planks constant, h, and the quantified angular momentum, known as spin, I.

$$\mu = \frac{h\gamma I}{2\pi} \tag{2.2}$$

The frequency at which precession takes place is called the Larmor frequency

$$\nu = \frac{\gamma B_o}{2\pi} \tag{2.3}$$

A schematic representation of the magnetic moment of a nuclei, and its Larmor precession, is illustrated in Figure 2.2.

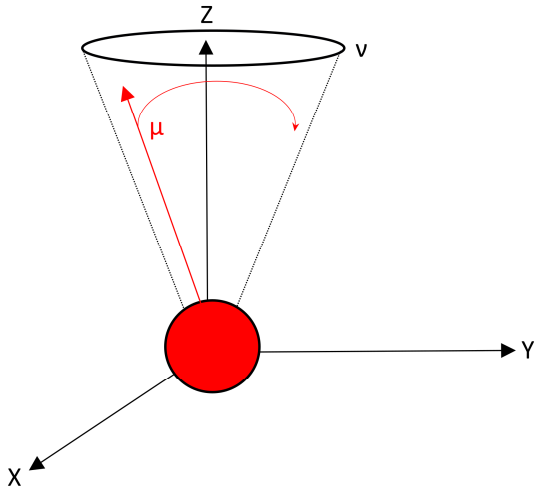

Figure 2.2. *Magnetic moment of a nuclei and its Larmor precession*

The spin quantum number, I, of a nucleus can be defined by the following values:

$$I = 0, \frac{1}{2}, 1, \frac{3}{2}, 2, \frac{5}{2}, \ldots.. \tag{2.4}$$

The overall spin of an atom, m_s, is governed by Pauli's Exclusion Principle that two electrons cannot hold the same values for the principal quantum number, n, the angular momentum, l, and the magnetic quantum number m_l. In atoms such as ^{12}C, the spins cancel each other out and the nucleus is not NMR active. Conversely, in atoms such as ^{1}H and ^{13}C, the nuclei possess an overall spin and are therefore NMR active. The nuclei's associated magnetic moment can have a possible 2n*I* + 1 projections which align themselves relative to B_o in parallel or anti-parallel fashion. A nucleus with spin = ½ will have two projections when a magnetic field has been applied. One spin will be with the field, α, and one spin will be against the field, β, as illustrated in Figure 2.3.

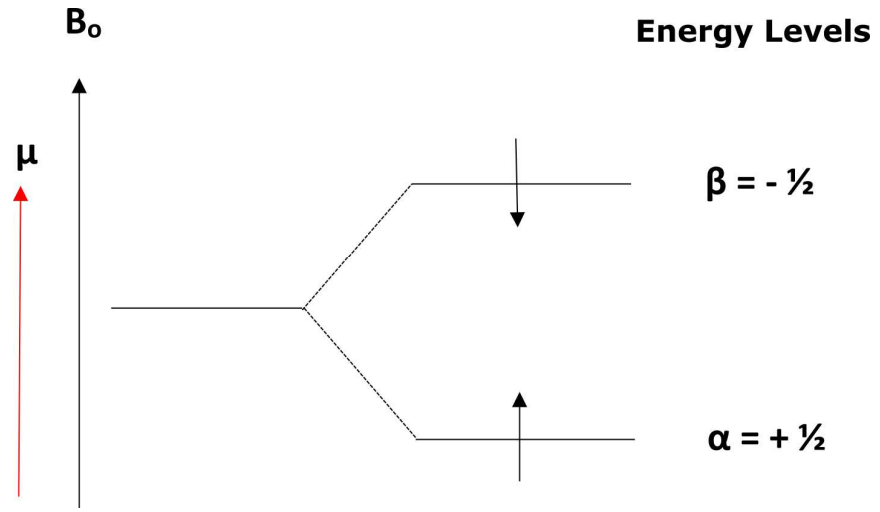

Figure 2.3. *Splitting of spins subjected to an applied magnetic field,* $\boldsymbol{B_o}$.

Spins which are parallel to the field are lower in energy than those which are not. The difference between the two spin states, ΔE, is proportional to Planck's constant multiplied by the frequency of radiation which is associated with the transition [14]. A transition between energy states can occur *via* the absorption of a photon if the energy of the photon exactly matches the energy difference between the two states. This occurs at the Larmor frequency and so the following expression can be derived:

$$\Delta E = \frac{h\upsilon}{2\pi} = \frac{h\gamma B_o}{2\pi} \qquad (2.5)$$

The difference in the number of spins in the higher and lower energy states is governed by the Boltzmann distribution:

$$\frac{\eta_{upper}}{\eta_{lower}} = e^{-\frac{\Delta E}{kT}} \qquad (2.6)$$

where k is the Boltzmann constant (1.38 x 10^{-23} J K^{-1}) and T is the temperature (K). The signal intensity is a result of the difference in energy emitted by the spins which make a transition from a higher to lower state and the energy absorbed by the spins which make a transition from the lower to higher state. Therefore, the signal intensity is proportional to the difference in population of energy levels.

The vector model is used as a qualitative means of describing how spins behave when subjected to a secondary field, otherwise known as an r.f. pulse, or B_1. It is a simple model which describes how the

static magnetic field, B_0, is applied along the z-axis of a set of Cartesian coordinates. The bulk magnetisation vector lies directly along the +z axis when in the absence of a secondary field and rotates when an r.f. pulse is applied so that the populations are equalised.

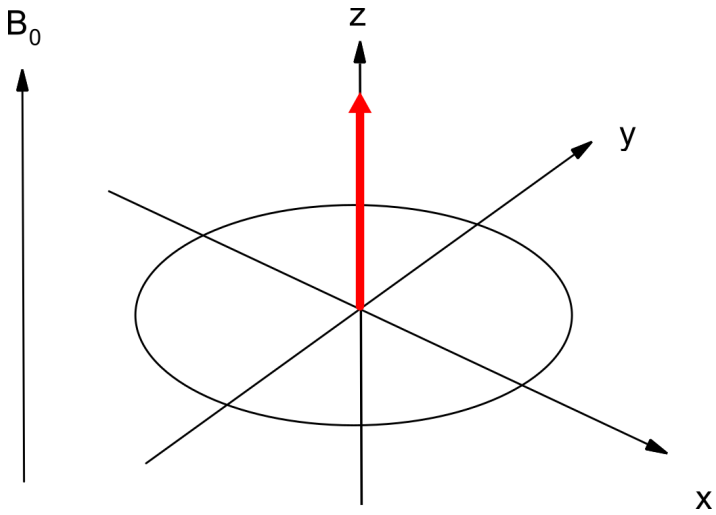

Figure 2.4. *Vector Model. When subjected to a magnetic field, the majority of spins align with the direction of the magnetic field, B_0.*

At equilibrium, the z component of magnetisation, M_z is equal to the equilibrium magnetisation, M_0. Following a 90° r.f. pulse, the magnetisation will be transferred into the transverse plane. Once the net magnetisation is placed in the transverse plane, it will start to rotate about the z-axis at the Larmor frequency.

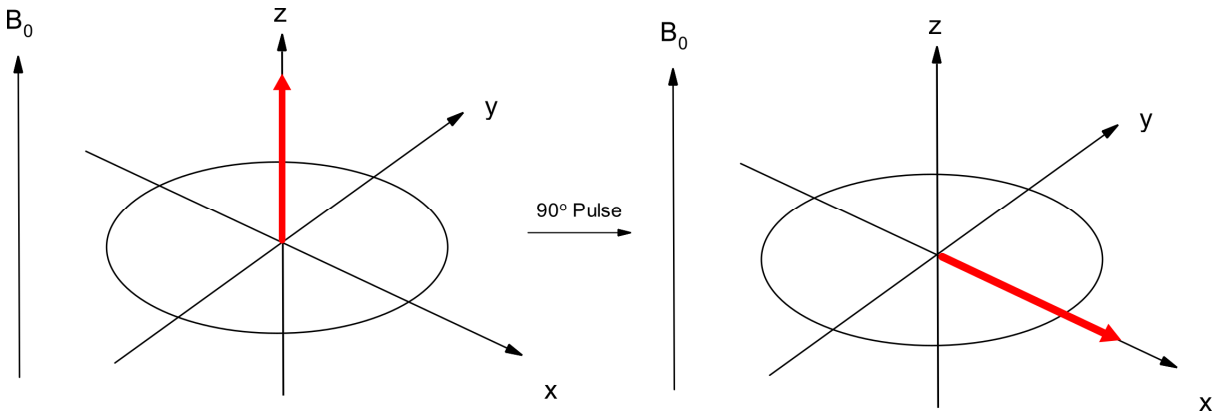

Figure 2.5. *Application of a 90° radio frequency pulse about the y-axis which transfers the magnetization into the transverse plane.*

In the stationary frame of reference, the magnetisation would now appear to be rotating about the z-axis. However, by assuming that the axis rotates, then the magnetisation would appear to be stationary. Implementing this rotating frame of reference is another way of observing the relationship between magnetic field and the magnetisation vector. There is an offset of difference in the frequencies of rotation of the frame and the Larmor precession, denoted by Ω [15].

$$\Omega = \omega_0 - \omega_{RF} \tag{2.7}$$

where ω_0 is the Larmor precession and ω_{RF} is the frequency of rotation of the field. A large offset would have an increasing effect on the magnetic field. This is referred to as the reduced field in the rotating frame of reference:

$$\Delta B = \frac{\Omega}{\gamma} \tag{2.8}$$

Therefore, in the rotating frame, the Larmor precession has been modified so that B_o is replaced by the reduced field, ΔB [15].

Routine NMR experiments mostly comprise of liquid solutions. When a liquid is located within a solid, the confined liquid will exhibit properties that are different to that of the bulk liquid. Understanding how and why they behave differently is key to understanding more about the system in which they are contained within. A recent area of interest for NMR analysis is the behaviour of liquids confined within porous solids.

2.3. Porous Materials

A porous material is one that contains a series of “voids” or “spaces” which can be filled by a gas or liquid [16]. Their structures can range from highly ordered, crystalline matrices to disordered, amorphous gels [17]. The pores can be isolated, or highly interconnected and their specific uses are dependent on their type of geometry and structure. Porous media are defined by a certain set of properties. These properties include pore shape [18], surface area [18], pore size distribution [19], pore

volume [18] and tortuosity [20]. The pore shape can affect the thermodynamics of the system and common pore shapes for ordered materials include cylindrical, spherical and ink-bottle (Figure 2.6).

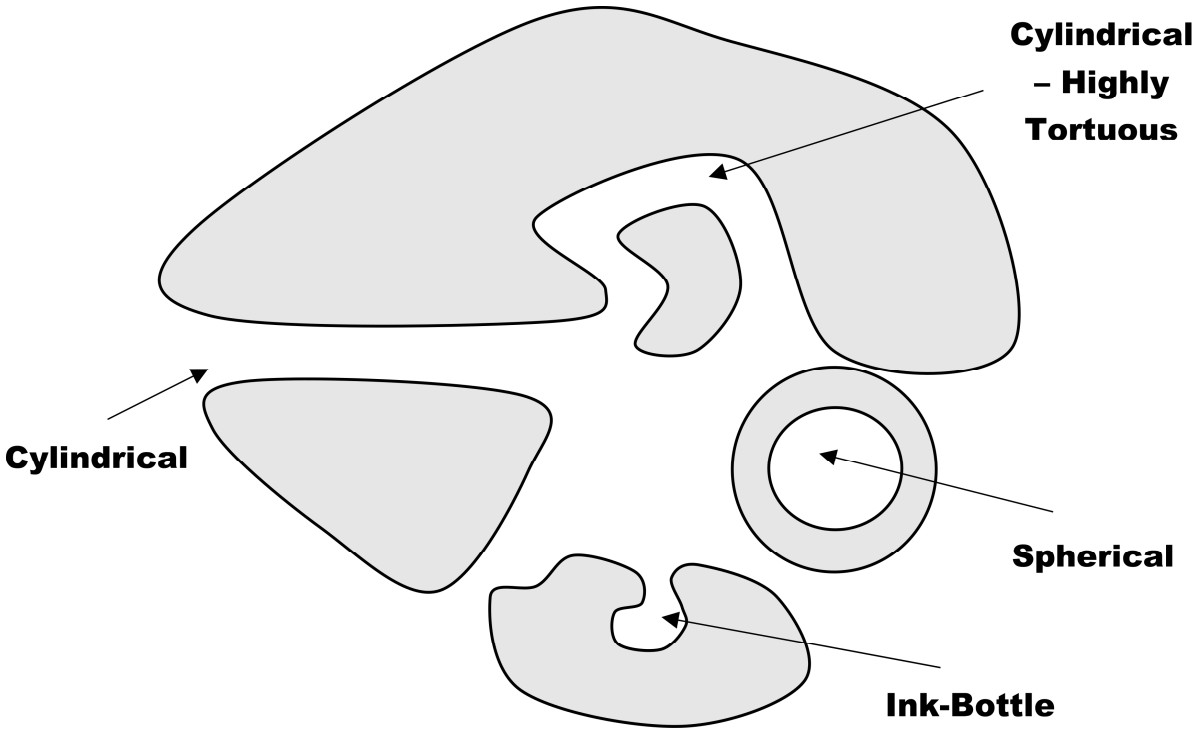

Figure 2.6. *Schematic showing the different types of pores possible.*

The size and shape of a pore is one of the factors which defines the ability of a molecule to penetrate the pore and interact with its surface. Table 2.1 illustrates a range of different types of porous materials with their typical pore size and surface.

Table 2.1. A range of different types of porous materials including their shape, size and surface type [21].

Species	Pore Shape	Typical Pore Sizes (nm)	Type of Surface
controlled pore glass	ordered cylindrical	7 - 70	SiO_2
silica	ordered cylindrical/spherical	3 - 20	Si, OH
zeolites	ordered cylindrical	0.8 - 1.3	O, Al, P
polymers	ordered/disordered	meso/macro	variable

Once inside the porous matrix, the motion of the liquid is highly influenced by the tortuosity. In a very ordered system, a particle can easily flow and diffuse through the matrix. However, if the system is very disordered, consisting of different sized pores which are connected via twisted channels, then the molecule is highly affected by interactions with the pore walls. As chemical reactions occur on the surfaces of porous materials, it is critical that substances, both reactants and products, are able to diffuse through the porous matrices to reach the active sites. Structures with large surface areas and high pore volumes are commonly used in gas separation, medicine and catalysis due to their ability to support the accessibility of the active site responsible for the catalytic activity [22]. Pore size distributions are often investigated to improve the transport of molecules within the porous matrix [23]. If the pores are completely isolated from one another, then the analysis into the size and shape of pores can be conducted individually.

A species' relaxation time will change depending on whether it's a solid or a liquid. In a solid, the relaxation is significantly quicker due to the molecules being frozen in place and therefore subsequently experiencing a larger rotational correlation time, τ_c. As such. the T_2 relaxation time is reduced when compared to that of the liquid (Figure 2.7). The relaxation of a species changes considerably when placed in a confined environment. The geometry of the pore can define the restrictions which are placed upon the molecular motion. As Forland [24] describes, a simple model is to

assume that the molecules are residing in two places, the surface layer and the middle of the pore. The molecules in these two environments will have different relaxation times. Those at the surface of the pore will relax much faster due to the pore wall interactions [25]. In the centre of large pores, the relaxation times approach the value of that of the bulk liquid. If there is a change in state, this observation is reversed as the molecules in the non-freezing surface layer experience significantly longer T_2 times than the crystalline centre [26].

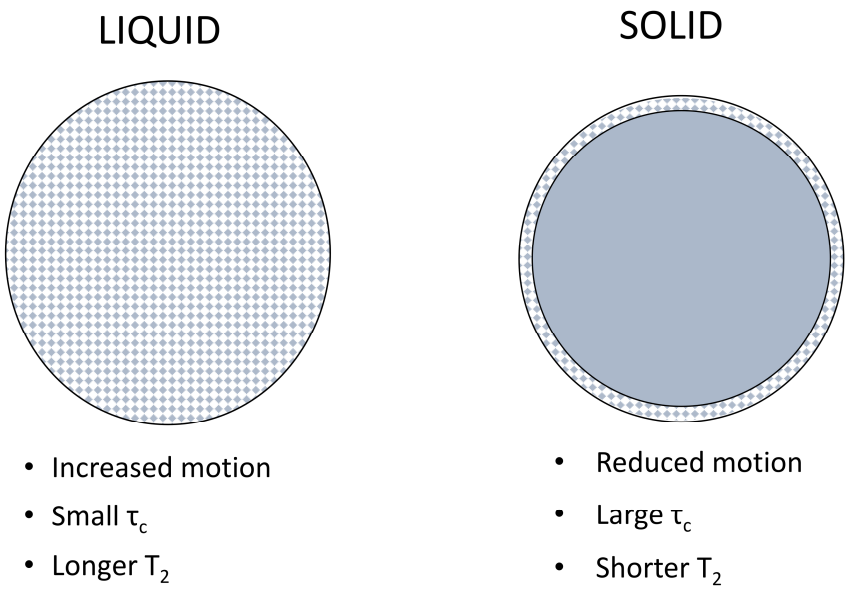

Figure 2.7. *Difference in* $\boldsymbol{T_2}$ *relaxation between a solid and a liquid.*

Relaxometry uses the enhanced relaxation of molecules at a pore surface to calculate the pore diameter, assuming rapid exchange between molecules at the surface and in the pores. The spin-lattice and spin-spin relaxation times are then proportional to the surface to volume ratio of the porous media [27]. This model was first proposed by Brownstein and Tarr [28] who calculated the following:

$$\frac{1}{T_{measured}} = \frac{1}{T_{bulk}} + \rho\frac{S}{V} \qquad (2.9)$$

Where ρ is a parameter that is governed by the surface relaxivity. For a particular material with a surface layer thickness of λ, the parameter ρ is expressed as:

$$\rho = \lambda \left(\frac{1}{T_{surface}} - \frac{1}{T_{bulk}} \right) \quad (2.10)$$

The above equations demonstrate how the relaxation of a material is affected by the geometry of the pore. However, the magnetic effect of the porous material has not been considered. Many materials, including natural porous media such as rocks, will exhibit large differences in the magnetic field susceptibility between the solid and the confined fluid [29]. Inaccurate diffusion and relaxation measurements [30], also leading to a significant loss of spectral resolution [31], are therefore often consequences of these inhomogeneities in the field. Several methods have been reported in the literature to obtain accurate T_2 measurements which compensate for these internal gradients. One method has been to incorporate the different diffusion regimes that a molecule may encounter when within a porous matrix. Mitchell *et al.* [32] describe how removing the influence of diffusion has allowed for accurate relaxation measurements to be obtained.

Mohnke and Yaramanci [33] minimise the effects of an inhomogeneous magnetic field and describe the relaxation of water in porous media via the following equation:

$$\frac{1}{T_2^*} = \frac{1}{T_{2bulk}} + \frac{1}{T_{2surface}} + \frac{1}{T_{2p}} \quad (2.11)$$

Where T_{2p} corresponds to the contribution of magnetic gradients. Using the spin echo sequence, the effect of T_{2p} can be minimised and be re-phrased as a diffusion term, T_{2D} [34]. According to Kleinberg and Horsfield [35], this diffusion term can be expressed as the following:

$$\frac{1}{T_{2D}} = D \frac{(\gamma g \frac{t_e}{2})^2}{3} \quad (2.12)$$

Where D is the diffusion coefficient, g is the gradient term, γ is the gyromagnetic ratio and t_e is the spacing between the pulse and the echo in the sequence. Therefore, by appropriate substitution, Equation 2.11 becomes Equation 2.13.

$$\frac{1}{T_2^*} = \frac{1}{T_{2bulk}} + \frac{1}{T_{2surface}} + \frac{D}{3}\left(\frac{\gamma g t_e}{2}\right)^2 \quad (2.13)$$

The effects of the internal gradient and subsequent diffusion can be minimised by choosing a small t_e so that the relaxation is purely dependent on the bulk and surface parameters only.

The physical properties that define a porous medium highly affect the behaviour of a liquid confined within it. Properties such as changes in state, diffusion and relaxation are examples of elements which can change depending on the environment in which the liquid is placed in. A technique which can accurately measure these properties is nuclear magnetic resonance. NMR methods offer a variety of opportunities for characterising molecular dynamics in confined environments due to the vast range of parameters that can be measured. The use of NMR is advantageous in understanding how solid structures, such as porous materials, impact upon liquid behaviour.

2.4. NMR Cryoporometry

2.4.1. Theory

Nuclear magnetic resonance cryoporometry is a non-invasive technique which investigates the distribution of pores sizes in a porous compound. The technique uses the thermodynamic phenomenon of a melting point depression, and the degree of depression is inversely related to the dimensions of the pore. Cryoporometry can accurately probe pore sizes down to *ca.* 2 nm in diameter and can be applied to a diverse range of structures from engineering and construction materials [36], to polymers and biological systems [37].

The thermodynamics behind melting point depression phenomena, and its dependence on surface curvature, was pioneered by J. W. Gibbs, J. Thomson, Sir W. Thomson (Lord Kelvin) and J.J. Thomson.

The equilibrium state of the formation of small crystals was discussed in the scientific papers published by Gibbs in the early 20th century, as he reflected the change in free energy that was caused by the curvature of the interfacial surface [38, 39]. J. Thomson also experimented in this area as he considered

the related theory of the melting point depression of ice that was caused by a change in pressure [40, 41]. J. J. Thomson explored this theory however he applied it to the temperature of a liquid droplet, rather than the pressure [42, 43]. Similarly, Sir W. Thomson developed a hypothesis for the equilibrium pressure at a curved interface describing capillary condensation, eventually leading to the formulation of the Kelvin equation [44]:

$$ln\frac{p}{p_o} = \frac{\gamma_{lv}v_m}{rRT} \tag{2.14}$$

where v_m is the molecular volume of the liquid and γ_{lv} is the surface tension of the liquid vapour interface. Rather than the curvature, the effect of confinement could also describe the condensation behaviour. The wetting of the pore wall by the liquid instead of the vapour may have caused a shift in equilibrium. In this case, the behaviour of the system is linked to the surface energy terms rather than the curvature.

The derivation of the Gibbs-Thomson equation can be best understood by considering two types of solid/liquid systems. The first is a generic sample cell comprising a liquid sitting on top of a solid. The system exists in complete equilibrium and will melt/freeze at the bulk temperature, T_m. With the addition of more heat, more liquid will form and with the removal of heat, more solid will form. The second is a system where a liquid is completely surrounded by a surface, such like a liquid confined in a pore. As no nucleation source is present, small crystals, with very high surface to volume ratios, will form at a lower temperature compared to that of the first system. The system itself is no longer in equilibrium.

The chemical potential of the liquid and the solid crystals in the second system can be related by the following equation:

$$\mu_l\,(T_m(x)) = \mu_s\,(T_m(x), P_2) \tag{2.15}$$

where μ_l is the chemical potential of the liquid at a temperature T_m inside a pore of x diameter, μ_s is the chemical potential of the solid that melts at a temperature T_m inside a pore of x diameter and P_2 is the Laplace pressure exerted on the crystal phase. The chemical potential of a system is related to temperature and pressure by the Gibbs Equation, $d\mu = -SdT + VdP$, where S is the entropy and V is the molar volume. The Laplace pressure is only applied to the solid phase whereas both phases are affected by a change in temperature. This is illustrated in Equation 2.16.

$$\mu_l\,(T_m) + -\int_{T_m}^{T_m(x)} S_l.\,dT = \mu_s\,(T_m) + -\int_{T_m}^{T_m(x)} S_s.\,dT + \int_{P_0}^{P_2} V_s.\,dP \quad (2.16)$$

where T_m is the bulk melting temperature, S_l is the molar entropy of the liquid, S_s is the molar entropy of the solid, V_s is the molar volume of the solid and P_0 is the initial pressure. All other terms remain the same as in Equation 2.15. As previously stated, the first system detailed above is in constant equilibrium. The chemical potential of the liquid is therefore equal to the chemical potential of the solid, at the same temperature. These can be cancelled to result in Equation 2.17.

$$-\int_{T_m}^{T_m(x)} S_l.\,dT = -\int_{T_m}^{T_m(x)} S_s.\,dT + \int_{P_0}^{P_2} V_s.\,dP \quad (2.17)$$

Assuming both the entropy of fusion and the molar volume of the solid remain constant over the temperature ranges studied, as well as applicable substitution of the Laplace pressure, Equation 2.17 can be simplified to produce Equation 2.18:

$$T_m(x) = T_m - \frac{4V_s\gamma_{sl}}{x\Delta S_f} \quad (2.18)$$

Equation 2.18 can then be re-written in terms of the enthalpy of fusion, ΔH_f, and the density to produce Equation 2.19:

$$\Delta T_m = T_m - T_m(x) = \frac{T_m}{\Delta H_f}\,\frac{4\gamma_{sl}}{x\rho_s} \quad (2.19)$$

where T_m is the bulk solid melting point, $T_m(x)$ is the melting point of a crystal with diameter x, ΔH_f is the bulk enthalpy of fusion, ρ_s is the density of the solid and γ_{sl} is the surface energy at the liquid-crystal interface. An additional term, the contact angle between the solid and liquid, also needs consideration [43, 45]:

$$\Delta T_m = -\frac{4\gamma_{sl}T_m}{x\Delta H_f \rho_s}\cos(\phi) \tag{2.20}$$

where $\cos(\phi)$ represents the contact angle. For cryoporometry experiments, the contact angle is assumed to be 180° due to the absorbents having a weak interaction with the surface. This ensures that the dimensions of the pore is the only defining parameter. For calculating the melting point depression of a small isolated spherical crystal of diameter x, the equation is given as:

$$\Delta T_m = T_m - T_m(x) = \frac{4\gamma_{sl}T_m}{x\Delta H_f \rho_s} \tag{2.21}$$

Assuming that γ_{sl} is isotropic and that the size of the crystal is large enough that it retains its bulk properties, the Gibbs-Thomson equation can be simplified into the following form [46]:

$$\Delta T_m = \frac{k_c}{x} \tag{2.22}$$

k_c is known as the melting point depression constant and incorporates a set of physical parameters which are indicative of the chosen liquid [47]. The melting point depression constant is geometrically dependent and a more accurate representation of ΔT_m takes the following form:

$$\Delta T_m = \frac{k_g.k_l.k_i}{x} \tag{2.23}$$

where k_g is a geometric constant that is dependent on the interfacial shape, k_l is a constant which relates to the crystal thermodynamic properties and k_i is a constant specific to the interfacial energy [47]. The geometry of the pores is determined by the k_g term and therefore it has been suggested that $k_g / x = S/V$ for a confined liquid freezing and that $k_g / x = dS/dV$ for a confined crystal melting [48], where *S* and *V* represent surface and volume respectively. The melting point depression constant is discussed further in Chapter 5.

A quantitative method of determining the pore size distribution was developed by Strange et al [49]. The pore volume, v, is proportional to the amount of liquid present in the sample and thereby, is a function of the pore diameter, x. When the pore is subsequently filled with a liquid, the volume becomes dependent on temperature, T. The change in pore volume with respect to pore diameter is given by:

$$\frac{dv}{dx} = \frac{k_c}{x^2} \cdot \frac{dv}{dT} \tag{2.24}$$

The distribution of pores is then determined from the slope of the melting curve, illustrated in Figure 2.8, to produce the distribution shown in Figure 2.9.

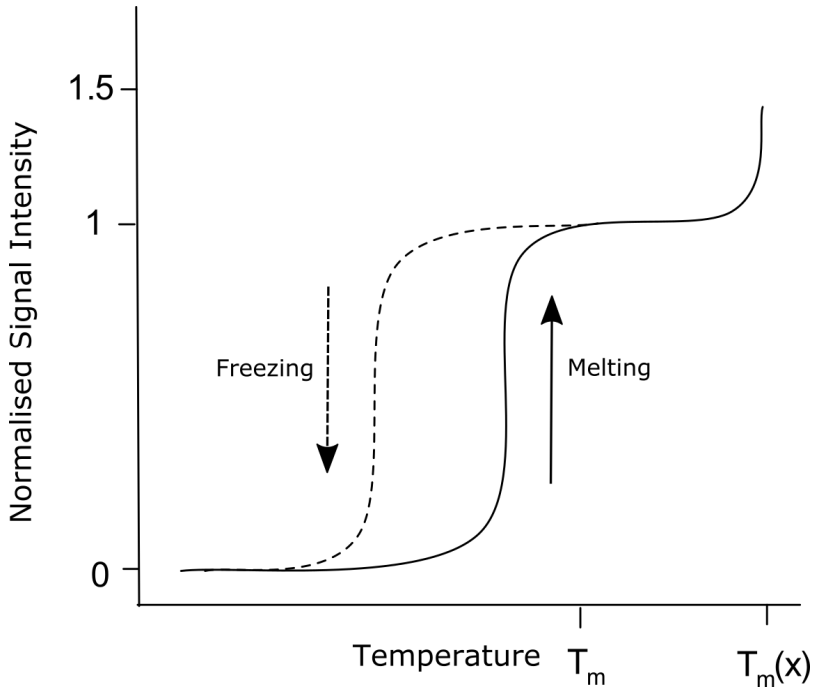

Figure 2.8. *Typical melting curve for a confined liquid (dashed line represents freezing curve, full line represents the melting curve).*

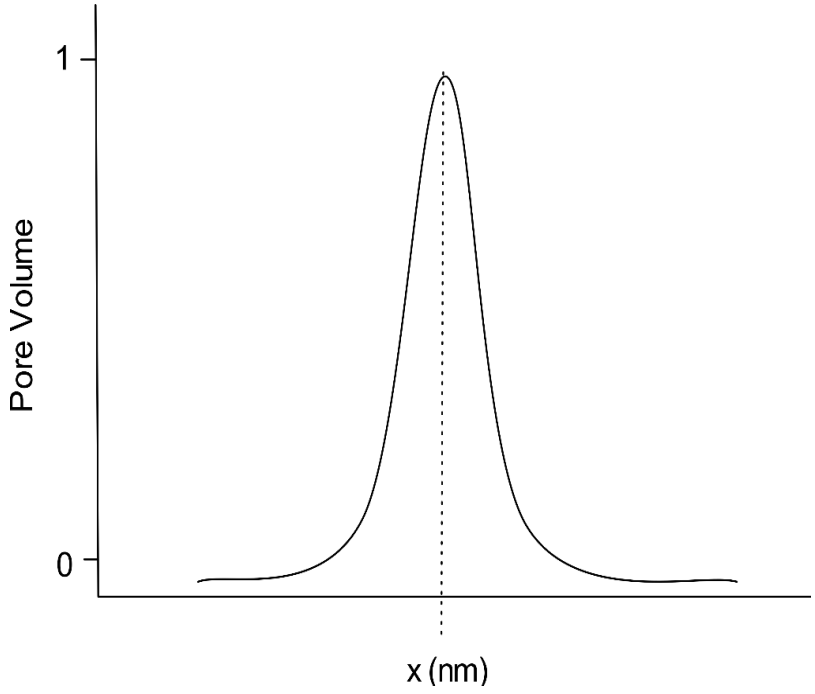

Figure 2.9. *A generic pore size distribution showing an average pore diameter of "x" nm. Pore volume is proportional to signal intensity therefore each change in signal intensity with temperature represents the change in pore volume with diameter.*

2.4.2. Deducing Pore Geometry

The measured signal intensity of an NMR peak is proportional to the amount of material present. It is possible to observe the liquid phase only, when in the presence of a solid, by careful choice of NMR experimental parameters. This is possible due to the difference in T_2 relaxation times between the solid and liquid phases. The transverse relaxation times for a solid are typically on the microsecond scale whereas the relaxation time of a liquid falls in the millisecond region. Upon reduction of the temperature, the signal intensity reduces until no residual signal is remaining – i.e. when the sample is completely frozen. When the temperature is increased, the signal intensity will also start to increase with the subsequent phase change however, a higher temperature is needed to initiate this phase change and overcome the activation energy barrier. A hysteresis between the freezing and melting cycles is observed (as depicted in Figure 2.8).

Several theories exist for the occurrence of a hysteresis in cryoporometry experiments [48, 50]. The first theory suggests that the confined liquid actually becomes super-cooled due to no nucleation source being present to initiate the freezing. Thus, the liquid falls into a metastable state. Super-cooling continues until freezing eventually occurs *via* homogeneous nucleation. Another explanation for the hysteresis phenomenon is that the freezing and melting processes initiate from different points and continue with different mechanisms. The freezing process will initiate the formation of a hemispherical meniscus with develops along the pore. Melting begins from the non-freezing layer at the surface of the pore and forms a sleeve-type meniscus [51]. In the case of an imbibed wetting liquid such as cyclohexane, the non-freezing layer propagates the melting phenomenon (from point Z in Figure 2.10 [51]) which leads to an increasing free energy as the dimensions of the solid changes.

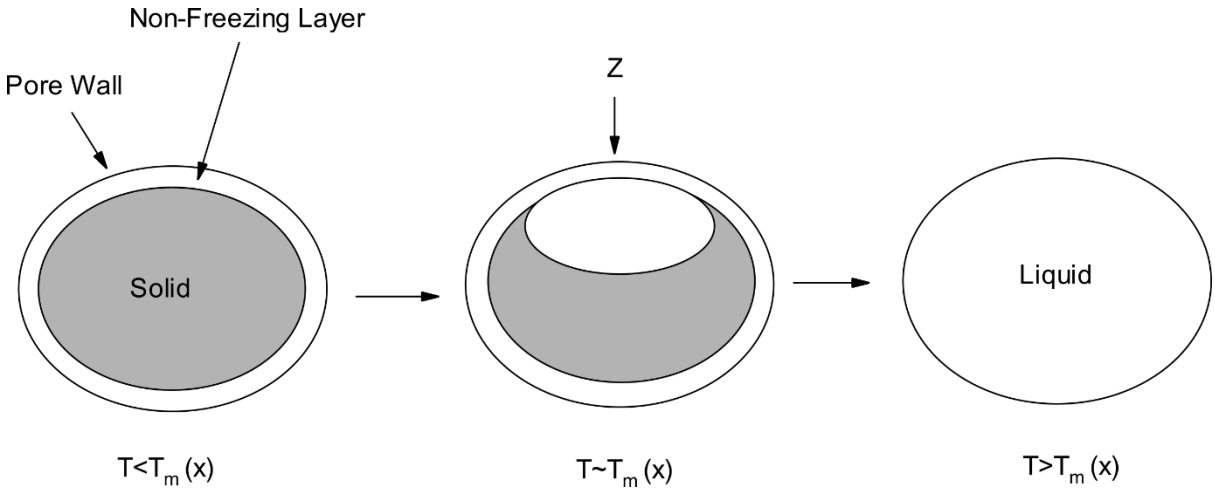

Figure 2.10. *Melting phenomenon of an imbibed wetting material.*

2.4.3. Experimental Considerations

The consistency of temperature regulation is essential throughout a cryoporometry experiment, especially in areas of phase transition, where temperature steps can be reduced to 0.1 K [52-55] to ensure that the data observed is as accurate as possible. The bulk melting temperature can also provide an *in-situ* reference for the temperature of the sample, only if an excess of liquid is present. Sufficient waiting times allow the sample to calibrate to its surroundings, with either at least 10 minutes being reported followed by repetitive acquisitions until the signal has stopped increasing [48].

The temperature cycle used in the experiment may change depending on the type of data that is being acquired. Petrov and Furo [56] detail the various protocols that can be used. A rapid initial freezing run will ensure that any potential supercooling effects are overcome [55]. However, Mitchell *et al.* [19] report that this process should be conducted very slowly to prevent the formation of metastable states. When frozen, the sample should be slowly warmed to obtain the melting curve. This two-step process is suited towards obtaining a pore size distribution in materials of known pore sizes, such as controlled pore glasses (CPGs). Petrov and Furo [56] also describe two other types of protocol. The second, a three step process, involves rapidly freezing the sample followed by slow warming and subsequent slow

cooling to obtain the depressed freezing point. The third protocol, suited for materials of unknown geometry, is a four-step process which involves two melting and two freezing steps.

During the course of a cryoporometry experiment, there are three main parameters that must be considered. The first is the effect on relaxation times. In order to observe the moment when a material changes state, a T_2 relaxation filter is used to distinguish between the solid and liquid phases. It is possible to observe this change due to the difference in T_2 times between a solid and a liquid. Applying a T_2 weighted filter also has the ability to suppress the effect and influence of diffusion in the inhomogeneous magnetic field [12, 57].

The second effect is the temperature dependence of Curie's law [58]. This law describes how the signal intensity will decrease with increasing temperature. In the plateau region between the pore and bulk melting, a decrease in signal intensity will be observed. One method of overcoming this, or more precisely compensating for it, is to normalise the signal intensity to that of a non-freezing liquid. This method is commonly used in cryoporometry experiments with liquids such as pentanol [59] and methylcyclohexane [24] being used. Alternatively, one could simply multiply the observed signal intensity by a factor of T/T_m where T_m is the bulk melting point and T is the temperature at which the current signal intensity is observed [60].

The other parameter which will impact the quality and accuracy of the observed signal is the tuning and matching of the probe. During the course of an NMR experiment, the sample experiences significant changes in temperature which will affect the electronics of the receiver coil. If the quality factor of the probe is high, then the excitation bandwidth will be small and consequently, there will be a shift in resonance frequency and a loss in signal [55]. Two independent experiments were conducted where the probe was only tuned at the lowest temperature and where the probe was tuned at every temperature step. The results indicated that both sets of data demonstrated the pore melting curve however, the melting of the excess water outside of the pores was only witnessed when the probe

was properly tuned. It was concluded that the intensity loss caused by a de-tuned probe could even mask the bulk melting step.

2.5. Alternative Pore Size Determination Techniques

2.5.1. Differential Scanning Calorimetry (DSC)

Differential scanning calorimetry (DSC), similarly to NMR cryoporometry, is a thermoporometry technique. DSC uses the high sensitivity to endothermic melting and exothermic freezing in order to produce a pore size distribution. The theoretical basis of the technique follows the Gibbs-Thomson thermodynamics outlined in Section 2.4.1 with more of a focus on surface curvature. Landry [61] describes how for curved surfaces, the Gibbs phase rule states that two independent degrees of freedom are present, based on a relationship between surface curvature and the solid/liquid phase transition derived by Defay *et al.*[43].

The procedure outlined in both Landry [61] and Majda *et al.* [62] allows one to transform the DSC melting curves into a pore size distribution. The temperature axis is converted into a pore size scale, in this particular case for water, by

$$D_p = 2\left(\frac{19.082}{\Delta T_m + 0.1207} + 1.12\right) \tag{2.25}$$

where D_p is the pore diameter in nm and ΔT_m is the melting point depression in K,. The heat measured heat flow is then converted into a pore volume using

$$\frac{dV_p}{dD_p} = \frac{dQ}{dt}\,\frac{dt}{d(\Delta T)}\,\frac{d(\Delta T)}{dD_p}\,\frac{1}{m\Delta H_f \rho_s} \tag{2.26}$$

where $\frac{dV_p}{dD_p}$ is the change in pore volume in cm^3 g^{-1} nm^{-1} , $\frac{dQ}{dt}$ is the heat flow in J s^{-1}, $\frac{dt}{d(\Delta T)}$ is inverse of the scanning rate of the experiment in s K^{-1}, $\frac{d(\Delta T)}{dD_p}$ is determined from the empirical equation for water

(Equation 2.25) in K nm^{-1}, m is the mass of the dry silica in g, ΔH_f is the bulk enthalpy of fusion in J g^{-1} and ρ_s is the density in g cm^{-3}.

2.5.2. Nitrogen Porosimetry

Both thermoporometry techniques, NMR and DSC, use the principle of a solid to liquid phase transition. In contrast, nitrogen porosimetry observes a phase change from gas to liquid due to capillary condensation. Porosimetry is an example of physisorption and due to the weak enthalpy of adsorption, it occurs only at temperatures lower than adsorbate boiling point [63]. The physisorption processes that occur within a porous material are dictated by two main factors. The first is the effect of the confining geometry on the thermodynamic stability of the adsorbate and the second is the relationship between fluid-fluid and fluid-wall interactions. These relationships give rise to the type of hysteresis observed for the corresponding isotherm [64]. For mesoporous materials, the systems of interest during this project, type IV and V isotherms are typically observed.

For pores which are ordered and uniform, such as the cylindrical pores in catalytic silica, a pore size distribution can be obtained using the Barrett-Joyner-Halenda (BJH) method. This method uses the thermodynamic principles behind the Kelvin equation (Equation 2.14). In the case of smaller pore sizes, from *ca.* 2 nm to 6.5 nm, such like those studied in this work, a modified Kelvin Equation was found to more accurately predict pore size. The corrected equation takes into account a small film that builds up on the surface of the pore. The analysis of Kruk [65] and Broekhoff and de Boer [66] demonstrated a good agreement of actual pore sizes of MCM-type silica and those obtained using the corrected equation.

Using the unmodified Kelvin equation to predict pore size has its disadvantages. It has been shown that in systems containing pores less than 10 nm, the BJH method appears to slightly underestimates pore size. Methods based on molecular simulation, such as the non-local density functional theory (NLDFT), are now widely used in pore size analysis. This methodology predicts a pore size by numerical

deconvolution of isotherm data using a set of model isotherms covering the entire range of pore sizes accessible for the adsorbate [67].

The aforementioned techniques all aim to use changes in state to produce a pore size distribution. One other major aspect of studying porous materials, key to areas such as drug delivery, is to understand how liquids diffuse through the, now well-defined sized, pores.

2.6. NMR Diffusometry

2.6.1. Diffusion in Relation to Molecular Size

By applying a magnetic field gradient to a relatively simple pulse sequence, NMR can be used to evaluate the diffusion and flow of molecules. All molecules exhibit Brownian motion which represents the random continuous motion of the compound in a homogenous field [68]. This motion, together with information about the size and shape of a molecule, can be used to characterise such molecules by a parameter known as the diffusion coefficient, D. The size of the molecule is governed by its hydrodynamic radius, r_s, and the molecule is assumed to take the shape of a sphere so that it fits the Stokes equation. Combining the molecular dimensions to Einstein's theory results in the Stokes-Einstein equation.

$$D = \frac{k_b T}{6\pi\eta r_s} \tag{2.27}$$

Other parameters include the temperature, T, the Boltzmann constant, k_b and the viscosity, η. The diffusion coefficient is therefore inversely related to the size of the assumed spherical molecule. Smaller molecules will have larger diffusion coefficients whereas larger molecules will have smaller diffusion coefficients, making these experiments perfect for mixture analysis [69, 70]. Diffusion is highly sensitive to changes in temperature and viscosity and as such, these parameters must be held constant during an experiment.

In the presence of a pulsed field gradient (PFG), the magnetic field is no longer constant. During the time the gradient is active, there is a spatial dependence of precession and a helix of phase is wound into the sample (Figure 2.11). The physical location of a molecule is encoded and the diffusion of the molecule can be observed. Due to the variation in magnetic field, Equation 2.1 is no longer valid. In order to measure the frequency, the gradient strength and the direction that the gradient is applied in have to be taken into consideration. Equation 2.28 more accurately reflects the relationship between magnetic field and the gyromagnetic ratio of the proton:

$$\omega = \gamma(B_o + z.G(z)) \tag{2.28}$$

Diffusion is measured via the application of these gradients. In the most simple diffusion NMR sequence, two gradients are applied [71]. One which winds in the helix of phase and one which unwinds it. As a result of this application, phase shift is refocused and the diffusion of the molecules leads to a distribution of signal phases – resulting in a subsequent attenuation of the NMR signal. This attenuation of signal can be quantitatively measured by factoring in several parameters which give rise to the signal. These parameters are the diffusion delay period (which is dependent on the pulse sequence used), Δ', the length of the gradient pulse, δ, the strength of the applied gradient pulse, g, the gyromagnetic ratio of the observed nuclide, γ, and the diffusion coefficient, D. A combination of these factors lead to the Stejskal-Tanner equation [72].

$$S = S_0\, e^{-D\gamma^2 g^2 \delta^2 \Delta'} \tag{2.29}$$

As the constants γ, δ, Δ' and g are known, the diffusion coefficient may be directly calculated from a linear plot of $\ln(S/S_0)$ vs gradient strength with the slope of the straight line yielding the diffusion data.

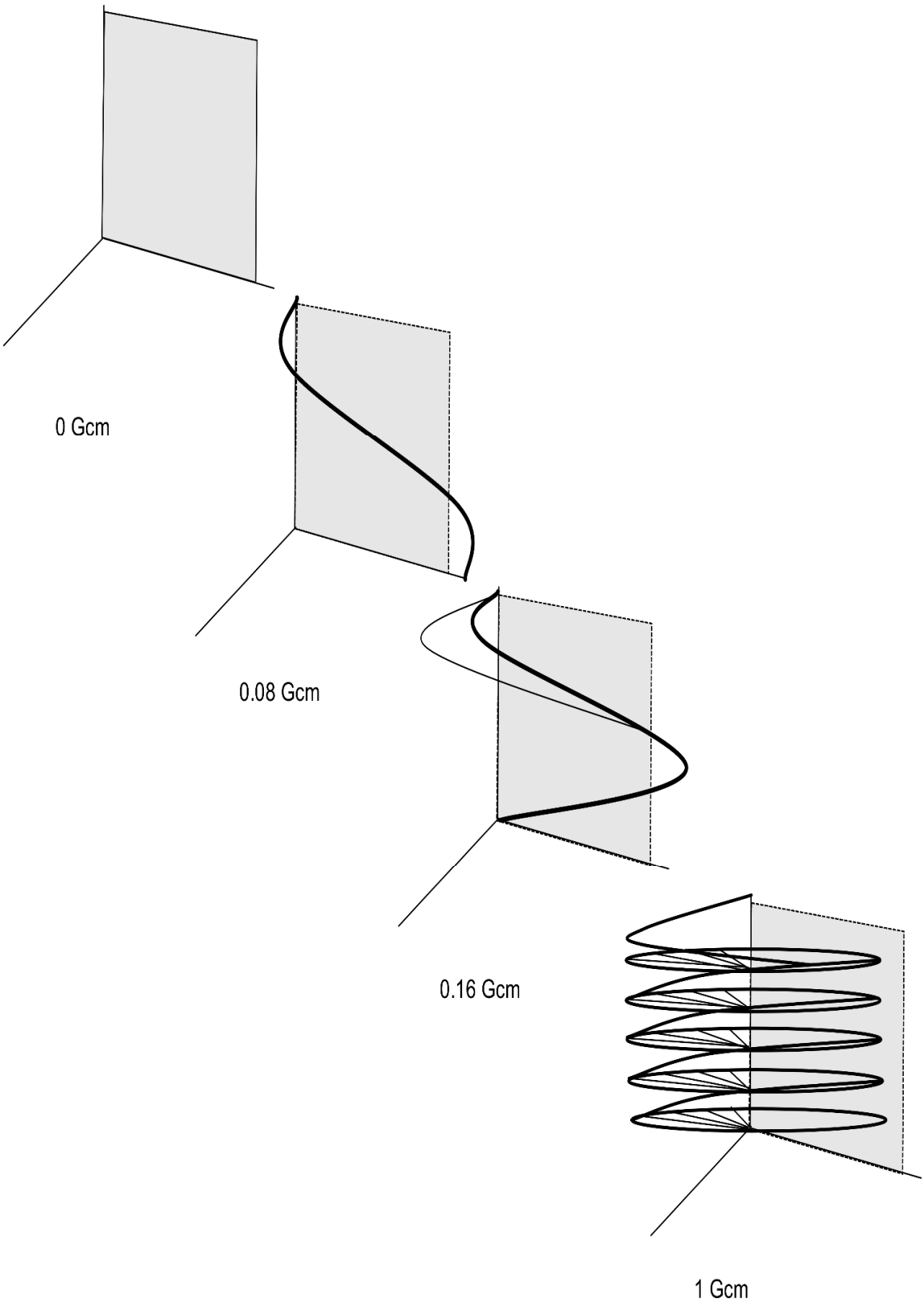

Figure 2.11. *Application of a gradient winds in a helix of phase in to the sample.*

2.6.2. Diffusion NMR Techniques

The most basic diffusion sequence is called the pulsed field gradient spin echo (PFGSE) (Figure 2.12). In this sequence the magnetisation is firstly placed into the transverse plane via a 90° pulse (thin black rectangle). The application of the first gradient then winds in a helix of phase into the sample followed by the unwinding via a second gradient of equal magnitude and duration. Prior to the second gradient pulse, a 180° pulse (thick white rectangle) is applied to invert the dispersed magnetisation and refocus part of the chemical shift. Complete refocusing of the signal is only achieved if the spin remains in the same physical location when the two gradients are applied. The time between the two gradients is the diffusion delay period, and is denoted by Δ. The longer the diffusion delay period, the more time the molecule has to move through the sample. Thus, significantly long delay times will result in an increased signal attenuation arising from relaxation losses [73].

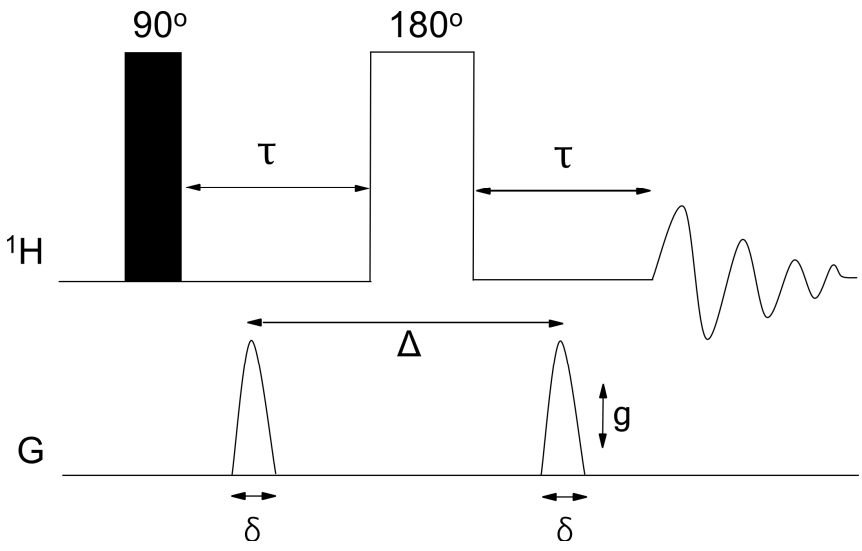

Figure 2.12. *Pulsed field gradient spin echo sequence. Each gradient pulse has the strength,* $\boldsymbol{g}$*, and has the duration,* $\boldsymbol{\delta}$*. The diffusion delay time is denoted as* $\boldsymbol{\Delta}$ *and the parameter* $\boldsymbol{\tau}$ *is a variable diffusion delay time parameter.*

In terms of characterisation, changes can be made to Δ, δ, or g, in order to analyse the effect on diffusion data. Increasing Δ allows more time for the molecule to move through the sample whereas increasing δ or g will increase the amount of dephasing the signal will suffer across the sample. One

major disadvantage of this pulse sequence is that during the diffusion delay period, there is evolution of coupling. The application of the first 90° pulse means that the magnetisation is in the transverse plane during the diffusion delay period and this leads to signal distortion. Furthermore, the loss of magnetisation is dictated by T_2 relaxation. This is a major problem for larger molecules as they would require a large Δ, and increased, undesirable signal attenuation.

In order to overcome this issue, the pulsed field gradient stimulated echo sequence (PFGSTE) is used [74] (Figure 2.13). This sequence replaces the 180° pulse with two 90° pulses and only half of the in-phase magnetisation is rotated back to the longitudinal axis from the transverse plane. As a result, only half of the magnetisation is in the transverse plane for the shorter period of τ, rather than the longer diffusion period, Δ. The loss of magnetisation is now dictated by T_1 relaxation [73].

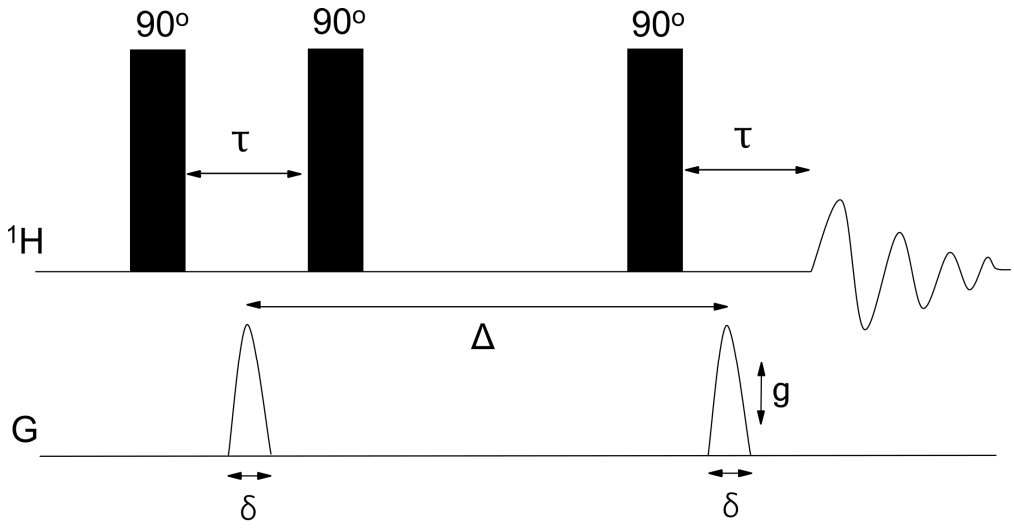

Figure 2.13. *Pulsed field gradient stimulated echo pulse sequence. Each gradient pulse has the strength,* $\boldsymbol{g}$*, and has the duration,* $\boldsymbol{\delta}$*. The diffusion delay time is denoted as* $\boldsymbol{\Delta}$ *and the parameter* $\boldsymbol{\tau}$ *is a variable diffusion delay time parameter.*

Despite the advantage of a cleaner spectrum, this result comes at a cost. In comparison to the spin echo sequence, there is a reduced signal intensity by a factor of two. This is due to only one component of transverse magnetisation being placed back along the z-axis during the diffusion delay period, as described above. The other component is removed via the phase cycling technique [73]. A further enhancement to this technique is the use of bipolar gradient pulse pairs (Figure 2.14). The introduction

of these pairs allows one to greatly reduce the distortions resulting from gradient application without the need for adjustments or additional hardware. The single gradient pulse, as seen in the conventional stimulated echo sequence, is now replaced by two pulses of half the duration which are opposite is sign to one another but equal in size. Between these two gradients is the application of an 180° pulse which as seen previously, inverts the dispersed magnetisation activated from the first gradient [75].

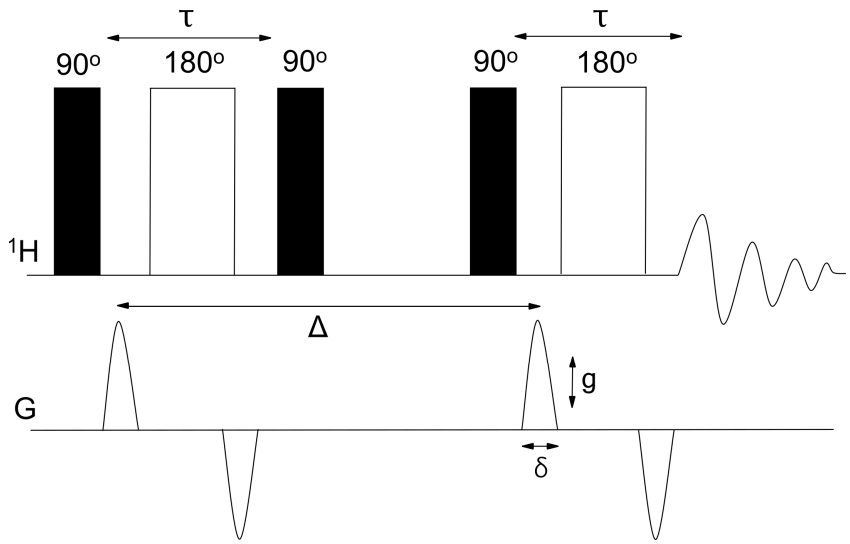

Figure 2.14. *Pulsed field gradient stimulated echo pulse sequence with bipolar gradient pairs. Each gradient pulse has the strength,* $\boldsymbol{g}$*, and has the duration,* $\boldsymbol{\delta}$*. The diffusion delay time is denoted as* $\boldsymbol{\Delta}$ *and the parameter* $\boldsymbol{\tau}$ *is a variable diffusion delay time parameter.*

A further advantage of this sequence is its effect on the lock system. A single gradient pulse, such as in the conventional stimulated echo sequence, will dephase the lock resonance. However, the bipolar pair of gradients do not affect the lock system and instead they refocus the signal. As a result, high resolution NMR spectra can be obtained without line shape distortions [76]. Despite the advantages of using a bipolar gradient pulse sequence, to determine extremely accurate measurements by ensuring the correct coherence pathway is chosen, extensive phase cycling is required.

To combat the issue of time/accuracy dependence, a new sequence was designed which implemented the accuracy of bipolar pulse pairs with the speed of a conventional spin-echo sequence. This sequence, known as one-shot [77], allows for diffusion data to be acquired in a single cycle without

compromising resolution. Any magnetisation that is not refocused by the 180° pulse is de-phased by the action of the unbalanced bipolar pulse pair of gradients. The gradient pairs are unbalanced by an intensity factor of 1+α and 1-α, respectively, plus a further 2 additional gradients of intensity 2α, either side of a purge gradient, which removes the unwanted magnetisation [73]. This sequence is discussed further in Chapter 3.

2.6.3. Diffusion in Porous Media

When a liquid is imbibed within a porous material, each particular spin has a slightly different diffusion coefficient depending on their spatial position within the pore. Spins which are near, or in contact with, the pore walls will relax much faster than the spins in the centre of the pore, impacting upon its motion. The overall diffusion coefficient then becomes an average of the values experienced by all spins. Monitoring the displacement of a fluid in a confined environment can also yield information on the solid structure, as well as the diffusing liquid. Solid properties such as pore size, surface to volume ratio and tortuosity will all impact upon the behaviour of the fluid.

The solid structures in porous media, such as pore walls, effectively provide barriers for diffusion. As a result, the diffusion of a substance is now restricted. The displacement of the fluid in an inhomogeneous matrix is highly dependent on the type of solid support. Two types of diffusion can occur when a molecule is subjected to a porous matrix. Either the molecule can diffuse in between the particle bed or inside the pores of the particle itself. Both cases are related to the porosity, ε, and tortuosity,τ, of the matrix [78].

$$\frac{D_t}{D_0} = \frac{D_{INTER}}{D_0} = \frac{\varepsilon}{\tau} \tag{2.30}$$

The restriction on diffusion now introduces a time-dependent root mean square displacement. The longer the molecule diffuses, the more restrictions it will encounter [78]. Geometrical barriers lead to a diffusion coefficient which will reduce with time. Valiullin and Skirda [79] introduce a dimensionless parameter, ξ, which combines the diffusion coefficient of the bulk material with the restrictions

implemented by the porous matrix. The region in which ξ<<1 is described as the short-term region, as the displacement of the substance is much less compared to the dimensions of the pores. In the region in which ξ>>1, the molecules have sufficient time to experience many collisions with the pore walls. Understanding these two regions, as well as the crossover between the two, allows for the determination of the specific characteristics of the porous medium. Stallmach and Karger [80] evaluated the theory of different diffusion regions by introducing three characteristic lengths in order to estimate the possible effects of pore geometry on the diffusion path and thus, on the NMR measurements. These three characteristics are l_{PFG}, l_{DIFF} and $< R >$. l_{PFG} represents the length scale over which enough diffusion occurs to cause a significant change in the spin echo attenuation. This value can be easily controlled by changing the diffusion parameters such as gradient strength and width. The second characteristic, l_{DIFF}, is the root mean square displacement of the molecule and is dependent on the observation time and the diffusion of the molecule according to Equation 2.31. It is assumed that the particle's diffusion is isotropic (in 3-dimensions).

$$l_{DIFF} = \sqrt{6D\Delta} \tag{2.31}$$

The third characteristic is the mean pore radius, $< R >$. The observed diffusion may well be dependent on the average pore diameter of the pore, if the pore size is sufficiently small enough. A combination of these characteristics can determine the different types of diffusion that occur in porous media. The first case is unrestricted, free diffusion within the pore space where $l_{DIFF} \ll < R >$. In this case the displacement of the diffusing molecule is considerably less than the radius of the pore and therefore, the diffusion is comparable to that of the bulk liquid. Under this condition, the diffusion does not reflect any properties of the confining pore geometry. In PFG-NMR measurements, this case can be matched by using short observation times so that:

$$\Delta \ll \frac{< R >^2}{6D} \tag{2.32}$$

The second case is diffusion in well-connected pores where $l_{DIFF} \gg < R >$. When the pores are well connected, the diffusion length may exceed the diameter of the pore. It is therefore not the size of the pore which is the determining factor in its diffusion, but the connectivity of the solid structure. The tortuosity, τ, is explored further in Chapter 8.

In PFG-NMR measurements, this condition can be met by using long observations times so that:

$$\Delta \gg \frac{< R >^2}{6D} \tag{2.33}$$

Under these parameters, the molecules will undergo interactions with the pore wall the measurements reveal an *effective* tortuosity, also dependent on the liquid species. The third case involves restricted diffusion in isolated pores where $l_{DIFF} = < R >$ and $l_{PFG} \gg < R >$. In this case the pores are isolated and the displacement is restricted by dimensions of the pore. The final position of a molecule is now not dependent on the starting position in the same pore. Consequently, the spin echo attenuation is independent of observation time and the pore size of the porous medium can be calculated from the equations outlined in Reference 80.

The final case involves the restricted diffusion on the pore surface. As long as l_{PFG} exceeds l_{DIFF}, the surface to volume ratio of the pore matrix can be derived from PFG-NMR measurements. The surface to volume ratio is an important parameter in systems in which the surface of a pore drives the chemistry, such as catalysis [81]. The surface to volume ratio can be incorporated into obtaining the diffusion coefficient via the following equation [82]:

$$D(\Delta) = D_0\left(1 - \frac{4}{9\sqrt{\pi}} \frac{S}{V} (D_0\Delta)^{\frac{1}{2}} + \cdots\right) \tag{2.34}$$

These characteristics have been outlined as described in Stallmach and Karger [80].

2.7. Summary

This chapter has introduced some of the fundamental principles of NMR spectroscopy that will be applied throughout this work. The background behind the techniques of cryoporometry, diffusometry and relaxometry have been explored and will be applied to a range of advanced materials in the forthcoming chapters.

CHAPTER 3

Calibration of Experimental Parameters

4.1. Introduction

The spectrometer used throughout this project had not previously been extensively used for NMR experiments involving significant temperature ranges nor any diffusion measurements. As such, in order to ensure accuracy and precision for all measurements, preliminary studies into the performance of the spectrometer was necessary.

Pulsed field gradient measurements can be severely affected by temperature fluctuation and errors in gradient application. An NMR spectrometer contains a series of gradient coils in the x, y and z directions. When a current is passed through these coils, a secondary magnetic field is created. This secondary field distorts the main field so that the resonance frequency of the protons will vary as a function of position, therefore encoding a spatial dependence on the signal. The size of this secondary field is related to the current passing through the coils, typically stated as a percentage, by a gradient calibration constant which is specific for each magnet. In order to ensure all diffusion measurements were as accurate as possible, it was essential to evaluate the value of the calibration constant using a set of solvents with known diffusion coefficients for a given temperature.

In temperature controlled experiments, the accuracy of diffusion measurements can be affected by heat loss, internal temperature gradients and cooling gas flow rate [83]. Furthermore, the temperature that the spectrometer states is not the actual temperature of the sample contained within the NMR tube. Experiments performed at temperatures away from ambient room temperature have a high chance of being affected by convection, especially in thin-walled NMR tubes. It was therefore necessary to carefully check all of these aspects of the spectrometers performance.

In variable temperature experiments, the temperature is dictated by the passing of a gas over the sample inside the spectrometer. The gas enters and first comes into contact with the base of the tube, resulting in the cooler part of the sample residing at the bottom. The resulting temperature gradient, $\frac{dT}{dz}$, will lead to the onset of convective flow as soon as it reaches a critical value. This process is known as Rayleigh-Bénard convection and is described by Equation 3.1.

$$R = \frac{g\alpha r^4 \Delta T}{\kappa \nu} \tag{3.1}$$

R is known as the Rayleigh-Bénard number and is dependent on the radius of the tube, r, the temperature gradient across the tube, ΔT, the kinematic viscosity of the liquid, ν, acceleration due to gravity, g, the volumetric thermal expansion coefficient, α, and the thermal diffusivity, κ.

It would be assumed that, if the warmer liquid was already at the top, no convection would occur [84]. However this is not the case. Due to the probe and incoming air not being perfectly symmetric, horizontal gradients also exist across the sample, producing a type of convection which is known as Hadley convection [85, 86]. Hadley convection, or transverse convection, is not a critical phenomenon and as such, should always assumed to be present to a certain extent [87]. The presence of both types of temperature gradients have been proved by Loening and Keeler [83] who illustrated the temperature profile within an NMR probe with both longitudinal and transverse temperature gradients present. As expected, the temperature varied much more along the z-axis, suggesting, that in the system studied, Rayleigh-Bénard convection was the dominating contribution to overall flow.

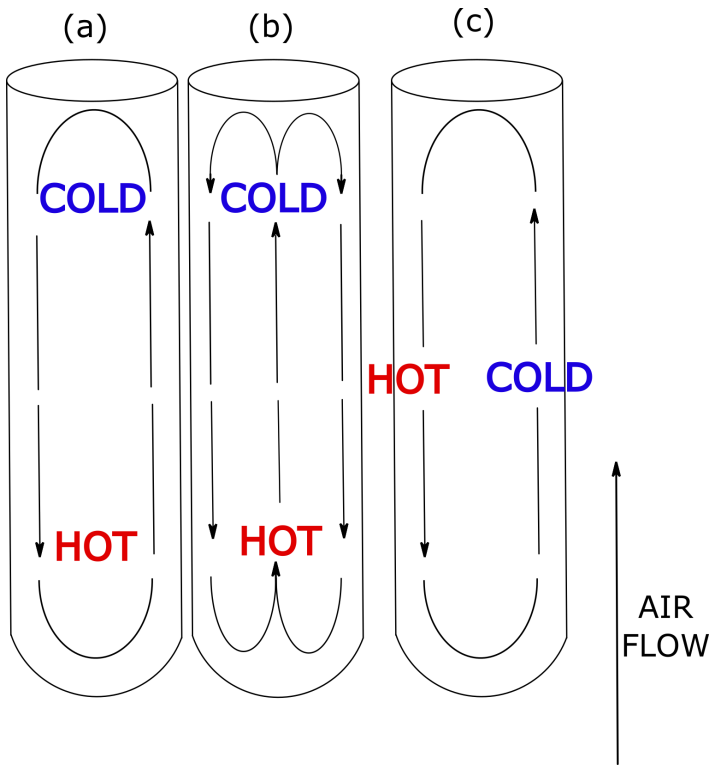

Figure 3.1. *Visual representation of the convection currents taking place in a sample. These include (a) asymmetric Rayleigh-Bénard convection, where molecules are convecting along a vertical temperature gradient either side of the tube, (b) symmetric Rayleigh-Bénard convection with the warmer molecules rise centrally in the tube and cooler molecules fall near the tube walls and (c) Hadley convection where molecules travel within the sample across a horizontal temperature gradient.*

Convection is a serious problem in modern day spectrometers as they lead to issues such as unreliable diffusion data, additional signal loss and phase distortions [84]. To combat this issue, the sample can be altered itself by changing the experimental parameters in the Rayleigh-Bénard equation. The radius of the tube can be decreased, the viscosity of the sample can be increased or the temperature gradient across the sample can be decreased [88]. The latter is the hardest of the three, as temperature gradients are often caused by the cooling system that the spectrometer operates. The fact that the gas first comes into contact with the bottom of the tube often results in Hadley convection – to which one may find it difficult to compensate for with practical adjustments. Alternatively, one may use a convection compensated NMR pulse sequence.

The existence of convection in an NMR experiment results in an increased reduction in signal intensity, with increasing gradient strength, leading to an increased observed diffusion coefficient. In the

presence of convection not only does there exist a spatially-dependent phase imposed by the gradient, there also exists a velocity-dependent phase. As a result, the signal attenuates faster than expected. Figure 3.2 illustrates how the signal intensity is affected by the additional flow factor and illustrates the resulting attenuation with increasing gradient strength.

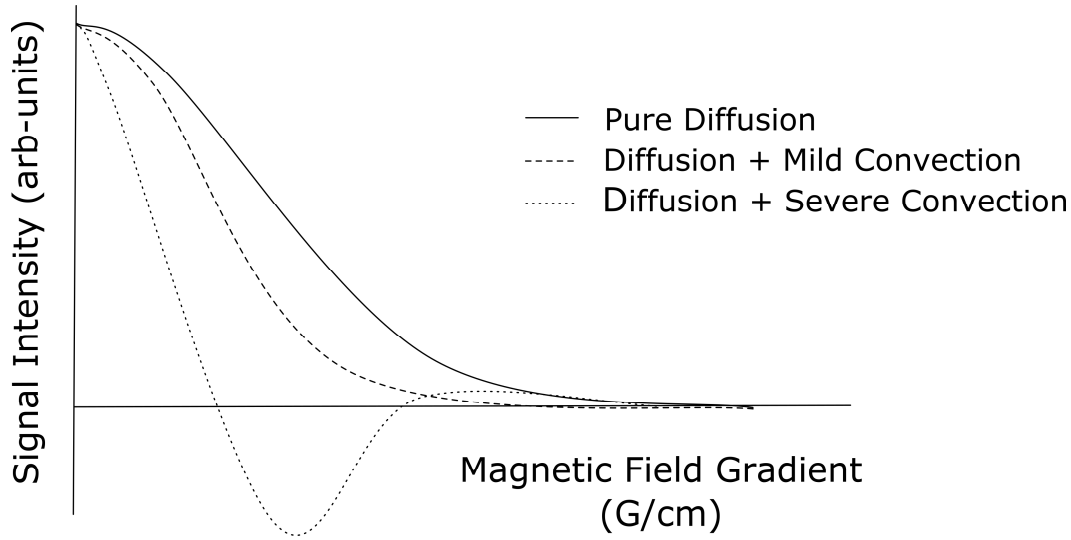

Figure 3.2. *Schematic representation of how the signal intensity is affected by the additional velocity phase. Figure adapted from Claridge [73].*

The additional velocity phase imposed by the influence of flow can be quantified by analysing the Stejskal-Tanner equation (Equation 2.29) for pure diffusion [89].

$$S = e^{-D\gamma^2 \int_0^t (\int_0^{t'} g^*(t'')dt'')^2 dt} \times e^{iv\gamma \int_0^t (\int_0^{t'} g^*(t'')dt'')dt} \tag{3.2}$$

Equation 3.2 can be simplified to yield Equation 3.3.

$$S = e^{-D \int_0^t (q)^2} \times e^{-iv \int_0^t (q)} \tag{3.3}$$

Using the Euler relationship, Equation 3.3 becomes Equation 3.4.

$$S = e^{-D \int_0^t (q)^2} \cos(v \int_0^t (q)) \tag{3.4}$$

Equation 3.4 can then be interpreted as the original Stejskal-Tanner equation for the diffusion experiment with an additional flow term (Equation 3.5).

$$S = S_0 e^{-D\gamma^2\delta^2G^2\Delta'}\cos(\gamma\delta\mathrm{G}\Delta v) \tag{3.5}$$

It is this additional cosine term which impacts upon one's ability to obtain reliable, accurate and precise diffusion measurements. The next section introduces pulse sequences that will not only compensate for convection, but will also quantify its extent. This, together with gradient calibration and temperature regulation, will ensure that all measurements present in this thesis are as accurate and reliable as possible.

4.2. Experimental

4.2.1. Gradient Correction

Three liquids with well-known diffusion coefficients,[90, 91] DMSO, cyclohexane and 1% H_2O in D_2O, were obtained from Sigma-Aldrich and not subjected to any further purification techniques. Using the convection compensated sequence illustrated in Figure 3.5, the diffusion of each liquid was measured using the pre-set gradient parameters and the coefficients obtained were compared to the values listed in the literature.

4.2.2. Temperature Regulation

To obtain a wide range of temperatures, a Bruker BVT3200 temperature control system, with an accuracy of 0.1 K, was used. A dewar of liquid nitrogen is connected to the spectrometer *via* a transfer line. The cooling system passes a combination of N_2 gas and air over the sample at a flow rate of between 125-400 l h^{-1} and operating at a maximum of 50% cooling output with the probe heater set to a maximum of 20%. Before the start of a cryoporometry experiment, the cooling system was allowed to equilibrate with the probe heater. The temperature control unit was optimized to ensure that over- and undershoot of the sample temperature was minimized effectively. The probe was also

tuned and matched in areas out of sample phase transition to account for the significant temperature changes. A schematic representation of the system set-up is provided in Figure 3.3.

Deuterated methanol (Sigma-Aldrich, 99.9% purity) was sealed under atmospheric pressure in a thick walled NMR tube and subjected to no further purification techniques. A simple proton spectrum comprising of 4 scans; 15 seconds; 3612 Hz spectral width; 16384 processed data points was obtained for a range of different temperatures.

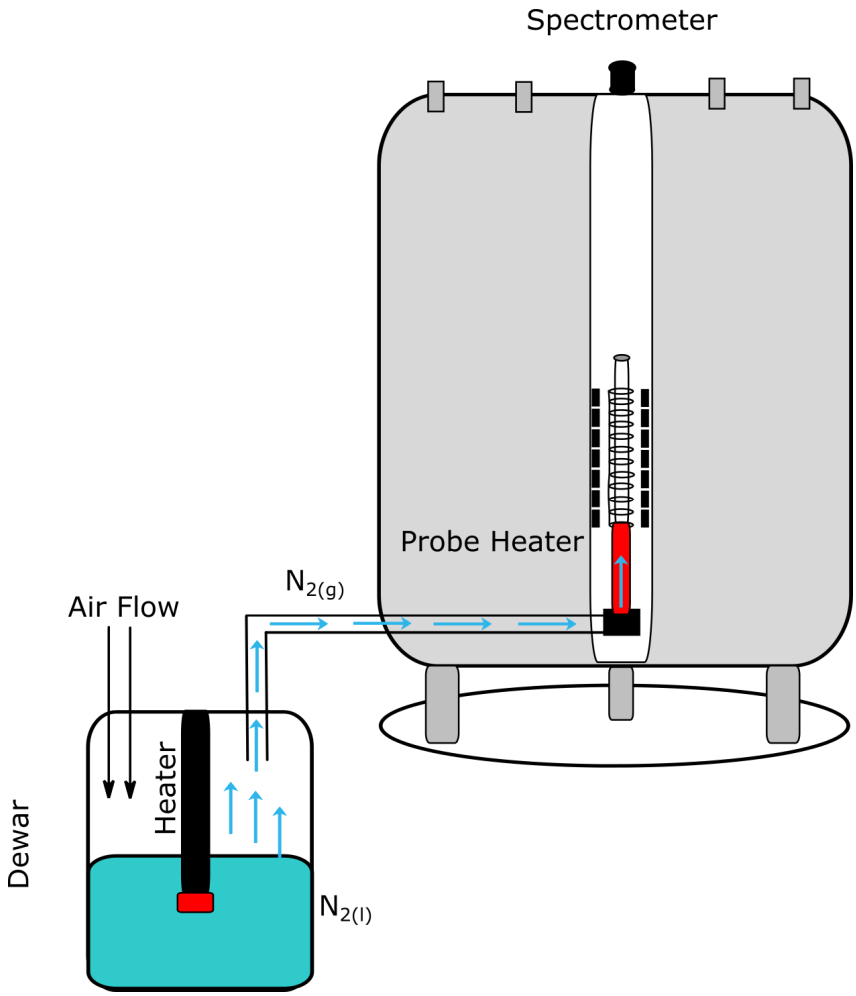

Figure 3.3. *Schematic representation of the temperature regulated experimental setup. A dewar of liquid nitrogen passes a mixture of N_2 gas and air over the sample which is firstly equilibrated with the probe heater. This allows for careful control of the sample temperature.*

4.2.3. Convection Compensation

A homologous series of carboxylic acids, in methanol, were chosen for the initial diffusion experiments. Formic acid, acetic acid, propionic acid, butyric acid, valeric acid, hexanoic acid, heptanoic acid, and deuterated methanol were obtained from Sigma-Aldrich and were not subjected to any further purification techniques. Their properties are detailed in Table 3.1. A 20 mmol solution of each acid was prepared with deuterated methanol and transferred to a thin-walled NMR tube. Initial diffusion measurements were obtained using the one-shot pulse sequence (Figure 3.4). Subsequent measurements were obtained using a convection compensated sequence (Figure 3.5). A commonly employed method of neglecting the velocity-dependent phase is to apply an inversion of sign for a pair of gradients in a double echo experiment.[73] One example of such sequence is the double stimulated echo. This sequence comprises of two basic stimulated echo sequences (Figure 2.13) which splits the total diffusion time in two.[92] A further improvement on this sequence is to incorporate bipolar pulse pairs. Despite their advantage in reducing convection, the sequence includes two stimulated echoes which leads to a reduction in sensitivity.

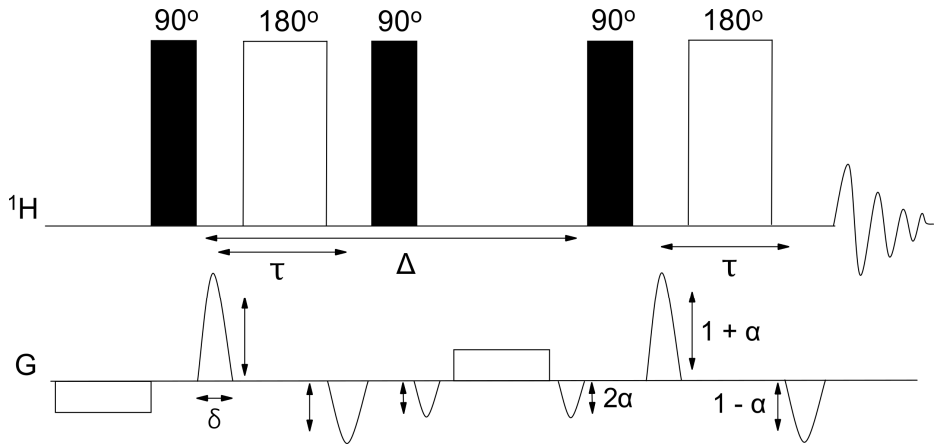

Figure 3.4. *One-shot pulse sequence for measuring the diffusion coefficient where in gradient pulse has a duration,* $\boldsymbol{\delta}$*, but the gradient strength is varied by an imbalance factor,* $\boldsymbol{\alpha}$*. The diffusion delay time is* $\boldsymbol{\Delta}$ *and* $\boldsymbol{\tau}$ *is an intergradient delay within the bipolar gradient pulses.*

Table 3.1. Properties of the homologous series of carboxylic acids used in the diffusion measurements.

Material	Molecular Weight (g mol^{-1})	Density (g cm^{-3})	Melting Point (^oC)	Appearance
formic acid	46.02	1.220	8.4	colourless liquid
acetic acid	60.02	1.049	16.0-17.0	colourless liquid
propionic acid	74.08	0.9880	-20.5	colourless liquid
butyric acid	88.11	0.9528	-5.1	colourless liquid
valeric acid	102.13	0.9300	-34.5	colourless liquid
hexanoic acid	116.16	0.9290	-3.4	colourless liquid
heptanoic acid	130.18	0.9181	-7.5	colourless liquid

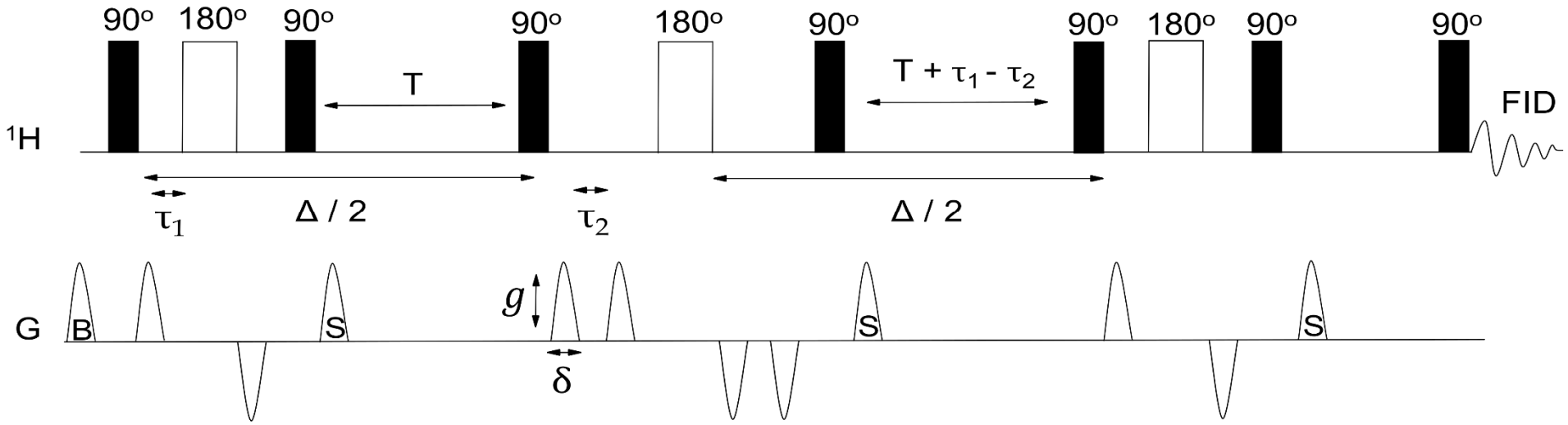

Figure 3.5. *Double-stimulated-echo-bipolar-pulse-gradient-pair sequence for accurately measuring diffusion data without the negative effect of convection. The diffusion delay time,* $\boldsymbol{\Delta}$*, is divided into two parts and the two adjacent sets of bipolar pulse pairs at the centre of the sequence have been combined to make sure that only one 180° pulse is needed to refocus the signal. The sequence contains spoiler gradients, denoted by "*$\boldsymbol{S}$*", which are included to remove any unwanted signal in the transverse plane. These are balanced by the gradient pulse denoted "*$\boldsymbol{B}$*". Each gradient pulse has the strength ,*$\boldsymbol{g}$*, and has the duration,* $\boldsymbol{\delta}$*. Parameters* $\boldsymbol{\tau_1}$ *and* $\boldsymbol{\tau_2}$ *are intergradient delays within the bipolar gradient pulses and* $\boldsymbol{T}$ *is variable diffusion delay time parameter.*

Having demonstrated the effect of convection on solutions of organic acids in methanol, a further series of experiments to measure and quantify the convective flow were performed. Deuterated acetone, deuterated chloroform, deuterated methanol, deuterated water and deuterated dimethyl sulfoxide were all obtained from Sigma-Aldrich and not subjected to any further purification techniques. Their properties are detailed in Table 3.2. Using an adapted convection measurement sequence [84, 93] (Figure 3.6) that uses a range of different delay imbalance times to measure the extent of flow in a sample, the convective velocity in the samples was measured at a range of temperatures using both thin and thick walled NMR tubes.

Table 3.2. Properties of the common laboratory solvents used in the convection measurements.

Material	Molecular Weight (g mol^{-1})	Density (g cm^{-3})	Melting Point (°C)	Appearance
acetone-d_6	64	0.872	-93.8	colourless liquid
chloroform-d	120	1.500	-64	colourless liquid
methanol-d_4	36	0.888	-98	colourless liquid
D_2O	20	1.110	3.8	colourless liquid
DMSO-d_6	84	1.190	20.2	colourless liquid

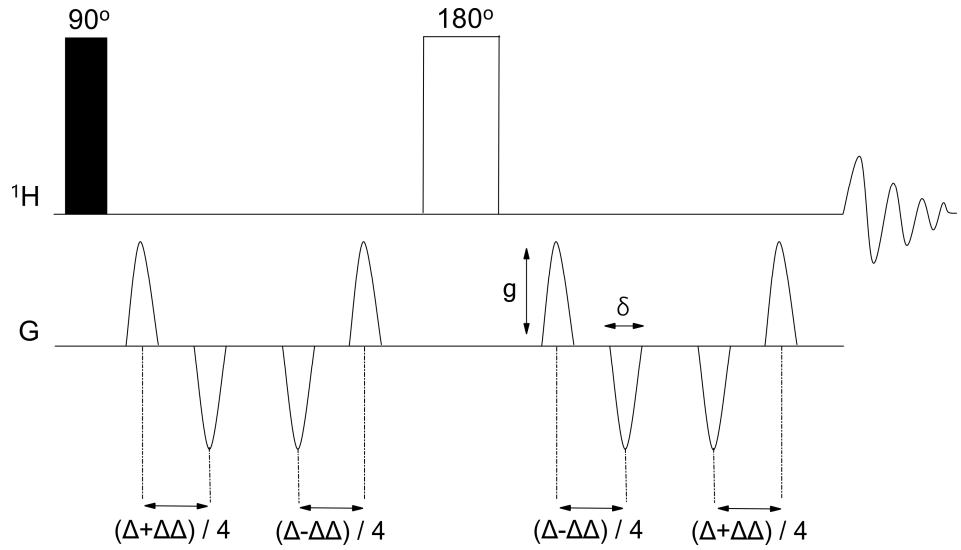

Figure 3.6. *Convection measurement sequence that can be used to measure the extent of convection by varying the delay time* $\boldsymbol{\Delta\Delta}$*, which has a gradient strength,* $\boldsymbol{g}$*, and a gradient length,* $\boldsymbol{\delta}$*.*

3.3. Results and Discussion

3.3.1. Gradient Calibration

The high resolution z-gradient probe installed in the spectrometer provides, nominally, 5.35 G cm^{-1}. To assess the current value of the calibration constant, the diffusion coefficient of each solvent was measured using the gradient values provided by the spectrometer. The obtained diffusion coefficients were then compared to a set of literature values at a specific temperature. Three common solvents were chosen due to their diffusion coefficients being widely reported. These were 1% H_2O in D_2O [91], DMSO [90] and cyclohexane [90]. The initial diffusion measurements are provided in Table 3.3, with a comparison to the literature values.

Table 3.3. Comparison of expected and obtained diffusion coefficients for DMSO, cyclohexane and 1% H_2O in D_2O

Solvent	Expected Diffusion Coefficient (X 10 $m^2 s^{-1}$)	Measured Diffusion Coefficient (X 10 $m^2 s^{-1}$)
DMSO	7.3 [90]	8.1 (± 0.1)
cyclohexane	14.2 [90]	15.8 (± 0.1)
H_2O in D_2O	19.0 [91]	21.2 (±0.1)

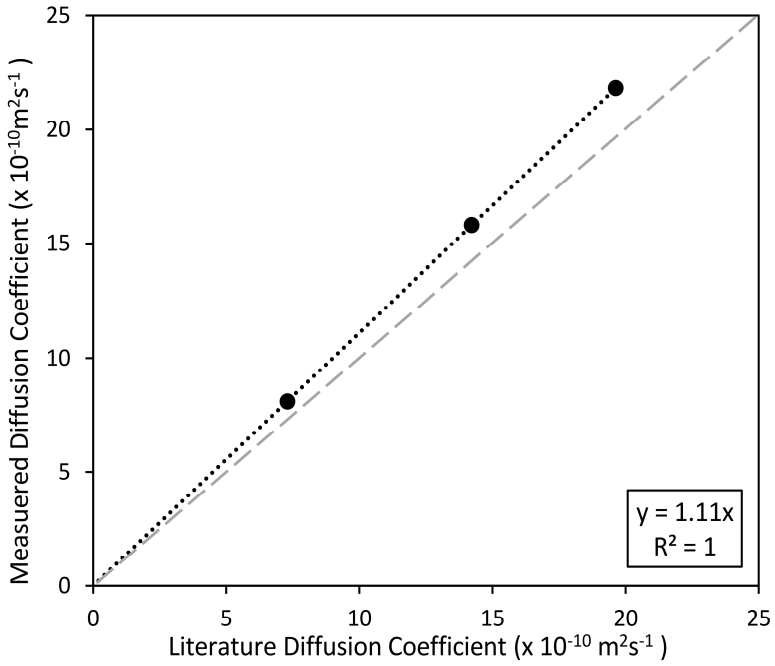

Figure 3.7. *The relationship between expected and measured diffusion coefficients for DMSO, cyclohexane and 1% H_2O in D_2O pre gradient calibration.*

The difference in literature and experimental diffusion coefficients illustrate a systematic error in gradient calibration; an error much larger than the inherent experimental error due to the fitting of the Stejskal-Tanner Equation. The measured diffusion coefficients were all larger than expected. Figure 3.7 highlights the relationship between the expected and obtained coefficients and there is a *ca.*10% error between the experimental and theoretical values. From Equation 2.29, the gradient contribution to signal attenuation is a squared term. In order to compensate for this error, a correction factor of $\sqrt{1.1127}$ was applied to the initial calibration constant of 5.35 G cm^{-1} to produce a new value

of 5.64 G cm^{-1}. Subsequent experiments were then conducted using this new value. Figure 3.8 shows the DOSY plot for deuterated water both prior and after gradient correction. Figure 3.9 illustrates the now corrected relationship between experimental and literature diffusion coefficients using the new calibration constant. A slight error remains in the diffusion measurement of cyclohexane after the gradient calibration. This may be down to either temperature fluctuation or errors in the fitting of the data. The fitting error of the Stejskal-Tanner equation has a value of approximately 0.2 x 10^{-10} m^2 s^{-1}, for these measurements.

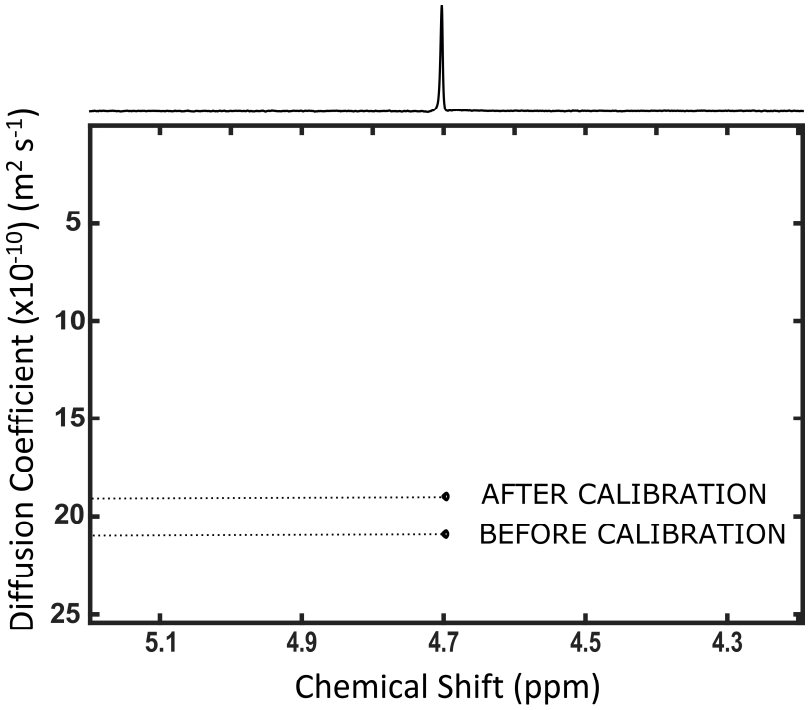

Figure 3.8. *The DOSY plots for 1% H_2O in D_2O before and after gradient calibration.*

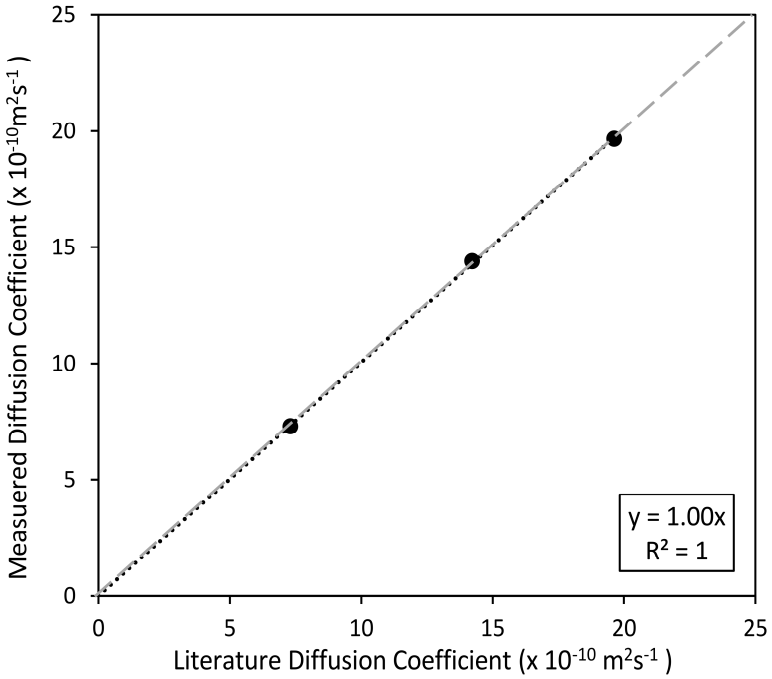

Figure 3.9. *The relationship between expected and measured diffusion coefficients for DMSO, cyclohexane and 1% H_2O in D_2O post gradient calibration*

3.3.1. Temperature Calibration

The sensor for variable temperature units is often fixed below the sample in the spectrometer and as such, will read slightly different temperatures to those of the sample. The temperature is regulated by passing a cold nitrogen/air gas mixture over the sample which has been heated to the required temperature prior to reaching the tube. To confirm the exact temperature of the species in the active region, it is useful to have a liquid which has a known temperature-dependent chemical shift. Using the method described in Findeisen *et al.* [94], deuterated methanol was used to determine a relationship between the stated temperature on the spectrometer and the actual temperature of the sample.

The ^{1}H NMR of deuterated methanol has two peaks (Figure 3.10). The first peak is a quintet at 3.3 ppm and the other peak consists of a singlet which is further downfield due to the proton being bonded to the electronegative oxygen. The chemical shift of the singlet changes with respect to temperature due to the effects and extent of hydrogen bonding. The following quadratic relationship was established between the chemical shift, $\Delta\delta$, and temperature, T: [94]

$$T = (-16.7467 \times (\Delta\delta)^2) - (52.5130 \times \Delta\delta) + 419.1381 \quad (3.6)$$

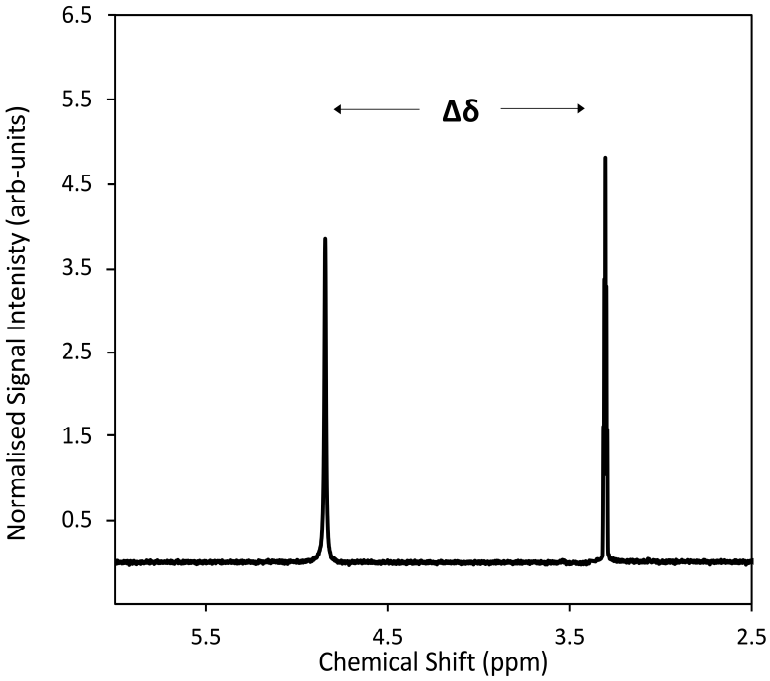

Figure 3.10. *^{1}H Spectrum of deuterated methanol. The difference in chemical shift is denoted as $\Delta\boldsymbol{\delta}$.*

The choice of temperature range measured (Figure 3.11) matched the range of temperatures used in the planned cryoporometry experiments. The relationship between stated and actual temperature of the sample can be applied to the temperatures just outside of this range. A conversion from the nominal spectrometer to the actual temperature was obtained by a fitting of the data, which was then used throughout this work.

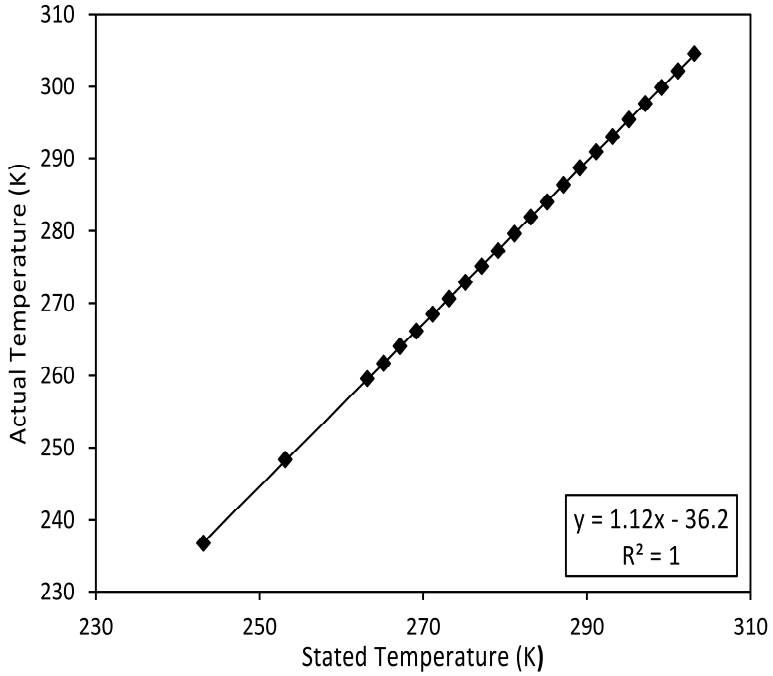

Figure 3.11. *Relationship between the stated temperature of the spectrometer and the actual temperature of the sample in the active region.*

The time taken for thermal equilibrium also needed to be considered. When the temperature is changed, the actual temperature change, complete homogeneously across the entire sample, may take significantly longer than stated by the spectrometer. If an insufficient amount of time is left before acquisition then the inhomogeneous, or incorrect, temperature will affect the measurement. Figure 3.12 illustrates the results from two experiments where this effect was measured. Using deuterated methanol, the temperature of the sample was changed and the time taken for this change was evaluated. It is evident to see from the data that as expected, the change observed from the temperature reading was quick and stable. The change observed using the equation derived in Figure 3.11 was also relatively rapid, but the temperature was not entirely stable when the required temperature had been reached. However the fluctuation was only less than 1% and such a fluctuation should be expected for temperature regulation systems.

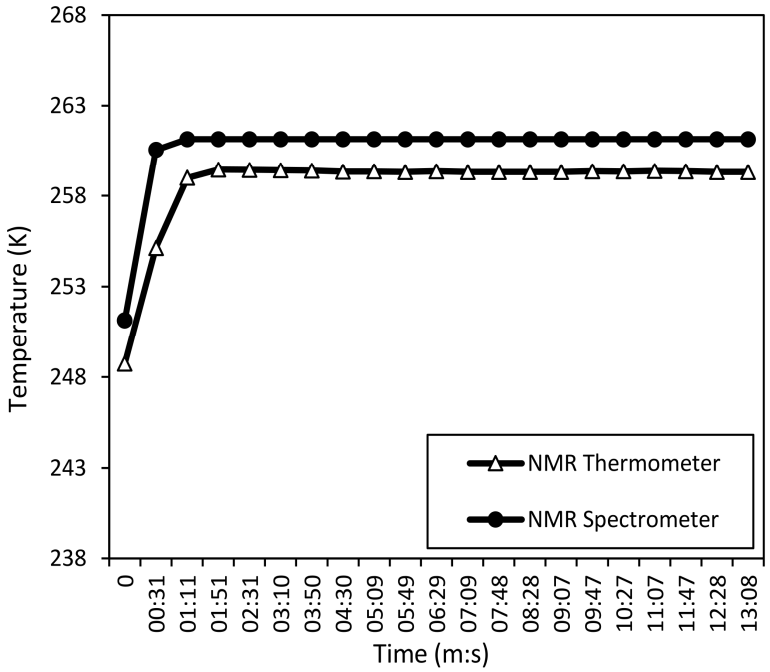

Figure 3.12. *Stability of the temperature change monitored using the stated and actual temperature of the sample.*

There is a further complication to NMR experiments that are conducted at variable temperatures: Curie's Law [95]. According to Curie, the signal intensity has an inverse relationship to temperature. In areas of no phase transition, increasing the temperature leads to a proportional decrease in signal intensity. The signal intensity of a non-freezing liquid, deuterated methanol, was observed over a wide temperature range to demonstrate this effect. Figure 3.13 shows an inverse relationship of signal intensity with temperature. Temperature steps of one degree intervals were used, starting from 263.15 K and increasing up to 303.15 K so that a sufficiently large range of temperatures were covered. All other experimental parameters were kept constant throughout. As the signal intensity decreases with temperature, it is clear that the effect of Curie's Law needs to be considered in future experiments.

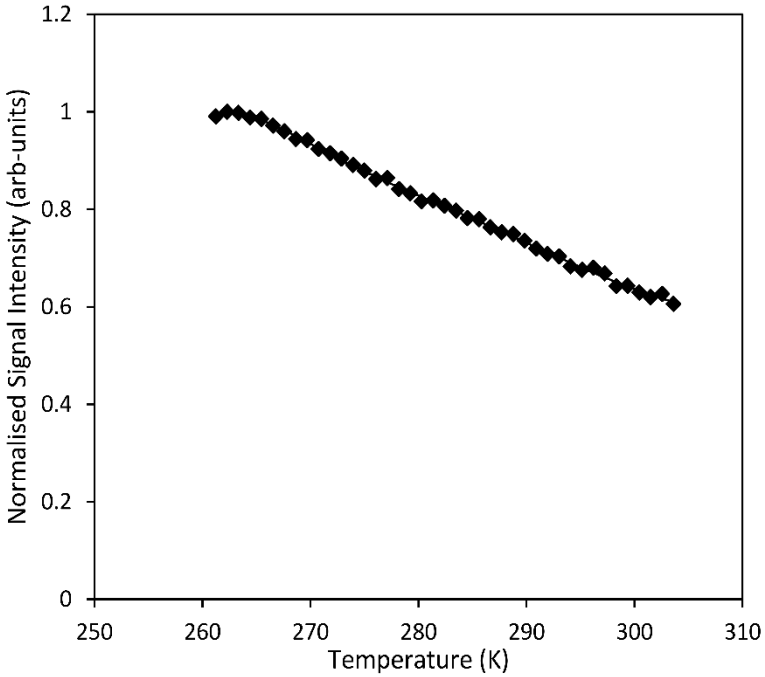

Figure 3.13. *The effect of Curie's Law for a deuterated methanol sample. The signal intensity decreases with increasing temperature.*

Using the observation that Curie's Law has a significant effect, it is important that the intensities outside of phase transitions should remain at a constant value. Signal intensity, being proportional to liquid volume, should consequently be normalised to ensure the validity of pore size distributions. This is discussed further in Chapter 4.

3.3.3. The Effect of Convection on Diffusion Experiments

Initial diffusion experiments were conducted using the one-shot pulse sequence [77] (Figure 3.4) for a homologous series of carboxylic acids (Table 3.1). Using the Stokes-Einstein relationship (Equation 2.27), one should expect that as the carbon chain length of the acid is increased, the diffusion coefficient would decrease accordingly. However as Figure 3.14 illustrates, this is not the case.

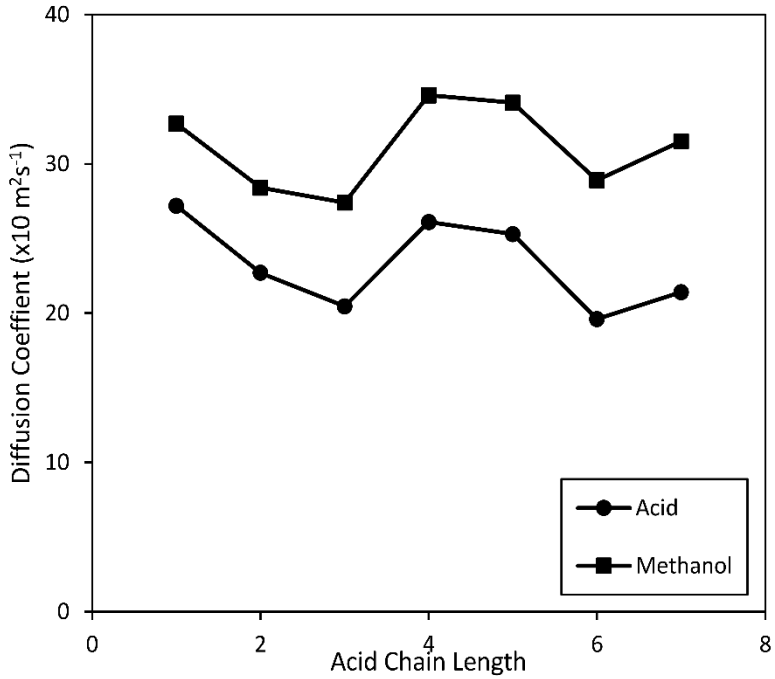

Figure 3.14. *Diffusion coefficients with increasing chain length for a homologous series of carboxylic acids in methanol. Results demonstrate an unexpected increase in diffusion for certain larger acids.*

This is a clear demonstration of the presence of convection and also its effect on diffusion data. Both butyric and valeric acid exhibited larger diffusion coefficients when compared to their smaller acid analogues and an even further increase was observed for heptanoic acid. All measurements were acquired at a constant temperature and such little fluctuation, as demonstrated in Section 3.3.2, would not be sufficient to cause this behaviour. Despite the constant temperature, small gradients, both vertical and horizontal, may still exist across the tube. The temperature would therefore not be uniform across the entire sample and the liquid will displace according to the temperature gradients present – resulting in convection.

To further demonstrate that convection was affecting the measurements, the diffusion coefficients of the two affected acids, butyric and valeric, were obtained whilst varying the diffusion delay time [73]. In a perfect diffusion experiment, changing the diffusion delay time would have little-to-no effect on the diffusion coefficient. However in the presence of convection, the diffusion coefficient would increase with increasing delay time. The results are illustrated in Figure 3.15.

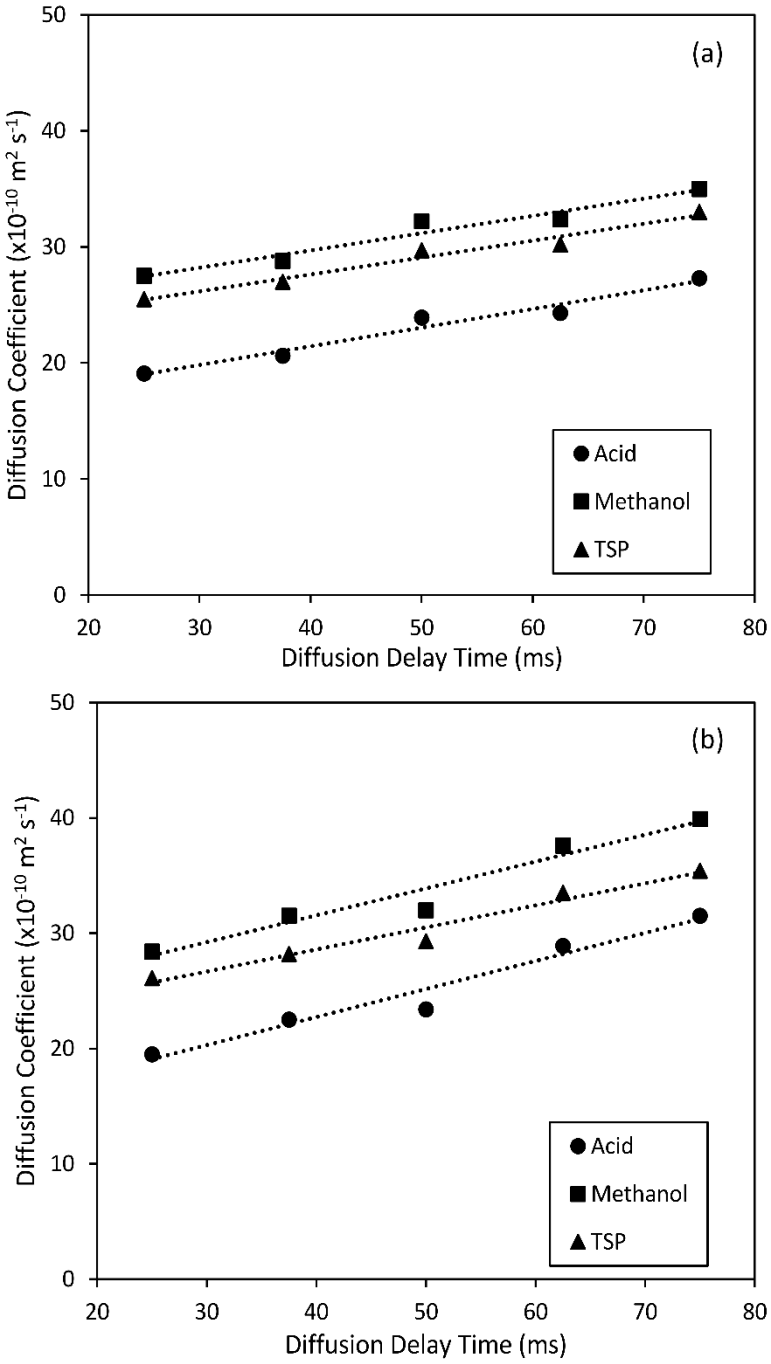

Figure 3.15. *Effect of convection on the diffusion coefficient measurement of (a) butyric acid and (b) valeric acid with increasing diffusion delay time.*

The diffusion coefficient increases proportionally to the increase in diffusion delay time, indicating clearly that convective flow is affecting the data. In order to cancel the effect of flow on the diffusion data, a convection compensated pulse sequence was used.

The efficiency of the convection compensated sequence was first tested by comparing the signal attenuation, for the maximum gradient application (80%), to that of a standard stimulated echo. The standard sequence used was a stimulated echo bipolar pulse gradient pair sequence (stebpgp_1s) (Figure 2.14) and for convection compensation, a double stimulated echo bipolar pulse gradient pair sequence (dstebpgp_3s) was used. When convection is accounted for, temperature should have little effect on the extent of signal attenuation. However by increasing the temperature, this will increase the amount of flow within the sample. As such, when convection is not accounted for, the signal will appear to attenuate faster than expected. This trend is observed in Figure 3.16.

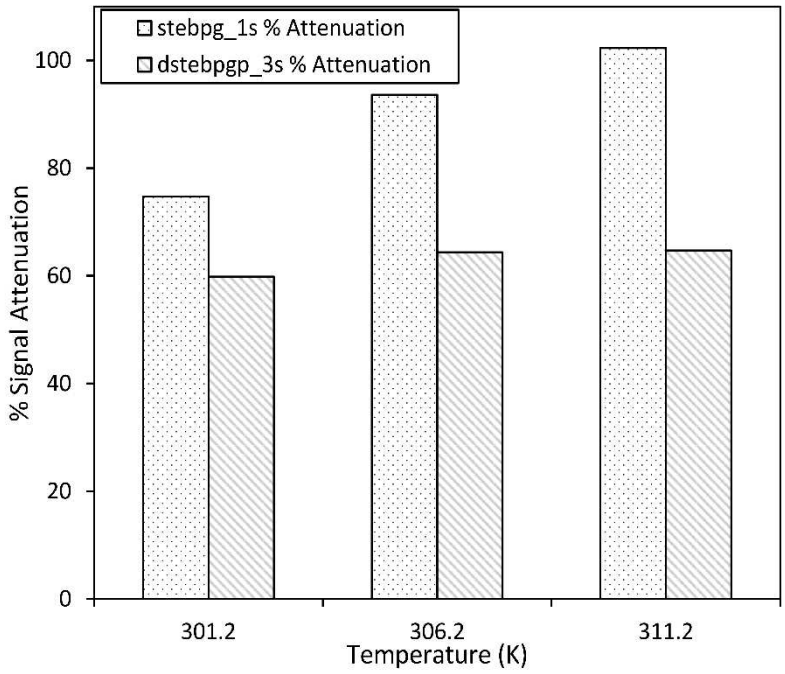

Figure 3.16. *Comparison of the % signal attenuation for the stebpgp1s and dstebpgp3s sequences for a maximum gradient application of 80%. There is an increased signal attenuation in the stebpgp1s pulse sequence due to the extra contribution from convective flow, even resulting in a negative signal at higher temperatures.*

The difference between the two sequences is significant. The double stimulated echo sequence experiences an approximate 60% signal attenuation from, mostly, pure diffusion, and this is relatively independent on temperature variation. However, the additional contribution to the signal attenuation is observed for the standard stimulated echo sequence, and this increases with increasing

temperature. The double stimulated echo sequence therefore effectively cancels out the effect of convection on experimental data.

To further evaluate the efficiency of the dstebpgp_3s sequence, the convection test detailed in Figure 3.15 (b) was repeated however, this time using the bipolar sequence. The diffusion measurements are illustrated in Figure 3.17 with a comparison to the previous data, for valeric acid in methanol. The diffusion coefficients for all three species remain relatively constant throughout, with standard experimental error, suggesting that there is no other contribution other than the pure diffusion of the species.

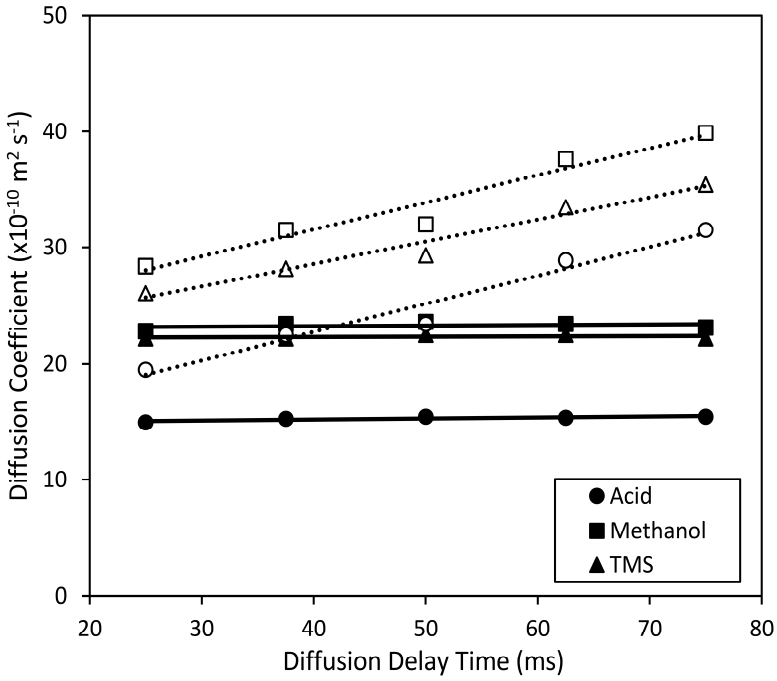

Figure 3.17. *Measuring the diffusion coefficient of valeric acid with increasing diffusion delay time using the dstebpgp_3s sequence. The dashed lines correspond to the data in Figure 3.15 (b).*

The extent of the convective flow caused by temperature gradients can be measured. Using the pulse sequence in Figure 3.6, the signal intensity was measured subject to varying delay imbalance time, $\Delta\Delta$. When $\Delta\Delta = 0$, flow is completely cancelled out and no convection occurs. However changing the delay imbalance time allows to fit the signal intensity as a sinc function to obtain a value for the velocity, illustrated in Equation 3.7.

$$F(\Delta\Delta) = S_0 \, sin(\gamma\delta g A_g v_{MAX} \, \Delta\Delta) \, / \, (\gamma\delta g A_g v_{MAX} \Delta\Delta) \quad (3.7)$$

where S_0 is the signal intensity prior to gradient application, γ is the gyromagnetic ratio for a proton, δ is the duration of the diffusion encoding gradient length, g is the diffusion encoding gradient strength, A_g is a gradient shape factor, $2/\pi$ for half-sine pulses and $\Delta\Delta$ is the delay imbalance. An example of the fitting is illustrated in Figure 3.18 for deuterated acetone at 308.15 K in both standard and thick walled NMR tubes.

Different temperature ranges were used to match the physical parameters of each solvent. It was paramount that the solvent did not solidify in the spectrometer as this would risk shattering of the tube, especially in the case of water. Figure 3.19 illustrates the change in velocity of flow within the tube as a function of temperature for five common laboratory solvents in standard NMR tubes. The results strongly suggest that convection is a serious problem in pulsed field gradient measurements using this particular spectrometer. When close to room temperature (293.15 K), the velocity exhibited by the solvents are at a minimum. However when deviation from this temperature occurs, the velocity in the tube starts to increase. Deuterated chloroform and acetone are likeliest to convect at seemingly normal temperatures whereas deuterated water and DMSO are less so.

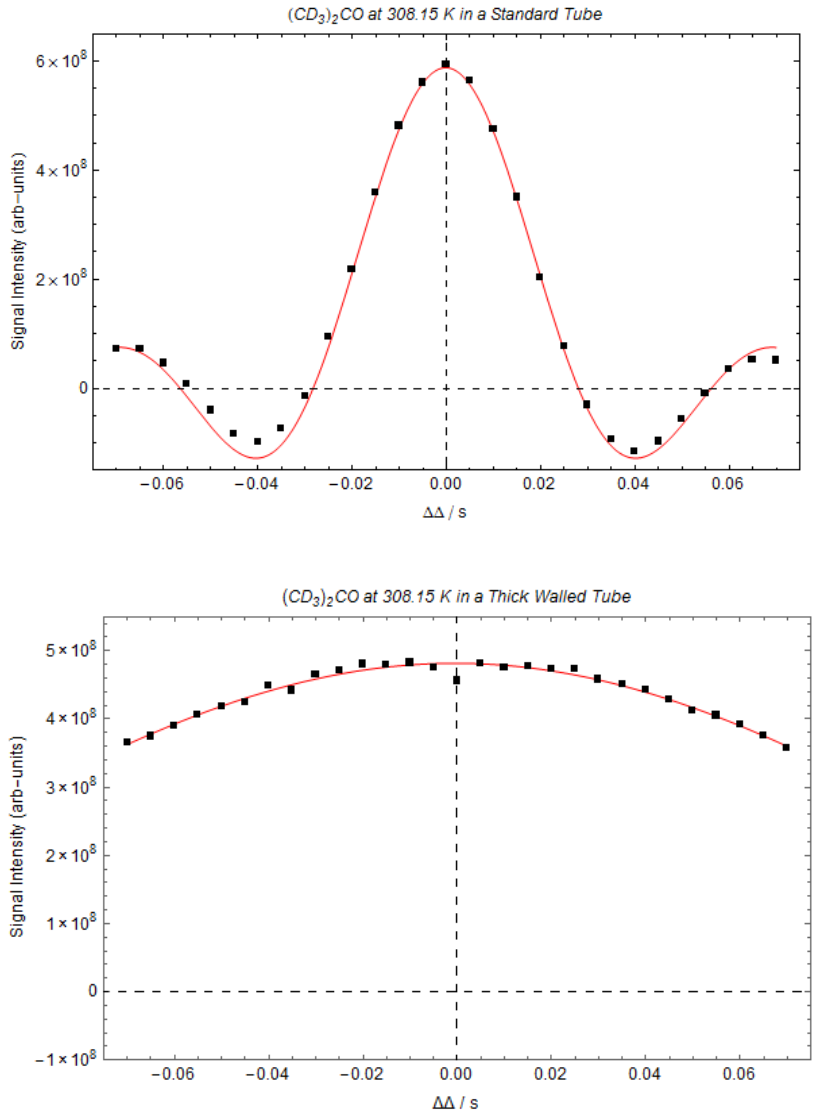

Figure 3.18. *Measuring the velocity of deuterated acetone at 308.15 K in both a) a standard NMR tube and b) a thick walled NMR tube by fitting of the sinc function to the change in signal intensity with respect to the delay imbalance time,* ***ΔΔ****.*

Figure 3.19 illustrates the extent of convection in thin-walled NMR tubes. Observing one of the liquids most susceptible to convection, deuterated chloroform, a convective velocity of over 2 mm s^{-1} is achieved at high temperatures. Figure 3.20 illustrates the convection measured for liquids in thick-walled NMR tubes. As intuitively expected by observing Equation 3.1, decreasing the radius of the tube reduced the amount of convection observed. Even for deuterated chloroform, a reduction of the radius of the tube reduces the velocity exhibited by the liquid up to approximately 75%. A comparison of the two tubes, taking acetone as an example, is shown in Figure 3.21.

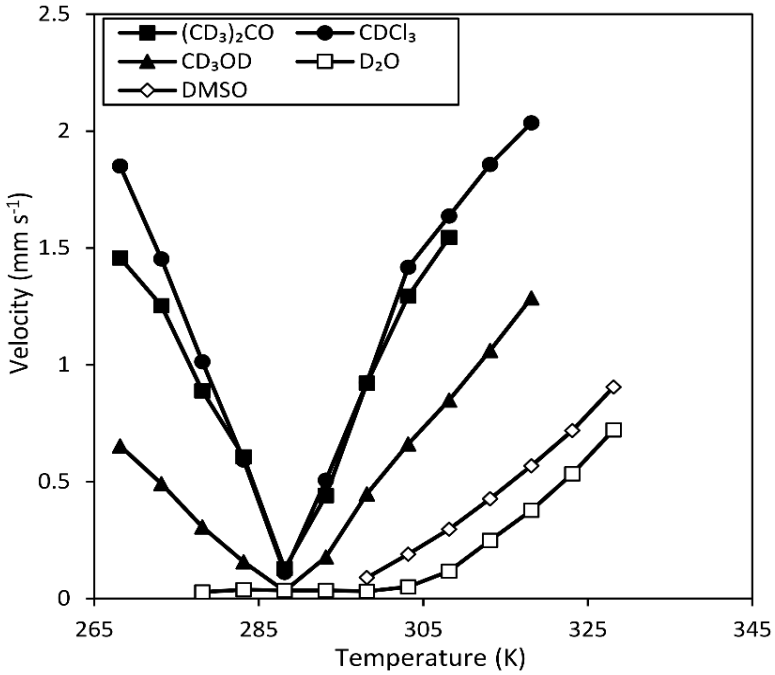

Figure 3.19. *Velocity of convection versus temperature for five different common laboratory solvents in a thin-walled NMR tube.*

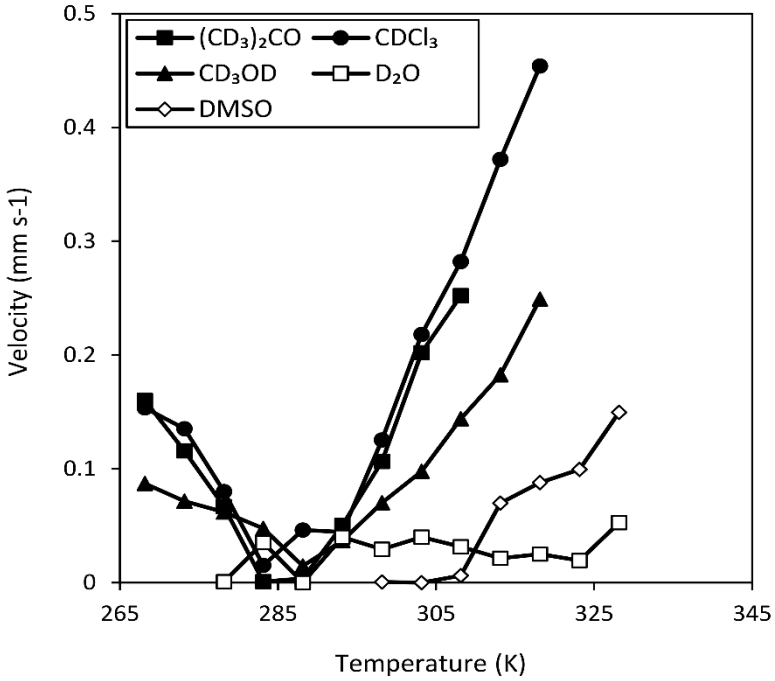

Figure 3.20. *Quantitative analysis for the convection of a range of laboratory solvents in a thick-walled NMR tube.*

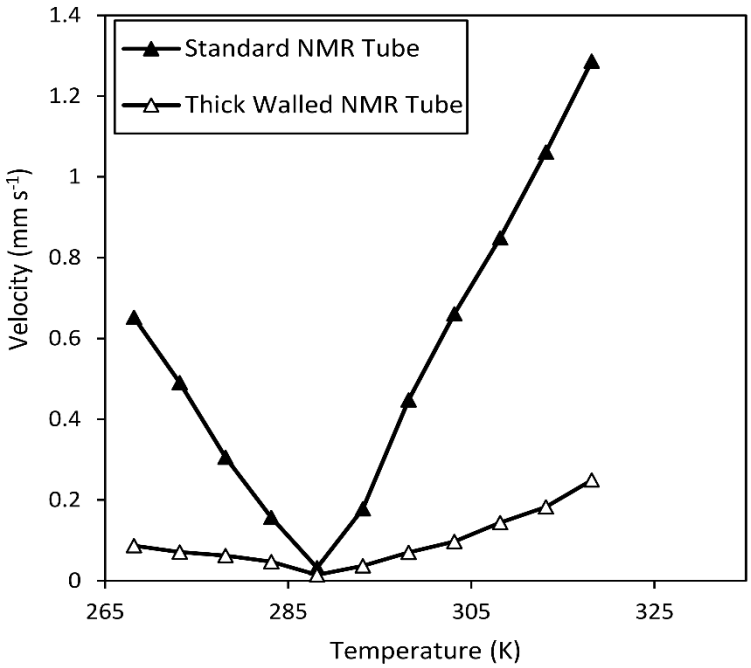

Figure 3.21. *A comparison of the convection measurements for deuterated acetone within standard thin-walled and thick-walled NMR tubes.*

The velocity of flow produced by Rayleigh-Bénard convection is not easily predicted. However, It is possible to predict a velocity, υ_{max}, for horizontal gradients based on a known solvent with known properties in a given temperature gradient [84]. In order to validate this data, the υ_{max} was predicted for all five solvents over the temperature ranges measured experimentally using the model provided by Swan et al. 84, and illustrated in Equation 3.8.

$$\upsilon_{max} = \chi \frac{R^3 g}{\sqrt{108}} \frac{dT}{dx} \tag{3.8}$$

The model basis its measurement on how likely a liquid is to convect from its thermal expansion coefficient, density and viscosity as denoted by χ. $\frac{dT}{dx}$ is the horizontal gradient across the tube, g is the acceleration of gravity and R is the internal radius of the tube. Table 3.4 compares the velocity values predicted from Equation 3.8 with those obtained experimentally.

Table 3.4. A comparison of the theoretical and experimental v_{max} values for the solvents in a standard NMR tube.

Solvent	Predicted v_{max} at 308.9 K	Experimental v_{max} at 308.9 K
deuterated chloroform	1.5 X 10^{-3}	1.6 X 10^{-3}
deuterated acetone	1.5 X 10^{-3}	1.5 X 10^{-3}
deuterated methanol	1.1 X 10^{-3}	8.5 X 10^{-4}
deuterated DMSO	2.2 X 10^{-4}	3.0 X 10^{-4}
deuterated water	7.3 X 10^{-5}	1.2 X 10^{-4}

The predicted values for v_{max} closely relate to those obtained experimentally. Deviation between the two values starts to increase with reducing velocity, suggesting that either the equation is more reliable for less viscous solvents, the spectrometer fails to accurately measure the velocity for more viscous solvents or that Rayleigh-Bénard convection is increasingly important.

3.4. Conclusions

Three essential experimental parameters have been evaluated in this section; error in gradient application, temperature accuracy and the problem of convective flow. By understanding each parameter and the possible errors associated with them, one can be sure that the results contained in the rest of this thesis have been measured as precisely as possible.

Initial temperature measurements suggested that the nominal temperature stated by the spectrometer was not the actual temperature of the sample contained within the tube. The sample temperatures were measured for a range of nominal spectrometer temperatures using a standard NMR thermometer and a linear conversion was obtained. The delay in observed temperature changes was also analysed and it was concluded that the temperature of the sample was stable after a period of 2 minutes. For all future changes in temperature, a minimum 5 minute waiting time would be used.

This can also be checked by acquiring appropriate NMR spectra. Furthermore, a continuous temperature fluctuation of less than 1% was not large enough to actively affect any temperature-regulated measurements.

One of the biggest barriers to obtaining accurate diffusion data is convection. It's presence was demonstrated through a series of diffusion measurements that clearly showed convection was a serious problem when using a regular diffusion NMR pulse sequence. Using the methodology developed in the Morris group [77, 84, 93], the maximum velocity was measured for 5 common solvents at a range of different temperatures to understand the significance of its effect. As expected, solvents of a low viscosity suffered severe flow at extreme temperatures. Convection was significantly reduced when the solvents were placed within a thick walled NMR tube however a convection compensated pulse sequence proved to be most effective in reducing the effects of convection on diffusion measurements. The compensated sequence incorporating bipolar pulse gradient pairs will be used for all further diffusion measurements contained herein.

Three common laboratory solvents were chosen to calibrate the strength of the pulsed field gradients applied by the spectrometer. The diffusion coefficients of DMSO, cyclohexane and 1% H_2O in D_2O were all measured and it was found that there was a systematic error in acquired diffusion coefficient for all species. The gradient strength calibration constant was changed in light of these results. Subsequent repeats of the experiments resulted in obtaining a series of diffusion coefficients with the expected values.

This chapter has explored some of the common parameters which may heavily impact upon trying to obtain accurate diffusion NMR experimental data. By ensuring that all are well understood, confidence can be taken that all future measurements are conducted to a suitable degree of accuracy and precision.

CHAPTER 4

Cryoporometry Method Development

4.1. Introduction

Prior to the application of NMR cryoporometry to materials such as catalytic silica, it was essential to develop the correct experimental protocol using a set of known materials. Many parameters and experimental conditions needed to be considered such as the amount of solid/liquid material being used, the wetting ability of the liquid, the treatment of the sample to aid imbibition and the type of NMR tubes being used. Many variations, in both method and in detail of method, have been reported in the literature, all differing from one to the other [19, 26, 52, 96].

The exact type of porous material being measured will influence the method of preparation. However in order to establish a general protocol, it was important to use a highly ordered solid support. The most common type of matrix for developing the method of cryoporometry has been controlled pore glass (CPG) [26, 96-100]. CPGs have found to be suited towards cryoporometry measurements due to their ordered cylindrical pore system, high thermal, mechanical and chemical stability and narrow pore size distribution. CPGs can be manufactured to suit a certain purpose and many different types of structures ranging from hexagonal to ultra-thin membranes can be designed. These materials can be produced by liquid extraction through the sol-gel process, acidic or alkaline, of phase separated borosilicate (SiO_2-B_2O_3-Na_2O) glasses [101, 102].

Cyclohexane is a nonpolar molecule that is suitable for cryoporometry analysis due to its highly accessible melting point (280 K), simple NMR spectrum and its ability to form a soft crystalline phase upon freezing that does not damage the pore matrix [103]. Bulk cyclohexane also has two well-defined phase transitions. The first, at approximately 186 K, involves the transition from a solid into a “mushy

ice" phase. The second is its solid-liquid bulk melting point at 280 K. Cyclohexane is also reported to have a relatively high melting point depression constant, k_c, compared to other common probe liquids such as water and benzene [56].

This short chapter establishes an experimental protocol that is applied throughout to accurately measure the melting point depression for liquids confined in porous materials, using NMR cryoporometry. Using well researched materials, the suitability of the spectrometer towards measurements at extreme temperatures was assessed. Setting up an initial protocol would then allow for further application to other materials and liquids.

4.2. Experimental

4.2.1. Sample Preparation

The CPGs were provided by both Sigma-Aldrich (24, 50 and 54 nm) and Prime Synthesis (38, 43, 63 and 100 nm) and their properties are listed in Table 4.1. Prior to sample preparation, all samples were dried in the oven at 373 K for 24 hours and then placed in a desiccator for a further 24 hours. The glasses were stored in the desiccator from thereon. Cyclohexane (Fischer-Scientific, 99%) was subjected to no further purification techniques. Its properties are detailed in Table 4.2. Two types of NMR tubes were used for analysis; thin-walled and thick-walled. Irrespective of the type of tube used, the preparation method remained relatively the same. The solid support was first placed in the tube and cyclohexane was pipetted over to ensure complete pore saturation, with a slight excess of bulk liquid. Initial measurements in the standard tube used approximately 100 mg of glass. Subsequent measurements in both standard and thick walled tubes used between 20-30 mg. The amount of liquid added to ensure complete pore saturated was determined by the method outlined in Petrov and Furo [99].

Table 4.1. Commercial properties of the controlled pore glasses provided by Sigma-Aldrich and Prime Synthesis.

CPG	Pore Diameter (nm)	Pore Volume (cc g^{-1})	Grain Size (mesh)	Specific Surface Area (m^2 g^{-1})
CPG24	24.0	-	20-80	-
CPG38	38.2	1.10	120-200	113
CPG43	42.8	1.40	120-200	130
CPG50	50.0	0.96	120-200	51
CPG54	54.0	1.06	120-200	44
CPG63	62.6	1.20	120-200	79
CPG100	99.6	1.40	120-200	55

Table 4.2. Physical properties of cyclohexane used to determine a melting point depression according to Equation 2.21.

Physical Parameter	Value
molar volume of the liquid, $\boldsymbol{\nu}$ (m^3 mol^{-1})	108.7 [99]
surface energy at the solid-liquid interface, $\boldsymbol{\gamma_{sl}}$ (mJ m^{-2})	4.6 [99]
bulk enthalpy of fusion, $\boldsymbol{\Delta H_f}$ (kJ mol^{-1})	2.70[99]
bulk melting point, $\boldsymbol{T_m}$ (K)	278-280[99]

4.2.2. NMR Measurements

All cryoporometry measurements were made using the Carr-Purcell-Meiboom-Gill (CPMG) [104, 105] pulse sequence illustrated in Figure 4.1. The sequence comprises of a basic spin echo and with careful selection of the total delay time, 2τ, it was possible to differentiate between the solid and liquid phases of the sample. A total delay time of 40 ms ensured that the solid signal was completely removed. The temperature was reduced until the all of the sample had frozen, where no liquid signal was present. The temperature was then increased incrementally, in steps of 0.1-5 K, to observe the phase change

from solid to liquid, with a minimum equilibrium time of 10 minutes from the when the signal intensity stopped changing. Smaller temperature steps were used in areas of phase transition. Each acquisition comprised of 8 transients of 8192 complex data points.

To obtain low temperatures, a Bruker BVT3200 temperature control system, with an accuracy of 0.1 K, was used. The cooling system passes a combination of N_2 gas and air over the sample at a flow rate between 125-400 l h^{-1} operating at 50% cooling with the probe heater set to a maximum of 20% output. Before the start of a cryoporometry experiment, the cooling system was allowed to equilibrate with the probe heater. The temperature control unit was optimized to ensure that over- and undershoot of the sample temperature was minimized effectively. Furthermore, the probe was tuned and matched in areas out of sample phase transition to account for the significant temperature changes. The calibration between actual and stated temperature, illustrated in Chapter 3, was applied here.

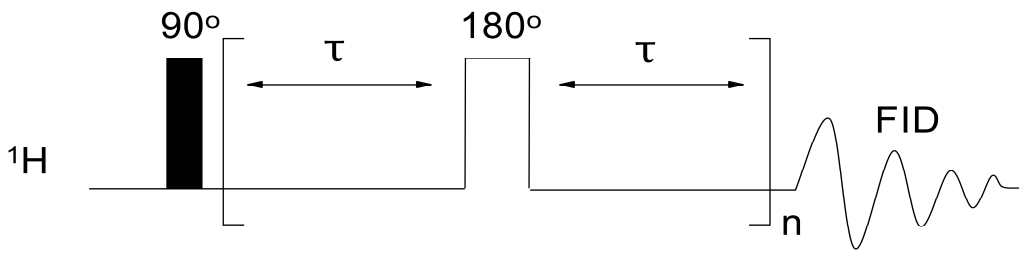

Figure 4.1. *CPMG pulse sequence used in NMR cryoporometry experiments, with a* T_2 *filter of* τ *= 20 ms to ensure that the solid phase is separated.*

4.3. Results and Discussion

4.3.1. Bulk Cyclohexane

To ensure the melting point depression, ΔT_m, was accurately measured, the bulk melting temperature first needed to be determined. A small amount of bulk liquid was added to a standard NMR tube and the melting curve was recorded. As the temperature was increased incrementally, the signal intensity also started to subsequently increase during the transition from solid to liquid. Figure 4.2 illustrates

how the cyclohexane starts to melt at 279.8 K and plateaus at 281.0 K. The freezing curve was also recorded and a hysteresis was observed. Both phase transitions are rapid and such behaviour is expected for a bulk liquid where there are no confinements to its physical state.

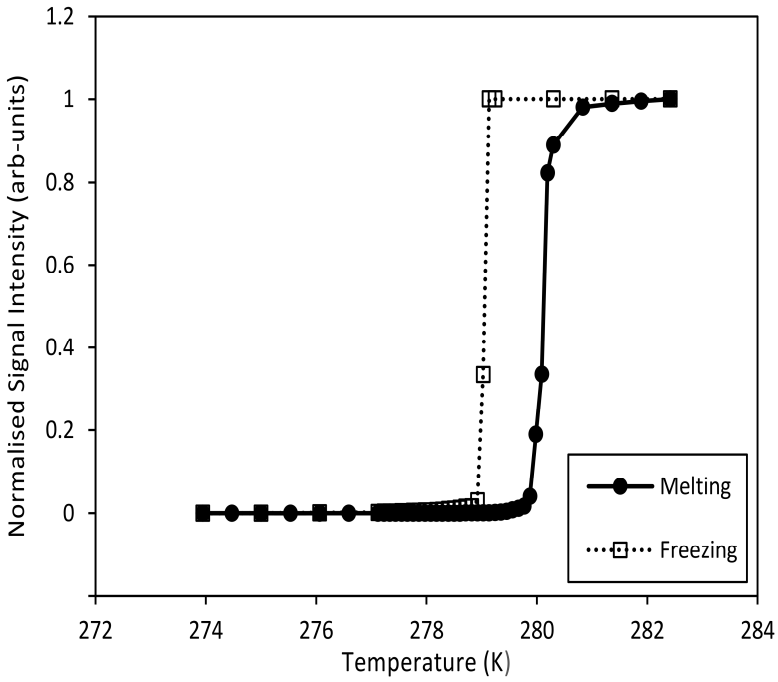

Figure 4.2. *The melting/freezing hysteresis of bulk cyclohexane in a standard 5 mm NMR tube achieved using a CPMG pulse sequence. The signal intensity is measured from height of the ^{1}H NMR peak.*

4.3.2. Standard Tube with Excess Material

With initial proof of principle acquired, cyclohexane was imbibed into the pores of CPG50 to assess the influence that the solid had on the NMR line shape. Figure 4.3 illustrates how the homogeneity of the sample was affected by the liquid/solid mixture. The peak for confined cyclohexane, with the addition of the bulk outside the grains, is considerable broader (ranging >2 ppm) than the peak for the pure bulk liquid (0.2 ppm). The overall signal intensity of the peak was also reduced significantly, as there was less liquid species present in the sample. The signal intensity of the bulk cyclohexane peak in Figure 4.3 has been reduced accordingly in order to highlight the contrast in line shape.

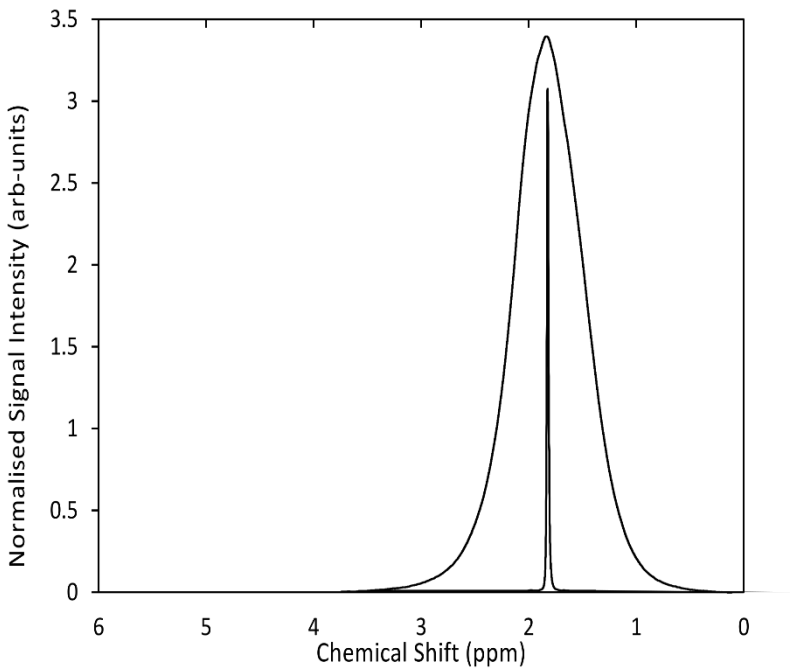

Figure 4.3. *The measured signal intensity for both bulk (sharp peak) and confined (broad peak) cyclohexane. The bulk cyclohexane peak has been reduced by a factor of 4.5 for comparative purposes.*

It was important to establish the correct temperature range prior to accurate measurement. The sample temperature was reduced until both the confined and bulk liquid cyclohexane was completely frozen, confirmed by the lack of NMR signal, and then reduced further to 220 K to ensure all of the confined liquid had frozen. Upon reducing the temperature, the sample was left frozen for 1 hour. The temperature was then increased at 0.5 K ramps to find the region where confined melting occurs. The first observed signal rise occurred between 276.1 K and 276.6 K, confirming the presence of cyclohexane confined in the pores. The signal, however, continued to rise and the peak started to become much sharper in shape; something that is not reported in the literature. As soon as the confined cyclohexane melts, the signal intensity should plateau and start to reduce slightly in accordance with Curie's law. However this was not the case here. The peak continued to increase in signal intensity up until the bulk melting point. At this point, the signal intensity of the peak reduced and broadened significantly, to resemble the peak shape prior to temperature reduction.

The ^{1}H NMR spectrum for cyclohexane in CPG50 is shown in Figure 4.4, illustrating the peak just below and just after the bulk melting temperature. There is a clear difference between the two types of peak

shape and intensity. During the pore melting period, the peak is much sharper and higher in signal intensity than the peak representing a homogeneous sample post bulk melting.

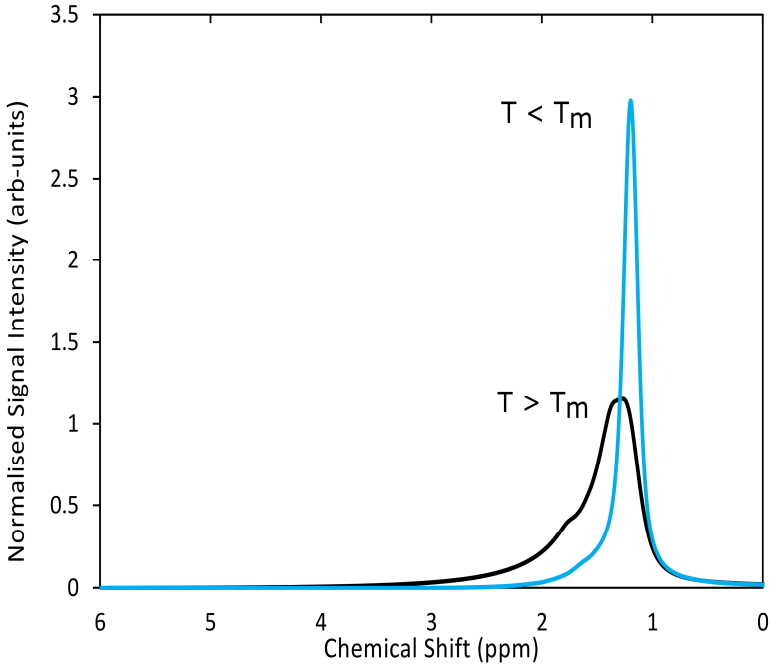

Figure 4.4. *The ^{1}H NMR spectrum for cyclohexane confined in the pores of CPG50 at two different temperatures. The unusual sharp peak is obtained at the temperature below bulk melting. The broader peak is obtained when all of the cyclohexane, confined and bulk, has melted.*

Figure 4.5 plots the measured signal intensity as a function of temperature. A continuous rise in signal intensity is observed with increasing temperature, with no plateau for when all of the confined cyclohexane had melted. A further reduction occurs when all of the liquid has melted. This behaviour is not indicative of a standard cryoporometry experiment and therefore this suggests that there is an issue with the sample preparation. The same experiment was repeated, with very similar results. Cyclohexane confined in various other pore sizes also demonstrated the same behaviour. One procedure detailed in the literature is to prepare a sample using a standard NMR tube and the use of vortex plugs [26]. Vortex plugs reduce the amount of volume so only a small amount of solid support is needed to cover the active ^{1}H NMR region. Vortex plugs were not readily available, however, so the next set of samples were made using thick-walled NMR tubes.

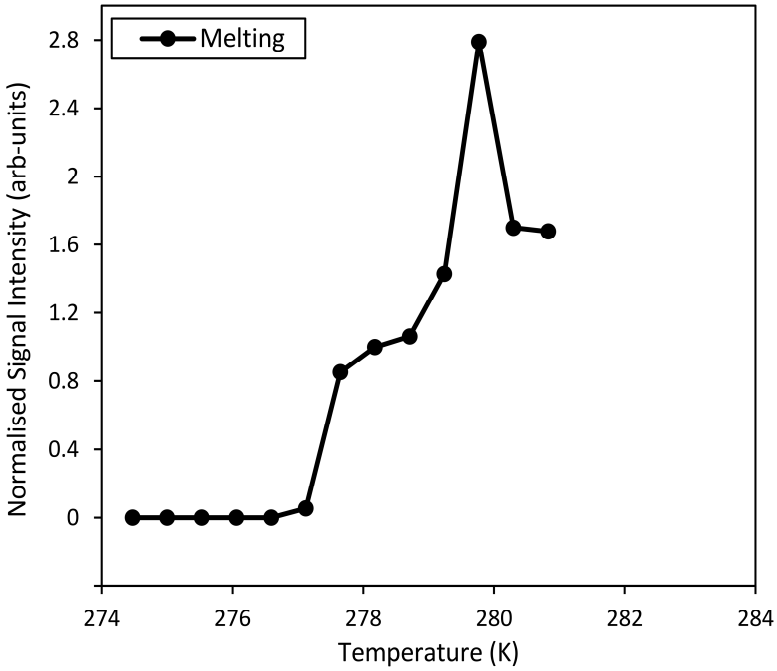

Figure 4.5. *NMR melting curve for cyclohexane confined in the pores of CPG50. The signal intensity increases with temperature however a reduction in signal intensity is observed from confined to bulk melting.*

4.3.3. Thick-walled Tube

Thick-walled tubes reduce the amount of material subjected to NMR analysis due to the smaller internal tube diameter. In theory, this should reduce the effect of the sharp peak that was observed for material confined in standard NMR tubes, if this was indeed the cause of the strange melting behaviour. To test this hypothesis, the same experimental procedure was followed this time using the thicker tube. The difference between the two tubes are illustrated in Table 4.3.

Table 4.3. Comparison between the two types of NMR tube used.

	Inner Diameter (mm) [84]	**Average Amount of CPG (g)**	**Average Amount of Cyclohexane (g)**
thin-walled NMR tube	4.20 ± 0.025	0.160	0.230
thick-Walled NMR tube	2.20 ± 0.025	0.030	0.038

The extra, sharper, peak was still evident. However, it was now possible to distinguish between the shaper peak and the broader melting peak indicative of confined cyclohexane, as observed in Figure 4.6. At lower temperatures closer to the onset of initial melting, only one clear peak is present. With each incremental temperature increase, the sharper peak (approximately 1.5 ppm) starts to become more dominant. Unlike in Figure 4.4 where only the sharper peak is present, the peak at approximately 2.9 ppm corresponds well to the literature for cyclohexane melting in a pore size of 50 nm [26]. Despite the ability to accurately measure the signal intensity for the confined cyclohexane, the reason for the presence of the sharper peak was still unknown.

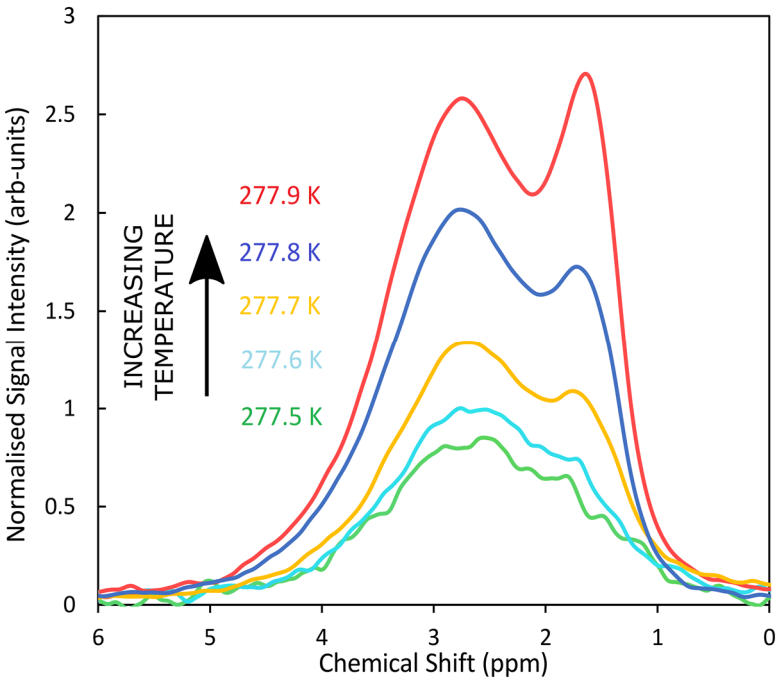

Figure 4.6. *The ^{1}H NMR spectrum for cyclohexane confined in the pores of CPG50 with increasing temperature from 277.5 K to 277.9 K. The sample was prepared using a thick-walled NMR tube. The peak for the melting of the confined cyclohexane (2.9 ppm) is now distinguishable from the unknown extra peak (1.5 ppm).*

When considering the possible environments for cyclohexane to exist, only within the pore itself and between the grains are commonly considered (if an excess of liquid is added during the preparation stage). However, it is the possible presence of a third environment which may be the cause of the unknown peak. When an excess of material, both liquid and solid, is used, the cyclohexane confined between the particles and the side of the NMR tube may have some other physical effect responsible

for the extra peak in the NMR spectrum. The type of line shape observed is indicative of the type of transverse relaxation, fast or slow, experienced by the molecules. When confined between the grains of the solid support and the side of the NMR tube, the cyclohexane molecules may be experiencing a variation to their T_2 relaxation which differentiates considerably from that of the confined and pure bulk liquid. Figure 4.7 is a schematic representation of the three different types of cyclohexane possibly present.

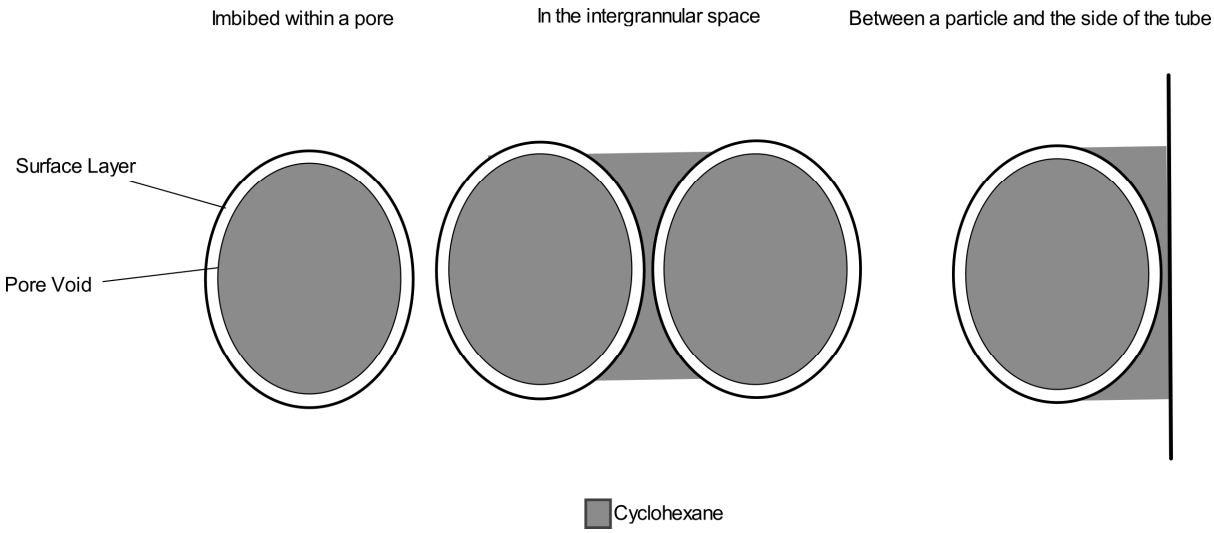

Figure 4.7. *A schematic representation of the three possible environments for cyclohexane to exist in a cryoporometry experiment; within the pores, in the intergranular space and between the particle and the side of the NMR tube.*

4.3.4. Standard Tube with Reduced Material

To reduce the contribution from this environment, it was necessary to revert back to using a standard NMR however this time adding significantly less material. As Figure 4.8 demonstrates, adding significantly less material will reduce the amount of cyclohexane present in the third environment in the active NMR region.

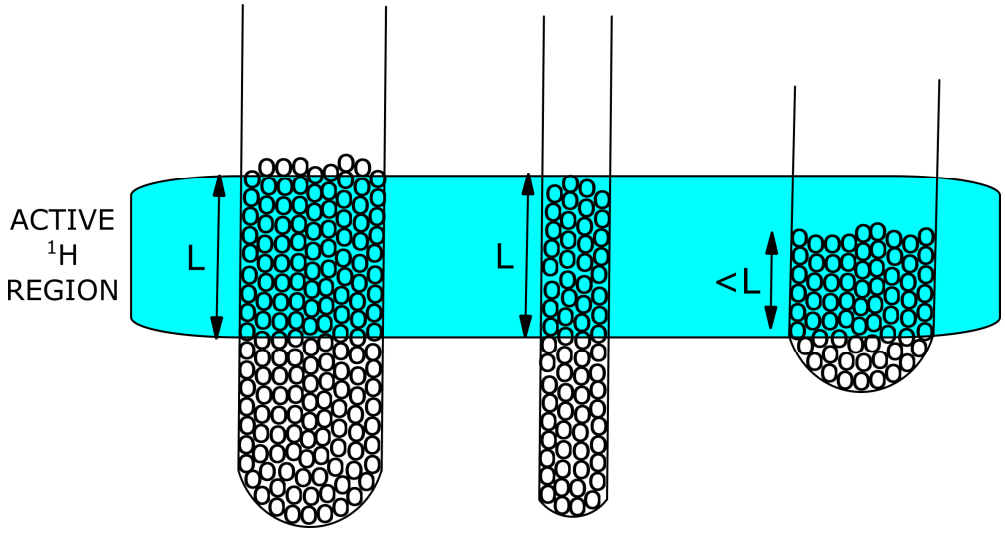

Figure 4.8. *A schematic representation of the differences between the three preparation techniques.*

The first preparation technique had a significant amount of material in the active region. This amount was reduced when using a thick-walled NMR tube however, the full length, L, of the active region was still covered. The next step was to test the same amount of material as used in the thick-walled tube but this time being placed in a standard tube. A subsequent reduction in L is then observed.

Using the same experimental procedure, a melting point depression was obtained for cyclohexane confined in the pores of CPG50. By incrementally increasing the temperature, only one peak for the confined liquid was observed. This implies that the contribution from the third environment was successfully reduced to ensure it did not affect the experimental data. Figure 4.9 follows the melting transition. The onset of melting starts to occur at 276.5 K and the peak starts to plateau at 278.1 K, where almost all of the cyclohexane had melted inside the pores. The signal intensity then started to reduce with increasing temperature according to Curie's Law up until the bulk melting temperature, where a subsequent rise in signal intensity was observed when the cyclohexane in the intergranular space started to melt. The melting/freezing hysteresis is shown in Figure 4.10.

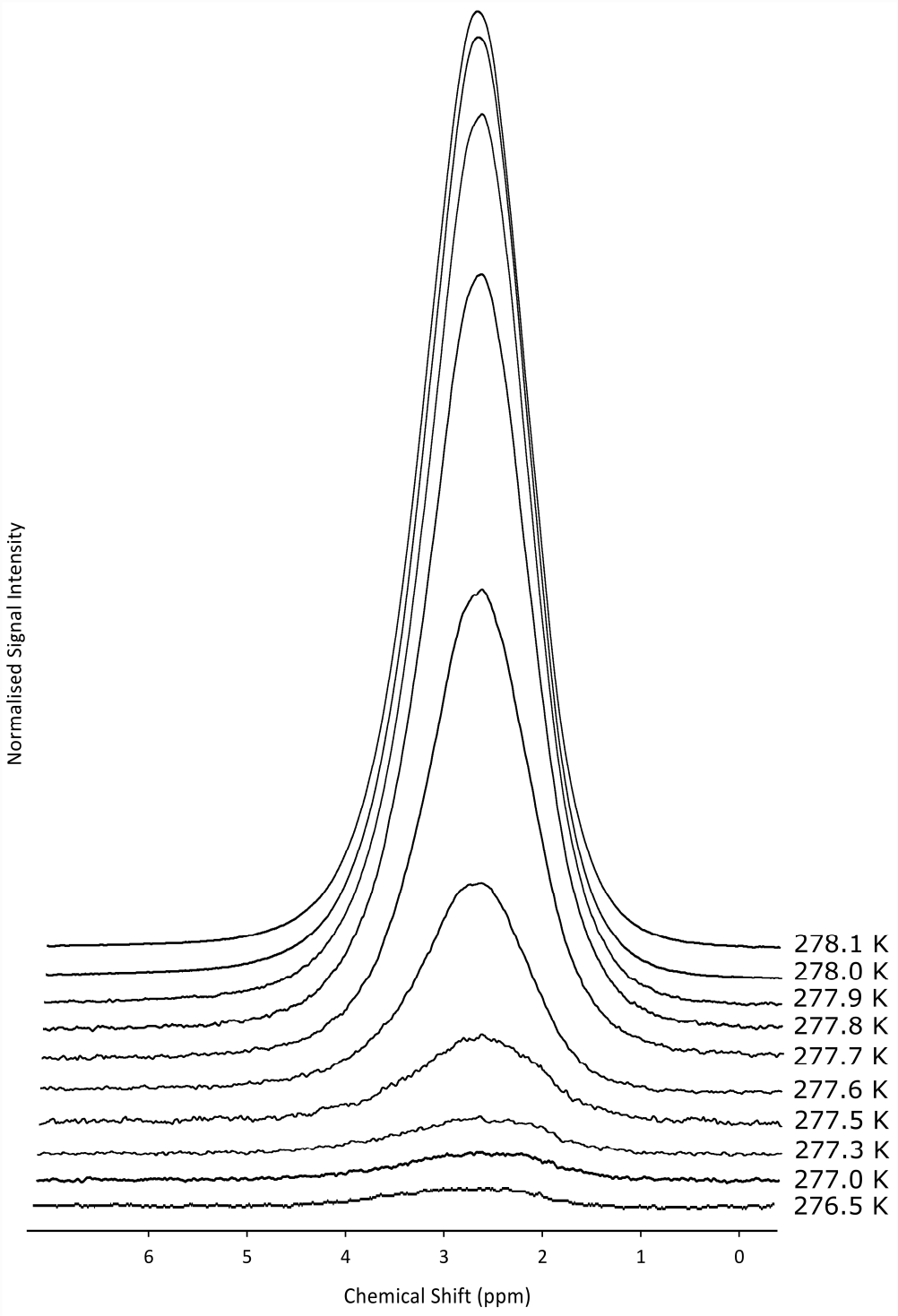

Figure 4.9. *The ^{1}H NMR spectrum for cyclohexane confined in the pores of CPG50 using a standard NMR tube with less material. The increase in peak intensity corresponds to the incremental increase in temperature. No extra peak is observed.*

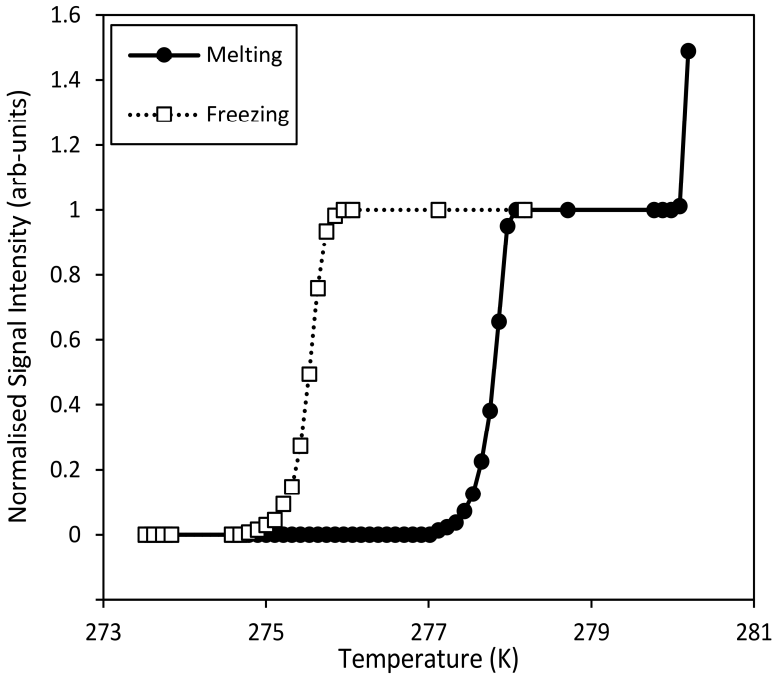

Figure 4.10. *The NMR melting and freezing curves for cyclohexane confined within the pores of CPG50.*

Prior to analysis of the remaining CPGs, one final test was conducted to analyse the change in melting behaviour with time. Using the established experimental protocol, a sample of cyclohexane in CPG50 was analysed 1, 2 and 3 days after its initial preparation. Figure 4.11 (a) illustrates its change in signal intensity at room temperature, prior to cryoporometry analysis. As intuitively expected, there is a slight reduction in intensity with time due to the volatility of the liquid. However, no significant difference is observed between the second and third days. Figure 4.11 (b) then measures the signal intensity with increasing temperature as the cyclohexane melts inside the pores. There is no clear difference over the three days suggesting that the freezing of cyclohexane does not in any way destroy the matrix of the solid support.

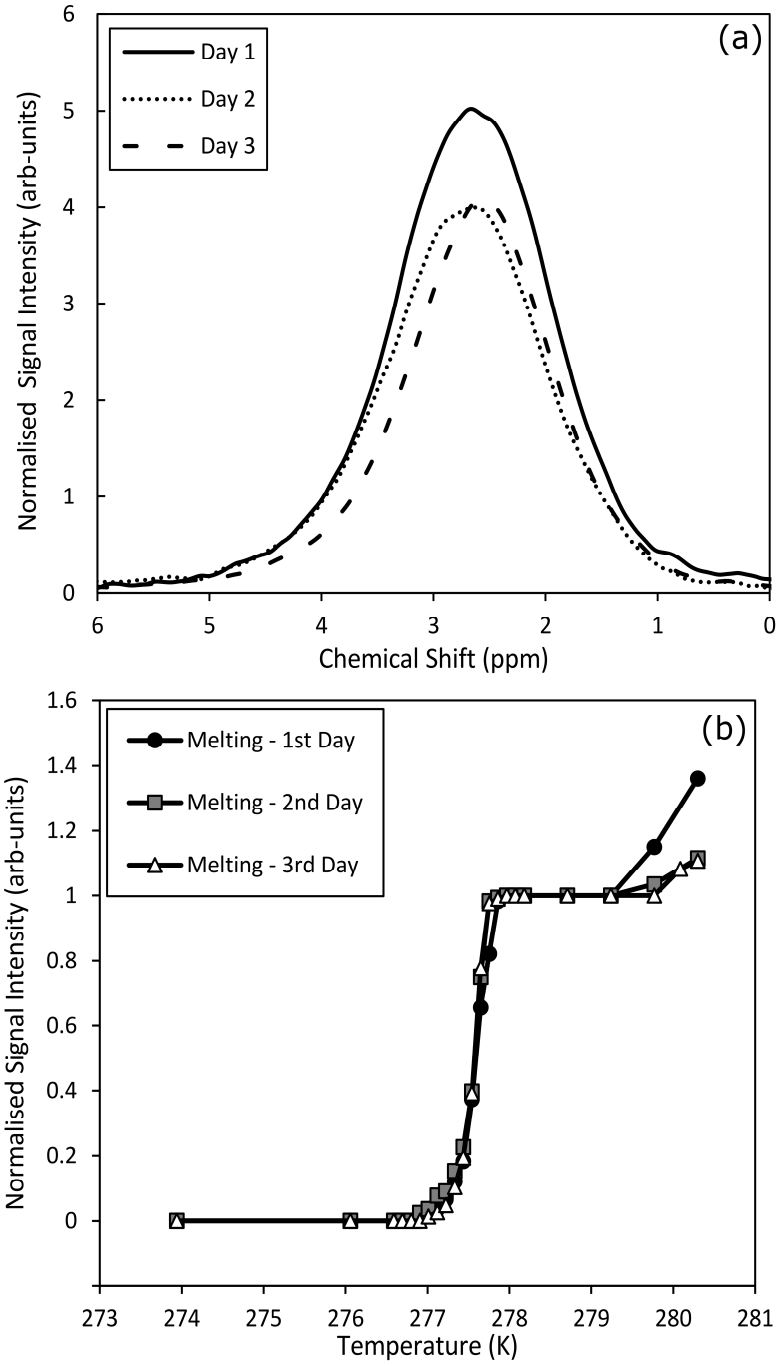

Figure 4.11. (a) *Signal intensity check for cyclohexane confined in CPG50, at room temperature, over three days post sample preparation and* ***(b)*** *the difference in melting between the three days.*

This established experimental protocol was then applied to analyse a range of CPGs with differing average pore size. The largest melting point depression was observed for the smallest pore size available, CPG24. This demonstrates the inverse relationship between pore size and temperature as described by Equation 2.22. Similarly, the smallest melting point depression was obtained for the

largest pore size, CPG100. The melting point data is provided in Figure 4.12. The conversion of melting point data into a pore size distribution is described in Chapter 5.

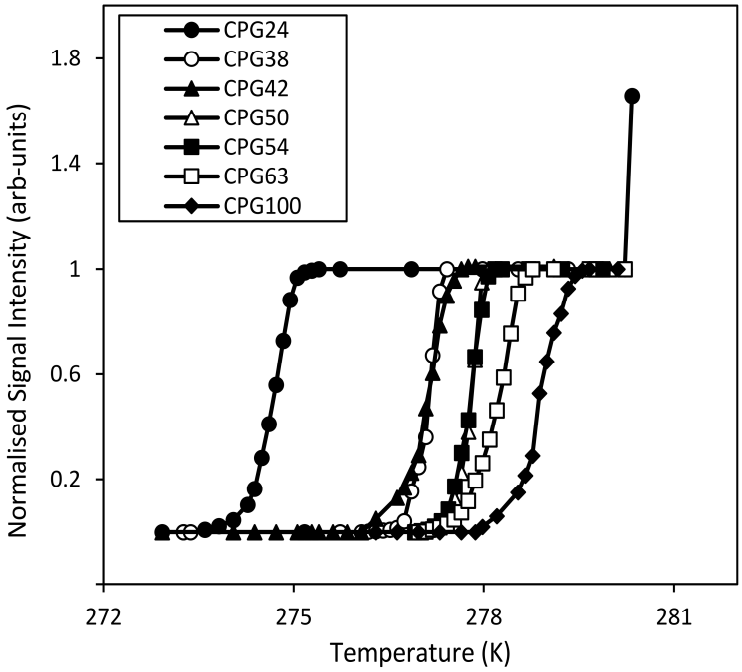

Figure 4.12. *The NMR melting curves for cyclohexane confined within the pores of a range of CPGs with differing average pore size.*

4.4. Conclusions

This chapter describes the work undertaken to set up a suitable protocol for cryoporometry analysis. A review of the literature determined that there was no one widely used preparation method for cryoporometry experiments. The sample preparation method was highly dependent on the type of solid support being used for the analysis. As such, it was necessary to determine a general method for cryoporometry measurements that could be applied throughout.

Initial measurements revealed a high dependence on the sample preparation methodology. Using a standard tube with excess material, both solid and liquid, meant that the NMR peak for confined cyclohexane was completely masked by an unknown contribution that caused an extra, much shaper, peak slightly up field from the peak of interest. A reduction in material, *via* the use of a thick-walled NMR tube, produced improved results. The unknown peak still existed however its contribution to the

overall signal intensity was reduced significantly, such that direct measurement of the confined cyclohexane peak could be determined. Reverting back to a standard NMR tube, this time with significantly less material, produced the optimum line shape required for analysis. Only one, smooth, broad peak was obtained for the confined cyclohexane which increased incrementally with increasing temperature. At the point of complete pore melting, the signal intensity then started to reduce, with increasing temperature, according to Curie's law.

This chapter has established an experimental procedure which has been applied to a range of different pore sizes. Using this methodology, data suitable for a conversion into a pore size distribution is now possible. The following chapters describe the application of the cryoporometry technique to different types of solid supports.

CHAPTER 5

A Novel Method for the Conversion of NMR Melting Point Data into Pore Size Distributions - Application to Porous Silica.

5.1. Introduction

As demonstrated in Chapter 4, and based on the Gibbs-Thomson thermodynamics for a liquid confined within a cylindrical pore [39-42, 44, 106], NMR cryoporometry observes a depression in the observed melting point of a confined liquid. The melting point depression for a small isolated spherical crystal of diameter x is given by Equation 2.21 where T_m is the bulk solid melting point, T_m (x) is the melting point of a crystal with diameter x, ΔH_f is the bulk enthalpy of fusion, ρ_s is the density of the solid and γ_{sl} is the surface energy at the solid-liquid interface [103]. These values are constants for a particular liquid and can be simplified to a melting point depression constant denoted as k_c. The value of k_c is dependent on the liquid being used, and is also reported as dependent on pore geometry and structure [56]. However, while the latter dependence is generally true of the melting point depression itself, k_c can be derived by several methods, which are not necessarily sensitive to pore geometry. The larger the value of k_c, the more suitable the liquid is for measuring larger pore sizes. Equation 2.21 relies upon a number of assumptions, such as γ_{sl} is isotropic and that the size of the crystal is large enough that it retains its bulk properties [103].

In order to convert the melting point depressions observed into a pore size distribution, a value for k_c must be known. There are several methods which have been used to calculate the value of k_c. The first method involves measuring the temperature depression for a range of different pore sizes that

have been confirmed by alternative methods. A value for k_c can be estimated from experimental data [107, 108] using Equation 5.1.

$$\Delta T_m = \frac{k_c}{x-2sl} \tag{5.1}$$

This equation closely resembles Equation 2.22, with the additional contribution from a non-freezing surface layer, $2sl$. Here, x is the pore diameter, k_c is the melting point depression constant and $2sl$ is the contribution from a non-freezing surface layer. There are several potential problems that are associated with this approach. The main issue is the presence of a non-freezing surface layer, $2sl$. The existence of the non-freezing surface layer is expected based on the wetting theory for the wetting of the pore wall by the imbibed liquid [109]. The thickness of this layer has been debated in the literature and is based on the assumption that the layer is independent of pore size. Previous NMR studies into the behaviour of water in silica systems have revealed the thickness as being between 1-3 monolayers of water, corresponding to a maximum value of approximately 0.8 nm [56, 110-115], but with little agreement between different studies. This literature data is summarized in Table 5.1 with differences in the contribution of a non-freezing surface layer resulting in the various results observed for k_c. The range of k_c values previously obtained for water lie between 49 and 58 K nm.

Table 5.1. A collection of historical data summarizing values of k_c and the thickness of the non-freezing surface layer used.

k_c (K nm)	Surface layer thickness (nm)	Method used to obtain k_c	Type of porous Solid
57.3	0	Calibration	SiO_2 [52]
49.4	0.20-0.50	Calibration	MCM-41[116]
51.4	0.60	Theoretical	MCM-41[113]
51.5	0.62	Calibration	SiO_2 [108]
52.4	0.76	Theoretical	MCM-41 + SBA-15 [114]
52	Unknown	Theoretical	SiO_2 [117]

A value for k_c can also be estimated. Taking into account the effect of the solid/liquid interface yields the following equation, Equation 5.2.

$$k_C = 2v\gamma_{Sl}\frac{T_m}{\Delta H_f} \tag{5.2}$$

In this equation, v is the molar volume of the liquid, γ_{Sl} is the surface energy at the solid-liquid interface, ΔH_f is the bulk enthalpy of fusion and T_m is the bulk melting point. When measuring the melting point depression for a liquid confined within a cylindrical pore shape, an additional factor of 2 needs to be added to Equation 5.2 to take into account the differences in pore curvature [56, 118, 119]. By obtaining values for molar volume, the free energy at the interface and latent heat of melting, an estimation for k_c can be obtained. Other estimations for k_c were found by using a two-parameter fit to experimental data, rather than one-parameter or linear fits. Vargas-Florencia *et al.* [98] describe applying this method for octamethylcyclotetrasiloxane (OMCTS) confined in large pores. OMCTS was found to have a much larger k_c value than water, making it more suitable for cryoporometry measurements of larger pores, up to a micrometer in size. However the k_c value obtained is based on assumptions of the size of γ_{Sl} [98].

Another method used to estimate k_c is to plot the freezing point depression against the surface to volume ratio [56]. The advantage of this procedure is that is does not require an assumption to be made

on the pore geometry. The disadvantage however is that the surface to volume ratio needs to be determined by other techniques such as gas adsorption [120]. A further disadvantage is that the method does not take into account the non-freezing surface layer and consequently, the value of k_c is overestimated. Despite the disadvantages, Petrov and Furo [56] describe how they have used this method to obtain values of k_c for liquids such as water and cyclohexane.

Mesoporous silica are key to many technological applications, including catalysis [121] and drug delivery [122], due to their characteristic porous structure. Consisting of highly ordered structures, uniform pore sizes and high surface-to-volume ratios, analytical methods such as differential scanning calorimetry (DSC) [113], nitrogen porosimetry [123], neutron diffraction [114] and gas adsorption [120] can effectively probe their structures. The structure of three common types of mesoporous silica are illustrated in Figure 5.1.

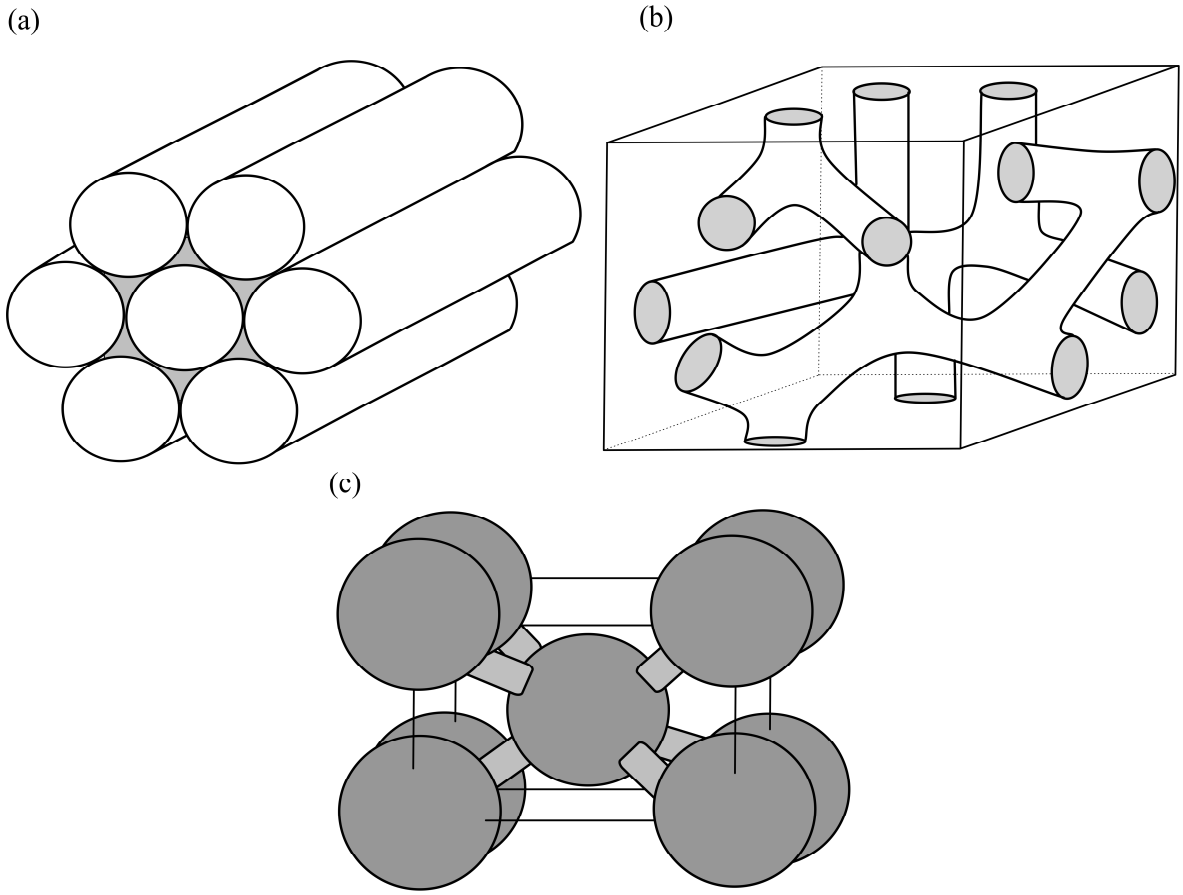

Figure 5.1. *Schematic representation of the cylindrical pores in* ***(a)*** *SBA-15 and* ***(b)*** *KIT-6 and the spherical pores in* ***(c)*** *SBA-16.*

NMR cryoporometry [19, 46, 49, 56, 111] has some advantages over the previously mentioned techniques as it offers a direct measurement of open pore volume and can be used for samples in the aqueous environment [19]. Its use has been demonstrated on ordered silica, such as MCM-41 [114-116] and SBA-15 [114, 124], characterizing their pore size distributions. This information is critical in the design of mesoporous silica as differences in pore sizes have significant effects on the effectiveness of these materials as catalysts [125].

This chapter introduces a novel method for obtaining pore size distributions by firstly determining values for k_c and $2sl$. By fixing the value of k_c, according to the liquids' inherent properties, and studying a series of literature data from a range of experimental studies, an estimate for the thickness of the non-freezing surface layer can be determined. This method has been applied to water in silica as well as the cyclohexane melting point data obtained in Chapter 4.

5.2. Experimental

5.2.1. Sample Preparation

SBA-15, SBA-16 and KIT-6 silica samples were provided by collaborators, C. M. A. Parlett and A. F. Lee, and were prepared by the methods of Stucky [126] and Ryoo, [127] respectively. Successful synthesis of both cylindrical supports has been confirmed by low-angle X-Ray diffraction (XRD) (Figure 5.2). All samples were dried in the oven at 373.15 K for 24 hours and then placed in a desiccator for a further 24 hours prior to being used.

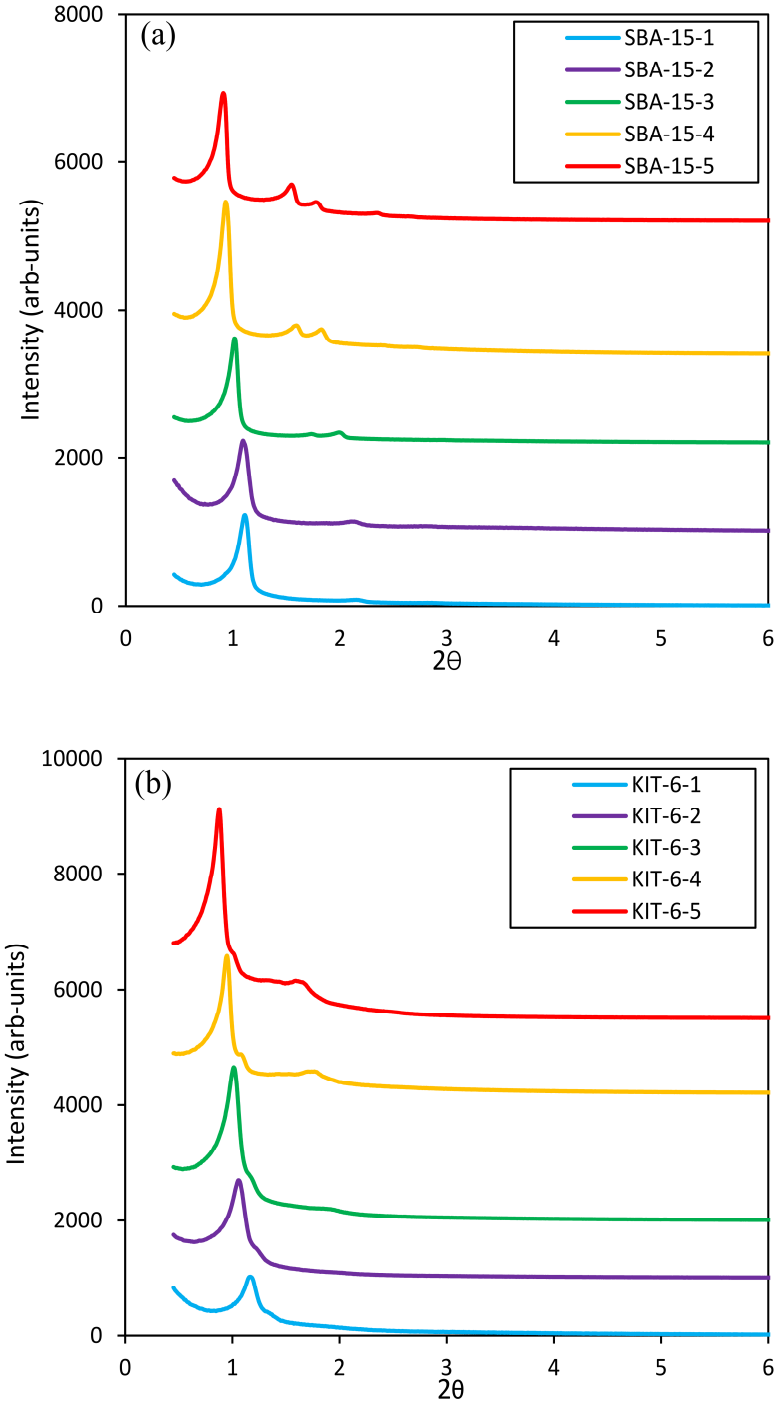

Figure 5.2. *Low angle X-Ray diffraction data confirming the successful synthesis of* ***(a)*** *SBA-15 silica and* ***(b)*** *KIT-6 silica. Data provided by C. M. A. Parlett and A. F. Lee.*

5.2.2. Nuclear Magnetic Resonance

All samples were prepared according to the experimental protocol established in Chapter 4. All cryoporometry measurements were made using the CPMG [104, 105] pulse sequence illustrated in Figure 4.1. In each cryoporometry experiment, a melting curve has been acquired. The sample was initially frozen, in a series of small temperature steps, beyond the freezing point of the in-pore liquid, until no NMR signal was acquired. At least 10 minutes passed after all temperature changes and NMR experiments were used to confirm no further changes in acquired signal. For each acquisition at a given temperature, 8 transients of 8192 complex data points were obtained. The typical total NMR experimental time to characterize one silica sample was 8 - 9 hrs, which compares well with about 12 hours for a full nitrogen isotherm, although these times are highly dependent on the material (degree of porosity and surface area), experimental parameters, such as rate of heating, and mass of sample analysed.

To obtain low temperatures, a Bruker BVT3200 temperature control system, with a precision of 0.1 K, was used. The cooling system passes a combination of N_2 gas and air over the sample at a flow rate of 400 l h^{-1} operating at 4% cooling with the probe heater set to a maximum of 17% output. Before the start of a cryoporometry experiment, the cooling system was allowed to equilibrate with the probe heater. The temperature control unit was optimized to ensure that over- and undershoot of the sample temperature was minimized effectively. Furthermore, the probe was tuned and matched in areas out of sample phase transition to account for the significant temperature changes. The calibration between actual and stated temperature, illustrated in Chapter 3, was applied here.

Following the approach detailed by Strange *et al.* [46] and using values of k_c and $2sl$ obtained in Section 5.3, the melting point depressions acquired by NMR cryoporometry can be converted into pore size distributions by the use of Equation 2.24.

5.2.3. Differential Scanning Calorimetry (DSC)

The DSC measurements were made using a Mettler-Toledo DSC 1 STAR^e system apparatus equipped with a liquid nitrogen cooling supply. Samples of approximately 2 mg of the dry silica were added to an aluminium pan followed by approximately 10 mg of water. The pans were then immediately sealed and re-weighed. The samples were initially taken down to 228 K prior to acquisition to ensure all of the liquid is frozen. A heating rate of 0.5 K min^{-1} was used through to a final temperature of 283 K. To transform the DSC melting thermograms into a pore size distribution, the procedure outlined in Majda *et al.* [62] was followed.

5.2.4. Nitrogen Porosimetry

Nitrogen porosimetry was undertaken on a Quantachrome Autosorb IQTPX porosimeter with analysis using ASiQwin v3.01 software. Samples were degassed at 523.15 K for 12 hours prior to recording N_2 adsorption/desorption isotherms. Mesopore properties were calculated applying the BJH method to the desorption isotherm for relative pressures of $P/P_0 > 0.35$.

5.2.5. Scanning Transition Electron Microscopy (STEM)

High resolution bright field STEM images were obtained by collaborators *via* the use of an aberration corrected JEOL 2100-F microscope operated at 200 kV, with image analysis using ImageJ 1.41 software. Samples were dispersed in methanol and drop cast on 200-mesh carbon coated copper grids and dried under ambient conditions.

5.3. Results & Discussion

5.3.1. Obtaining Values for k_c and $2sl$

A number of methods for estimating values of both k_c and the thickness of the non-freezing surface layer, $2sl$, have been reported in the literature for the freezing of water in silica. For example, assuming that there is no non-freezing layer, and forcing the data through the origin, a higher value of k_c is obtained. There is no consensus on the thickness of the surface layer itself, with estimated

values ranging from 0 to 0.76 nm, the choice of which affects the value of k_c obtained. These values have been summarized in Table 5.1.

An alternative method is presented here for obtaining values for the two parameters. By taking into account all of the raw melting curve data used in the references cited in Table 5.1, it is possible to use all measurements of the melting point of water obtained in porous silica for different pore sizes, different geometries and different structures.

Figure 5.3 plots the pore size distributions against observed melting point depressions for 37 different materials, all with pore sizes lower than 10 nm, from 6 previous cryoporometric studies of porous silica. Characterization of the pore sizes of the silica used here was done using N_2 porosimetry. Literature values for the physical constants and parameters used in the melting point depression constant, k_c, are summarized in Table 5.2, were used to calculate a value of 49.53 K nm, using Equation 5.2, so only a single-parameter fit of the literature data, using Equation 5.3, is required to estimate the thickness of the non-freezing surface layer, where the line crosses the vertical axis. The thickness of the surface layer according to Figure 5.3 is 0.533 ± 0.062 nm.

$$x = \frac{k_c}{\Delta T_m} + 2sl \tag{5.3}$$

Given the assumptions made, not only in the development of the theory (for example, enthalpy changes depend on the temperature at which they occur) but also assuming, for example, that k_c is a constant for any cryoporometry experiment using the same liquid/porous material and that $2sl$ is constant over the temperature ranges specified [112, 115, 128], the quality of the fit, with an uncertainty of 11 %, is good.

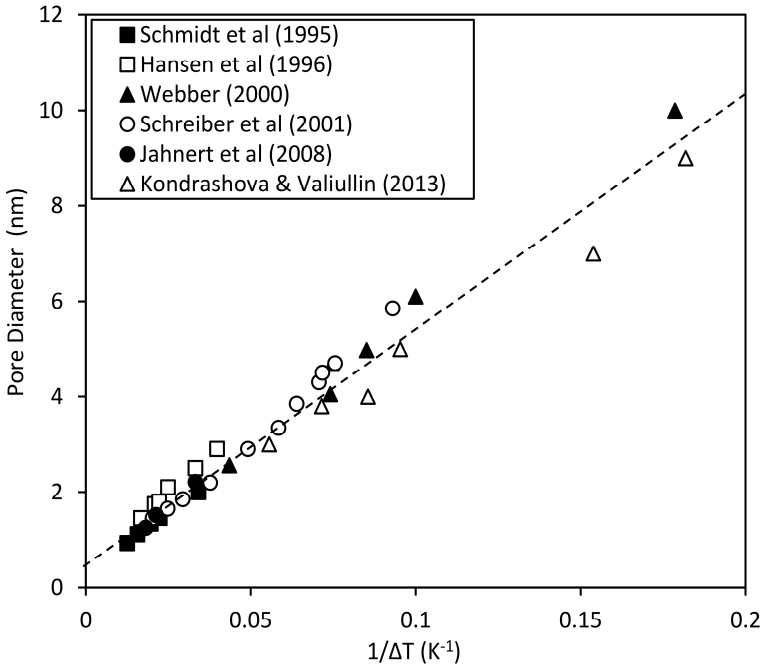

Figure 5.3. *A plot of average pore diameter, obtained by N_2 porosimetry, versus the inverse of the melting point depression for the set of cryoporometry data reported in the literature. The intercept of the trend line reveals a value of 0.53 nm for the thickness of the non-freezing surface layer.*

Table 5.2. Literature values for the physical parameters and constants used in calculating k_c for water.

Physical Parameter	Value
molar volume of the liquid, $\boldsymbol{\nu}$ (m^3 mol^{-1})	18.1 [99]
surface energy at the solid-liquid interface, $\boldsymbol{\gamma_{Sl}}$ (mJ m^{-2})	30 [99]
bulk enthalpy of fusion, $\boldsymbol{\Delta H_f}$ (kJ mol^{-1})	5.99 [99]
bulk melting point, $\boldsymbol{T_m}$ (K)	273.2[99]

The uncertainty in pore size distributions generated from these values can be estimated from the uncertainty in $2sl$, ± 0.062 nm, and from the intrinsic error in our temperature control unit. For the experiments here, in order to characterize the pore size distributions with highest resolution, a minimum temperature ramp was employed, with an uncertainty of ± 0.04 nm estimated for a 5 nm pore size material. This gives the overall technique demonstrated here an experimental error of only

± 0.07 nm. Reduced experimental times can be achieved, with a coarser temperature ramp, but at the expense of pore size distribution resolution.

The utility of this new approach can be further illustrated by demonstrating the method with a different liquid in a different porous material; for example, cyclohexane in controlled pore glasses from Chapter 4. Figure 5.4 shows a plot of reciprocal temperature depression against pore diameter for cyclohexane in glass, for 13 measurements taken from 5 references [97, 99, 100, 103, 129], with 7 additional measurements acquired in Chapter 4. Fitting of this data to the rearranged Gibbs-Thomson equation (Equation 5.3), using a value of k_c of 103.7 K nm, estimated a value for $2sl$ of 3.27 ± 0.47 nm. This compares well with previous studies [130] and corresponds to a layer of approximately 4 molecules stacked upon one another. Without the added data acquired here, a $2sl$ value of 3.13 ± 0.39 nm is obtained.

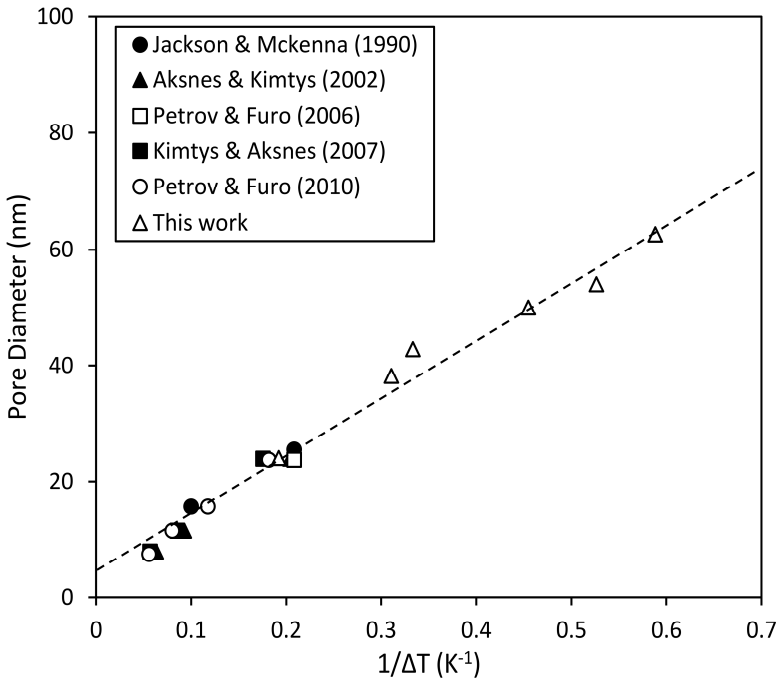

Figure 5.4. *A plot of average pore diameter versus the inverse of the melting point depression for the set of cryoporometry data using cyclohexane in controlled pore glass. The intercept of the trend line reveals a value of 3.27 ± 0.47 nm for the thickness of the non-freezing surface layer.*

5.3.2. Pore Size Distributions of CPGs

In order to validate the approach detailed in 5.3.1, the technique was first applied to the melting point data acquired in Chapter 4 for cyclohexane confined in the pores of CPG. Figure 5.5 illustrates the size distributions up to 63 nm. Above this size, the accuracy of cyclohexane as a liquid used to probe pore size starts to reduce significantly. This is further explored in Chapter 6.

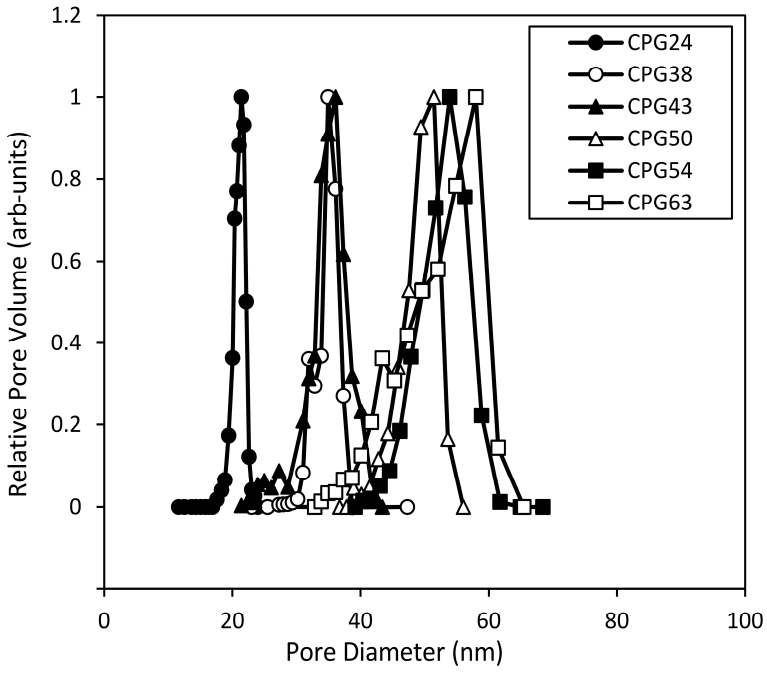

Figure 5.5. *Pore size distributions for controlled pore glass of six differing average pore diameters obtained by NMR cryoporometry experiments with cyclohexane as the probe liquid.*

5.3.3. Pore Size Distributions of SBA-15 and KIT-6 from NMR

Pore size distributions were produced for three different types of porous silica: SBA-15, KIT-6 and SBA-16. The results of all CPMG spin echo measurements for water confined within the pores of the three porous silica materials are illustrated in Figures 5.6, 5.7 and 5.8. Comparative DSC melting curves are provided Appendix 2, Figures A2.1, A2.2 and A2.3. In all cases, there is an increase in signal intensity as the temperature increases and the water confined in the pores melts. A subsequent rise in signal intensity at the bulk melting temperature is also observed. Each sample demonstrates a smooth transition from solid to liquid. Those which are smaller in average diameter experience a

broader pore melting transition region compared to those larger in size. A small amount of signal was observed at temperatures much less than the onset of significant melting, particularly in experiments using KIT-6. This may be due to the interconnected nature of the pores. Some water may reside in the twists of the torturous matrix and suffer a subsequent enhancement to its onset of melting. Nonetheless, this small amount of signal observed was less than 5 % in overall signal intensity when compared to the melting of the water confined within the pores.

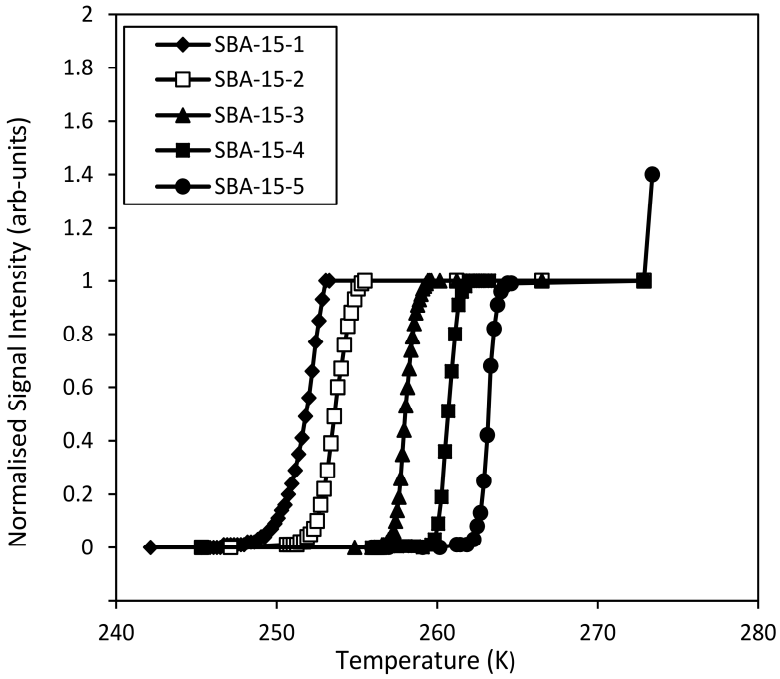

Figure 5.6. *NMR melting curves for water confined in the pores of SBA-15 silica of different average pore diameters.*

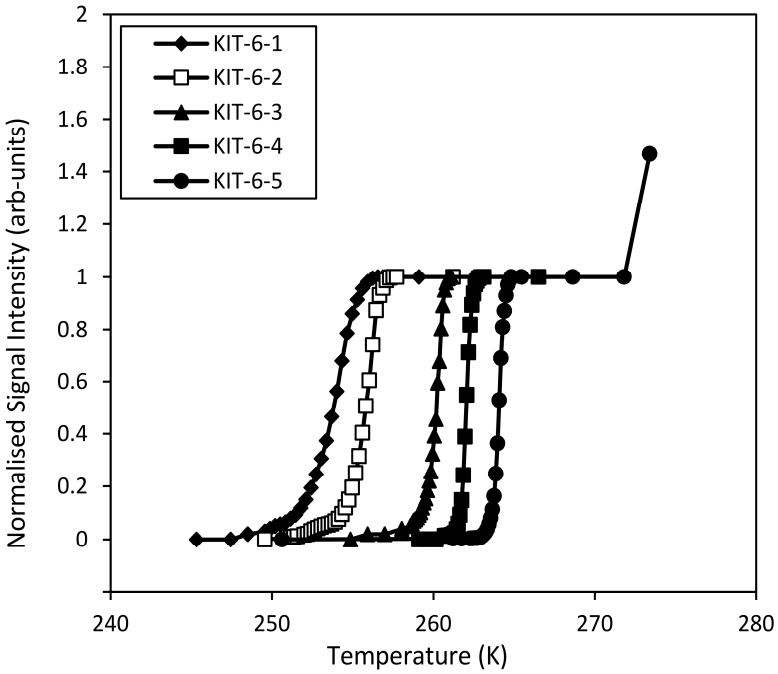

Figure 5.7. *NMR melting curves for water confined in the pores of KIT-6 silica of different average pore diameters.*

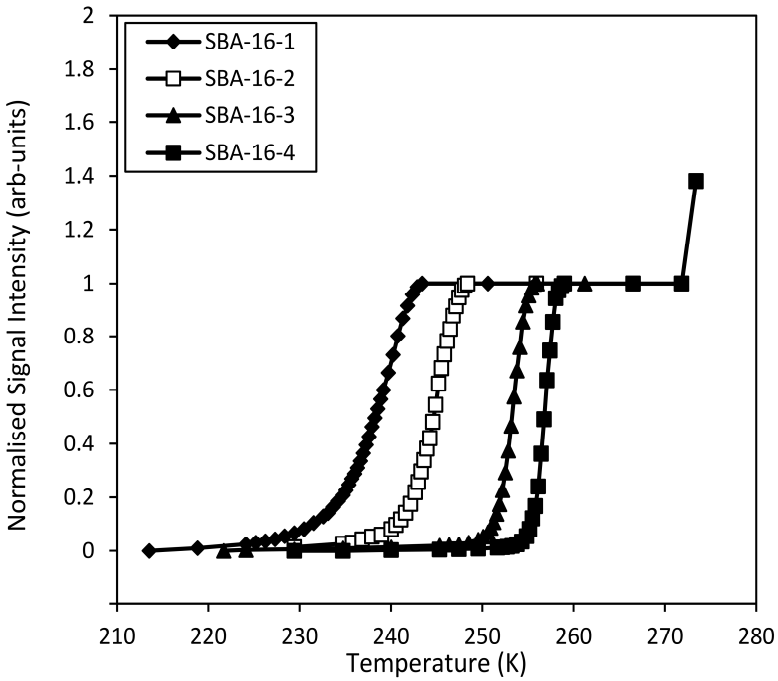

Figure 5.8. *NMR melting curves for water confined in the pores of SBA-16 silica of different average pore diameters.*

Pore size distributions were obtained by the use of Equation 5.3, using the values for k_c and $2sl$, 49.53 K nm and 0.533 nm respectively, and the subsequent melting point data. The pore size

distributions measured for SBA-15 are shown in Figure 5.9. These measured pore sizes can be verified by the use of N_2 porosimetry (Figure 5.10) and DSC (Figure 5.11). To the knowledge of the author, KIT-6 has not been characterized using NMR cryoporometry. While it has cylindrical pores, their geometry within a unit cell is different from SBA-15. Instead of packed channels, the pores form an intertwined 3D cubic network. The pore size distributions measured for KIT-6 are shown in Figure 5.12. Figures 5.13 and 5.14 show the KIT-6 pore size distributions as acquired by N_2 porosimetry and DSC, respectively. The pore size distribution data for both SBA-15 and KIT-6 are summarized in Tables 5.3 and 5.4 for both silica materials, for all measurements. The NMR methods shows very good agreement with the DSC data, with a RMS error of only 5.2 %. The differences between the NMR data and N_2 porosimetry were similar at lower pore sizes, but increased to over a nanometer in the silica with larger pore sizes.

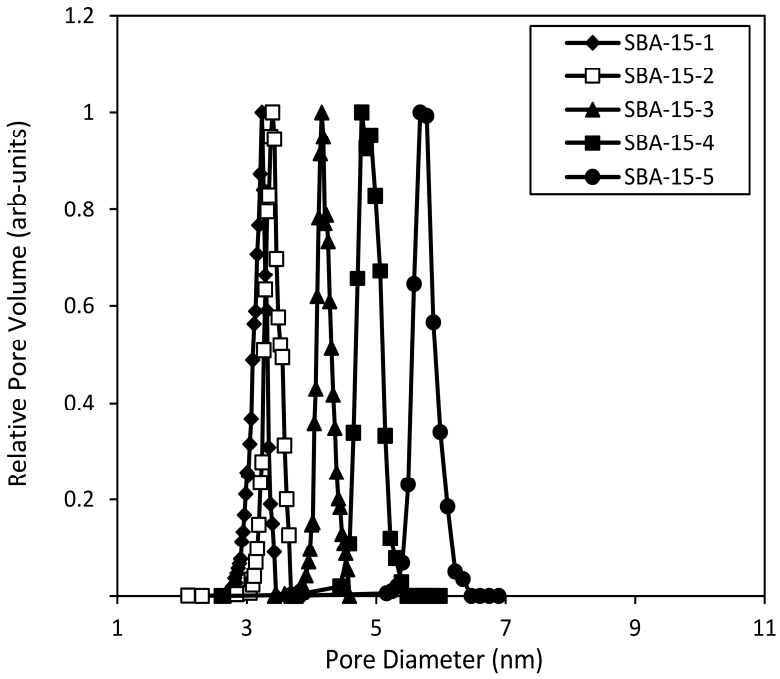

Figure 5.9. *Pore size distributions for SBA-15 silica of five differing average pore diameters obtained by NMR cryoporometry experiments.*

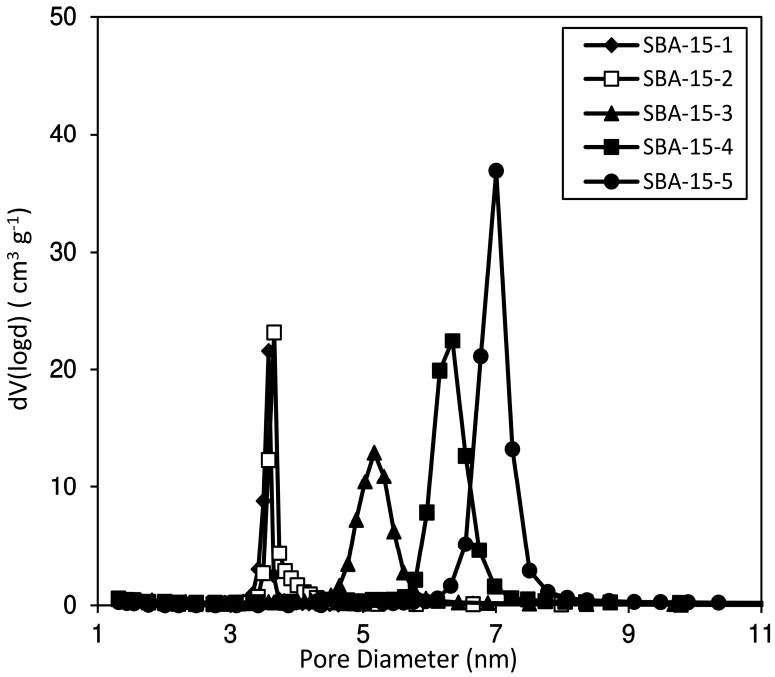

Figure 5.10. *Pore size distributions for SBA-15 silica of five differing average pore diameters obtained using N_2 porosimetry.*

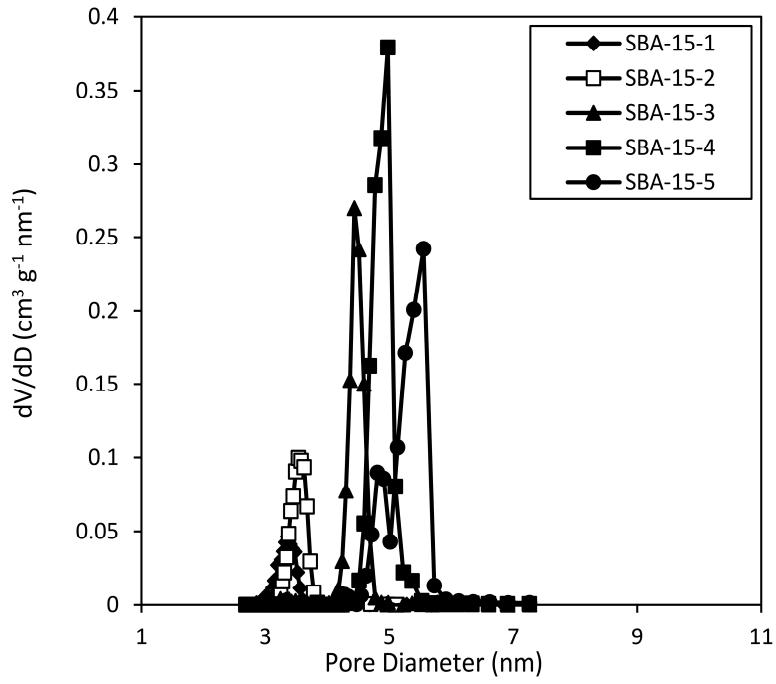

Figure 5.11. *Pore size distributions for SBA-15 silica of five differing average pore diameters obtained using DSC.*

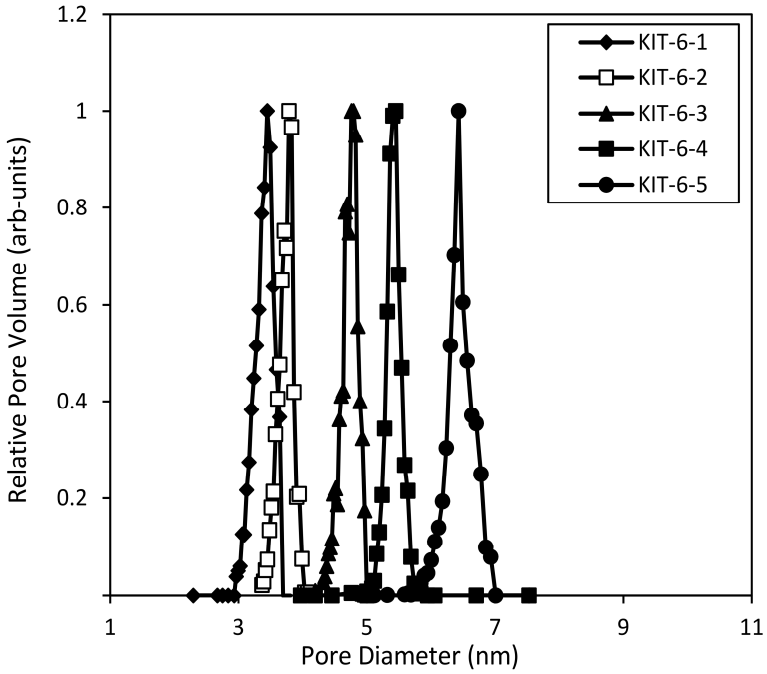

Figure 5.12. *Pore size distributions for KIT-6 silica of five differing average pore diameters obtained by NMR cryoporometry experiments.*

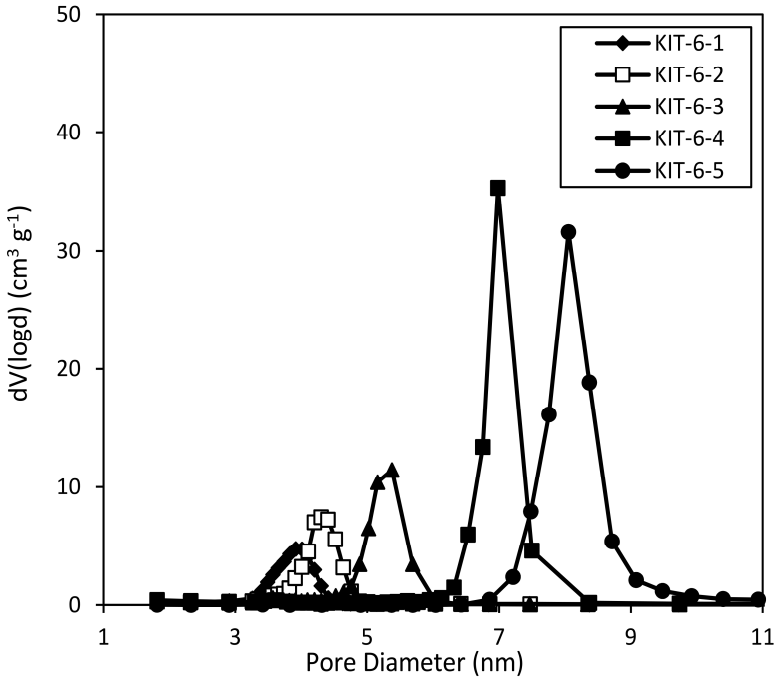

Figure 5.13. *Pore size distributions for KIT-6 silica of five differing average pore diameters obtained using N_2 porosimetry.*

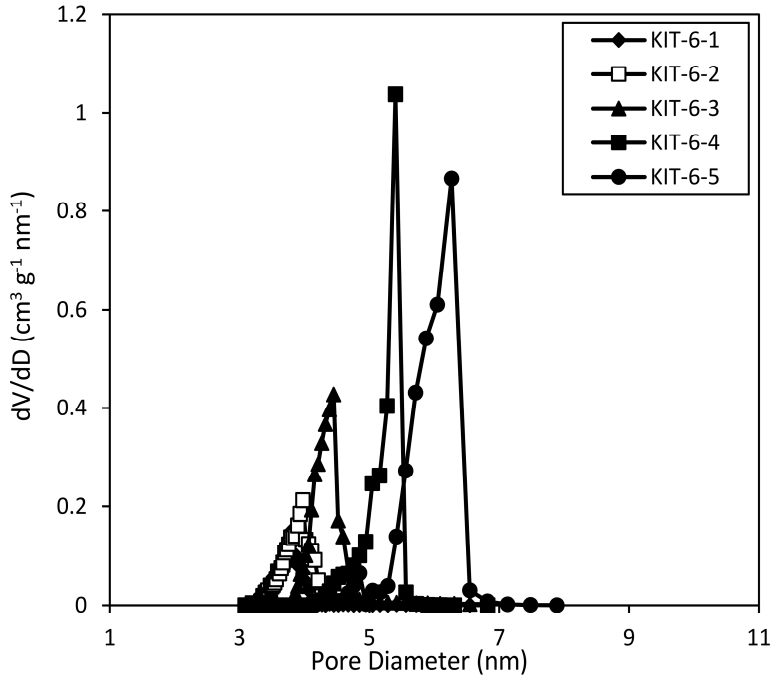

Figure 5.14. *Pore size distributions for KIT-6 silica of five differing average pore diameters obtained using DSC.*

Table 5.3. Nitrogen porosimetry, calorimetry and NMR data for the average pore diameters of SBA-15 materials characterized in this work.

Sample	Pore Diameter - N_2 Porosimetry (nm)	Pore Diameter - DSC (nm)	Pore Diameter - NMR (nm)
SBA-15-1	3.6	3.4	3.4
SBA-15-2	3.7	3.5	3.6
SBA-15-3	5.1	4.4	4.3
SBA-15-4	6.3	5.0	4.9
SBA-15-5	7.0	5.6	5.9

Table 5.4. Nitrogen porosimetry, calorimetry and NMR data for the average pore diameters of KIT-6 materials characterized in this work.

Sample	Pore Diameter - N_2 Porosimetry (nm)	Pore Diameter - DSC (nm)	Pore Diameter - NMR (nm)
KIT-6-1	3.9	3.8	3.6
KIT-6-2	4.3	4.0	4.0
KIT-6-3	5.3	4.4	4.9
KIT-6-4	6.9	5.4	5.5
KIT-6-5	8.0	6.3	6.4

For the measurement of pore size, DSC and NMR cryoporometry share many similarities, none more so than the fact they both measure a depression in the melting point of confined water. Nitrogen porosimetry, however, measures changes in pressure as the nitrogen flows in and out of the pores. This method obtains slightly larger pore sizes than NMR and DSC for both types of silica materials studied in this work. Similar differences in estimated pore sizes have been reported elsewhere in the literature [131, 132]. In some cases, the differences have been related to the structures of the porous material. For both gas adsorption and thermoporometric methods, assumptions have to be made about the phase changes being studied. In N_2 adsorption method, the molar volume and surface tension of the liquid nitrogen are required. These are normally taken as their bulk properties. In the NMR method, there are four parameters (Equation 5.2), all of which are assumed to be both constant and the same as their bulk values. A further set of assumptions made by both methods lies in the liquid-solid interface and its thickness. This work offers a method for estimation of this layer, and has been used this in all of the pore size distribution estimations. For the nitrogen method, the thickness of this layer is estimated for each pore diameter. A liquid-gas interface will also be more sensitive to changes in temperature and pressure. A thorough analysis, using other porosimetry models, is included in Appendix 4.

STEM images were provided for one sample of each type of silica together with the frequency distributions of the pore sizes present (Figures 5.15 and 5.16). The associated pore diameters for SBA-15-3 and KIT-6-3 obtained by microscopy analysis were 5.0 nm and 5.2 nm respectively. The agreement with the data provided in Tables 5.3 and 5.4 illustrate the suitability of the techniques demonstrated herein to accurately study the pore size.

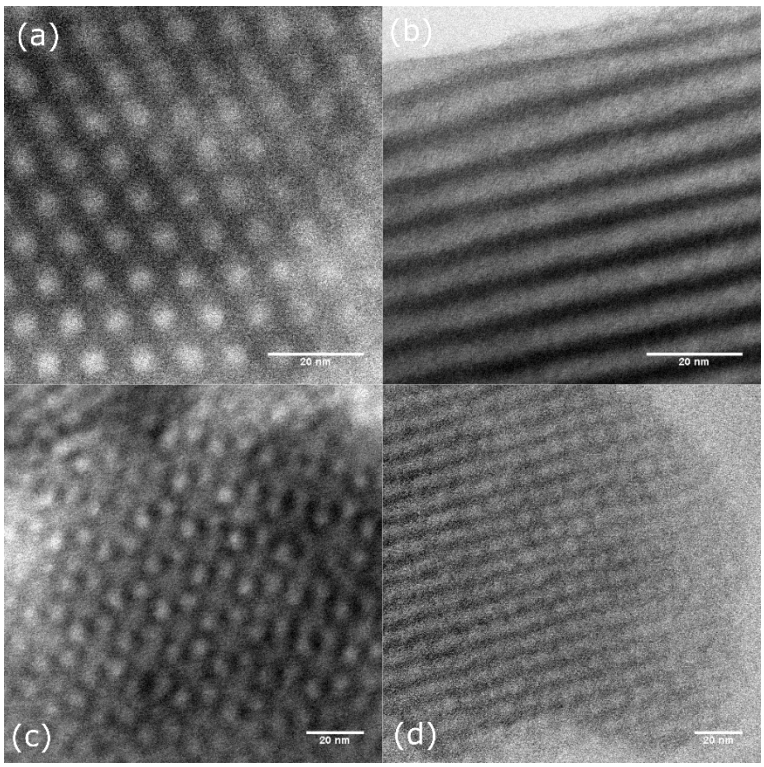

Figure 5.15. *Bright field STEM images of the cylindrical pores in SBA-15-3 (**(a)** and **(b)**) and KIT-6-3 (**(c)** and **(d)**).*

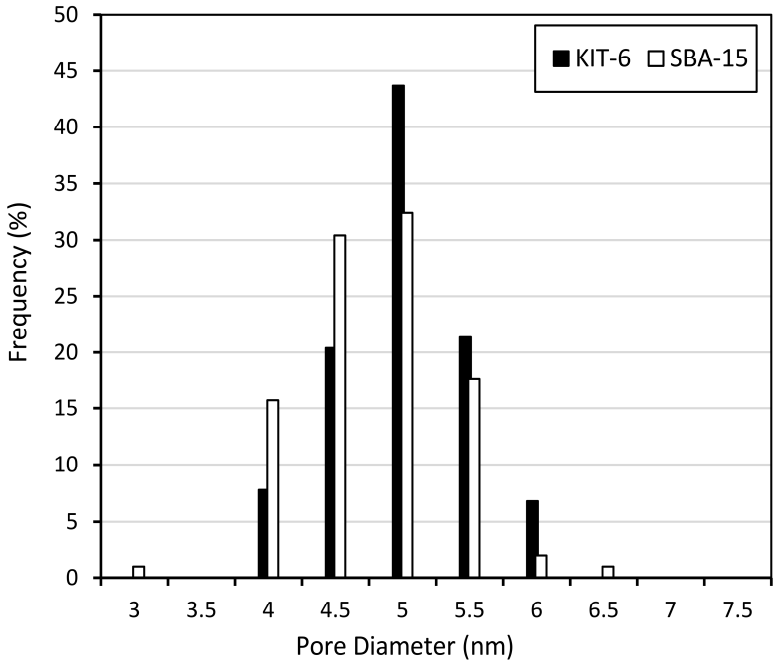

Figure 5.16. *Frequency data for the bright field STEM imaging of the cylindrical pores in SBA-15-3 and KIT-6-3.*

5.3.4. Spherical Pore Size Distributions from NMR

While SBA-16 has a different, spherical, pore structure to the materials studied previously, the same pair of fitting parameters can be used to obtain pore size distributions from the melting point depression data acquired. In this case, an additional factor of 2 is required to account for the difference in geometry [56, 118, 119]. The pore size distributions for water confined in SBA-16 are shown in Figure 5.17. These pore size distributions can be verified, as before, with DSC (Figure 5.18) and the pore size distributions are summarized in Table 5.5 for SBA-16 silica with four different pore sizes, between 1 and 10 nm. The NMR methods shows very good agreement with the DSC data, with a RMS error of only 1.3 %.

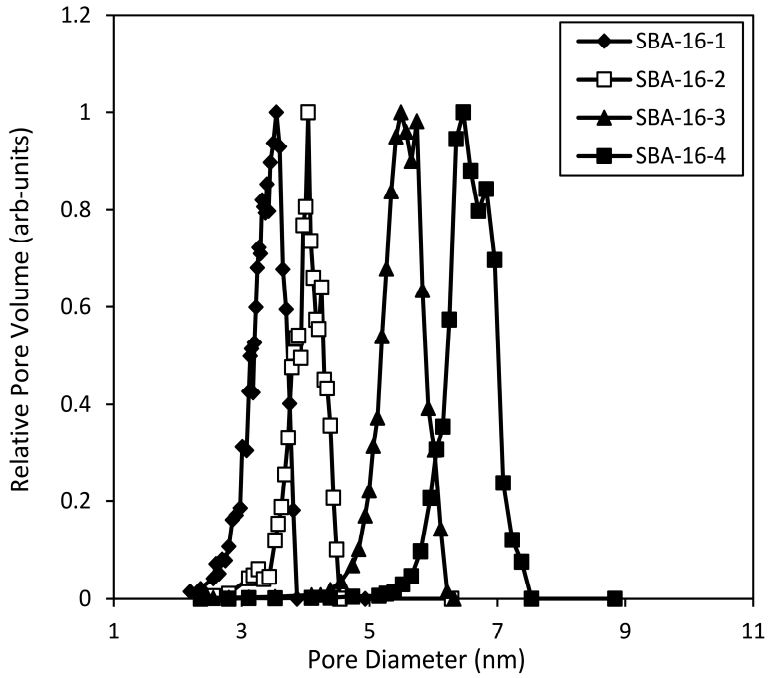

Figure 5.17. *Pore size distributions for SBA-16 silica of four differing average pore diameters obtained by NMR cryoporometry experiments.*

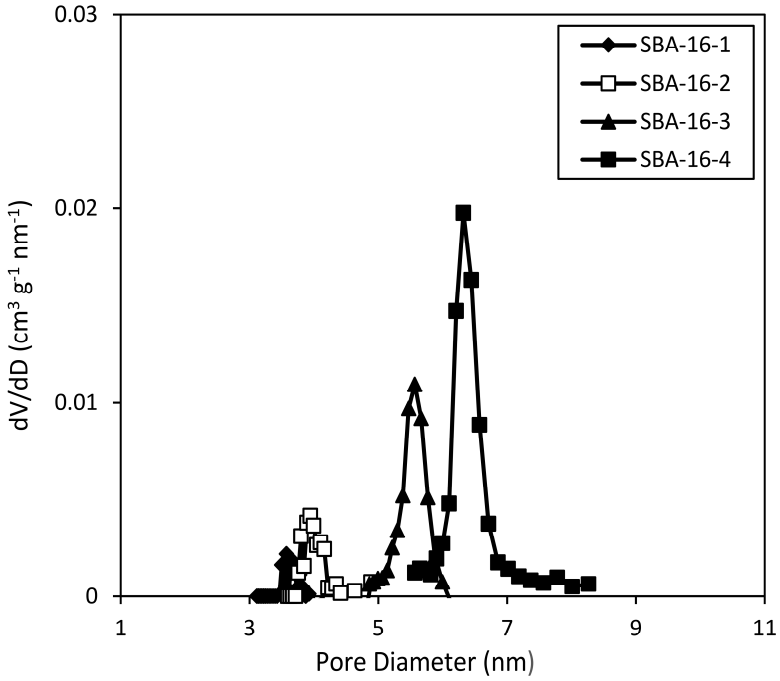

Figure 5.18. *Pore size distributions for SBA-16 silica of five differing average pore diameters obtained using DSC.*

Table 5.5. Nitrogen porosimetry, calorimetry, NMR and STEM data for the average pore diameters of SBA-16 materials characterized in this work.

Sample	Pore Diameter - N_2 Porosimetry (nm)	Pore Diameter - DSC (nm)	Pore Diameter - NMR (nm)	Pore Diameter - STEM (nm)
SBA-16-1	3.1	3.6	3.5	3.7
SBA-16-2	3.3	3.9	4.0	4.2
SBA-16-3	3.5	5.6	5.5	5.3
SBA-16-4	3.6	6.3	6.5	6.5

Verification of the pore sizes using N_2 porosimetry is hindered by the structure of the silica. If the cylindrical windows between the spherical pores are smaller than a critical diameter (*ca*. 6 nm for nitrogen analysis), a process known as cavitation occurs, where spontaneous nucleation and growth of gas bubbles in the metastable, condensed fluid will occur. The pore size distributions calculated in these conditions no longer reflect the actual pore sizes [64, 133, 134]. Figure 5.19 shows pore size distributions, obtained using N_2 porosimetry, for the SBA-16 samples studied here, with the key feature of a sharp peak at a smaller pore diameter. The NMR method only measures the liquid within the pore, giving an accurate measurement of the spherical pore size.

STEM images were obtained for all SBA-16 samples to enable comparison with both thermoporometry techniques (Figure 5.20). The results, listed in Table 5 with a maximum standard deviation of 12%, show good correlation with both the NMR and DSC analysis. Figure 5.21 shows the frequency percentages with respect to pore size for each spherical sample.

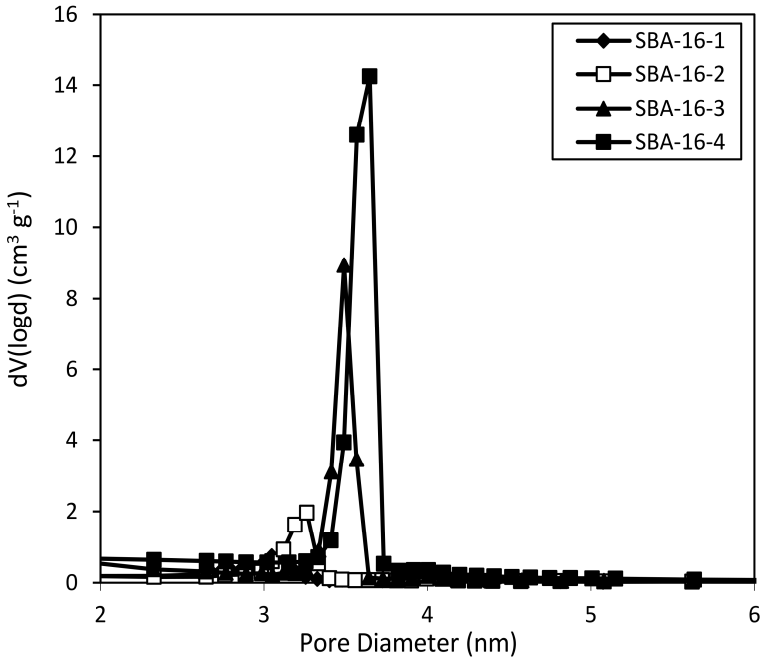

Figure 5.19. *Pore size distributions for SBA-16 silica of five differing average pore diameters obtained using N_2 porosimetry.*

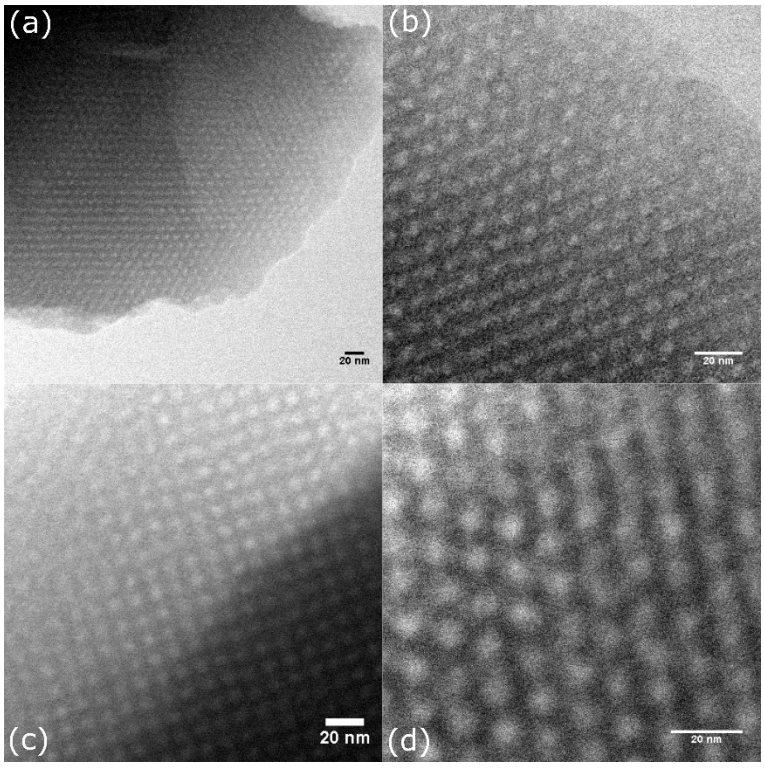

Figure 5.20. *Bright field STEM images of the spherical pores in* ***(a)*** *SBA-16-1 (3.7 nm),* ***(b)*** *SBA-16-2 (4.2 nm),* ***(c)*** *SBA-16-3 (5.3 nm) and* ***(d)*** *SBA-16-4 (6.5 nm).*

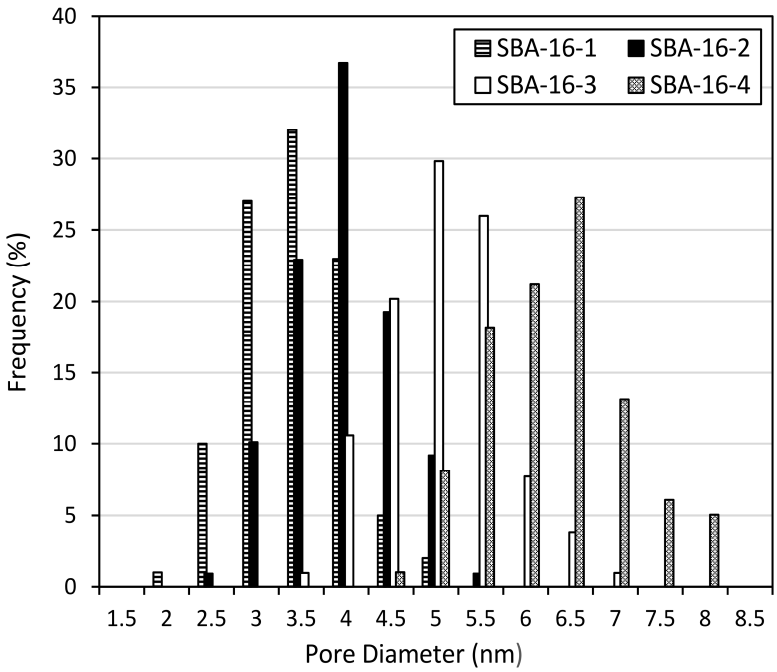

Figure 5.21. *Frequency data for the bright field STEM imaging of the spherical pores in four different sized samples of SBA-16.*

5.4. Conclusions

While NMR cryoporometry is well established as an analytical method for determining pore size distributions, no real consensus has yet been reached on what values of k_c and $2sl$ to use in NMR cryoporometry experiments [56]. In the case of water, reported values of k_c range from 21 to 53 K nm while the treatment of $2sl$ ranges from it being completely neglected to values of *ca.* 0.8 nm reported.

This work offers values for both. Using a fixed value of k_c, based on theory, and fitting to a literature set of cryoporometric data, covering several different silica pore geometries and two decades of research, an estimate for the thickness of the non-freezing surface layer was determined for water/porous silica samples. With the values of k_c and $2sl$ obtained here, NMR cryoporometry was used to the determine pore size distributions of porous silica with cylindrical or spherical pore structures, and different unit cell geometries. Pore size distributions have been obtained for the 2D isolated parallel pores of SBA-15, the spherical pores of SBA-16 and, for the first time, the 3D interconnected pores of KIT-6. Good agreement with pore size distributions obtained by alternative

methods was achieved, validating the method for obtaining k_c and $2sl$. In particular, the pore size distributions of spherical pores obtained; the NMR method measures the true pore diameter whereas N_2 porosimetry fails to do so here. NMR can be seen as a complementary technique here, as both measurements are critical to understanding the materials and their potential applications.

More generally, the use and analysis of literature melting point depression data demonstrated here can be applied to other liquids confined in other porous materials, with cyclohexane in glass an additional example illustrated. The methodology used to obtain these values highlights the versatility of NMR cryoporometry. No one particular liquid is suited to measuring the complete range of pore sizes and materials available. Water will not easily imbibe into hydrophobic materials and there is an upper limit to the pore sizes it can measure, determined by k_c and the temperature control of the spectrometer. Through an educated choice of probe liquid, NMR experiments can be tailored to the pore diameter and surface characteristics of the material being studied. There is a wealth of available literature data for the study of liquids in confined pores and related melting point depressions. This resource can be used to obtain suitable parameters for cryoporometric studies for many other liquids, other than water and cyclohexane.

Given that NMR spectrometers have near ubiquitous use in chemistry research, the flexibility offered by liquid choice, the capability to measure different pore structures and geometries and the possibility of use of literature melting point data for obtaining values of k_c and $2sl$ should serve to make NMR cryoporometry more widely used, particularly in fields such as catalysis where such silica supports find wide application and the pore sizes and structures of such species has such an important role.

CHAPTER. 6

Extending the Range of Liquids Available for NMR Cryoporometry Studies of Porous Materials

6.1. Introduction

As introduced in previous chapters, NMR cryoporometry is a well-established technique used to accurately measure the pore size distribution of mesoporous materials [1-6]. Cryoporometry can non-invasively measure the phase transition of a liquid, confined in various pore geometries, in discrete steps [3], however, a major disadvantage of the technique is that a single liquid cannot probe a wide range of pore sizes; a range of liquids, with differing thermodynamic properties, are therefore required to span the full range of pores sizes amenable for NMR investigations.

A list of potential cryoporometric liquids, with estimates for k_c, are detailed by Petrov and Furo [56], and includes water, cyclohexane, octamethylcyclotetrasiloxane (OMCTS), menthol, and t-butanol. Cyclohexane and water are two of the most common liquids for cryoporometry analysis due to their favourable melting points and suitable melting point depression constants [26, 97, 99, 103, 108]. Water (k_c = 49.53 K nm) is suited to analysing hydrophilic materials, such as silica, with pore diameters < 10 nm, whereas cyclohexane (k_c = 103.7 K nm) is more suited to hydrophobic materials, such as porous glasses, with pore diameters between 10-50 nm. Glasses smaller in size can be pre-treated with hexamethyldisilazane to make the glass more hydrophobic and promote the wetting of the pore by cyclohexane [97]. Larger pore diameters can be probed by two methods. The first is to use a liquid with a much larger k_c value. The second is to use appropriately smaller temperature steps for liquids which have a relatively high k_c, although this method will still ultimately fall short when the pore diameter exceeds a certain limit. OMCTS has recently been demonstrated as a suitable liquid for

larger pore analysis [98]. Despite its similar k_c to cyclohexane, OMCTS can accurately measure the pore size distributions of glass into the micron range when sufficiently small temperature steps are used.

Neither menthol nor t-butanol have been used previously as probe liquids for NMR cryoporometry. The only previous studies of their melting behaviour are provided by Christenson [135], and Qiao and Christenson [136], for t-butanol and menthol respectively. Both studies describe the capillary condensation of the alcohols between mica surfaces and provide estimates of the solid-liquid interfacial tension. With accessible melting points, both liquids are ideal candidates as probe liquids in NMR cryoporometry experiments. Their properties are listed in Table 6.1

Table 6.1. Thermodynamic properties of selected cryoporometric liquids.

Liquid	v (m^3 mol^{-1})	T_m (K)	γ_{Sl} (N m^{-1})	ΔH_f (kJ mol^{-1})	k_c (K nm)
t-butanol	95.6	296-299	0.014 [135]	6.7 [137]	119.2
menthol	175.6	305-309	0.024 [136]	11.9 [138]	219.3

In cryoporometry experiments, k_c is typically calibrated against experimental data, however such calibrations are highly susceptible to the choice of fitting function, particularly in estimating the non-freezing surface layer ($2sl$) which can lead to significant errors. The melting point depression constant and the influence of a non-freezing surface layer, for water confined in mesoporous silica and cyclohexane confined within CPGs, have been investigated previously in Chapter 5. Here the methodology is extended to estimate these two parameters for t-butanol and menthol, and hence demonstrate the suitability of both alcohols for NMR cryoporometry. With a similar k_c value to cyclohexane, t-butanol can be used to study melting point depression in moderately sized pores which cyclohexane struggles to access. Menthol, possessing a larger k_c value, is better suited for large pore analysis.

6.2. Experimental

6.2.1. Sample Preparation

Controlled pore glasses (CPGs) were provided by both Sigma-Aldrich (24, 50 and 54 nm) and Prime Synthesis (38, 43, 63 and 100 nm), and their properties are listed in Chapter 4, Table 4.1. The pore expanded silica was obtained from collaborators, C. M. A. Parlett and A. F. Lee. Samples were dried in an oven at 373 K for 24 h and stored in a desiccator for a further 24 h prior to their analysis. Menthol (Sigma-Aldrich, 99 %), t-butanol (Sigma-Aldrich, 99 %) and cyclohexane (Fisher Scientific, 99 %) were used without additional purification. A small amount of the solid glass (20 mg) was added to a thin-walled NMR tube, and the probe liquid probe molecule then pipetted over the solid to ensure complete pore saturation, following a literature method [15] and the procedure established in Chapter 4. To ensure complete imbibition of each liquid into the pore network, samples were subsequently centrifuged at 1500 rpm for 1.5 h. The same procedure was utilised for the silica.

6.2.2. NMR Measurements

Cryoporometry measurements were made using the CPMG pulse sequence (Figure 4.1) [22, 23], comprising a basic spin echo, and carefully selected delay time, Δ, to differentiate between the solid and liquid phases of the sample. Total delay times of 4 ms and 40 ms for menthol and t-butanol respectively successfully isolated the liquid signal. The sample temperature was reduced until the entire sample was frozen, evidenced by the loss of all liquid signal. The temperature was then increased in increments of 0.2 – 0.5 K, to initiate and observe the phase transition from solid to liquid, using a minimum equilibration time of 10 min at each temperature to stabilize the signal intensity. Each acquisition comprised of 8 transients of 8192 complex data points. The melting point depressions obtained by NMR cryoporometry were converted into pore size distributions using the methodology outlined in Chapter 5.

Transverse relaxation time, T_2, distributions for the liquids were obtained using the PROJECT pulse sequence [139]. Each acquisition comprised of 8 transients of 16384 complex data points, with a

maximum experimental time of 8 minutes. The total delay time was varied from 0.006 ms to 0.2 ms, over 10 increments, depending on the liquid used and the phase of the sample. Relaxation time distributions were calculated using the CONTIN program [140].

To obtain low temperatures, a Bruker BVT3200 temperature control system with an accuracy of 0.2 K was used. The cooling system passed a N_2/air mixture over the sample at a flow rate between 125-400 l h^{-1}, operating at 50 % cooling with the probe heater set to a maximum of 20 % output. Before starting a cryoporometry experiment, the cooling system was allowed to equilibrate with the probe heater. The temperature control unit was also optimized to minimize over- and undershoot of the sample temperature. Furthermore, the probe was tuned and matched in areas out of sample phase transition to account for the significant temperature changes.

6.2.3. Nitrogen Porosimetry

Nitrogen porosimetry was undertaken on a Quantachrome Autosorb IQTPX porosimeter using ASiQwin v3.01 software. Samples were degassed at 523.15 K for 12 h prior to recording N_2 adsorption/desorption isotherms. Mesopore properties were calculated using the non-local density functional theory (NLDFT) approach.

6.3. Results and Discussion

6.3.1. Complexity of the Phase Transition

To be considered a viable probe liquid for cryoporometry experiments, the phase transition from solid to liquid has to be relatively simple, with the absence of any intermediate stages or plastic crystals, crystalline structures with high molecular mobility [46]. There must also be measurable differences in transverse relaxation time between the pore liquid and the bulk liquid. In order to assess the melting behaviour of t-butanol and menthol, hysteresis data was acquired for the bulk liquids (Figure 6.1).

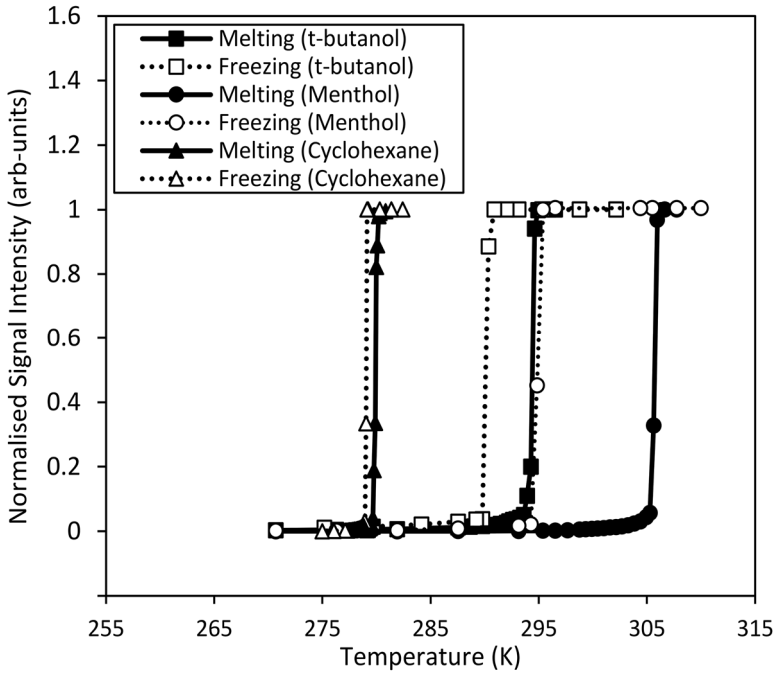

Figure 6.1. *Melting/Freezing hysteresis data for bulk cyclohexane, t-butanol and menthol. Solid lines represent melting and dashed lines represent freezing.*

For both alcohols, as well as the cyclohexane standard, the transition from solid to liquid occurred over a narrow range of temperatures and was free of any secondary phases. The freezing of the liquids, although at different temperatures due to the well-established super-cooling phenomena of liquids in pores [19], also occurred over a narrow range of temperatures.

The confining environment of a pore may contribute to the complexity of the melting process. In any event, there needs to be a difference between the transverse relaxation times of the solid and liquid phases such that they can be differentiated by the use of a spin-echo NMR experiment. In order to evaluate this, T_2 distributions were acquired for all three liquids over a range of temperatures near that particular liquid's melting point. Figure 6.2 illustrates the increase in T_2 times going from a solid through to a pore-constrained liquid. In all three cases, the transition is clear and there is a distinct difference between the solid (ca. 0.001 s) and liquid (ca. 0.01-0.1 s) T_2 times. Hardware restrictions meant that the T_2 times of the solids far below the pore melting region could not be measured, due to problems in acquiring the required spectral widths. In spite of this, Figure 6.2 still highlights the

relatively simple transitions between solid and liquid for both alcohols and the greater than ten-fold differences in T_2.

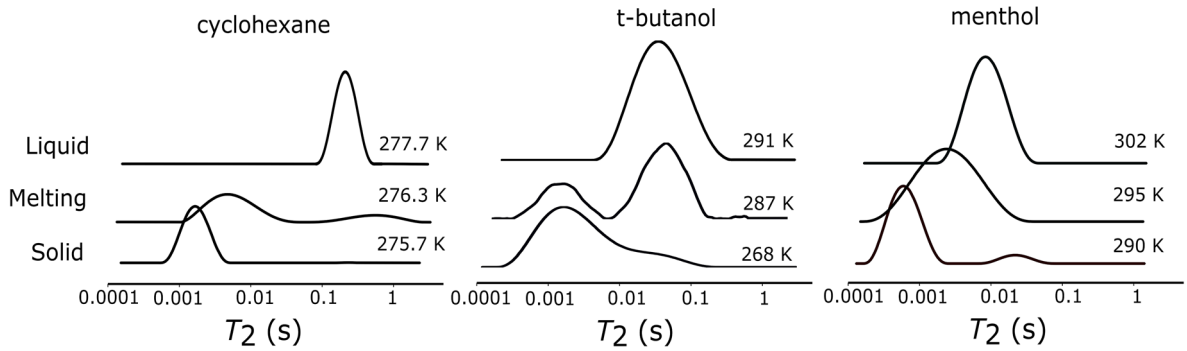

Figure 6.2. *Indicative* $\boldsymbol{T_2}$ *distributions for cyclohexane, t-butanol and methanol, confined within the pores of CPG24, when solid, during the pore melting transition and when all of the species inside of the pore has melted.*

While the 100 fold difference in T_2 times observed for cyclohexane is ideal, the differences between the T_2 times of the solid and liquid phases of alcohols used in this work allow for the two states of matter to be distinguished by a spin-echo experiment. Appropriate timings for the spin-echo NMR experiments are still crucial for accurately determining the phase transition temperature of a liquid melting in a confined environment. The total experimental delay time in a spin-echo experiment, Δ, allows the solid and liquid signals to be separated due to the significant differences between the T_2 times of the two phases, as illustrated in Figure 6.3.

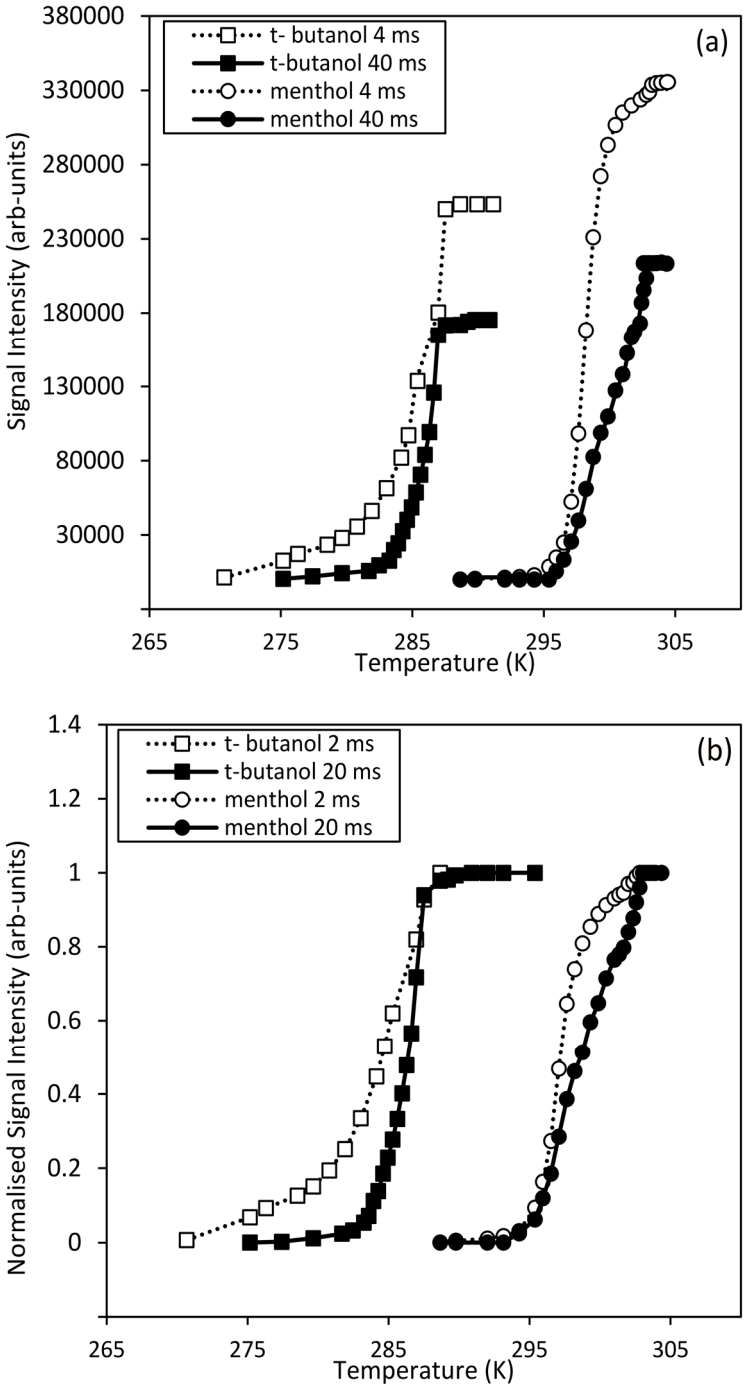

Figure 6.3. *The (a) raw and (b) normalised melting curves for t-butanol (squares) and menthol (circles) acquired using two different spin-echo delays: 20 ms (filled) and 2ms (hollow).*

If the optimal delay time is not used, then the acquired melting curves will not reflect the true pore size distributions of the materials. A simple procedure to identify the optimal delay time is to first reduce the temperature of the sample so that both bulk and confined liquid freeze. The temperature is then increased incrementally to ensure that only the confined material melts, and a freezing curve

is acquired at a series of different delay times. Using a delay time which is too long will result in the loss of the liquid signal from smaller pores, and the resulting melting curve will not reflect a sigmoidal function. Figure 6.3 (a) illustrates the raw signal intensity data with respect to the change in temperature. Figure 6.3 (b) includes the normalised data. As expected, the longer delay times remove signal. The curve shape dependency on delay time is key. This is firstly illustrated for menthol confined in 50 nm mean diameter porous glass, where the use of long delay times (20 ms) would skew the pore size distribution towards larger pores. Too short a delay time would result in an apparent phase transition at a lower temperature than expected, illustrated for t-butanol confined in 50 nm mean diameter porous glass, where signal intensity is observed < 285 K when a 2 ms delay is used.

6.3.2. Obtaining a Pore Size Distribution

In order to successfully convert good quality NMR melting curve data into a pore size distribution, both the melting point depression constant, k_c, and the thickness of the non-freezing surface later, $2sl$, need to be known. Figure 6.4 plots the inverse melting point depressions obtained in this work, and from two literature references [135, 136], against the pore diameter obtained by other methods. A one-parameter fit for $2sl$ for menthol and t-butanol (using data collected in Table 6.1), gives estimates for this layer of 1.9±1.1 and 1.7±1.0 nm respectively. Both fits have R^2 values of 0.99. Note that the source of data is not an NMR cryoporometry study. This work demonstrates the use and analysis of literature melting point depression data and the additional insight from and application of these sources of data.

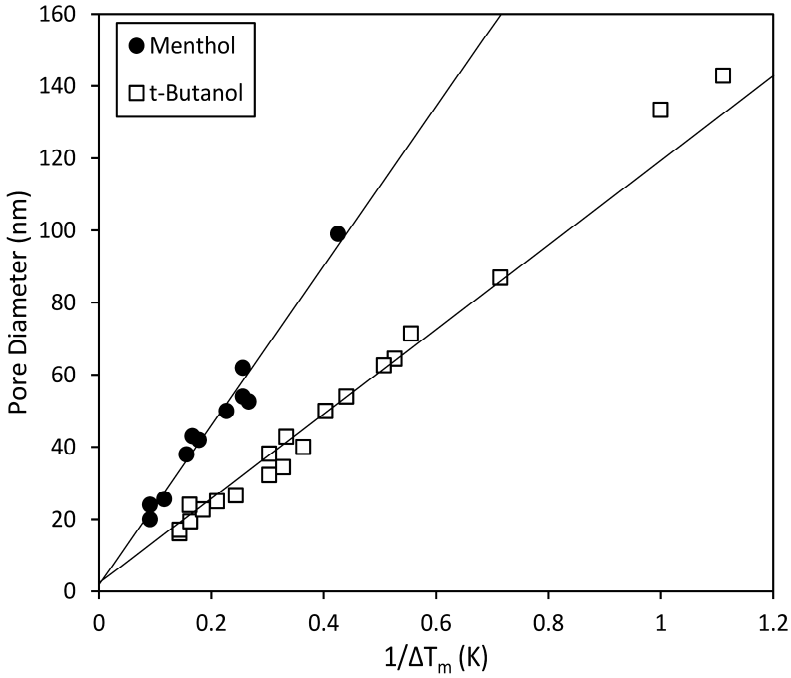

Figure 6.4. *Plot of average pore diameter versus the inverse of the measured melting point depression for cryoporometry data obtained in the present work and references 135 and 136. The intercept of the linear fits yield values of 1.9 nm and 1.7 nm for the thickness of the non-freezing surface layer for menthol and t-butanol respectively.*

The NMR melting curves for both t-butanol and menthol confined within CPG63 were acquired and both follow the expected sigmoidal shape for such data. The melting curves, with cyclohexane as a comparison, are depicted in Figure 6.5 (a), together with their corresponding pore size distributions in Figure 6.5 (b). The pore size measurements are all in good agreement. An average pore diameter of 61.5 nm was obtained using cyclohexane, 62.0 nm using t-butanol, and 64.8 nm using menthol. Of the three liquids, cyclohexane has a phase transition that occurs over the narrowest temperature range, whereas both alcohols have relatively broader melting points, reflected in their wider pore size distributions. Despite having a phase transition that occurs over a wider temperature range, the size distribution from menthol in CPG63 is narrower than that obtained from t-butanol. This may reflect that the latter probe molecule is approaching the upper limit of the pore sizes it can measure; each temperature step leads to a larger gap between the corresponding pore diameters as the temperature approaches T_m, an effect that dominates the pore size distribution of CPG63 as measured by t-butanol.

Pore size distributions were acquired using both menthol and t-butanol for the remaining controlled pore glasses. The pore size distributions obtained for every CPG sample measured by both liquids can be found in Figures 6.6 (a) and (b). As the pore sizes increase, broader temperature ranges for each melting curve are acquired resulting in broader pore size distributions, especially for t-butanol in CPG63. This behaviour is similar to that observed using OMCTS as a probe liquid [98]. Menthol also appears to slightly underestimate pore diameters <50 nm, for which t-butanol may be better suited to analysing. Figure 6.7 compares the pore sizes measured using NMR cryoporometry, for the materials that both liquids were able to accurately measure, with those supplied by the manufacturer. Overall, both alcohols were used to obtain pore size measurements in good agreement with manufacturers' reported values.

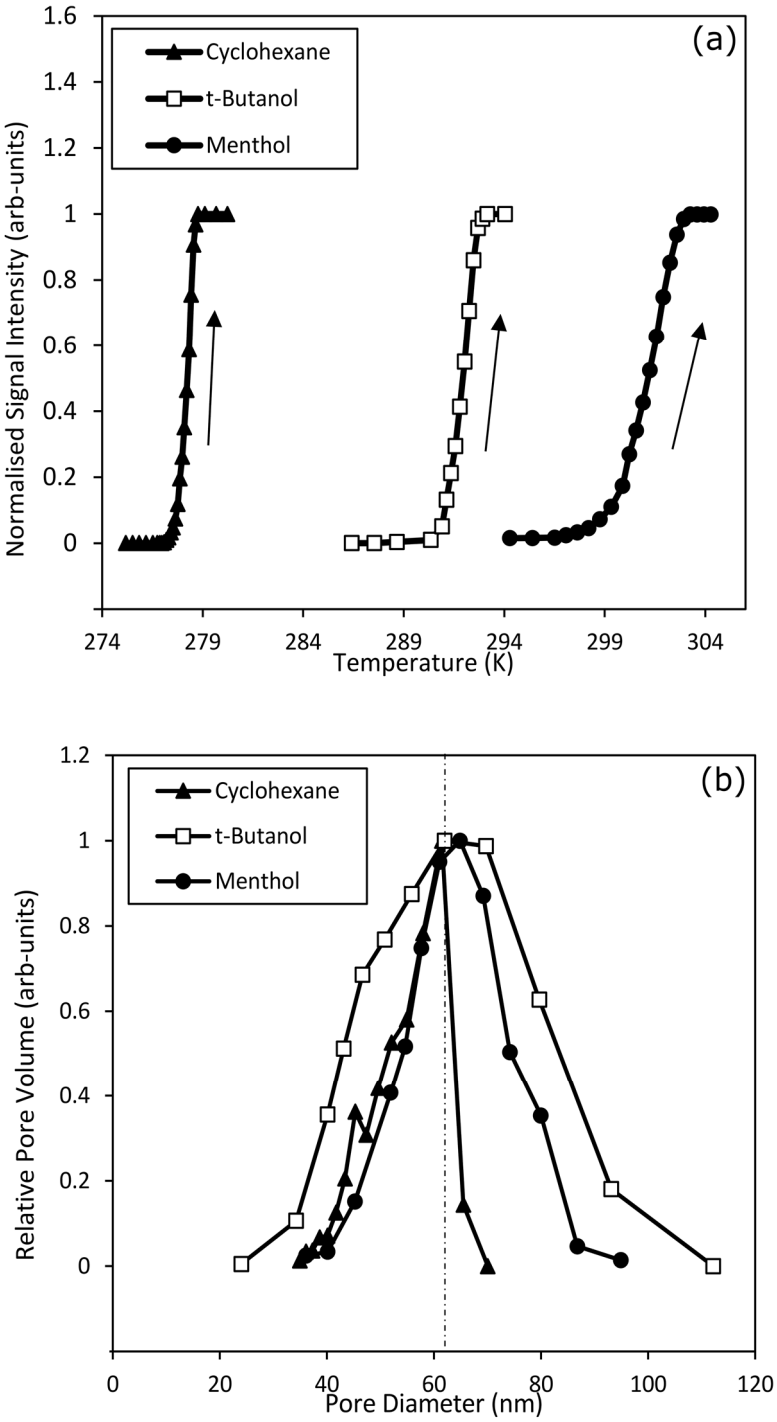

Figure 6.5. (a) *Melting curves for cyclohexane, t-butanol, and menthol in CPG63 and* ***(b)*** *corresponding pore size distributions for the three liquids.*

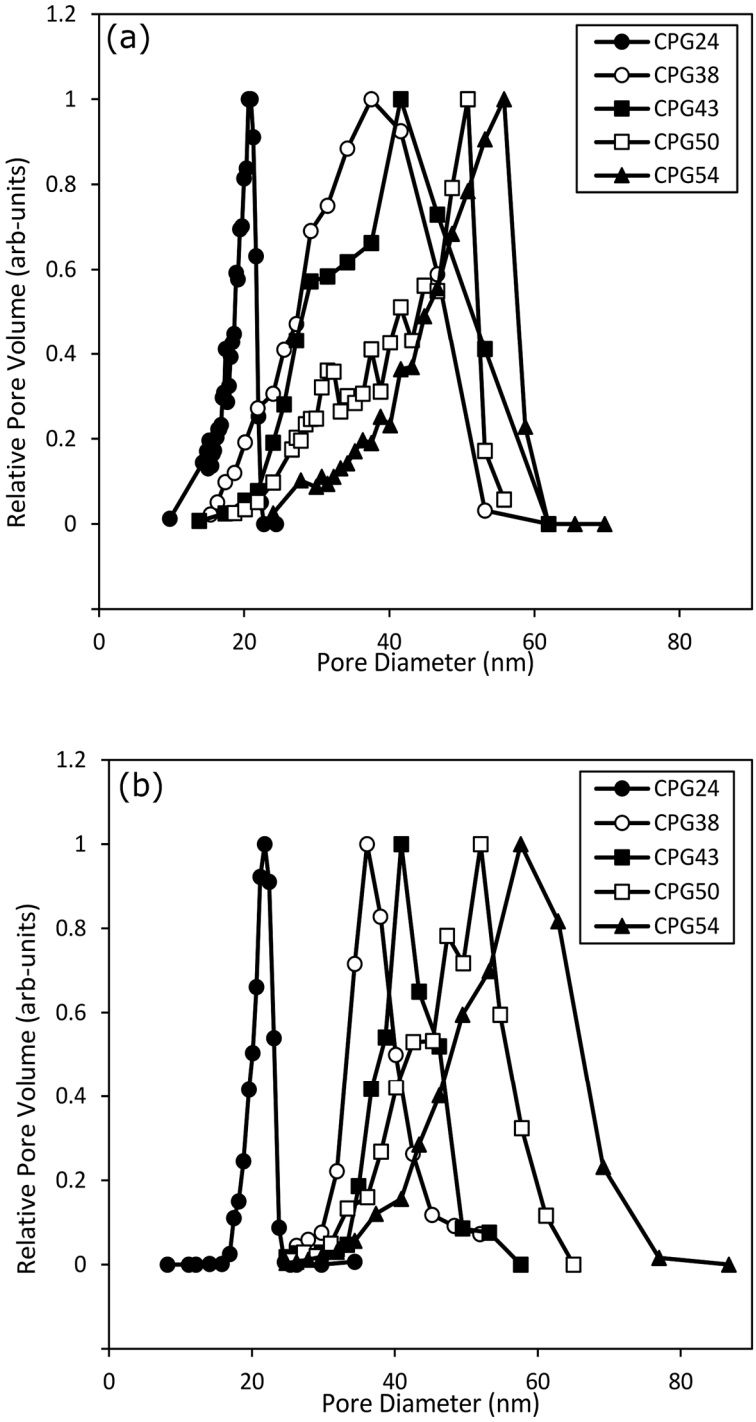

Figure 6.6. (a) *The pore size distributions for 5 controlled pore samples acquired using t-butanol as a probe liquid and* ***(b)*** *pore size distributions for 5 controlled pore samples acquired using menthol as the probe liquid.*

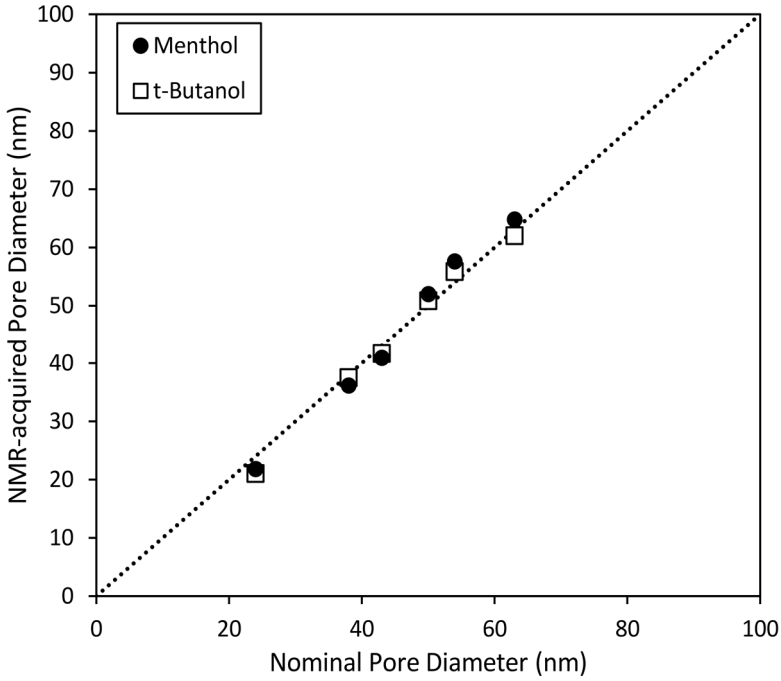

Figure 6.7. *Comparison of pore sizes, measured using NMR cryoporometry, with nominal pore sizes as supplied by the manufacturer for a set of 5 controlled pore glass samples.*

Neither cyclohexane nor t-butanol were able to accurately measure the size distribution of the largest pore CPG100 material, reflecting their similar melting point depression constants (ca. 100 K nm) and subsequent limited ability to probe larger pore sizes. Menthol, which has the largest k_c value of the liquids used in this study, was used to successfully measure the pore sizes of the widest bore controlled pore glass in this study, CPG100, as shown in Figure 6.8. The k_c value estimated for menthol renders it a potential probe liquid for analysing even larger pores than those reported in this work. However, disadvantages of menthol do include longer waiting times to achieve equilibrium during the melting process, perhaps necessitating fewer temperature steps to maintain a practical total experimental time, or experimental set-ups capable of automated, accurate 0.1 K temperature increments.

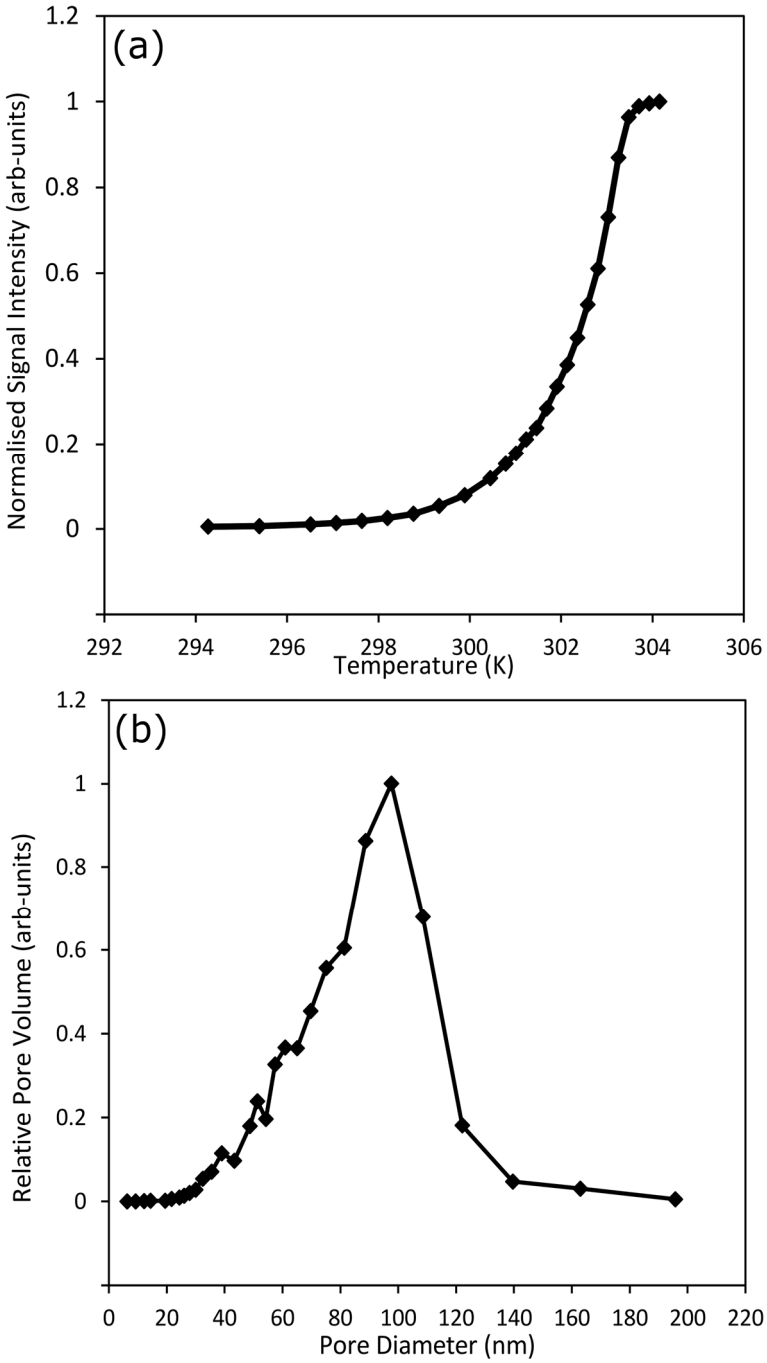

Figure 6.8. (a) *The NMR melting curve for menthol confined in CPG100 and* ***(b)*** *the subsequent pore size distribution using a* $\boldsymbol{k_c}$ *value of 219.3 K nm and a* $\boldsymbol{2sl}$ *of 1.9 nm.*

6.3.3. Application to Silica

Menthol and t-butanol are well-suited to probing porous materials with hydrophilic surfaces, such as mesoporous silica, which exhibits superior thermal, mechanical and chemical resistance. Mesoporous silicas are integral to many applications in chemistry such as drug delivery [122] and as structured supports in heterogeneous catalysis [125]. Applications of pore-expanded silicas include the adsorption of volatile organic compounds [141] and as supports in biocatalysis [142]. The pore dimensions are often tuned to improve in-pore accessibility, and/or molecular mass transport [143].

The pore expanded silica sample was imbibed with menthol and t-butanol in order to probe the alcohols' ability to estimate the pore size of a catalytic material. Figure 6.9 illustrates the pore size distributions for t-butanol and menthol in a pore-expanded silica material, compared with those obtained using water (a well-established probe liquid in non-expanded silica systems [144]) and by nitrogen porosimetry. The resulting pore diameters are given in Table 6.2. With a k_c value of 49.53 K nm water is expected to significantly underestimate the size of the pores >10 nm, consistent with these observations. Menthol likewise appears to underestimate pore diameters, presumably a consequence of its limitations in probing smaller pores. It is noticeable that the NLDFT porosimetry method, as well as the NMR method using water and t-butanol as probe liquids, appear to show a slight bi-model distribution. The pore diameter, where the extra peak arises, is relatively well agreed upon in all three cases. A diameter of 11.7 nm is obtained for NMR with t-butanol, 11.6 nm for NMR with water and 12.1 nm for NLDFT porosimetry analysis. This suggests that the pore-expanding procedure has resulted in the formation of this additional peak, rather than it being an artefact of the experiments; a common observation during pore-expansion [145]. Menthol, however, does not appear to identify the extra peak. This may be reflective of its inability to effectively probe lower pore sizes, due to its significantly higher k_c value.

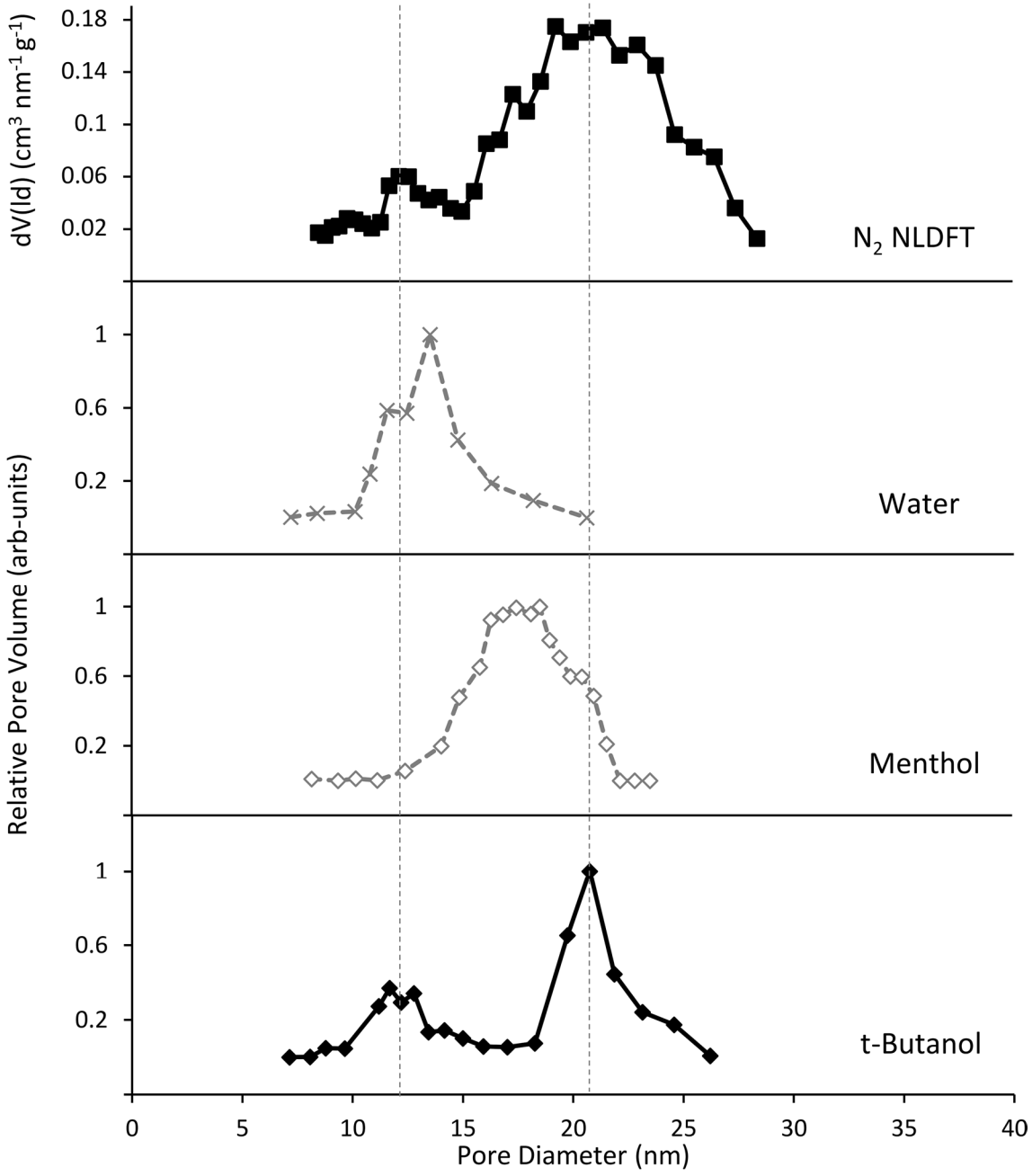

Figure 6.9. *Pore size distributions for water, t-butanol and menthol confined within the pores of pore expanded silica using NMR cryoporometry, with a comparison to NLDFT nitrogen porosimetry desorption branch data.*

Table 6.2. The average pore diameters for pore-expanded SBA-15 determined by four different method/material combinations.

Method	Probe molecule	Pore diameter major peak (nm)	Pore diameter minor peak (nm)
NMR	menthol	18.5	-
NMR	water	13.5	11.6
NMR	t-butanol	20.7	11.7
NLDFT porosimetry	nitrogen gas	19.2	12.1

6.4. Conclusions

Although NMR cryoporometry has been established as an accurate pore size determination technique, it has its limitations. These include the inability of any one liquid to analyse a wide pore size range, and the preference to match the probe liquid to the chemistry of the solid being studied. In this work, we have demonstrated for the first time, the ability of menthol and t-butanol to be introduced as probe liquids for cryoporometry analysis.

The melting point depression constants, k_c, obtained for both alcohols were estimated according to their thermodynamic parameters, enabling a value for the non-freezing surface layer, $2sl$, to be predicted based on recently established methodology. The estimated melting point depression constant for t-butanol is similar to that of the established probe liquid, cyclohexane. Its advantage is in being able to penetrate into materials more easily where the hydrophobicity of cyclohexane may prevent it from doing so. Menthol has a significantly larger k_c than most liquids currently reported in NMR cryoporometry analysis. It appears to slightly underestimate smaller pore sizes; however, with the correct experimental set-up, it is possible to probe larger pore sizes effectively.

There is potential for wider application of this methodology in more complex samples of engineering and scientific interest, such as templated silicas. Pore expanded silica is becoming increasingly ubiquitous in catalytic research and pore size analysis of these materials is routinely done by

techniques such as nitrogen porosimetry. This chapter not only describes the first demonstration of the use of t-butanol and menthol in NMR cryoporometry experiments, illustrating that pore sizes up to 100 nm, and potentially beyond, can be measured using the latter alcohol, but also highlights further application into catalytic silica. The use of different probe liquids, with different functional groups and chemistry, renders NMR cryoporometry a versatile complement to N_2 porosimetry.

CHAPTER. 7

Application of NMR Cryoporometry on Polymers

7.1. Introduction

In addition to ordered silica, as demonstrated in Chapters 5 and 6, NMR cryoporometry can be used to analyse the porosity of polymers. The cryoporometric method has been utilized effectively on ordered matrices such as polymeric nanoparticles [146], porous polymer particles [37] and biodegradable polymer microparticles [147]. However, gel phase hydrogels and ion exchange resins are two types of polymers that have not actively been probed using cryoporometry.

Polymer hydrogels exist in many forms ranging from gels [148], to simple copolymer networks [149] through to ordered polymers which have been produced by the hard and soft templated approach [150]. The macroporous architecture, with pores greater than 50 nm, of polymer hydrogels is well studied [151, 152] however, the mesoporous region, containing pores of 2-50 nm in diameter, is less so. These hydrogels have been successfully utilized in the biomedical industry [153] due to their properties of high water content, gel-like nature and diverse porosity [154-157]. These properties make them extremely biocompatible [158] and as such, they are commonly used for various applications including contact lenses [159], tissue engineering [160, 161] and drug delivery [162].

In disordered polymeric systems comprising only of a cross-linked environment, the polymers have an effective porosity which is created through the differing extents of linkage [163, 164]. In this case, the effective porosity is subject to the environment in which it is placed. Depending on the nature and affinity of the polymer, the effective porosity will change with the swelling of the polymer and the polymer is said to be gel-phase. The matrix is built upon a co-polymerisation of a monomer, such as styrene, with a cross-linking agent. The porosity is inversely related to the cross-linking extent,

exhibiting pore diameters up to 2 nm [165]. Figure 7.1 illustrates schematically the change in structure as the cross-linking percentage is increased.

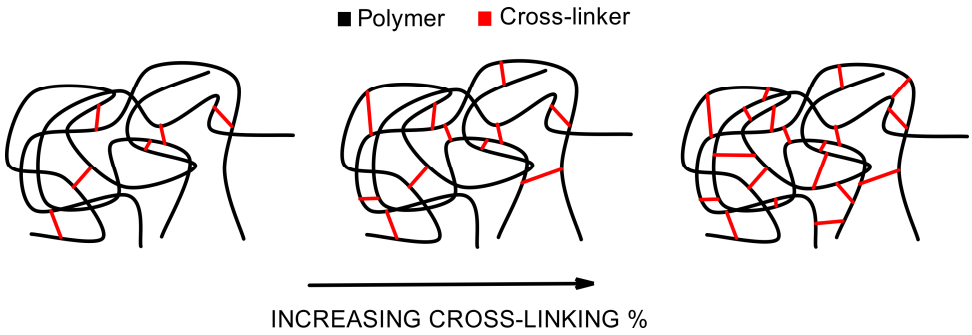

Figure 7.1. *Schematic representation of increasing the percentage of cross-linking within the polymer network.*

One particular type of cross-liked polymer that may be of interest for NMR analysis are ion exchange resins (IERs). IERs are insoluble solid supports which are generally in the form of microbeads that are used to facilitate the trapping and release of certain ions. Four main types of IER exist; strongly acidic cation exchange resins (SAC), weakly acidic cation exchange resins (WAC), strongly basic anion exchange resins (SBA) and weakly basic anion exchange resins (WBA). Table 7.1 lists the different type of resins together with their corresponding functional groups.

Table 7.1. The different types of exchange resins [166].

Type of Exchange Resin	Functional Group	Purpose	Example
SAC	Sulfonic acid	In sodium form they remove water hardness, in hydrogen form they remove cations	Amberjet™ 1000 Na
WAC	Carboxylic acid	In hydroxyl form they remove divalent ions	Amberlite™ IRC86
SBA	Quaternary ammonium	In chloride form they mainly remove nitrate and sulphate, in hydroxyl form they remove all anions.	Amberlyst™ A26
WBA	Amine	After cation exchange they remove anions of strong acids only	Amberlite™ IRA67

Macroreticular IERs, often also referred to as macroporous resins despite not necessarily containing macropores, differ from conventional gel-phase cross-linked polymers as they have the added meso/macro porosity created by the addition of a porogen during the polymerisation process [165]. The porogen creates a void in the structure as the polymerisation continues around it. The size of the void can be tailored by increasing or decreasing the amount of porogen used. This can induce structural frailties if too much porogen is added [167]. Examples of porogens include toluene, ethylbenzene and isobutanol [168]. The ordered structure of macroreticular resins make them suitable materials for thermoporometry analysis. However, they have proven to swell differently depending on the polarity of the media they are subjected to. Macroreticular resins prove to be effective catalysts, particularly in non-polar media where their lack of affinity for the reactants improves the product separation capability [165]. The other major application of IERs is in water treatment [169]. Water may often contain ions such as calcium and magnesium. This hard water causes an undesirable build-up of scale in places including boiler systems. IERs work by interchanging the divalent cations with sodium ions, followed by subsequent regeneration of the resin [165]. The choice of resin, detailed in Table 7.1, is tailored to remove different types of impurities contained in water.

Macroreticular resins hold two main advantages over their gel-phase analogues; (1) they have a high degree of porosity which can reach up to hundreds of nanometres, allowing larger species to travel through their architectures and (2), a higher cross-linking density can be achieved in the dual-phase system. The importance of a higher density of cross-links lies in the fact that this creates a more chemically stable system which is far more resistant to oxidation, for example [168]. One disadvantage of macroreticular resins is that they cost significantly more to make than their gel-based counterparts. A schematic representation of the difference between a gel phase conventional cross-linked polymer and a macroreticular polymer is shown in Figure 7.2.

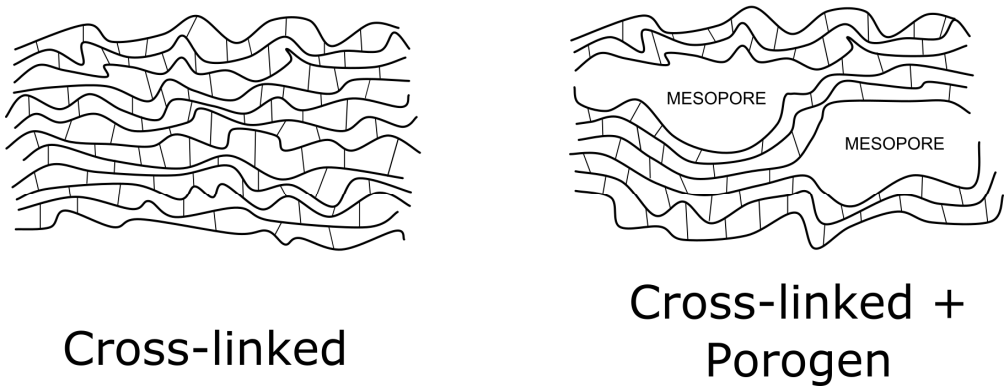

Figure 7.2. *The structural difference between a gel phase cross-linked polymer, such as the HEA-HMAA system studied here, and a macroreticular ion exchange resin, such as Amberlyst A26 OH.*

Nitrogen porosimetry is a well-established technique for analysing polymeric materials in their dry state [45]. However, ion exchange resins find their application in science when swollen with a relevant liquid. As such, it is preferable to find out more about their structures when in the working state [170]. Differential scanning calorimetry (DSC) thermoporometry is a commonly used technique of analysing the saturated porous structure of polymers. Weber *et al*. [171] synthesized a series of ordered mesoporous poly(2-hydroxyethyl methacrylate-*co*-ethylene glycol dimethacrylate) networks employing the hard-templating methodology. Analysis by DSC yielded pore sizes of 10-12 nm with little dependency on the cross-linking density. The technique, however, has its limitations as Iza *et al.*[149] revealed when attempting to study the structure of poly(*N*-(2-hydroxypropyl) methacrylamide) (PHPMA) hydrogels in an aqueous solvent as a significant variation in pore sizes was obtained. The authors suggested that this variation was due to effects such as the heterogeneity of the structure and the cutting of the sample, as well as sensitivity issues with the technique.

In this chapter, NMR cryoporometry is used to analyse the porosity of a swollen Amberlyst A26 OH polymer resin using a series of imbibing liquids. The ability of the cryoporometry technique to accurately probe smaller pore sizes is then assessed by attempting to analyse the microporosity of a disordered gel-phase HEA-HMAA polymer hydrogel. Both systems have a cross-linked region with an effective microporosity. The cross-linking density was varied in the disordered hydrogel in order to assess the ability of cryoporometry to study the cross-linking density. However in addition to this, the

Amberlyst has an additional, ordered, mesoporosity created by pore expansion. Four different liquids were used; water, t-butanol, menthol and cyclohexane to further illustrate the dependence of liquid chemistry on the ability of cryoporometry to accurately analyse the porosity of a support.

7.2. Experimental

7.2.1. Amberlyst A26 Resin Synthesis

The resin was provided by the Dow Chemical Company. The synthesis of this polymer requires two stages. Initial polymerisation of the resin matrix is completed *via* a suspension polymerisation of styrene and divinylbenzene (DVB). The next stage requires functionalisation of the resin matrix to produce the salt form given in Scheme 7.1. The first step in Scheme 7.1 involves chloromethylation of the polymer to produce a covalent chloride intermediate. This process involves the use of the carcinogenic CH_3OCH_2Cl. Alternatively, one can use 1,4-bis(chloromethoxy)butane in dichloromethane with a stannic chloride catalyst [172]. Amination of this intermediate then forms the quaternary ammonium chloride salt. The chloride salt is then converted into the final hydroxyl form (Figure 7.3) by reaction with a base, such as NaOH.

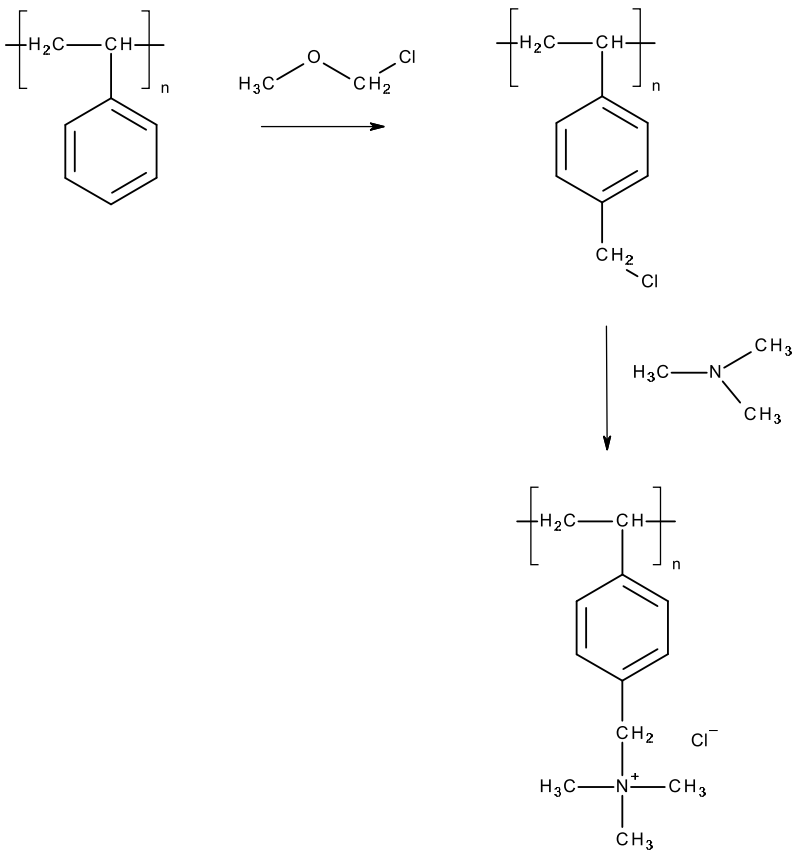

Scheme 7.1. *Reaction scheme for the formation of the quaternary ammonium chloride salt.*

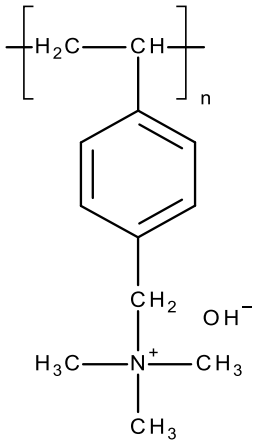

Figure 7.3. *Chemical structure of the Amberlyst A26 OH resin used in this work.*

7.2.2. HEA-HMAA Polymer Synthesis

The polymer hydrogels were synthesised at the Aston Institute of Materials Research by the Topham research group. The polymer hydrogel was prepared by a RAFT [173] copolymerisation of the hydrophilic monomer, 2-hydroxyethyl acrylate, with the cross-linking agent, N-hydroxymethyl acrylamide. The first step in the polymerisation process was the initial copolymerisation, as shown in Scheme 7.2.

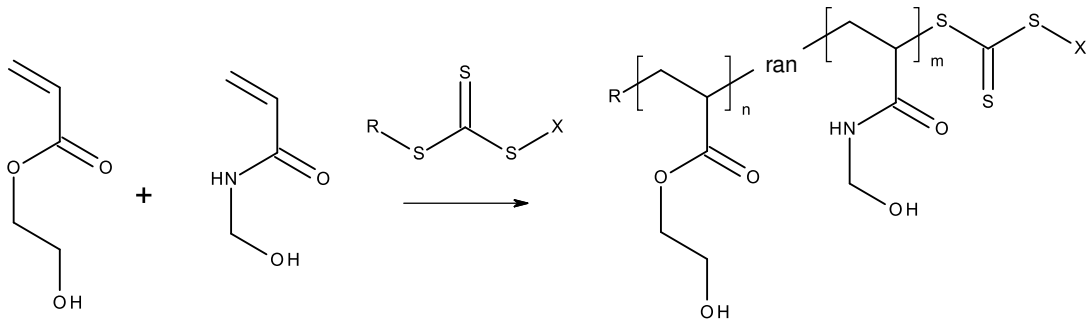

Scheme 7.2. *Copolymerisation of 2-hydroxyethyl acrylate with n-hydroxymethyl acrylamide.*

In order to initiate the crosslinking, the polymer was then subjected to high temperatures (150°C) for approximately 1 hour. Acyl amides can readily cross link at high temperatures. Firstly, a bis(methylene ether) is formed via the elimination of water. A methylene bridge is subsequently formed with by elimination of formaldehyde.

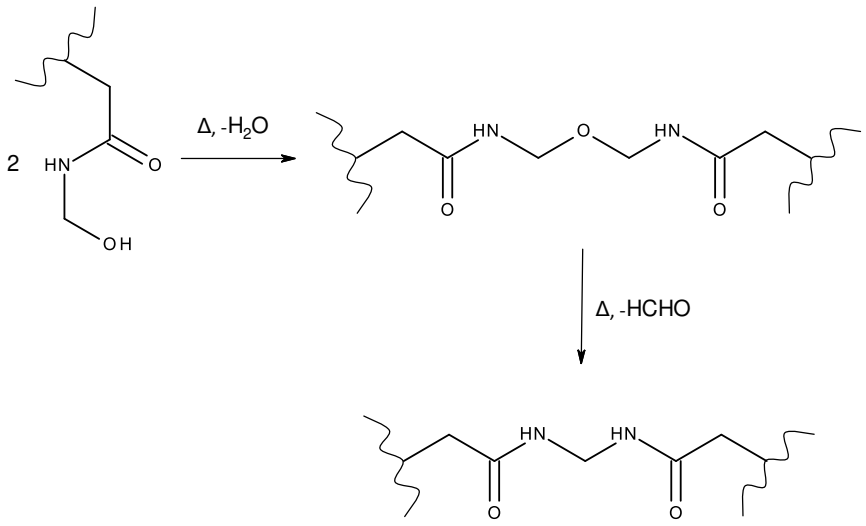

Scheme 7.3. *Initiation of the cross-linking by loss of water at first, followed by formaldehyde.*

7.2.3. Sample Preparation

Menthol (Sigma-Aldrich, 99 %), t-butanol (Sigma-Aldrich, 99 %) and cyclohexane (Fisher Scientific, 99 %) were used without additional purification. A small amount of each polymer (*ca.* 20 mg) was placed in a sample tube and a small amount of each solvent was added. The polymer was allowed to swell in the solvent for approximately 24 hours. The polymer was then carefully removed from the liquid and blotted in pre-soaked filter paper to remove any excess liquid. The sample was transferred to a 5 mm standard NMR tube and sealed with parafilm. The samples containing t-butanol and menthol were kept above their corresponding bulk melting temperatures to prevent the freezing of the solvent from possibly destroying the network of pores.

7.2.4. Nuclear Magnetic Resonance

All cryoporometry measurements were made using the CPMG [104, 105] pulse sequence (Figure 4.1). The temperature was initially decreased until no signal was observed – i.e. when the sample was completely frozen. When the temperature was increased, the signal intensity increased with the subsequent melting of the sample. The temperature step within the phase transition region were 0.2-0.3 K and the sample was left to equilibrate for at least 10 minutes from when the NMR signal stopped changing in intensity.

7.2.5. Differential Scanning Calorimetry

The DSC measurements were made using a Mettler-Toledo DSC 1 STAR^e system apparatus equipped with a liquid nitrogen cooling supply. Samples of approximately 2 mg of the water swollen HEA-HMAA polymer were added to an aluminium pan. The pans were then immediately sealed and re-weighed. The samples were initially taken down to 228 K prior to acquisition to ensure all of the liquid was frozen. A heating rate of 0.5 K min^{-1} was used through to a final temperature of 283 K. To transform the DSC melting curves into a pore size distribution, the procedure outlined in Majda *et al.* [62] was followed.

7.2.6. SEM Imaging

SEM images of the 25% cross-linked HEA-HMAA polymer were obtained from TESCAN using a JSM-7200F Field Emission SEM. The procedure as described by TESCAN is as follows. The sample was first attached to the cryo-holder and frozen in liquid N_2. The sample was cryo-fractured, sublimated for 5 minutes at -95^{o}C and then coated under the cryo condition with a thin layer of platinum. For the sample analysis, lower acceleration voltages of approximately 1-2 kV and a detection system, including chamber-SE and in-beam SE detectors, were used.

7.3. Results and Discussion

7.3.1. NMR Analysis of the Amberlyst A26 OH Polymer

The Amberlyst IER has porosity on two different length scales. It is the first region of microporosity, caused purely by the cross-linking, that defines how well the Amberlyst can swell in solution. Commonly, the degree of cross-linking for an ion exchange resin ranges between 4-12% [163]. The swelling is also known to depend on the polarity of the solvent to which the resin is subjected to. Macroreticular resins, especially those with a low cross-linking density, remain collapsed [164] or only swell slightly in nonpolar solvents [163]. The second, mesoporous, region of porosity is highly ordered which defines the species as macroreticular. This region is created by the addition of a porogen in the polymerization process and is readily accessible for analysis using NMR Cryoporometry.

The IER was analysed firstly using water as the swelling liquid. Figure 7.4 (a) follows the melting of water confined within the polymer matrix. The absence of a plateau in signal intensity with respect to temperature, as usually observed in ordered systems, suggests that the polymer swells significantly in water and the effective porosity of the polymer is affected. As described in Savina et al. 174 there are three types of water present in polymer hydrogels. These are (1) free water, which is present in the macropores, (2) weakly bound water which may interact with the polymer and (3) strongly bound hydrogen bonded water which remains liquid below 258.15 K. It appears in the system studied here, types (1) and (2) are present. Strongly bound water is simply not observable. Weakly bound water

exists in the region of microporosity, where the signal first starts to rise. Free water is then identified as the temperature is increased due to the swelling of the polymer which creates effective macropores.

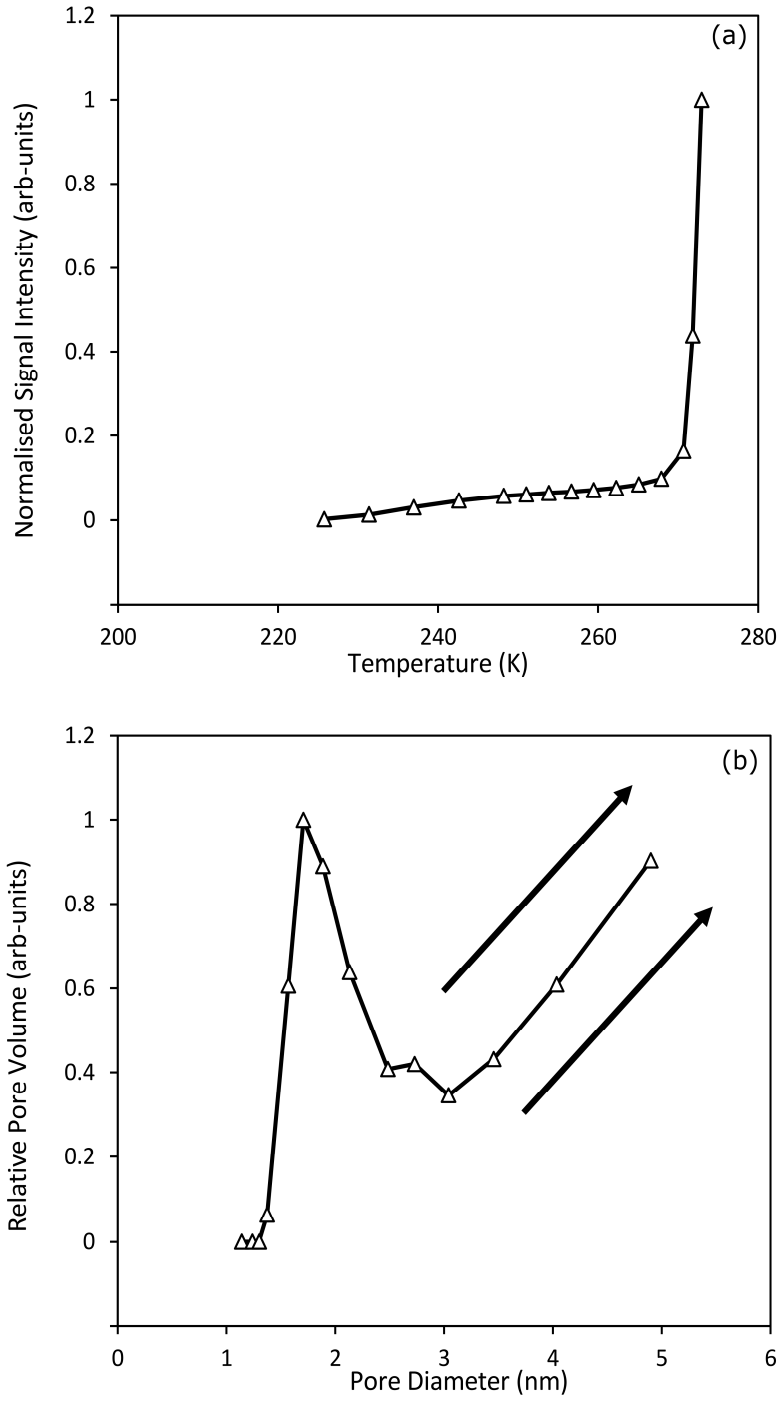

Figure 7.4. (a) *NMR melting curve for the macroreticular IER swollen in water and* ***(b)*** *the subsequent pore size distribution for pores smaller than 6 nm. The arrows indicate the contiual rise of signal intensity, with temperature, past 6 nm in pore size with no average pore size determination.*

The pore size distribution up to 6 nm in diameter is shown in Figure 7.4 (b). An initial increase in relative pore volume is observed with a peak at *ca.* 2 nm, indicating a small amount of weakly bound water in the polymer. The pore volume then appears to increase from then on to the extent where no information about the porosity can be obtained. These results suggest an inability of NMR cryoporometry to measure an accurate pore size using water as the probe liquid in a polymer system. The swelling of the polymer, even with the added macroreticular structure, leads to the substantial presence of "free" water and effective pore sizes which are too large for thermoporometry analysis.

To probe the macroreticular structure of the resin only, the polymer was saturated in t-butanol. NMR was able to detect confined melting for t-butanol in the mesopores of the Amberlyst. Figure 7.5 (a) follows the melting transition from completely frozen through to complete pore melting. The sigmoidal curve is indicative of a standard NMR cryoporometry experiment without complications, as demonstrated in Chapter 4. No further rise in signal intensity was observed at the bulk melting temperature due to a lack of excess liquid added during the sample preparation procedure. The melting curve was repeated twice and the same results were obtained. The melting curve data was converted into a pore size distribution using the methodology set out in Chapter 5 and the melting point depression data parameters from Chapter 6. An average pore diameter of 29 nm was obtained. This is in excellent agreement with the average pore diameter reported by the manufacturer in the dry state, obtained by nitrogen porosimetry (29 nm). Using the observations from previous chapters, porosimetry tends to over-estimate the pore size when compared to NMR. As a result, it could be argued that the actual pore size of the polymer in the dry state is smaller than 29 nm, and it subsequently swells to 29 nm when saturated with t-butanol.

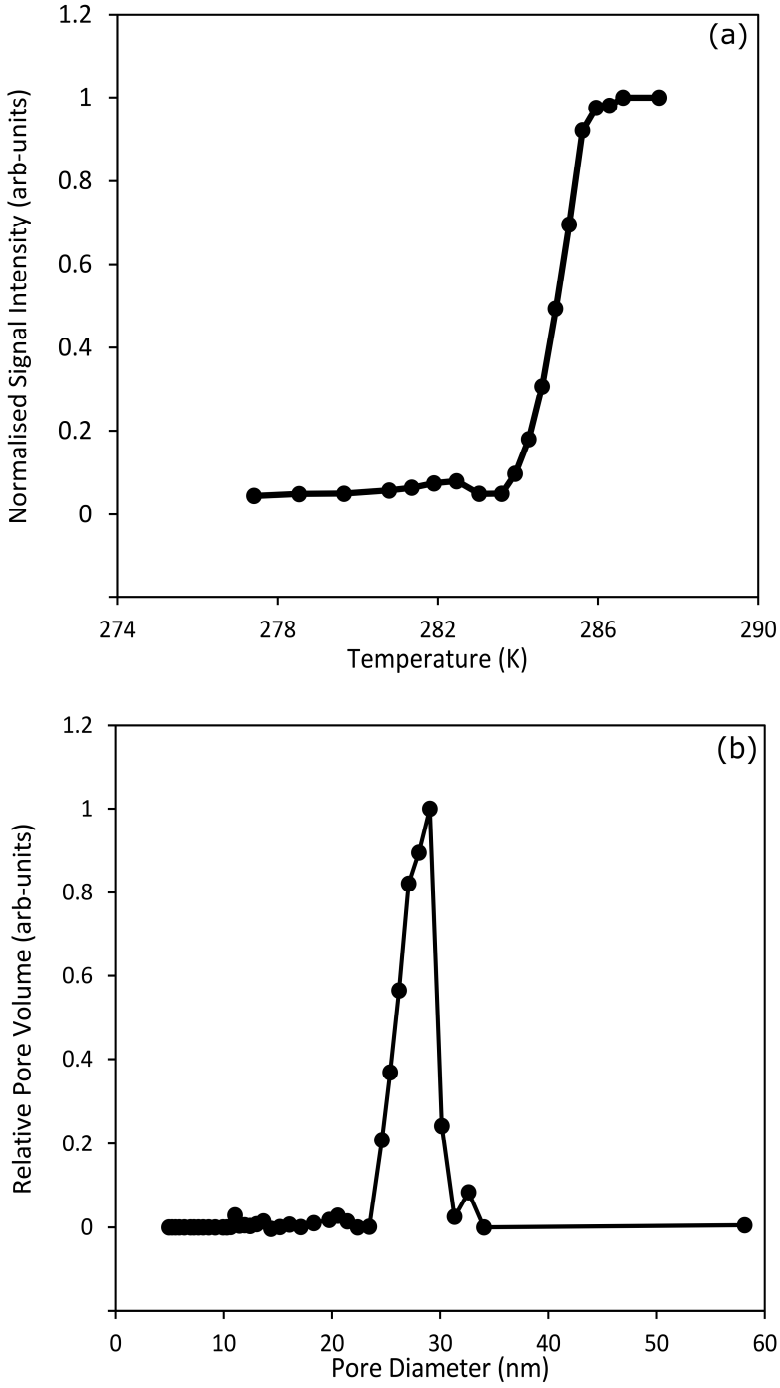

Figure 7.5. (a) *NMR melting curve for the macroreticular IER swollen in t-butanol and* ***(b)*** *the subsequent pore size distribution.*

Chapter 6 describes the ability of menthol to probe the porosity of solids. Here, the suitability of menthol as a cryoporometric liquid is studied further by subjecting the alcohol to a polymeric environment. NMR was able to detect for menthol, like t-butanol, a melting point depression confined with the mesopores of the macroreticular region of the polymer (Figure 7.6).

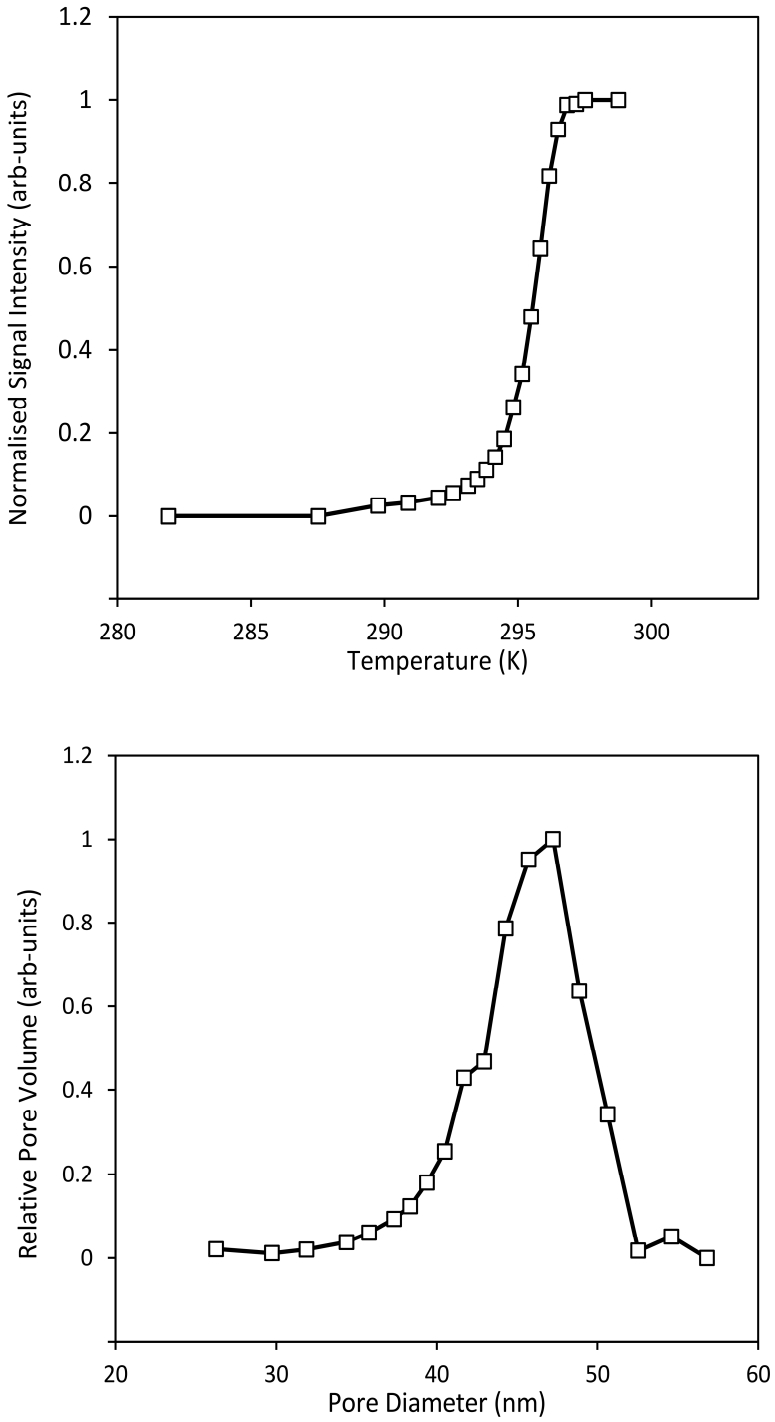

Figure 7.6. (a) *NMR melting curve for the macroreticular IER swollen in menthol and* ***(b)*** *the subsequent pore size distribution.*

Figure 7.6 (a) illustrates the smooth, sigmoidal-like, transition from solid to pore liquid. A further rise in signal intensity was observed for the bulk liquid outside of the polymer matrix. The subsequent pore size distribution, Figure 7.6 (b), reveals an average pore diameter of 47.2 nm. This is significantly larger

than the pore diameter obtained using t-butanol as the probe liquid. Chapter 6 describes how both alcohols have been used in cryoporometry experiments, using both glass and silica as the solid support, and have generally agreed on pore sizes to good effect. Here, however, there is a contrast in the average diameter obtained. One can therefore attribute this difference in average pore size to the swelling behaviour of the ion exchange resin, as it is known to swell to different extents depending on the nature of the liquid it is subjected to. Additionally, no pore melting was observed for cyclohexane. Cyclohexane may simply be too hydrophobic to swell the polymer.

NMR has been shown to accurately determine pore sizes for a macroreticular polymer network in the swollen state. This holds the advantage over other analytical techniques, such as N_2 porosimetry, where the porosity can only be probed when the polymer is dry. It has been shown that the porosity of macroreticular resins change depending on the polarity of the liquid to which it is subjected to [163, 164]. It would not be possible to explore this phenomena using the gas-based technique. NMR cryoporometry reveals this behaviour. In comparison to the other thermoporometry technique, DSC, NMR holds two further advantages. First is the known lower sensitivity of the DSC technique [175]. Second, calibration methods have not yet been obtained for alcohols such as t-butanol and menthol in order to convert the heat flow data into a pore size distribution. There are also further complications in preparation of the sample, due to the relatively high bulk melting point of menthol, which can be controlled more easily during the sample preparation process when the sample is in an NMR tube, compared to a DSC crucible.

7.3.2. NMR Analysis of the HEA-HMAA Polymer

To further test the robustness of the cryoporometry technique, the microporous structure of the disordered polymer hydrogel was analysed by attempting to swell the polymer in four different liquids. The liquids differ either in values of their melting point depression constant or in polarity. As the polymer is only composed of a gel phase, the aim was to assess how this phase behaves in different environments.

7.3.2.1. HEA-HMAA Analysis: Water as the Probe Liquid

Figure 7.7 follows the melting of water in the HEA-HMAA polymer which has been cross-linked to different extents. In all cases the NMR signal intensity increases with temperature, as the water confined within the cross-linking networks melts. No further rise is observed past the bulk melting temperature suggesting that no water was present on the exterior of the gels.

By increasing the cross-linking percentage, it is plausible that the density of smaller effective pores would increase. Thus, this would suggest that any imbibed liquid would, subject to its wetting properties, be present within these smaller “pores” and would melt at a lower temperature. This is partially reflected in Figure 7.7 (a). Having the highest cross-linking percentage and a subsequent theoretical denser region of effective microporosity, the 25% sample demonstrates an increase in signal intensity at lower temperatures when compared to samples with a lower cross-linking density. As the temperature is increased closer to that of the bulk melting, it tends towards that of the other thee samples.

The reproducibility of the technique is also demonstrated. The melting of water confined within the 6.25% cross-linked polymer is illustrated in Figure 7.7 (b). The polymer was saturated in water for both 24 and 48 hours prior to NMR analysis. The results are indistinguishable, confirming the reproducibility and stability of the technique.

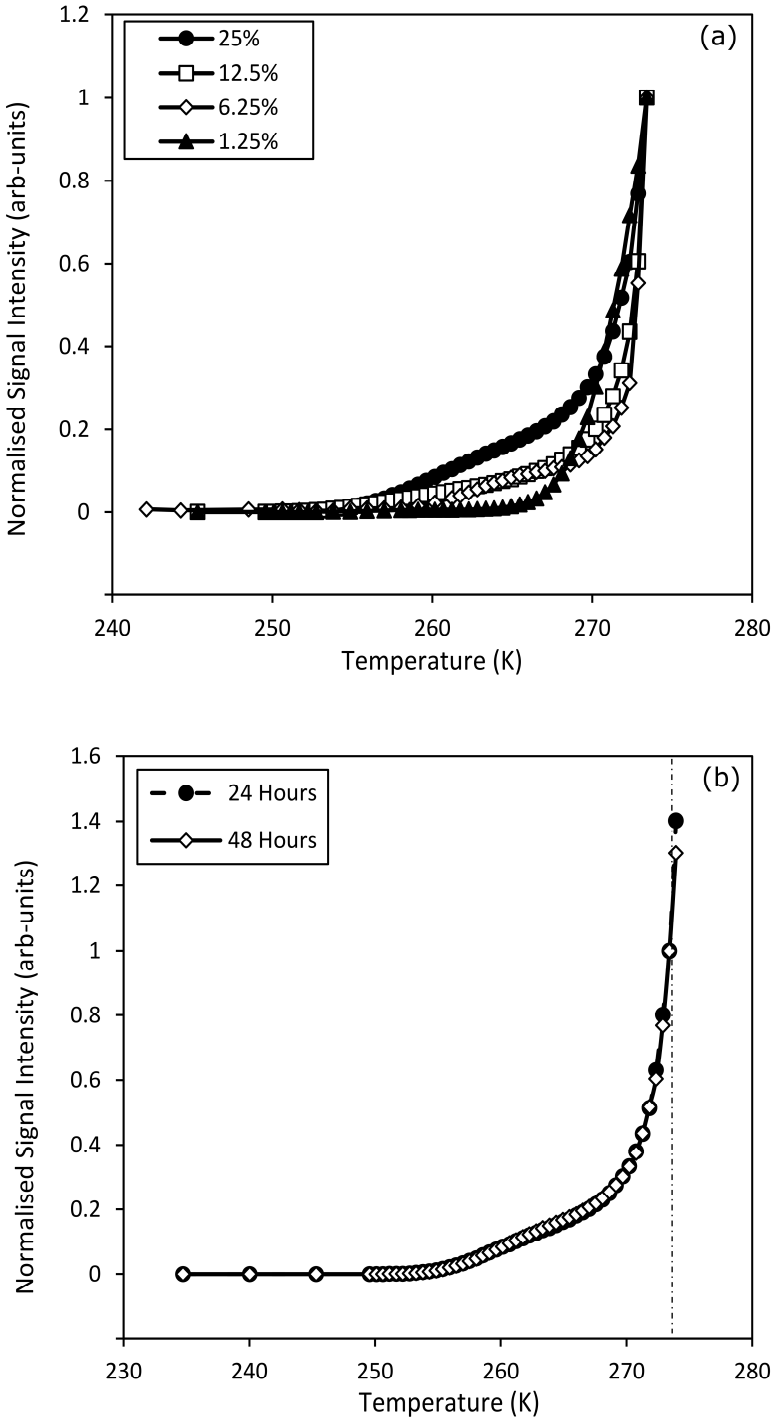

Figure 7.7. (a) *NMR melting curves for the water swollen HEA-HMAA polymer with differing cross-linking percentages and* ***(b)*** *NMR melting curve for the 6.25% cross-linked polymer left to saturate in water for both 24 and 48 hours.*

Water has a melting point depression constant of 49.53 K nm. As a probe liquid in cryoporometry experiments, water is much more suited to analysing structures which have far smaller pores. Figure 7.8 (a) shows the attempted conversion of the melting point data, from Figure 7.7, into a pore

size distribution. As expected from the melting curve data, the relative pore volume for water continuously increases with no plateau prior to the bulk melting region – illustrating the extent of swelling of the polymer in water. As such, on first reflection it would appear that NMR cryoporometry has failed as a technique to evaluate the pore sizes of a disordered cross-linked polymer gel system. However, focusing on the pore diameter range most suited towards analysis with water (2-8 nm; a reflection of its k_c) reveals a different result. A clear trend is observed when analysing pore diameters in the region below 10 nm, as illustrated in Figure 7.8 (b).

A correlation is observed between the percentage cross-linking and the average pore diameter for pore sizes less than 10 nm, as shown for the increase in relative pore volume for up to 5 nm. The trend is also consistent between 5-10 nm. As expected, a larger volume of water is present in the 25% cross-linked polymer, confirming the hypothesis that the polymer has an increased amount of smaller effective pores compared to the other samples as a result of the higher cross-linking density. Similarly, the 1.25% cross-linked polymer contained the least amount of water and thus, has the smallest density of effective pores which are smaller in size. The relative pore volume continues to increase significantly at higher temperatures in all cases, illustrating the presence of free water. The results demonstrate the ability of NMR cryoporometry, using water as the probe liquid, to distinguish between cross-linking density for a disordered polymer gel system.

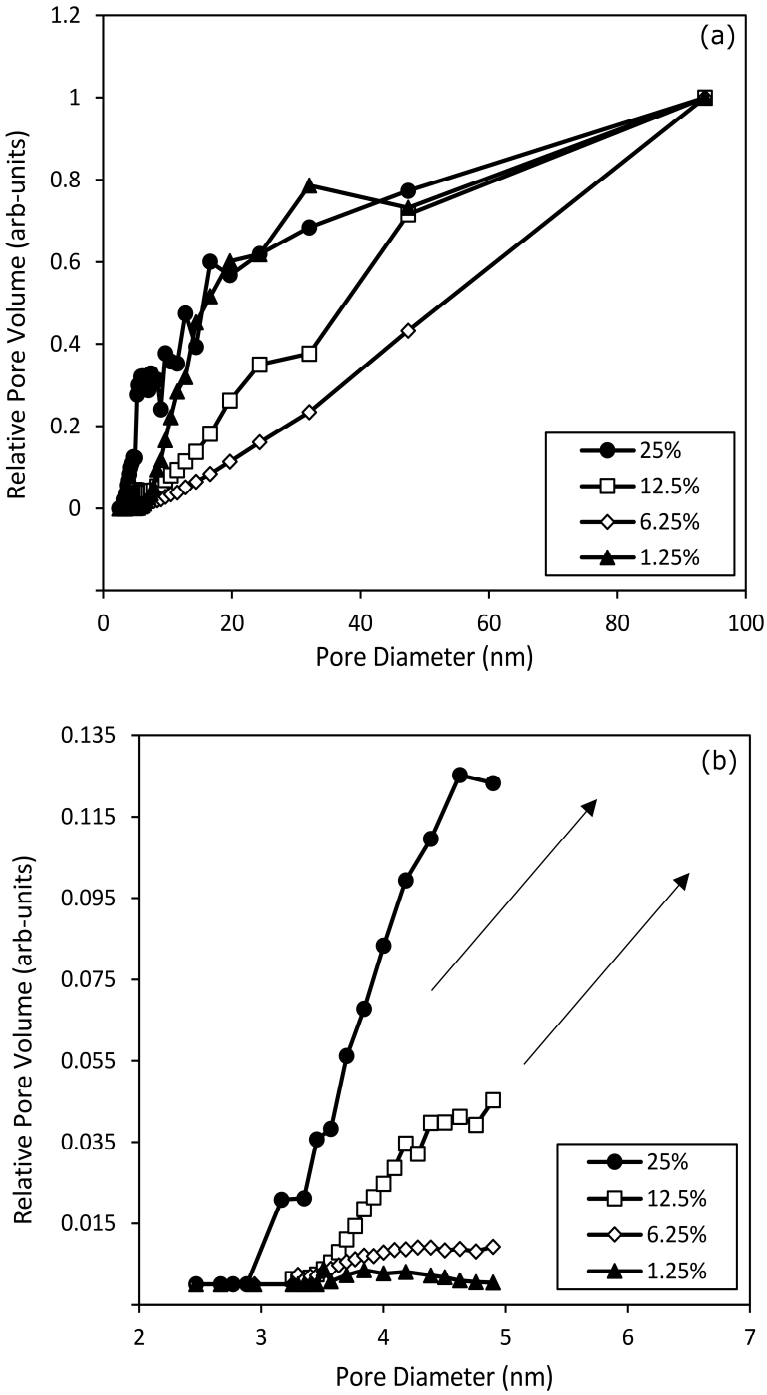

Figure 7.8. (a) *Pore size distribution data for water confined in the pores of the HEA-HMAA polymer hydrogel with differing cross-linking percentages, with a limit of 100 nm and* ***(b)*** *region less than 7 nm that demonstrates a difference between the extents of cross-linking.*

7.3.2.2. HEA-HMAA Analysis: Other Probe Liquids

The same procedure was followed using t-butanol, menthol and cyclohexane as probe liquids. No pore melting was observed for any of the three liquids. Despite their favourable polarity, both t-butanol

and menthol were not able to cause the polymer to swell significantly enough to enter the microporous structure of the cross-linked polymer. Figure 7.9 illustrates that little to no signal intensity at lower temperatures was observed below the bulk melting point, with a significant rise when the liquid outside of the matrix started to melt at T_m. Both alcohols have considerably larger molecular sizes than water. As such, it is plausible that this prevented their access into the microporosity region of the gel. Figure 7.10 shows a similar pore size region than in Figure 7.8 (b), with no evidence of mesoporous pores or bound probe liquid. Similar results were obtained using cyclohexane, due to the hydrophobicity of the probe liquid.

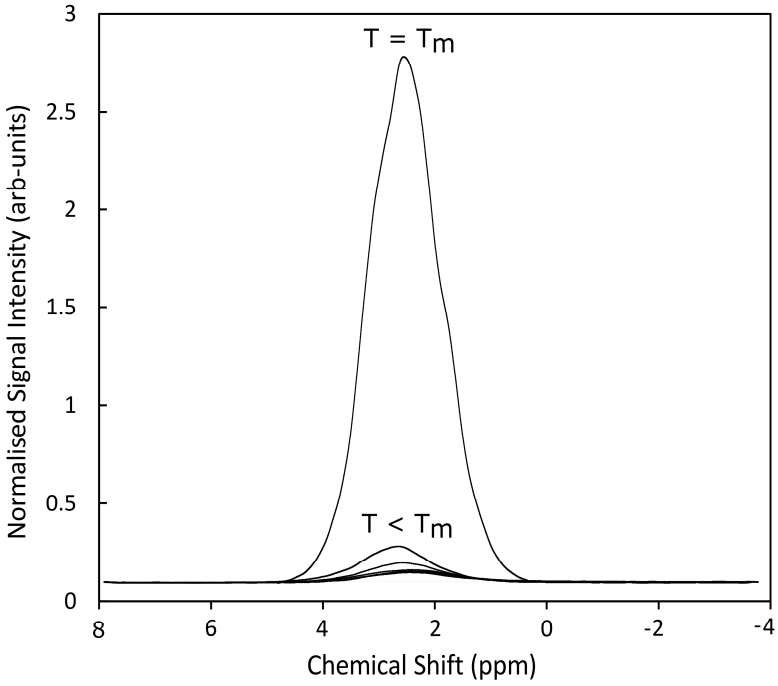

Figure 7.9. *NMR cryoporometry study of t-butanol and 1.25% cross-linked HEA-HMAA polymer. The signal intensity starts to rise only as it reaches T_m. No pore melting is observed below the bulk melting temperature.*

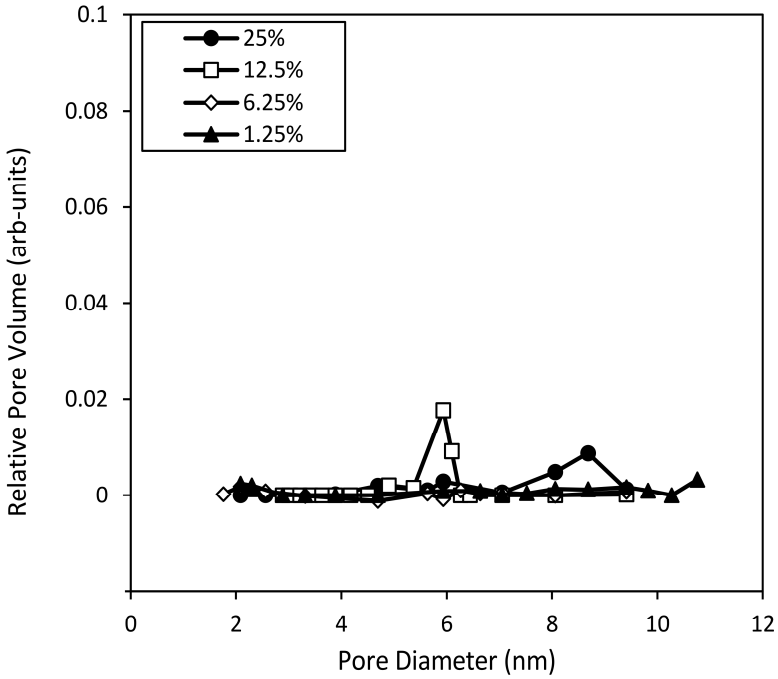

Figure 7.10. *Pore size distribution data for t-butanol and the HEA-HMAA polymer. No small pores are identified due to the polymer not swelling in t-butanol.*

7.3.3. DSC Analysis of the HEA-HMAA Polymer

To validate the results obtained by NMR, the freezing/melting behaviour of water in the swollen polymer was followed using DSC. However, DSC was not able to provide any quantitative information on the effective porosity of the gel due to the excessive swelling of the matrix. The use of DSC also proved to be disadvantageous, when compared to NMR, even at the lower end of the pore size domain, as Figure 7.11 illustrates. DSC was unable to detect the same pore melting that NMR illustrated in 7.8 (b). This finding suggests that the lower sensitivity of the DSC technique results in no-observable melting, let alone observable differences in water behaviour between the cross-linked analogues, in this case. As such, NMR holds some clear advantages over DSC, even though both fail to quantitatively deduce the nature of water throughout the swollen polymer.

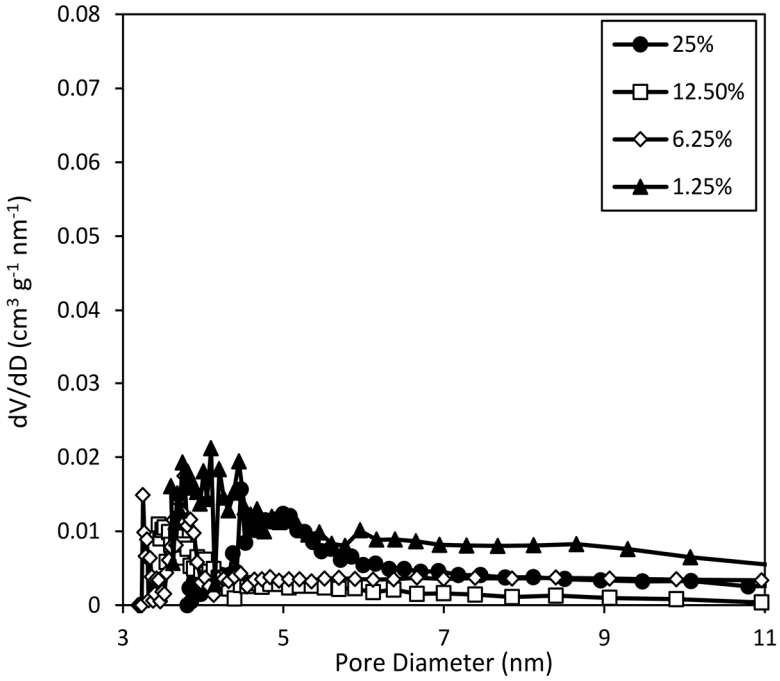

Figure 7.11. *DSC analysis into the polymer gel system swollen in water. No quantitative information is obtained, even at the lower end of the pore size region.*

7.3.4. SEM Analysis of the HEA-HMAA Polymer

There is still the need to validate the NMR experiments. As such, SEM images were obtained for the 25% cross-linked polymer swollen in water. The collection of images with a scale between 100-10 µm are shown in Figure 7.12 and Figure 7.13 illustrates the SEM images between 10-1 µm in scale. The images revealed structural information about the polymer matrix, including the possible identification of polymer fibres in Figure 7.12 (b). Most interestingly, Figure 7.13 (b) illustrates the first possible indication of an effective porosity. The cross-linking creates voids, approximately 2-3 µm in diameter, support melting pattern data obtained using NMR as these pore sizes are far too big, to depress a liquid melting point enough, for quantitative NMR analysis. The regions off of the main polymer chains are most visible in Figure 7.13 (c) and (d), where the effective microporosity on a nanometre scale, observed with the melting in Figure 7.8 (b), may be present.

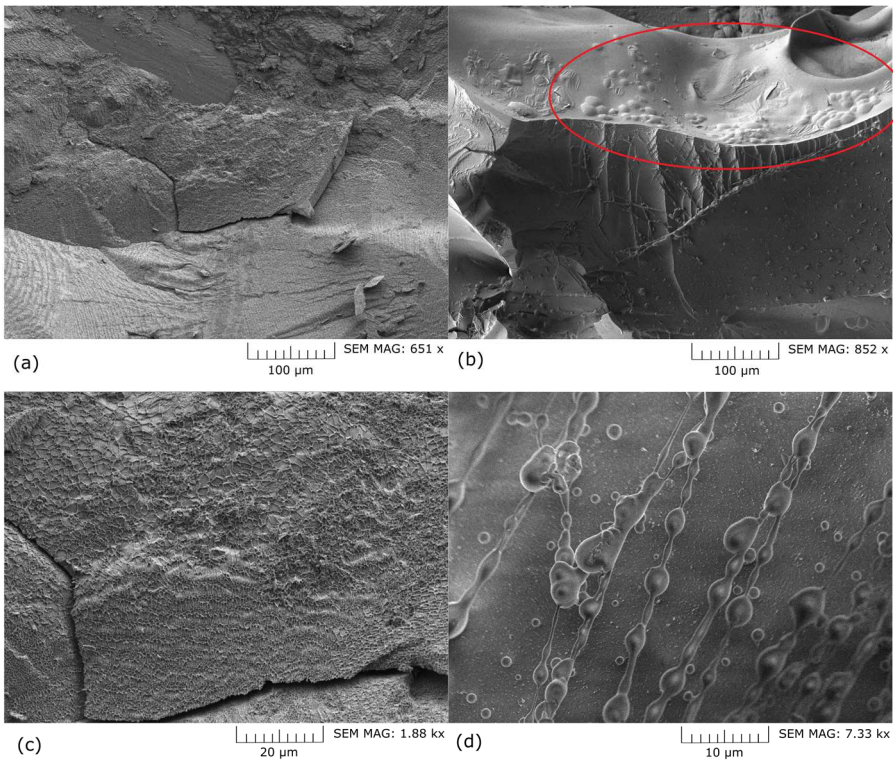

Figure 7.12. *SEM Images of the water swollen 25% cross-linked HEA-HMAA polymer at a magnification of* ***(a)*** *651 ×,* ***(b)*** *852 ×,* ***(c)*** *1.88 k× and* ***(d)*** *7.33 k×*

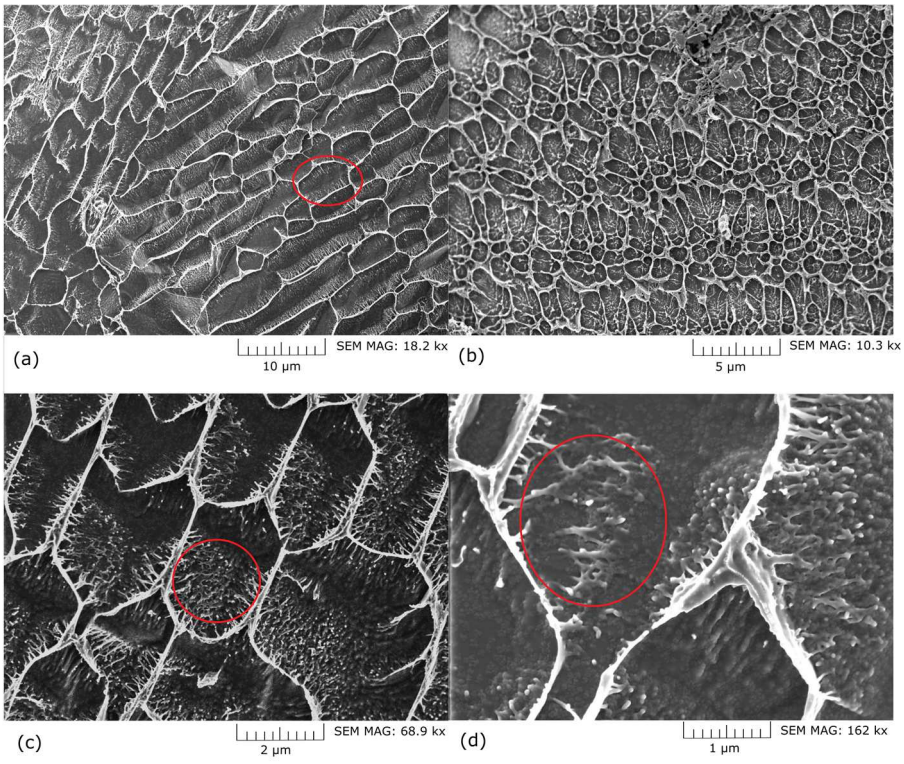

Figure 7.13. *SEM Images of the water swollen 25% cross-linked HEA-HMAA polymer at a magnification of* ***(a)*** *18.2 k×,* ***(b)*** *10.3 k×,* ***(c)*** *68.9 k× and* ***(d)*** *162 k×*

7.4. Conclusions

The information contained when polymer resins are in the dry state are seldom relevant to their properties in the wet state. The relevance to the working environment improves significantly if the resin is swollen, without collapsing the porous network. This chapter explores how the technique of NMR cryoporometry can be applied to a solvent-swollen Amberlyst ion exchange resin. A series of four different liquids; water, t-butanol, menthol and cyclohexane, were identified as potential probe liquids. The differing extent of hydrophobicity would also allow a study into how the swelling of the polymer changes with polarity. The robustness and applicability of the NMR technique was then tested further by applying the cryoporometry method to study the microporous region of a gel-phase HEA-HMAA polymer hydrogel.

The Amberlyst resin differs from the HEA-HMAA hydrogel as it contains ordered regions of mesoporosity created by the addition of a porogen during the polymerisation process. It was difficult to obtain any quantitative information about the porosity using water as the probe liquid due to the excessive amount of free water present however, a small population of weakly bound water was identified. Pore size distributions, of the larger mesopores, were successfully obtained using both alcohols. It is known that IERs swell to different extents dependent on the type of liquid that they are swollen with, and this behaviour is observed here. It was not possible to obtain cryoporometry data with all liquids trialled here. However, the highly hydrophobic liquid, cyclohexane, did not enter the hydrophilic polymer.

The analysis of the HEA-HMAA polymer suggested that cryoporometry may have its limitations when trying to analyse a microporous polymer gel system. The polymer swelled significantly when subjected to water which suggested, at first instance, that no porosity data, qualitatively or quantitatively, could be obtained. However, by focusing on the region that has proven to be most effective for water (< 10 nm), differences between samples with different cross-linking percentages became apparent. A larger proportion of weakly bound water was found in the highest-crosslinked polymer due to the

higher density of smaller micropores formed through the increased cross-linking. However, the polymer failed to swell in the other three liquids. This may be due to two reasons. First, the molecular size of t-butanol and menthol are significantly larger than that of water. The effective microporosity has been identified by NMR and SEM. As such, it could be argued that the alcohols are simply too large to cause the polymer to swell. The second reason may be a mismatch of chemical properties. There is no region of polarity in cyclohexane and as such, the pores remained collapsed and cyclic alkane does not swell the polymer.

This chapter has demonstrated that NMR cryoporometry may be used to study the effective porosity in polymer systems. However, the probe liquid needs to be matched to the properties of the polymer, both in terms of chemistry and also in terms of the size of the pores being studied. Ion exchange resins are key to many areas of science and their proficiency lies in the fact that their properties change in the swollen state. NMR offers the ability to probe their mesoporous structure in their functional, wet, state in order to elucidate structural information from the active resin.

CHAPTER. 8

Diffusion NMR Characterization of Catalytic Silica – A Tortuous Path

8.1. Introduction

Porous silica supports that have been characterised using NMR cryoporometry in Chapter 5, SBA-15 and KIT-6 (Figure 5.1), have shown potential for the production of biodiesel [125, 176], with sulfonic acid functionalization resulting in materials that can perform both the transesterification of triglycerides and the esterification of free fatty acid impurities [177, 178]. The effectiveness of these supports towards esterification is highly dependent on pore structure, with Pirez *et al.* [125] showing that reaction rates over sulfonic acid analogues possessing similar size mesopores are enhanced for the 3-dimensional *Ia3d* cubic architecture of KIT-6 relative to the 2-dimensional *p6mm* hexagonal structure of SBA-15 [125]. This rate enhancement is attributed to the different silica architectures and the corresponding effect on the diffusion of reactants and products throughout the support since the two sulfonic acid silicas possessed similar active site densities and operating through an identical catalytic reaction mechanism. The esterification reaction is illustrated in Scheme 8.1.

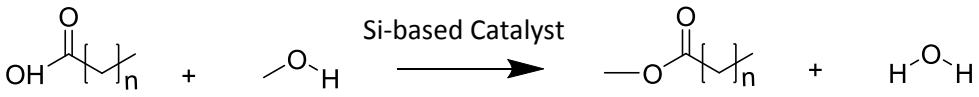

Scheme 8.1. *Catalytic esterification of carboxylic acids with methanol.*

NMR methods have been developed to measure the diffusion of small molecules through solution, as described in Chapter 2. These can be applied to study molecules in porous materials by using the changes in the properties of a fluid in contact with the surface of the solid to elucidate information about the solid structure. Diffusion NMR, a pulsed field gradient (PFG) technique [179], non-invasively

measures the displacement of a particular fluid even in constrained environments, such as the porous network of mesoporous silica. The relationship between the bulk diffusion coefficient and the diffusion coefficient of the confined fluid, D/D_0, yields information on the structural properties of the porous network.

Recent work by Mantle *et al.* [180] studied the diffusion behaviour of a series of alcohols in the pores of supported gold catalysts. While most species were hindered by being placed in a porous network, butanediol isomers exhibited an enhancement to their diffusion coefficients in the bulk liquid. It was suggested that this behaviour may be down to a disruption of the hydrogen bonding network by the porous solid. This theory was investigated further by D'Agostino *et al.* [181] who studied the diffusion of a series of liquids inside different porous environments. An interaction parameter was introduced, ξ, the ratio of the diffusion coefficient of the bulk liquid, D_0, to the diffusion coefficient of the confined liquid, D [182]. This ratio of the diffusion coefficient of a species measured in a porous material to that measured when in solution, D/D_0, is equal to the reciprocal of the tortuosity and allows for the use of diffusion NMR as a means of characterizing the porous material [20, 79, 183]. The tortuosity of a material is an inherent property of its structure that defines how twisted and curved the pore walls are [184]. In the case where different tortuosities are produced for different chemical species in the pores, ξ rather reflects an *effective* tortuosity due to the additional interactions of the fluid with the surface of the pore wall. A true value for the tortuosity can be obtained using a non-interacting fluid such as a straight chained alkane [20, 79, 185-187].

In this chapter, NMR diffusometry was used to characterize catalytic silica supports by studying the in-pore diffusion of reactants and products pertinent to the esterification of fatty acids with methanol within two different silicas. Diffusion coefficients of a series of straight chain carboxylic acids, as well as alkanes and esters, within the pores of both SBA-15 and KIT-6 were acquired, enabling determination of the effective and actual tortuosities of the two silica catalytic supports. The effect of alkyl chain length of the fatty acids on their diffusion behaviour was also studied. Analysis of reactant

and product diffusion behaviour within mesoporous silicas offers insight into the different esterification activity of their sulfonated counterparts reported in the literature.

8.2. Experimental

8.2.1. Sample Preparation

The SBA-15 and KIT-6 powders provided had previously been prepared by the methods of Stucky [126] and Ryoo [127] respectively and the confirmation of their successful syntheses are shown in Chapter 5, Figure 5.2. Propionic acid, valeric acid, hexanoic acid, octanoic acid, lauric acid, myristic acid, palmitic acid, deuterated water and deuterated methanol were obtained from Sigma-Aldrich and were not subjected to any further purification techniques. Their properties are detailed in both Tables 3.1 and 3.2. Methyl hexanoate was prepared following a standard esterification procedure outlined elsewhere [188]. An NMR spectrum confirming the successful synthesis is illustrated in Appendix 3, along with the relevant peak assignment. For the diffusion measurements, a 20 mmol solution of each acid was prepared with deuterated methanol. SBA-15 and KIT-6 were dried in the oven at 100 ^{o}C for 24 hours and then placed in a desiccator for a further 24 hours prior to being used. The acid solution was then pipetted onto each support and the silica was left to soak for at least 12 hours. The excess liquid was then removed by carefully blotting on pre-soaked filter paper. The samples were transferred to a thin-walled NMR tube, sealed with parafilm and placed on a centrifuge at 1500 rpm for 1.5 hours. Centrifuging the sample ensures imbibition of the liquid into the pores of the silica [115]. When placed into the spectrometer, the samples were allowed at least 20 minutes before any acquisitions were made to ensure thermal equilibrium had been reached.

8.2.2. NMR Measurements

All of the measurements were carried out on a Bruker Avance spectrometer with a frequency of 300 MHz and operating at a magnetic field strength of 7.05 T. For diffusion measurements, a 5 mm PABBO BB-^{1}H Z-GRD probe head was used with a maximum gradient of 3.6 x 10^{-1} T m^{-1}. The diffusion coefficients were then determined and processed using the DOSY Toolbox software package [189]. Errors

of approximately 1% in individual diffusion measurements were obtained from the DOSY fitting of the Stejskal-Tanner equation. However the main source of error in diffusion experiments is the reproducibility of data acquisition. Parameters such as spectrometer performance and, more significantly, temperature fluctuation, will affect the data. This has resulted in a maximum experimental error of 4.0 % for KIT-6 and 3.3% for measurements in SBA-15. All NMR measurements were made at 298 K and used the double stimulated echo bipolar pulse pair sequence (DSTEBPGP_3S) (Figure 3.5) to remove any possible effects of convection from the diffusion measurements in bulk solution [84, 93]. The same pulse sequence was then used for all later NMR diffusometry experiments. The signal, S, attenuates according to [89]

$$\frac{S}{S_0} = e^{-D\gamma^2\delta^2\sigma^2 g^2[\Delta + \frac{2\kappa - 2\lambda - \delta}{2} - \frac{\tau_1 + \tau_2}{2}]} \quad (8.1)$$

where S_0 is the signal before a gradient is applied, D is the diffusion coefficient, γ is the gyromagnetic ratio of a proton, δ is the diffusion encoding gradient length (0.001 s), g is the diffusion encoding gradient strength, τ_1 and τ_2 are intergradient delays within the bipolar gradient pulses (both 0.001 s) and σ, κ and λ are all parameters associated with shaped gradient pulses. σ ("gradient area") is an expression on the efficiency of the gradient pulse and, for a half-sine shape, it has a value of $\frac{2}{\pi}$. κ and λ are further shape parameters used in the Stejskal-Tanner equation and have values of $\frac{1}{2}$ and $\frac{3}{8}$, respectively, for half-sine gradient pulses [89]. The delay time, T, corresponds to a value of Δ = 0.3 s for the majority of the data presented, apart from the variable delay time studies, illustrated in Appendix 3. Ten magnetic field gradient amplitudes from 7.19 x 10^{-3} to 2.87 x 10^{-2} T m^{-1} were used and incremented in equal steps of gradient squared. For each gradient amplitude, 16 transients of 16384 complex data points were acquired for a total experimental time of 15 minutes.

8.3. Results and Discussion

8.3.1. Tortuosity as a Structural Parameter

Figure 8.1 (a) shows diffusion NMR data for propionic acid in bulk methanol solution and within two distinct silicas, SBA-15 and KIT-6 with mean mesopore diameters of 4.9 nm and 5.2 nm respectively. Figure 8.1 (b) is a combined DOSY spectra of propionic acid in methanol, for bulk methanolic solution, in SBA-15 and in KIT-6. When confined within a pore, the acquired diffusion coefficients are lower than for the species measured in bulk solution. The measured diffusion coefficients are in the order: bulk > SBA-15 > KIT-6. The further reduction in diffusion coefficient for the acids within KIT-6 compared to SBA-15 suggests that the Brownian motion of the fluids are subjected to increased restrictions. The knowledge that the pores in KIT-6 are interconnected and winding intuitively supports this result. The log attenuation and DOSY plots for the remaining acids in methanol are illustrated in Figures 8.2-8.7, respectively.

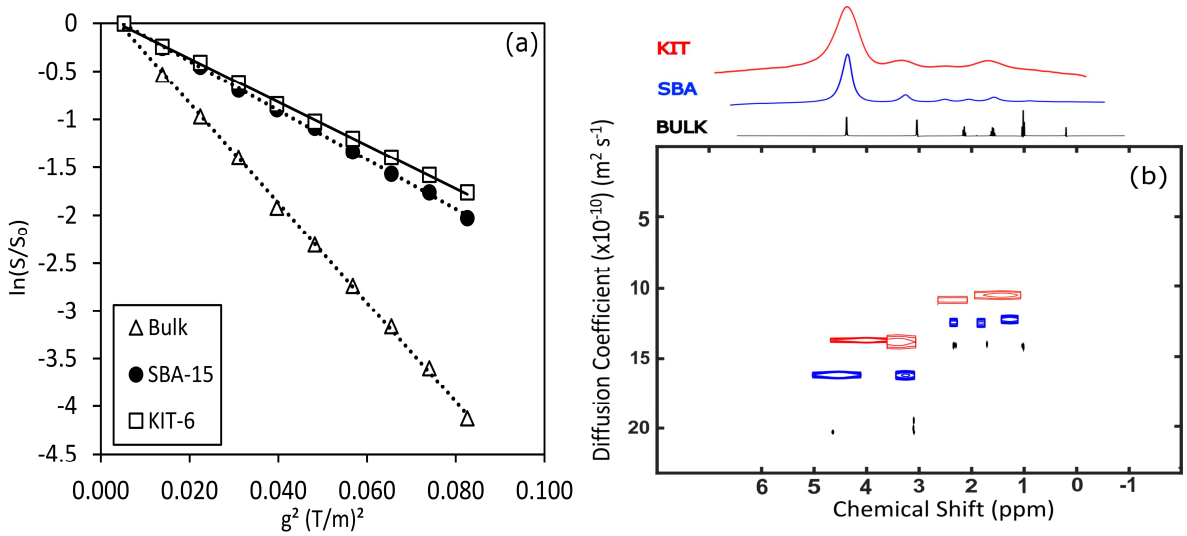

Figure 8.1. (a) *Natural logarithm plot of the signal attenuation versus the gradient strength squared for propionic acid in bulk solution, in SBA-15 (4.9 nm) and in KIT-6 (5.2 nm) and* ***(b)*** *the DOSY spectra for propionic acid in methanol-d_4 in bulk solution (black), SBA-15 (blue) and KIT-6 (red).*

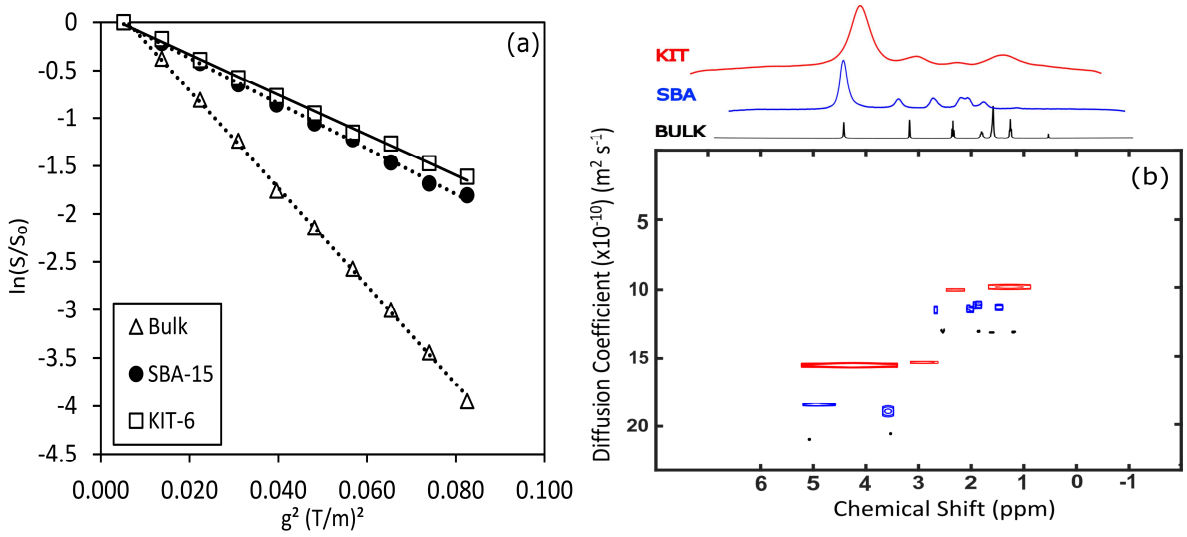

Figure 8.2. (a) *Natural logarithm plot of the signal attenuation versus the gradient strength squared for valeric acid in bulk solution, in SBA-15 (4.9 nm) and in KIT-6 (5.2 nm) and* ***(b)*** *the DOSY spectra for valeric acid in methanol-d_4 in bulk solution (black), SBA-15 (blue) and KIT-6 (red).*

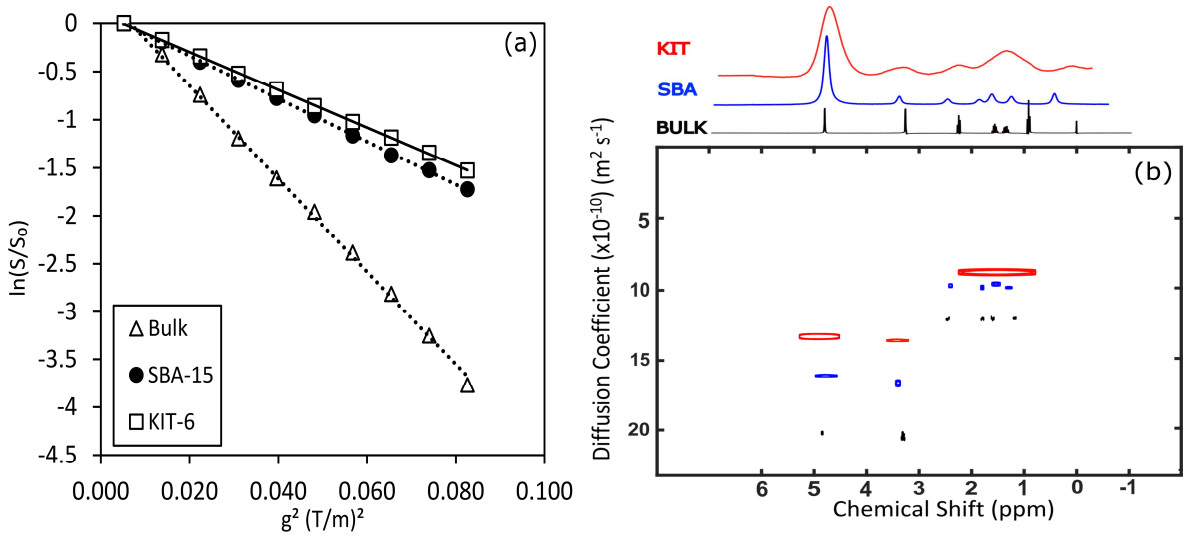

Figure 8.3. (a) *Natural logarithm plot of the signal attenuation versus the gradient strength squared for hexanoic acid in bulk solution, in SBA-15 (4.9 nm) and in KIT-6 (5.2 nm) and* ***(b)*** *the DOSY spectra for hexanoic acid in methanol-d_4 in bulk solution (black), SBA-15 (blue) and KIT-6 (red).*

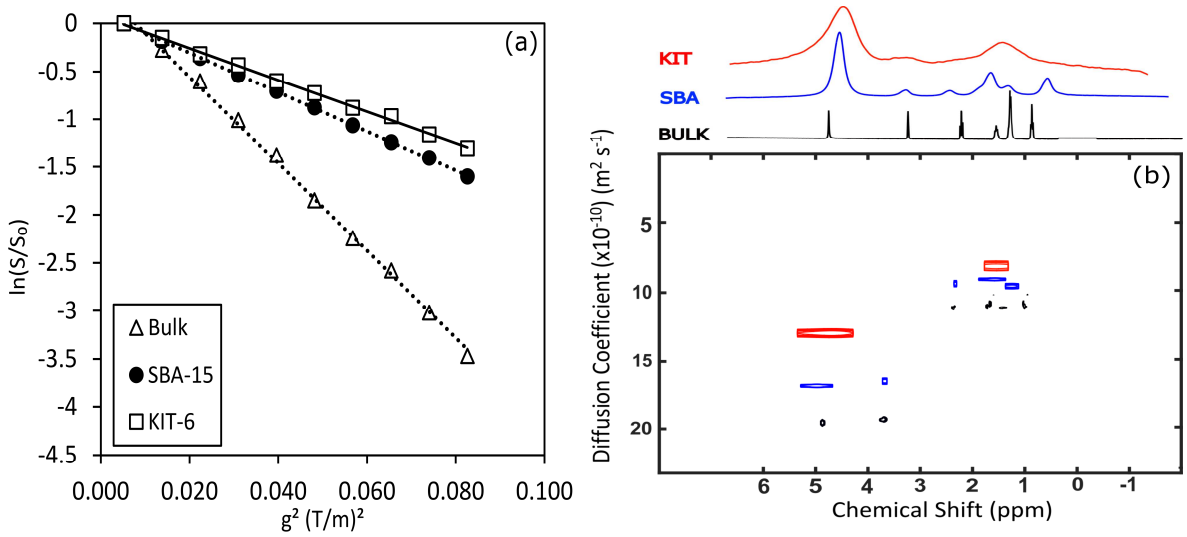

Figure 8.4. (a) *Natural logarithm plot of the signal attenuation versus the gradient strength squared for octanoic acid in bulk solution, in SBA-15 (4.9 nm) and in KIT-6 (5.2 nm) and* ***(b)*** *the DOSY spectra for octanoic acid in methanol-d_4 in bulk solution (black), SBA-15 (blue) and KIT-6 (red).*

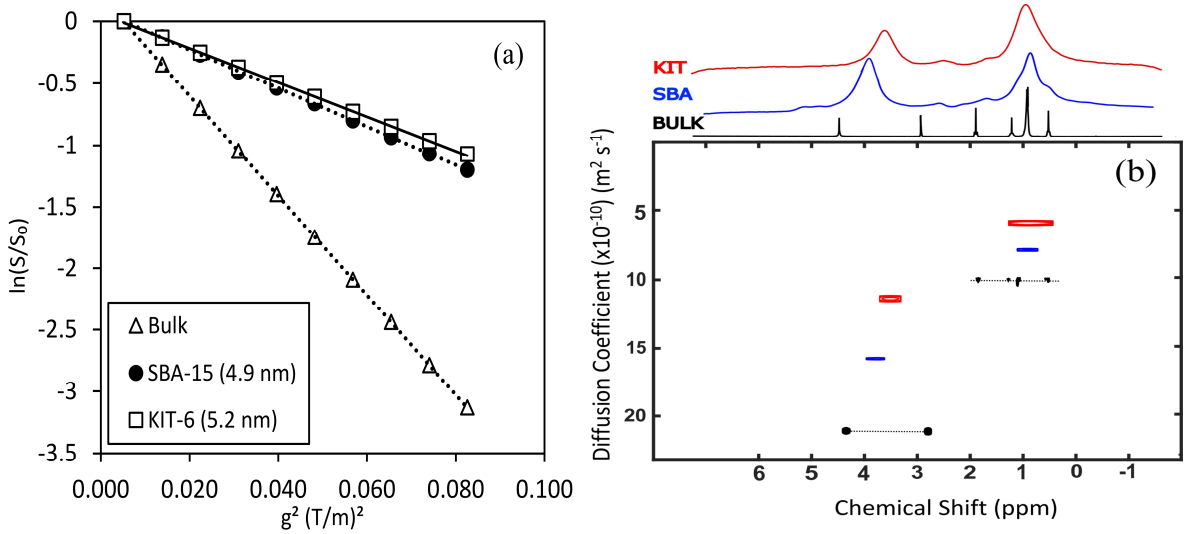

Figure 8.5. (a) *Natural logarithm plot of the signal attenuation versus the gradient strength squared for lauric acid in bulk solution, in SBA-15 (4.9 nm) and in KIT-6 (5.2 nm) and* ***(b)*** *the DOSY spectra for lauric acid in methanol-d_4 in bulk solution (black), SBA-15 (blue) and KIT-6 (red).*

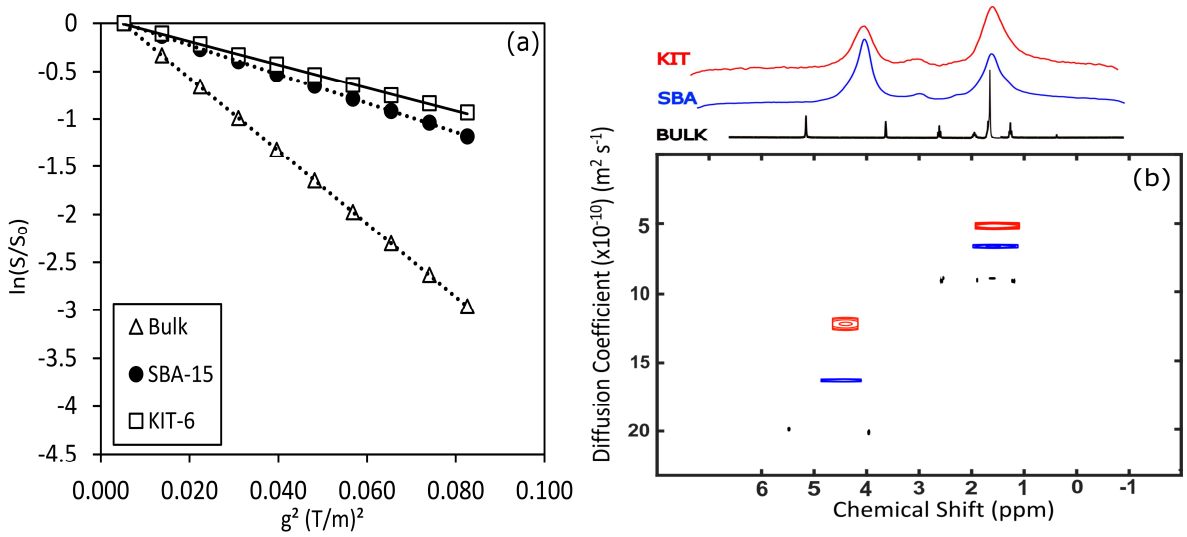

Figure 8.6. (a) *Natural logarithm plot of the signal attenuation versus the gradient strength squared for myristic acid in bulk solution, in SBA-15 (4.9 nm) and in KIT-6 (5.2 nm) and* ***(b)*** *the DOSY spectra for myristic acid in methanol-d_4 in bulk solution (black), SBA-15 (blue) and KIT-6 (red).*

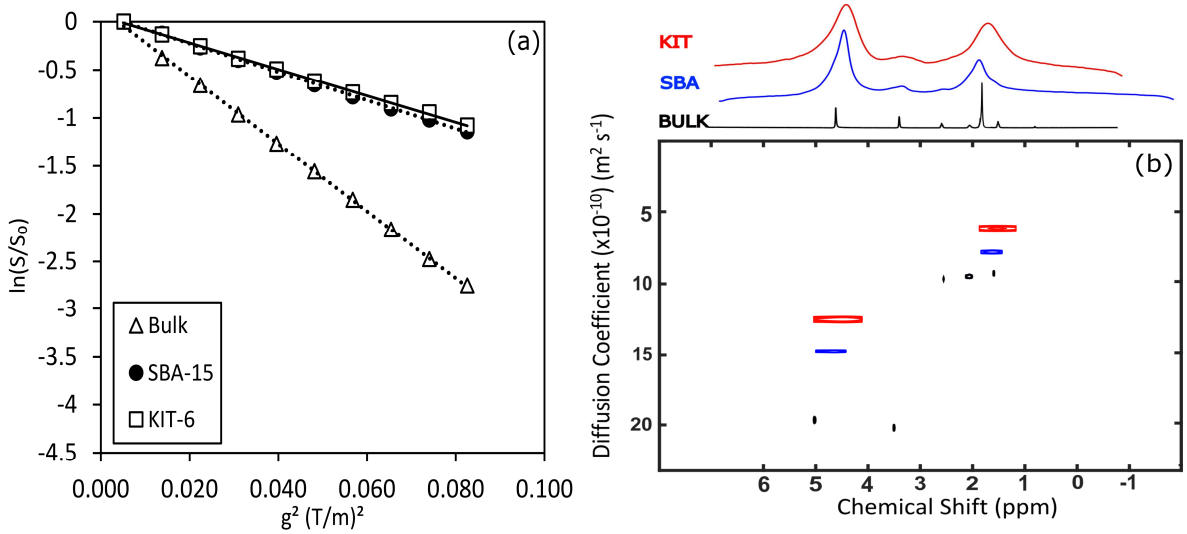

Figure 8.7. (a) *Natural logarithm plot of the signal attenuation versus the gradient strength squared for palmitic acid in bulk solution, in SBA-15 (4.9 nm) and in KIT-6 (5.2 nm) and* ***(b)*** *the DOSY spectra for palmitic acid in methanol-d_4 in bulk solution (black), SBA-15 (blue) and KIT-6 (red).*

Taking into account the typical observation times used in a NMR diffusometry experiment, the root mean square displacement of a molecule confined within the silica supports exceeds the pore size and falls into the long diffusion delay time limit, given by Equation 2.33 [80]. For heptane, one of the species studied here, confined within a pore of 4.9 nm in diameter, $\frac{<R>^2}{6D}$ equates to 1.3 x 10^{-9} s, which is significantly smaller than diffusion delay times used in the NMR experiments (0.02-0.30 s). As the diffusion delay time is suitably long enough, the molecules experience many collisions with the walls of the solid and the reduction in observed diffusion coefficient will reflect the tortuosity of the solid being studied.

The log-attenuation plots produced for the diffusion experiments performed are all straight lines with no deviation. Non-linear or curved log-attenuation plots can arise for one of a number of reasons: (1) multiple components (e.g. two different diffusing species); (2) the combination of bulk and surface diffusing species (e.g. one species in two different diffusion environments); (3) the root mean squared displacement of the diffusing molecule approaching the average pore diameter; (4) instrumental artefacts, like eddy currents, internal magnetic field gradients, or incomplete phase cycling [180]. Such linear plots indicate two things. First, that the molecules travel much further than the average pore dimension during the NMR experiment and hence likely interact with the pore walls many times during this period. Second, that for each measured signal, only one species is present, moving with a single diffusion coefficient.

Species which possess functional groups, such as carboxylic acids, undergo further interactions with the pore walls. The diffusion measurements now reveal an effective tortuosity, dependent on both solid structure and surface-liquid interactions. This relationship is shown in Equation 8.3.

$$\tau_{eff} = \sigma_s \tau \tag{8.3}$$

The term σ_s represents the extra interactions between the liquid and the surface and can depend on both fluid and solid.

The true tortuosity of the solid can be acquired by measuring the diffusion coefficients of non-interacting species such as a straight chain alkanes. The diffusion coefficients of both heptane and cyclohexane were acquired at a series of diffusion delay times and the tortuosity of the silica supports were obtained for both. Tortuosities obtained for the silica support using the two compounds were identical. Methyl esters are the product of esterification, and hence the diffusion coefficients of methyl hexanoate were also acquired, both within the porous silica and in solution. The ester exhibited an effective tortuosity within 5 % of the tortuosities obtained using straight-chained alkanes, indicating weaker interactions with the walls of the porous silica than carboxylic acids in line with expectations.

Table 8.1. Effective tortuosity measured for non-interacting species confined within the pores of SBA-15 (4.9 nm) and KIT-6 (5.2 nm).

Species	D_0 (x10^{-10} m^2 s^{-1})	τ (KIT-6 (5.2 nm))	τ (SBA-15 (4.9 nm))
n-heptane	30.10 ± 0.2	**1.48** ± 0.03 (2.1%)	**1.20** ± 0.02 (1.8%)
cyclohexane	14.14 ± 0.17	**1.50** ± 0.05 (3.1%)	**1.23** ± 0.03 (2.4%)
methyl hexanoate	13.50 ± 0.20	1.58 ± 0.06 (4.0%)	1.19 ± 0.04 (3.2%)

To confirm that this behaviour is a characteristic of the pore structures, the tortuosity was measured within the same silica architectures possessing a range of mesopore sizes using cyclohexane and heptane as the non-interacting liquids. The migration of the liquids through the pores should not depend on the pore size of the material if they share the same structures. The results are illustrated in Figure 8.8. The diffusion coefficients of the alkanes were measured with Δ = 0.3 s. Further diffusion measurements indicated that, in pores of a smaller diameter, the diffusion was increasingly reduced. Above a certain pore size (*ca*. 4.9 nm for SBA-15 and 5.2 nm for KIT-6), the effective tortuosity was independent of pore size for both SBA-15 and KIT-6 with their respective τ values tending to those in Table 8.1. As this behaviour is observed for both materials and the measurements were all acquired in the long diffusion time limit, it suggests that it is a property of the supports rather than an artefact

of the NMR experiments. These tortuosities are similar to those reported elsewhere for fused SiO_2 ($\tau \approx 1.6$ [181]).

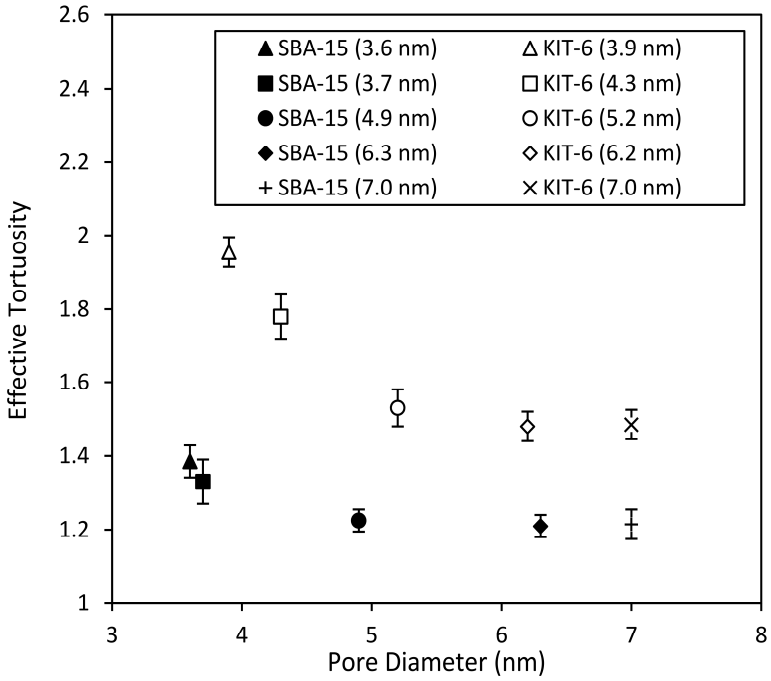

Figure 8.8. *The average values of tortuosity for heptane and cyclohexane confined within the pores of SBA-15 and KIT-6. A diffusion delay time of 0.3 s was used for all measurements to ensure the diffusion was within the long diffusion delay time limit. Values for heptane and cyclohexane were indistinguishable.*

8.3.2. The Effect of Chemical Structure on Diffusion

Propylsulfonic acid functionalized analogues of the two silica supports studied in this work have previously been used in carboxylic acid esterification with methanol, and the resulting kinetic data [125] indicated that slower diffusion within the two-dimensional SBA-15 mesopore channels may result in slower turnover frequencies (TOFs) relative to KIT-6 possessing mesopores of a similar average diameter. This hypothesis was therefore investigated through determining the diffusion coefficients of a homologous series of carboxylic acids in the bulk liquid, and when contained within the pores of both SBA-15 and KIT-6 silica supports. The impact of mesopore diameter of carboxylic acid was also studied for KIT-6.

Figure 8.9 illustrates the changes in diffusion coefficient for the homologous series of carboxylic acids in bulk solution, SBA-15 (pore size of 4.9 nm) and KIT-6 (5.2 nm). When in the bulk, the acids have no restriction on their motion and the diffusion coefficients decrease accordingly with increasing chain length – according to the Stokes-Einstein relation [32]. The same trend of reducing diffusion coefficients with increasing molecular weight and size are also observed for measurements of shorter chained acids in both porous supports. However, when the chain length of the acids reaches approximately twelve carbon atoms, the observed diffusion coefficients in the silica no longer decrease with increasing chain length and even increases in the case of palmitic acid in KIT-6. When in the pores of the silica, the diffusion coefficient will depend on both the bulk diffusion coefficient, the structure of the pores and any further interactions between the molecule and pore surface, giving rise to the observed differences.

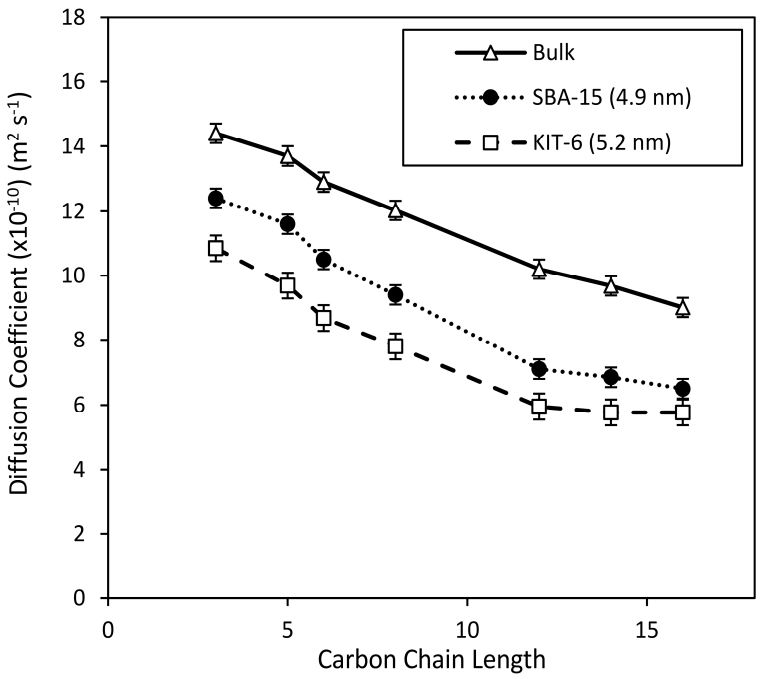

Figure 8.9. *Diffusion coefficients of a homologous series of carboxylic acids acquired in bulk solution, SBA-15 (4.9 nm) and KIT-6 (5.2 nm). A diffusion delay time of 300ms was used for all experiments to ensure that measurements were carried out in the long diffusion delay time limit.*

Effective tortuosities, obtained from the diffusion data in Figure 8.9, for all acids studied are shown in Table 8.2 for a diffusion delay time of 300 ms. Additional data showing changes in D/D_0 with reduced

diffusion delay times are provided in Appendix 3, Figures A3.2-A3.4, hence confirming that the data presented here were acquired in the long diffusion delay time limit. The carboxylic acids in both silica supports follow the same trend. A small upwards trend in diffusion coefficients was observed at shorter values of Δ for acids in KIT-6 only. The smallest diffusion delay time used is still significantly larger than that required for the long diffusion time limit while log-attenuation plots of the data remain straight lines. Future work is planned to determine the source of this increase in observed diffusion coefficient.

Table 8.2. Effective tortuosity measured for carboxylic acids confined in SBA-15 (4.9 nm) and KIT-6 (5.2 nm).

Acid	τ_{eff} *(KIT-6)*	τ_{eff} *(SBA-15)*
Propionic acid	1.33 ± 0.06 (4.6%)	1.16 ± 0.04 (3.1%)
Valeric acid	1.41 ± 0.06 (4.0%)	1.18 ± 0.04 (3.1%)
Hexanoic acid	1.49 ± 0.05 (3.4%)	1.22 ± 0.04 (3.3%)
Octanoic acid	1.54 ± 0.05 (3.5%)	1.27 ± 0.03 (2.2%)
Lauric acid	1.72 ± 0.06 (3.2%)	1.43 ± 0.03 (2.4%)
Myristic acid	1.68 ± 0.05 (2.7%)	1.41 ± 0.03 (2.0%)
Palmitic acid	1.56 ± 0.05 (3.2%)	1.39 ± 0.04 (2.5%)

To compare the effective tortuosities, obtained using the homologous series of acids, to the actual tortuosities, obtained using the non-interacting liquids, the change in effective tortuosity with chain length is illustrated in Figure 8.10 (a). For short chain length acids (C_n< 6), the effective tortuosity is lower than the actual tortuosity in both supports. This is consistent with the prior work of D'Agostino *et al.* [181], where disruption to the hydrogen bonding network by the solid affects the diffusion of species within it. Smaller molecular weight acids such as propionic will experience stronger hydrogen bonding in the bulk solution and a subsequent disruption of their networks by the catalytic silica leads to an enhanced diffusion in the porous network.

The effective tortuosity increases with increasing chain length at first, but then, for acids with a chain length of C_{12} and higher, it starts to fall back towards the tortuosity of the silica itself. This result

suggests that, as the alkyl chain increases in size, the effect of the hydrogen-bonding polar acid group decreases. When the size of the acid becomes large enough, the significance of the functionality which defines the strength of the interaction between acid and silica is reduced enough so that the effective tortuosity experienced by the acids eventually tends towards the tortuosity of the system. The geometry of the support is now the determining factor in the diffusional behavior, reducing the significance of the chemistry of the system.

The strength of the interaction between silica and acid can be assessed by comparing the effective tortuosity of the acids to the tortuosity of the system obtained from the non-interacting species. These data are shown in Figure 8.10 (b), and allows the comparison of the behavior of the same acids in the two silica supports studied. The dependence of tortuosity on alkane chain length was independent of pore size. The analogous figures to Figure 8.10 (a) and (b) for KIT-6 with larger pore sizes are provided in Figures 8.11 and 8.12.

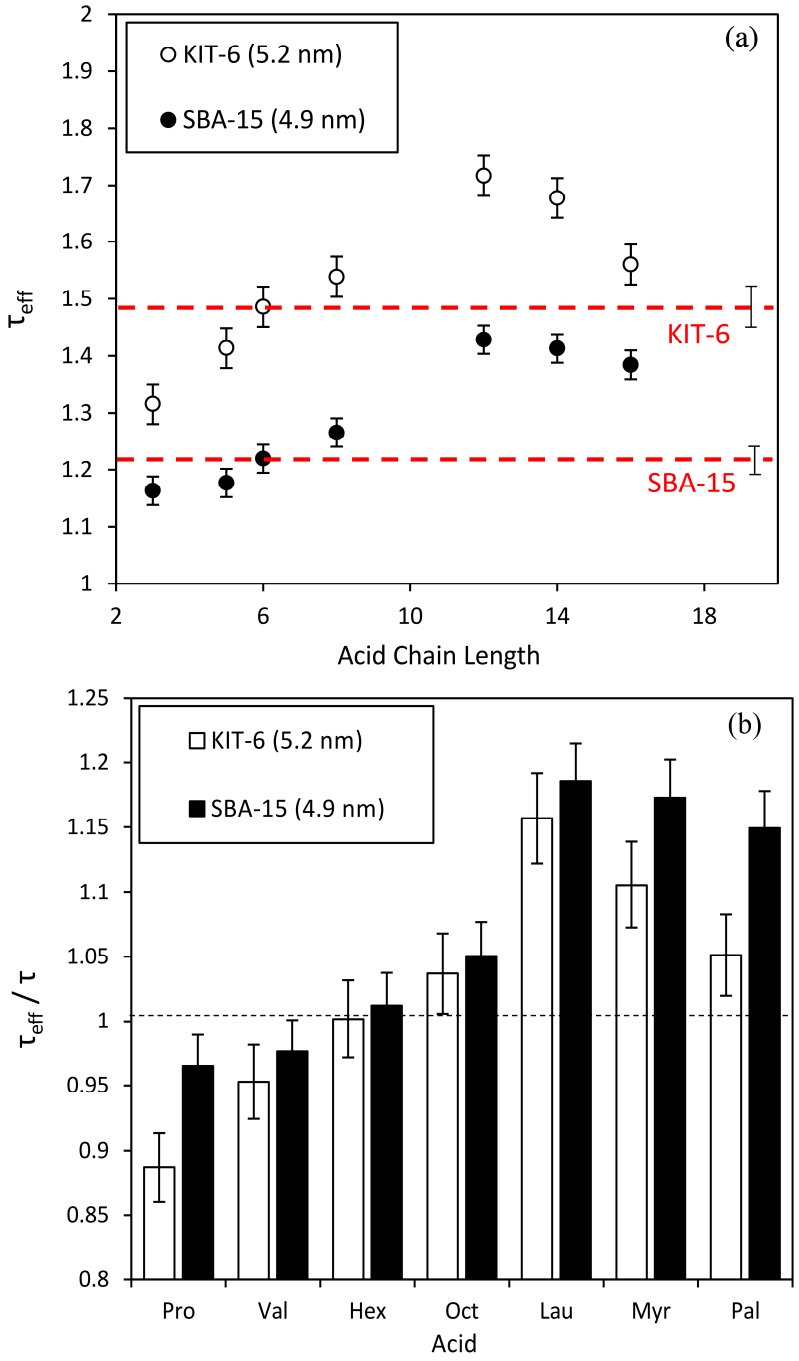

Figure 8.10. (a) *The effective tortuosity for the acids confined within the pores of SBA-15 (4.9 nm) and KIT-6 (5.2 nm) at a diffusion delay time of 300 ms and* ***(b)*** *ratio of the structural tortuosity to the effective tortuosity for the homologous series of carboxylic acids in SBA-15 and KIT-6. The dashed line represents the actual tortuosity of the silica, with error bars to the right.*

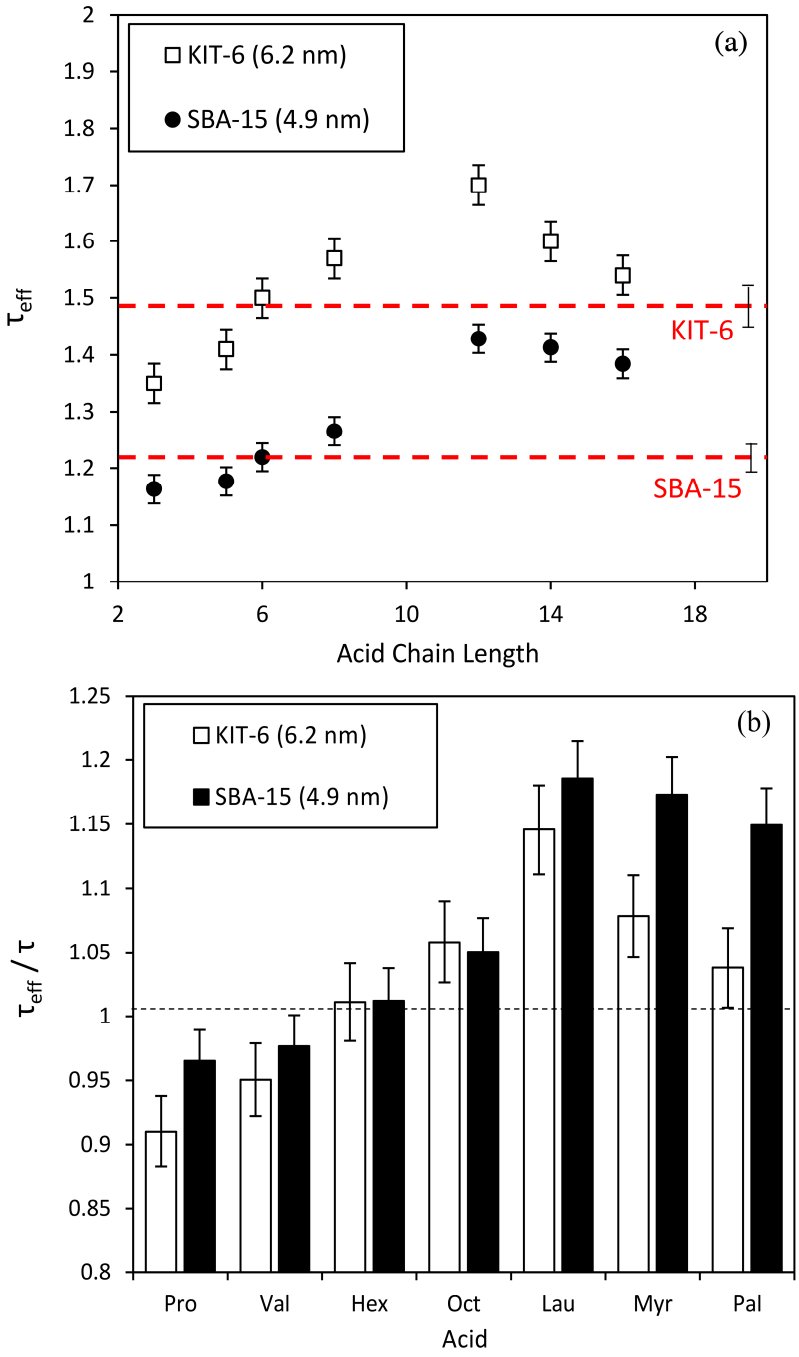

Figure 8.11. (a) *The effective tortuosity for the acids confined within the pores of SBA-15 (4.9 nm) and KIT-6 (6.2 nm) at a diffusion delay time of 300 ms and* ***(b)*** *a comparison to the actual tortuosity defined by the non-interacting liquid. The dashed lines represent the actual tortuosity of the silica, with error bars to the right.*

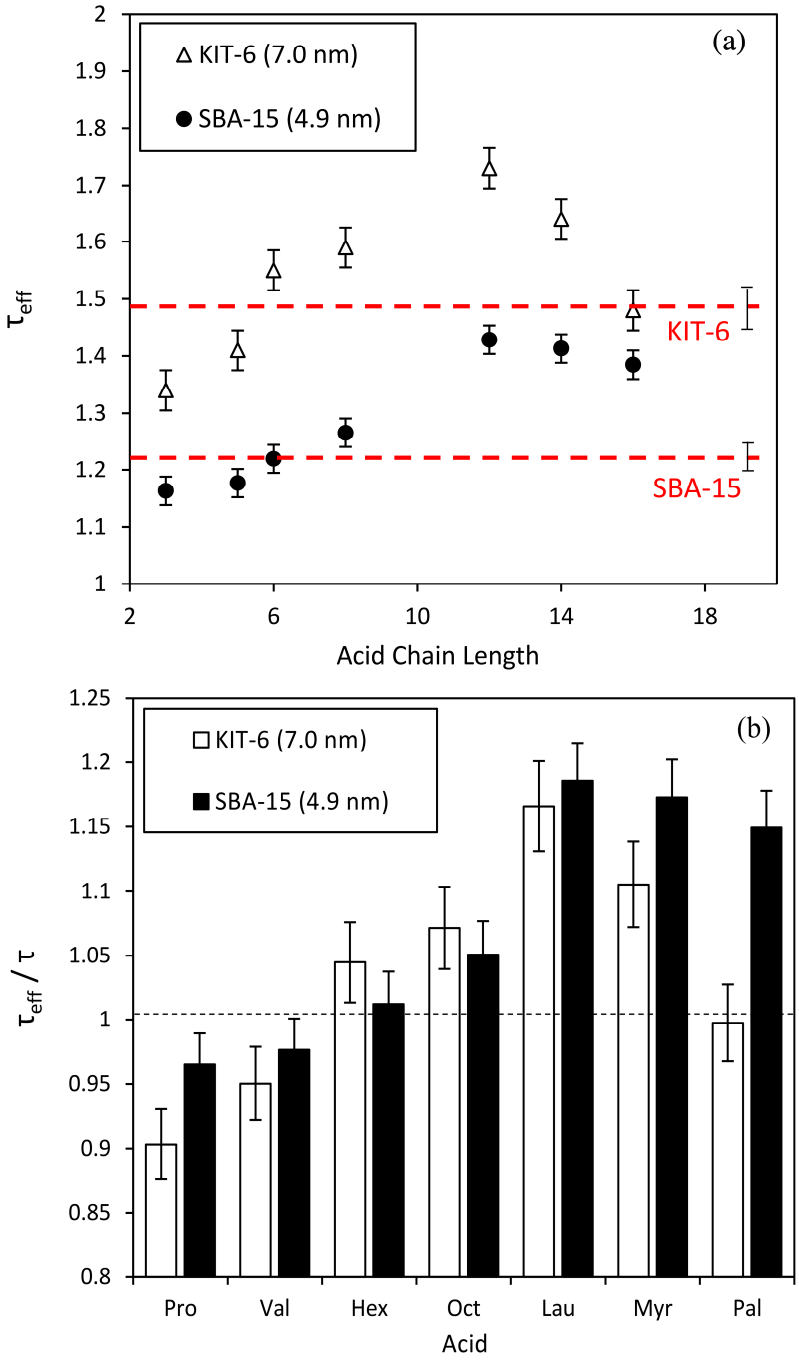

Figure 8.12. (a) *The effective tortuosity for the acids confined within the pores of SBA-15 (4.9 nm) and KIT-6 (7.0 nm) at a diffusion delay time of 300 ms and* ***(b)*** *a comparison to the actual tortuosity defined by the non-interacting liquid. The dashed lines represent the actual tortuosity of the silica, with error bars to the right.*

Figure 8.13 compares the enhancement in TOF for carboxylic acid esterification with methanol (Scheme 8.1) over propylsulfonic acid KIT-6 (5.2 nm) relative to propylsulfonic acid SBA-15 (4.9 nm) with the ratio of the effective tortuosities for equivalent unfunctionalized silicas. The ratio of the

effective tortuosity of the KIT-6 to SBA-15 supports is a direct, quantitative measure of their structural differences and associated paths taken by reactant/product molecules through them. An increase in the tortuosity implies a more convoluted path through the pore network, and hence slower mass transport through a given section of the porous material.

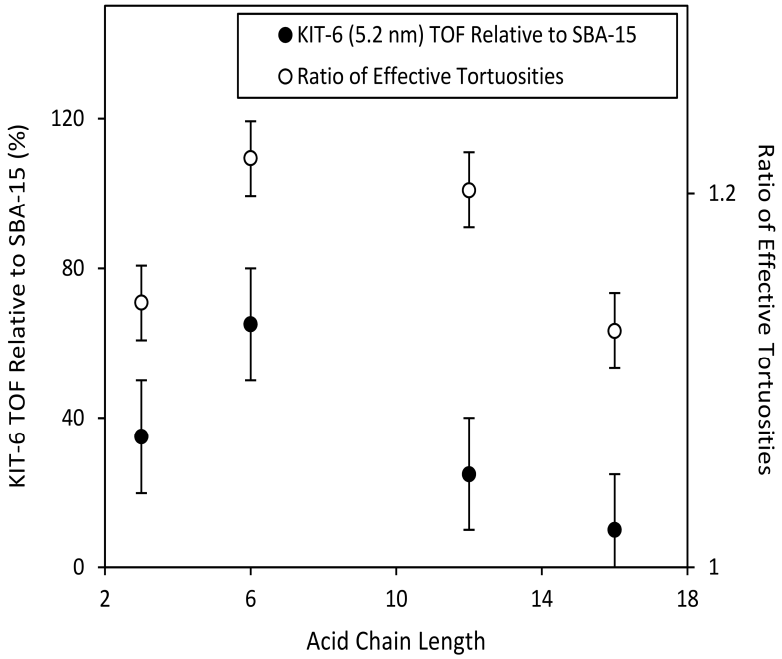

Figure 8.13. *Relative TOF for esterification over propylsulfonic acid functionalized KIT-6 (5.2 nm) versus SBA-15 (4.9 nm) from Pirez et al. [125], and ratio of effective tortuosity of unfunctionalized KIT-6 and SBA-15 from NMR, as a function of carboxylic acid chain length*

Figure 8.13 indicates, counter-intuitively, an apparent weak correlation between the effective tortuosity of the unfunctionalized mesoporous architectures in this work, and observed catalytic performance of their sulfonated analogues, with esterification over the more tortuous sulfonated KIT-6 significantly enhanced relative to sulfonated SBA-15 [125]. However, quantitative analysis of the relative catalytic activity versus effective tortuosity for a range of KIT-6 mesopore sizes reveals that these two properties are in fact uncorrelated, as Figure 8.14 illustrates. This finding is important, since it was previously proposed that the superior catalytic activity of sulfonated KIT-6 versus SBA-15 for esterification arose from either enhanced reactant/product diffusion or greater accessibility to the pore network through its higher density of pore openings [125]. The work here shows that diffusion

coefficients are always faster for acid and ester within SBA-15, and hence the former hypothesis can now be discounted. The higher esterification activity of sulfonated KIT-6 can be attributed to its 3-dimensional nature which affords access to the interior of crystallites via pore entrances uniformly distributed across the entire external surface (in contrast to SBA-15 for which pore entrances preferentially dominate the smaller end faces of wormlike particles). Previous calculations suggest KIT-6 possesses ~6400 pore entrances μm^{-3} versus only ~290 pore entrances μm^{-3} for SBA-15 [125]. Diffusion NMR is thus shown to be a powerful tool for distinguishing whether in-pore diffusion, or diffusion from the bulk media into a pore network, is likely rate-determining for a heterogeneously catalyzed liquid phase reaction. This methodology should be broadly applicable to discriminating the impact of pore architecture on in-pore diffusion of any organic molecule.

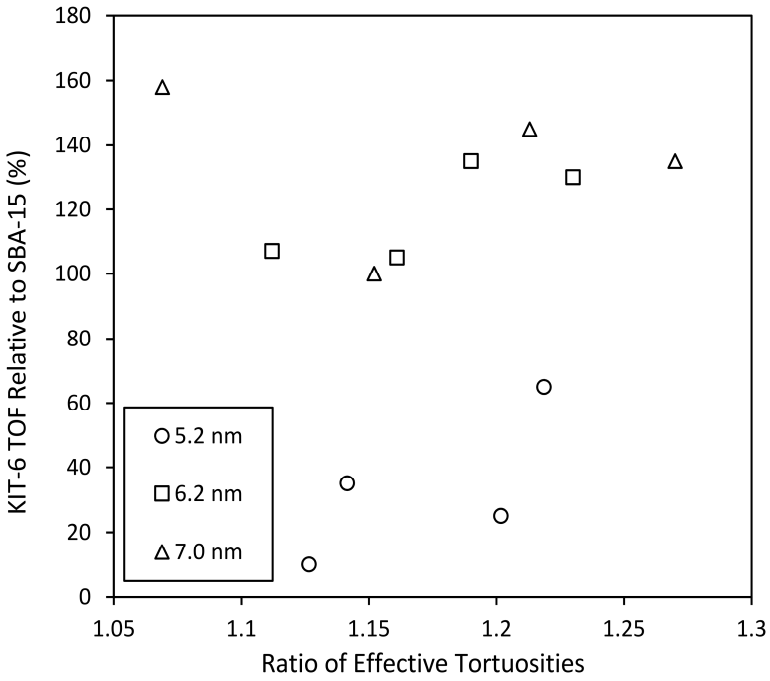

Figure 8.14. *Lack of correlation between the relative TOF for esterification over propylsulfonic acid functionalized KIT-6 (5.2, 6.2 and 7 nm) versus SBA-15 (4.9 nm)[4], and ratio of effective tortuosity of unfunctionalized KIT-6 and SBA-15 from NMR.*

8.4. Conclusions

NMR diffusometry has been used to characterize SBA-15 and KIT-6 silica used as catalytic supports in free fatty acid esterification for biodiesel productions for the first time. The tortuosity of such supports plays a key role in the mass transport of material through the catalyst however, this parameter is not widely measured. Differences in the observed rates of reaction occurring in SBA-15 and KIT-6 silica are typically rationalized in terms of increased diffusion of the species through the materials [125]; here its shown that in-pore molecular diffusion is unlikely to be rate-determining in carboxylic acid esterification over sulfonated analogues, and further insight into the mass transport of reactants and products within a porous support is provided in the hope of aiding future catalyst design.

The diffusion coefficients of a homologous series of carboxylic acids are reduced, relative to diffusion in bulk solution, when measured in the pores of the two types of silica supports studied and this reduction is dependent on both the structure of the host silica, regardless of their average pore diameters, and on the structure of the acid. This work confirms that the tortuosities of the two silica supports are different. As intuitively expected, the 3-dimensional interconnected system of KIT-6 has a higher tortuosity than the isolated porous system of SBA-15. The effective tortuosities of the two silica supports were measured using a homologous series of carboxylic acids, and were found to change with carbon chain length, implying that an extra interaction was affecting the motion of the acids through the porous materials. The stronger networks of hydrogen bonding associated with smaller acids are broken down by the silica and slight enhancements to the diffusion are observed. However, longer chained acids exhibit a reduction in apparent diffusion coefficient, due to the tortuous nature of the silica supports. As the alkyl chains of the acids increase further in size, the observed diffusion behavior starts to tend towards that of an alkane, indicating a dependence of the diffusion coefficient on the silica geometry only.

The work presented in this chapter represents the first application of NMR diffusometry to characterize the pore networks of catalytically relevant silica supports in regard of their tortuosity.

Chapter 8

The diffusion behavior of reactants and products related to carboxylic acid esterification provides chemical insight into the likely rate-determining step in fatty acid methyl ester (biodiesel) production. This work demonstrates that widely available NMR methods can be adopted to non-invasively measure the motion of a confined liquid, and obtain key information about the structure and chemistry of porous architectures. This methodology should find widespread use in the design and optimisation of mesoporous materials with application in liquid phase chemistry, such as heterogeneous catalysis, separation science and adsorption.

CHAPTER 9

Conclusions and Future Work

9.1. Conclusions

The aim of this project was to develop liquid state NMR methods of cryoporometry and diffusometry as routine experiments to characterise highly ordered porous materials with further application of these experimental techniques towards studying interesting and scientifically relevant porous supports. The results contained herein will contribute to the field of using magnetic resonance to further understand the behaviour of liquids in confined environments, such as pores.

It was essential that the performance of the spectrometer was assessed prior to application of these techniques. Temperature stability, convection and gradient strengths were all parameters that could affect the accuracy and precision of NMR measurements. **Chapter 3** describes how initial temperature measurements using a d-methanol probe revealed that the temperature stated on the spectrometer was not the actual temperature of the sample. As such, a temperature calibration was obtained and applied to all variable temperature data collected throughout this piece of work. Similarly, at extreme temperatures it was proved that convection was a serious problem. To regulate and control this issue, convection compensated pulse sequences were found to significantly reduce the extent of convection by reversing the additional contribution of flow to the diffusion measurements, despite the unfavourable loss of overall signal. The gradient strength calibration constant was also adjusted to ensure the experimental diffusion coefficients were similar to that of the literature reported values.

Using a series of highly ordered materials, the cryoporometry methodology was initially established using the well-researched probe liquid, cyclohexane, in **Chapter 4**. A wide pore size range of controlled pore glasses enabled a series of melting point depressions to be obtained with the purpose of converting the melting point data into a pore size distribution. Initial challenges included an unknown

"shoulder peak" which was formed during the period between pore and bulk melting. A hypothesis for this extra contribution to signal intensity was an assumption of an extra environment in which the cyclohexane was present. Reducing the amount of material, both solid and liquid, whilst using a standard 5 mm NMR tube removed this experimental artefact.

With the development of a reliable experimental protocol, the cryoporometric methodology was applied to a water/catalytic silica system. While NMR cryoporometry is an established technique for pore size analysis, no real consensus has been reached on what values to use for the melting point depression constant, k_c, and the non-freezing surface layer, $2sl$. The work contained in **Chapter 5** determines values for both, based on a list of historical data and the experimental results obtained in this work. Using a constant, $k_{c,}$ based on the liquid's physical properties, an estimation of the thickness of the non-freezing surface layer was obtained through a one-parameter fit to the melting data covering several different pore geometries. Using these values, pore size distributions were then obtained for the 2D isolated parallel pores of SBA-15 and the 3D interconnected isolated pores of KIT-6 silica. Good agreement was found with other pore size determination techniques, such as differential scanning calorimetry and nitrogen porosimetry, with NMR holding the advantage over the physisorption technique when analysing the pore size of spherical porous solids such as SBA-16. The parameter determination methodology is not just restricted to water/silica systems. The technique was demonstrated for cyclohexane and controlled pore glass systems to good effect. Using the wealth of available literature for the study of liquids in confined pores, this resource can be used to obtain melting point parameters for many other liquids, other than water and cyclohexane.

When researching into the possible use of liquids in cryoporometry experiments, parameters such as the value of the bulk melting temperature need to be suitable and accessible for study by NMR. Two novel liquids for use in cryoporometry studies, menthol and t-butanol, were introduced in **Chapter 6**. The potential advantages of these two liquids, menthol in particular, include their large melting point depression constants and the subsequent ability to probe larger pore sizes outside of the common

mesoporous range. Despite a similar melting point depression constant to the well-researched cyclohexane, t-butanol holds the advantage of being able to probe porous materials where the hydrophobicity of cyclohexane may prevent it from doing so. Using a set of controlled pore glasses with varying pore diameter, their suitability as cryoporometric probes was confirmed by measuring the melting point depressions with subsequent conversion into pore size distributions using the method detailed in the previous chapter. Not only does **Chapter 6** describe the first demonstration of the use of t-butanol and menthol in NMR cryoporometry experiments, illustrating that pore sizes up to 100 nm, and potentially beyond, can be measured using the latter alcohol, but it also highlights further application into catalytic silica. A significant advantage of t-butanol, over other probe liquids used here, was its ability to observe the bi-model distribution of a mesoporous silica sample, in good agreement with the distribution obtained using the density functional theory approach. Therefore, the ability to be able to tailor the choice of liquid to the chemistry of the solid being studied renders NMR cryoporometry a more than versatile complement to N_2 porosimetry.

The potential for further application of the cryoporometry technique was assessed in **Chapter 7**. Two polymeric systems; a gel-phase disordered polymer hydrogel and a macroreticular ion exchange resin, were analysed. Both systems have similar polymeric environments in which they have been cross-linked to leave an effective microporosity. However, the ion exchange resin has the additional, ordered, mesoporosity created by pore expansion. Based on results from previous chapters; water, t-butanol, menthol and cyclohexane were all chosen as probe liquids to further illustrate the dependence of liquid chemistry on the ability of cryoporometry to accurately analyse the porosity of a support. Pore size distributions for the Amberlyst resin were successfully obtained using both alcohols as probe liquids. It is known that IERs swell to different extents dependent on the type of liquid that they are swollen with, and this behaviour is observed here. It was not possible to obtain cryoporometry data with all liquids trialled. The highly hydrophobic liquid, cyclohexane, did not enter the hydrophilic polymer. Analysis of the HEA-HMAA polymer suggested that cryoporometry may have its limitations when trying to analyse a microporous polymer gel system. The polymer swelled

significantly when subjected to water which suggested, at first instance, that no porosity data, qualitatively or quantitatively, could be obtained. However, by focusing on the region that has proven to be most effective for water (<10 nm), differences between samples with different cross-linking percentages became apparent. A larger proportion of weakly bound water was found in the highest-crosslinked polymer due to the higher density of smaller micropores formed through the increased cross-linking. However, the polymer failed to swell in the other three liquids. **Chapter 7** demonstrated that NMR cryoporometry may be used to study the effective porosity in polymer systems. However, the probe liquid needs to be matched to the properties of the polymer, both in terms of chemistry and also in terms of the size of the pores being studied. Ion exchange resins are key to many areas of science and their proficiency lies in the fact that their properties change in the swollen state. NMR offers the ability to probe their mesoporous structure in their functional, wet, state in order to elucidate structural information from the active resin.

The key theme throughout this piece of work is understanding the behaviour of liquids when confined within scientifically relevant porous solids. Porous silica supports, including SBA-15 and KIT-6, have shown potential for the production of biodiesel, with sulfonic acid functionalization resulting in materials that can perform both the transesterification of triglycerides and the esterification of free fatty acid impurities. The effectiveness of these supports as catalysts appears to depend on the pore geometry, with a faster esterification rate for the acids confined in the 3D interconnected pores of KIT-6 when compared to the acids confined in the 2D parallel pores of SBA-15. The enhancement is attributed to either the diffusion of the species through the pores of the support or the density of pore openings. The technique of NMR diffusometry is explored in **Chapter 8** as the diffusion coefficients of a homologous series of carboxylic acids was obtained both in the bulk and confined within the pores of the silica. Using the relationship between bulk and confined diffusion, the effective tortuosities of both supports were determined with, as intuitively expected, an apparent higher tortuosity for the *Ia3d* porous architecture of KIT-6. The effective tortuosities were also found to change with carbon chain length, implying that an extra parameter of interaction was affecting the

motion of the acids through the silica. This was reaffirmed by comparing the effective tortuosities to the actual tortuosities of the supports, obtained using a series of non-interacting liquids such as straight-chained alkanes. A direct comparison of the ratio of effective tortuosities to the enhancement in turn over frequency for KIT-6 over SBA-15 revealed, in fact, a relatively weak correlation between the two. As such, the higher esterification activity of KIT-6 was attributed to the 3D nature and increased density of pore openings, rather than the diffusion of the acids when inside the pores. The diffusion behaviour of reactants and products related to the esterification rates provides a chemical insight into the rate-determining step in biodiesel production, with the methodology having the potential to be involved in the design of catalytically active mesoporous materials.

9.2. Future Work

Studying the change in fluid behaviour within a solid is an interesting phenomena and one that can branch out into many different fields. The work contained in this thesis contributes to understanding more about how liquids are affected by different confining environments. However, there are many different routes for further application.

9.2.1. New Probe Liquids in NMR Cryoporometry

This work introduces two new probe liquids for cryoporometry experiments, t-butanol and menthol. There is potential for further research into different liquids which have the required properties to make them useful thermoporometric liquids. The main parameter to consider is the bulk melting temperature, T_m. This needs to be accessible, not only for controlling the temperature within the spectrometer but also for sample preparation. The table of potential probe liquids, provided in Petrov and Furo [56], is a useful platform for further experimentation. The introduction of new liquids may provide a route to analysing even larger pore sizes than have previously been reported.

9.2.2. Further Application of NMR Cryoporometry

The main focus of this work has been applying the cryoporometry technique to ordered materials, including mesoporous silica. The pore structures of cylindrical materials, primarily SBA- and MCM-type architectures have been well studied. There is more opportunity for cryoporometric studies into spherical materials, such as FDU-12. FDU-12 has a face-centred cubic geometry with *Fm3m* symmetry (Figure 9.1).

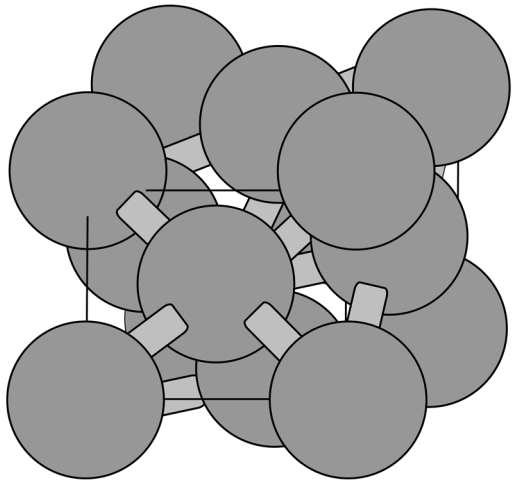

Figure 9.1. *Schematic representation of the spherical porous structure of FDU-12.*

FDU-12 belongs to a vast family of novel porous materials that, due to their structural symmetries, pore diameters and pore entrance sizes, often surpass their cylindrical analogues in areas such as catalysis [190]. As Chapter 5 describes, other pore size determination techniques, such as gas porosimetry, have their limitations when it comes to probing the spherical structures of silica. Therefore NMR cryoporometry would, once again, prove to be a useful complement to other techniques.

Chapter 7 has opened a door of opportunities for analysing the swollen macroreticular structure of ion exchange resins. Amberlyst A26 OH is a strongly basic anion exchange resin. There is a wealth of different exchange resins available for study with NMR cryoporometry, including other SBA-type resins with differing functionality, as well as strongly acidic cationic (SAC), weakly acidic cationic (WAC)

and weakly basic anionic (WBA) resins [166]. NMR has the advantage of being able to study the porous structure of these materials in the active state. Therefore, it would be interesting to evaluate how the different types of resins swell when saturated with a series of different liquids, and how this may impact upon their ion exchange ability.

The development of sophisticated porous systems is continually advancing with the aim of tackling issues that modern society faces, such as the removal of environmentally harmful substances from the atmosphere [191]. Focus has turned to developing new materials that can absorb and remove harmful gases, such as volatile organic compounds (VOCs), from the environment. Hyper-cross-linked polymers (HCPs) are one example of materials that are exhibiting promising gas absorption properties [192]. Their gas absorption abilities stem from their highly cross-linked, porous, structure which can therefore be probed using cryoporometry. Generally, the HCPs comprise mainly of micropores [193]. It would, therefore, be relatively difficult to quantifiably probe the microporous structure with the liquids currently available for use, as proven in Chapter 7. However, HCPs produced *via* the suspension polymerization route often result in the formation of nanoparticles, where the pore size can be tuned, by varying the cross-linking extent, up to 30 nm in diameter [194]. Similarly to IERs, it would be of great advantage to study the porous structures of HCPs when in the swollen state, with the further potential to elucidate information on their gas absorption properties.

One further application of NMR cryoporometry may lie in analysing the phosphate mineral, apatite, with the ultimate aim of providing a better understanding on the physical and biological properties of bone. Apatite, in its hydroxyl form, is not only a major component in bone mineral and tooth enamel, but it can also be templated, in analogy to mesoporous silica. The apatite domains of bone structures exhibit porosity on the nanoscale [195]; observable using NMR cryoporometry. Being able to probe the pore size of this material, together with understanding the diffusion of species through the pores, would be key in aiding the further study of bone pathologies and the development of biomimetic strategies for tissue engineering [196].

9.2.3. Complementary Techniques

Differential scanning calorimetry (DSC) has been used as a complementary technique to NMR throughout this work. Pore size distributions were obtained through the conversion of heat flow data using Equation 2.23. However, the values used in this conversion have only been obtained through the fitting of experimental data, such like the cryoporometry method for the determination of the melting point depression constant, k_c. The integers used in Equation 2.23 are therefore subject to a certain aspect of error. An alternative method would be to use the methodology in Chapter 5, introduced for NMR measurements, and apply it to DSC. The disadvantage of this, however, is the limited database of liquids that have been used in DSC experiments to estimate a pore size. The methodology presented here focuses on using a literature database to obtain a fitting. Unfortunately, for liquids such as t-butanol and menthol, limited, if any at all, data is available for use with DSC.

9.2.4. Continuation of Diffusion Work

Diffusion of species confined within ordered mesoporous silica has been well studied. However, there is a discrepancy between NMR methods and other techniques. Pulsed field gradient measurements suggest that the diffusion of a species, when in the long diffusion delay time limit, is primarily dependent on the tortuosity of the support. Where there is an extra interaction parameter, the tortuosity becomes an effective measurement. Zero-length column methods, for example, suggest that the diffusion is actually dependent on the secondary porosity, found within the silica walls, which is the mitigating factor in controlling the diffusive behaviour of species within the pores [197]. This discrepancy between methods needs to be addressed. One potential research avenue would be to observe the effect, if any, of tortuosity on reaction rate with the same structural material. If all other parameters are kept constant, mainly the number of pore openings, then a change in reaction rate with tortuosity would indicate a definitive relationship between confined diffusion and tortuosity, as suggested by PFG NMR. Alternatively, one can tailor the size of the pores in the secondary porous region and evaluate what effect this has on diffusion measurements. This then probes the question

on what is considered an ideal structure for, in the case of mesoporous silica, optimum catalytic activity.

This thesis has demonstrated the ability of liquid state NMR techniques to be applied to materials with key functions in scientific research. The introduction of new liquids, in particular, has developed and enhanced the cryoporometry technique, with further application to mesopores silica and polymers, elucidating structural information about the materials in their working states. Optimisation of synthetic design routes for porous materials will also be aided by the insights derived here from diffusion NMR. The work demonstrated here opens up a series of avenues for further potential applications of these techniques.

References

(1) Pauli, P. W. Zur Quantenmechanik des Magnetischen Elektrons. *ZS. f. Phys*. **1926**, *37*, 601-623.

(2) Goudsmit, S.; Uhlenbeck, G. E. Over Het Roteerende Electron En de Structuur der Spectra. *Physica*. **1926**, *6*, 273-290.

(3) Heisenberg, W.; Born, M.; Jordan, P. Zur Quantenmechanik. II. Zeitschrift für Physik A Hadrons and Nuclei. *Zeitschrift für Physik*. **1926**, *35*, 557-615.

(4) Schrodinger, E. Quantisierung als Eigenwertproblem. *Ann. Phys.* **1926**, *384*, 361-376.

(5) Rabi, I. I. On the Process of Space Quantization. *Phys. Rev.* **1936**, *49*, 324-328.

(6) Bloch, F.; Hansen, W. W.; Packard, M. Nuclear Induction. *Phys. Rev.* . **1946**, *69*, 127.

(7) Purcell, E. M.; Torrey, H. C.; Pound, R. V. Resonance Absorption by Nuclear Magnetic Moments in a Solid. *Phys. Rev.* . **1946**, *69*, 37-38.

(8) Arnold, J. T.; Dharmatti, S. S.; Packard, M. E. Chemical Effects on Nuclear Induction Signals from Organic Compounds. *J. Chem. Phys.* **1951**, *19*.

(9) Lauterbur, P. C. Image Formation by Induced Local Interactions: Examples Employing Nuclear Magnetic Resonance. *Nature*. **1973**, *242*, 190-191.

(10) Mansfield, P.; Grannell, P. K. NMR Diffraction in Solids. *J. Phys. C. Solid. State.* **1973**, *6*, L422-L426.

(11) Hahn, E. L. Spin Echoes. *Phys. Rev.* **1950**, *80*, 580-594.

(12) Carr, H. Y.; Purcell, E. M. Effects of Diffusion on Free Precession in Nuclear Magnetic Resonance Experiments. *Physical Review*. **1954**, *94*, 630-638.

(13) Torrey, H. C. Bloch Equations with Diffusion Terms. *Phys. Rev.* **1956**, *104*, 563-565.

(14) Hore, P., *Nuclear Magnetic Resonance*; Oxford University Press. 2011.

(15) Keeler, J., *Understanding NMR Spectroscopy*; Wiley. 2010.

(16) Su, B. L.; Sanchez, C.; Yang, X. Y., *Hierarchically Structured Porous Materials: From Nanoscience to Catalysis, Separation, Optics, Energy and Life Science.*; Wiley-VCH. 2012.

(17) Liu, P. S.; Chen, G. F., *Porous Materials*; Elsevier Inc. 2014.

(18) Valiullin, R., *Diffusion NMR of Confined Systems: Fluid Transport in Porous Solids and Heterogeneous Materials* Royal Society of Chemistry. 2016.

(19) Mitchell, J.; Webber, J. B. W.; Strange, J. H. Nuclear Magnetic Resonance Cryoporometry. *Phys. Rep.* **2008**, *461*, 1-36.

(20) Latour, L. L.; Kleinberg, R. L.; Mitra, P. P.; Sotak, C. H. Pore Size Distributions and Tortuosity in Heterogeneous Porous Media. *J. Magn. Reson.* **1994**, *112*, 83-91.

(21) Geib, L. D.; Gubbins, K. E.; Radhakrishnan, R.; Sliwinska-Bartkowiak, M. Phase Separation in Confined Systems. *Rep. Prog. Phys.* **1999**, *62*, 1573-1659.

(22) Budinova, T.; Ekinci, E.; Yardim, F.; Grimm, A.; Bjornbom, E.; Minkova, V.; Goranova, M. Characterization and Application of Activated Carbon Produced by H_3PO_4 and Water Vapor Activation. *Fuel. Process. Technol.* **2006**, *87*, 899-905.

(23) Lastoskie, C.; Gubbins, K. E.; Quirke, N. Pore Size Distribution Analysis of Microporous Carbons. A Density Functional Theory Approach. *J. Phys. Chem.* **1993**, *97*, 4786-4796.

(24) Forland, K., *NMR Studies of Organic Liquids Confined in Mesoporous Materials*, in *Department of Chemistry*. 2005, University of Bergen: Norway.

(25) Kleinberg, R. L.; Kenyon, W. E.; Mitra, P. P. Mechanism of NMR Relaxation of Fluids in Rock. *J. Magn. Reson. Ser. A.* **1994**, *108*, 206-214.

(26) Aksnes, D. W.; Førland, K.; Kimtys, L. ^{1}H and ^{2}H NMR Studies of Cyclohexane Nanocrystals in Controlled Pore Glasses. *J. Mol. Struct.* **2004**, *708*, 23-31.

(27) Valckenborg, R. M. E.; Pel, L.; Kopinga, K. Combined NMR Cryoporometry and Relaxometry. *J. Phys. D. Appl. Phys.* **2002**, *35*, 249-256.

(28) Brownstein, K. R.; Tarr, C. E. Importance of Classical Diffusion in NMR Studies of Water in Biological Cells. *Phys. Rev. A.* **1979**, *19*, 2446-2453.

(29) Muncaci, S.; Boboia, S.; Ardelean, I. The Effect of Diffusion in Internal Gradients on Nuclear Magnetic Resonance Transverse Relaxation Measurements. *J. Chem. Phys.* **2013**, 133-136.

(30) Grebenkov, D. S. NMR Survey of Reflected Brownian Motion. *Rev. Mod. Phys.* **2007**, *79*, 1077-1137.

(31) Chen, Q.; Marble, A. E.; Colpitts, B. G.; Balcom, B. J. The Internal Magnetic Field Distribution, and Single Exponential Magnetic Resonance Free Induction Decay, in Rocks. *J. Magn. Reson.* **2005**, *175*, 300-308.

(32) Mitchell, J.; Chandrasekera, T. C.; Gladden, L. F. Obtaining True Transverse Relaxation Time Distributions in High-Field NMR Measurements of Saturated Porous Media: Removing the Influence of Internal Gradients. *J. Chem. Phys.* **2010**, *132*, 244705.

(33) Mohnke, O.; Yaramanci, U. Pore Size Distributions and Hydraulic Conductivities of Rocks Derived from Magnetic Resonance Sounding Relaxation Data using Multi-Exponential Decay Time Inversion. *J. Appl. Geophys.* **2008**, *66*, 73-81.

(34) Ronczka, M.; Müller-Petke, M. Optimization of CPMG Sequences to Measure NMR Transverse Relaxation Time, T_2 , in Borehole Applications. *Geosci. Instrum. Method. Data. Syst.* **2012**, *1*, 197-208.

(35) Kleinberg, R. L.; Horsfield, M. A. Transverse Relaxation Processes in Porous Sedimentary Rock. *J. Magn. Reson.* **1990**, *88*, 9-19.

(36) Leventis, A.; Verganelakis, D. A.; Halse, M. R.; Webber, J. B.; Strange, J. H. Capillary Imbibition and Pore Characterisation in Cement Pastes. *Transport. Porous. Med.* **2000**, *39*, 143-157.

(37) Hansen, E. W.; Fonnum, G.; Weng, E. Pore Morphology of Porous Polymer Particles Probed by NMR Relaxometry and NMR Cryoporometry. *J. Phys. Chem. B*. **2005**, *109*, 24295-24303.

(38) Gibbs, J. W. The Scientific Papers of J. Willard Gibbs, New Dover Edition. *Thermodynamics*. **1906**, *1*.

(39) Gibbs, J. W., *The Collected Works of J. Willard Gibbs*; Longmans, Green & Co: London. 1928.

(40) Thomson, J. Theoretical Considerations on the Effect of Pressure in Lowering the Freezing Point of Water. *Trans. Roy. Soc.* **1849**, *5*, 575-580.

(41) Thomson, J. On Crystalisation and Liquefaction, as Influenced by Stresses Tending to Change the Form in the Crystals. *Proc. Roy. Soc.* **1862**, *11*, 473-481.

(42) Thomson, J. J., *Applications of Dynamics to Physics and Chemistry*; Macmillan & Co: London. 1888.

(43) Defay, R.; Prigogine, I.; Bellemans, A.; Everatt, D., *Surface Tension & Adsorption*; Longmans, Green & Co: London. 1966.

(44) Thomson, W. On the Equilibrium of Vapour at a Curved Surface of Liquid. *Phil. Mag. Series.* **1871**, *42*, 452-488.

(45) Gregg, S.; Sing, K., *Adsorption, Surface Area and Porosity*; Academic Press: London. 1967.

(46) Strange, J. H.; Rahman, M.; Smith, E. G. Characterization of Porous Solids by NMR. *Phys. Rev. Lett.* **1993**, *71*, 3589-3591.

(47) Strange, J. H.; Mitchell, J.; Webber, J. B. Pore Surface Exploration by NMR. *Magn. Reson. Imaging.* **2003**, *21*, 221-226.

(48) Petrov, O.; Furo, I. Curvature-Dependent Metastability of the Solid Phase and the Freezing-Melting Hysteresis in Pores. *Phys. Rev. E.* **2006**, *73*, 011608.

(49) Strange, J.; Mitchell, J., *Characterising Porous Media*; Springer: Berlin. 2006.

(50) Hitchcock, I.; Holt, E. M.; Lowe, J. P.; Rigby, S. P. Studies of Freezing-Melting Hysteresis in Cryoporometry Scanning Loop Experiments using NMR Diffusometry and Relaxometry. *Chem. Eng. Sci*. **2011**, *66*, 582-592.

(51) Khokhlov, A.; Valiullin, R.; Karger, J.; Steinbach, F.; Feldhoff, A. Freezing and Melting Transitions of Liquids in Mesopores with Ink-Bottle Geometry. *New. J. Phys.* **2007**, *9*, 272-272.

(52) Webber, J. B. W., *Characterising Porous Media*. 2000, Univerisity of Kent.

(53) Petrov, O. V.; Furo, I. NMR Cryoporometry: Principles, Applications and Potential. *Prog. Nucl. Mag. Res. Sp.* **2009**, *54*, 97-122.

(54) Strange, J.; Mitchell, J., *Characterising Porous Media*; Springer: Berlin. 2006.

(55) Mitchell, J.; Webber, J. B. W.; Strange, J. H. Nuclear Magnetic Resonance Cryoporometry. *Phys. Rep.* **2008**, *461*, 1-36.

(56) Petrov, O. V.; Furo, I. NMR Cryoporometry: Principles, Applications and Potential. *Prog. Nucl. Mag. Res. Sp.* **2009**, *54*, 97-122.

(57) Meiboom, S.; Gill, D. Modified Spin-Echo Method for Measuring Nuclear Relaxation Times. *Rev. Sci. Instrum.* **1958**, *29*, 688.

(58) Abragam, A., *The Principles of Nuclear Magnetism*; Clarendon Press: Oxford. 1961.

(59) Strange, J. H.; Rahman, M.; Smith, E. G. Characterization of Porous Solids by NMR. *Phys. Rev. Lett*. **1993**, *71*, 3589-3591.

(60) Jeon, J.-D.; Kim, S. J.; Kwak, S.-Y. ^{1}H Nuclear Magnetic Resonance (NMR) Cryoporometry as a Tool to Determine the Pore Size Distribution of Ultrafiltration Membranes. *J. Mem. Sci*. **2008**, *309*, 233-238.
(61) Landry, M. R. Thermoporometry by Differential Scanning Calorimetry: Experimental Considerations and Applications. *Thermochim. Acta.* **2005**, *433*, 27-50.
(62) Majda, D.; Makowski, W.; Manko, M. Pore Size Distribution of Micelle-Templated Silicas Studied by Thermoporosimetry using Water and n-Heptane. *J. Therm. Anal. Calorim.* **2012**, *109*, 663-669.
(63) Parlett, C. M. A., *Tuning Palladium Selective Oxidation Catalysts via Mesoporous Supports*, in *School of Chemistry*. 2012, Cardiff University.
(64) Thommes, M. Physical Adsorption Characterization of Nanoporous Materials. *Chem. Ing. Tech.* **2010**, *82*, 1059-1073.
(65) Kruk, M.; Jaroniec, M.; Sayari, A. Application of Large Pore MCM-41 Molecular Sieves to Improve Pore Size Analysis using Nitrogen Porosimetry Measurements. *Langmuir*. **1997**, *13*, 6267-6273.
(66) Broekhoff, J. C. P.; De Boer, J. H. Studies on Pore Systems in Catalysis. XIII. Pore Size Distributions from the Desoprtion Branch of a Nitrogen Sorption Isotherm in the Case of Cylindrical Pores. *J. Catal.* **1968**, *10*, 377-390.
(67) Oliver, J. P.; Conklin, W. B. *Characterization of Porous Solids from Physical Adsorption Data using Theory of Constrained States*. in *7th International Conference on Surface and Colloid Science*. 1991. Compeigne, France.
(68) Einstein, A., *Investigations on the Theory of Brownian Motion*; Dover Publications. 1956.
(69) Evans, R.; Hernandez-Cid, A.; Dal Poggetto, G.; Vesty, A.; Haiber, S.; Morris, G. A.; Nilsson, M. Matrix-Assisted Diffusion-Ordered NMR Spectroscopy with an Invisible Matrix: A Vanishing Surfactant. *RSC Adv.* **2017**, *7*, 449-452.
(70) Evans, R.; Deng, Z.; Rogerson, A. K.; McLachlan, A. S.; Richards, J. J.; Nilsson, M.; Morris, G. A. Quantitative Interpretation of Diffusion-Ordered NMR Spectra: Can we Rationalize Small Molecule Diffusion Coefficients? *Angew. Chem. Int. Edit.* **2013**, *52*, 3199-3202.
(71) Johnson Jr, C. S. Diffusion Ordered Nuclear Magnetic Resonance Spectroscopy: Principles and Applications. *Prog. Nucl. Magn. Reson. Spectrosc.* **1999**, *34*, 203-256.
(72) Stejskal, E. O.; Tanner, J. E. Spin Diffusion Measurements: Spin Echoes in the Presence of a Time Dependent Field Gradient. *J. Chem. Phys.* **1964**, *42*, 288-292.
(73) Claridge, T. D. W., *High-Resolution NMR Techniques in Organic Techniques*; Elsevier. 2009.
(74) Tanner, J. E. Use of the Stimulated Echo in NMR Diffusion Studies. *J. Chem. Phys.* **1970**, *52*, 2523-2526.
(75) Wider, B.; Dotsch, V.; Wuthrich, K. Self-Compensating Pulsed Magnetic Field Gradients for Short Recovery Times. *J. Magn. Reson.* **1994**, *108*, 255-258.
(76) Wu, D.; Chen, A.; Johnson Jr, C. S. An Improved Diffusion-Ordered Spectroscopy Experiment Incorportaing Bipolar Gradient Pulses. *J. Magn. Reson.* **1995**, *115*, 260-264.
(77) Morris, G. A.; Pelta, M. D.; Stchedroff, M. J.; Hammond, S. J. A One-Shot Sequence for High-Resolution Diffusion-Ordered Spectroscopy. *Magn. Reson. Chem.* **2002**, *40*, S147-S152.
(78) Veith, S. R.; Hughes, E.; Vuataz, G.; Pratsinis, S. E. Restricted Diffusion in Silica Particles Measured by Pulsed Field Gradient NMR. *J. Colloid. Interface. Sci*. **2004**, *274*, 216-28.
(79) Valiullin, R.; Skirda, V. Time Dependent Self-Diffusion Coefficient of Molecules in Porous Media. *J. Chem. Phys.* **2001**, *114*, 452-458.
(80) Stallmach, F.; Karger, J. The Potentials of Pulsed Field Gradient NMR for Investigation of Porous Media. *Adsorption*. **1999**, *5*, 117-133.
(81) Sen, P. N. Time-Dependent Diffusion Coefficient as a Probe of Geometry. *Concept. Magn. Res. A*. **2004**, *23A*, 1-21.
(82) Price, W. S.; Stait-Gardner, T.; Willis, S. A.; Yadav, N. N.; Zheng, G. NMR Diffusion Measurements in Complex Systems. *The Open Access Jounal for the Basic Principles of Diffusion Theory, Experiment and Application*. **2009**, *15*, 1-22.
(83) Loening, N. M.; Keeler, J. Temperature Accuracy and Temperature Gradients in Solution State NMR Spectrometers. *J. Magn. Reson.* **2002**, *159*, 55-61.
(84) Swan, I.; Reid, M.; Howe, P. W.; Connell, M. A.; Nilsson, M.; Moore, M. A.; Morris, G. A. Sample Convection in Liquid-State NMR: Why it is Always With Us, and What We Can Do About it. *J. Magn. Reson.* **2015**, *252*, 120-129.
(85) Lappa, M., *Thermal Convection: Patterns, Evolution and Stability*; John Wiley & Sons. 2009.

(86) Hedin, N.; Furo, I. Temperature Imaging by ^{1}H NMR and Supression of Convection in NMR Probes. *J. Magn. Reson.* **1998**, *131*, 126-130.
(87) Chung, K. C.; Yu, H. Y.; Ahn, S. D. Convection Effects on PGSE-NMR Self-Diffusion Measurements at Low Temperature: Investigation into Sources of Induced Convective Flows. *Bull. Korean Chem. Soc.* **2011**, *32*, 1970-1974.
(88) Goux, J. W.; Verkruyse, L. A.; Saltert, S. J. The Impact of Rayleigh-Benard Convection on NMR Pulsed Field Gradient Diffusion Measurements. *J. Magn. Reson.* **1969**, *88*, 609-614.
(89) Sinnaeve, D. The Stejskal-Tanner Equation Generalized for any Gradient Shape-An Overview of Most Pulse Sequences Measuring Free Diffusion. *Concept. Magnetic. Res.* **2012**, *40a*, 39-65.
(90) Holz, M.; Heil, S. R.; Sacco, A. Temperature-Dependent Self-Diffusion Coefficients of Water and Six Selected Molecular Liquids for Calibration in Accurate ^{1}H NMR PFG Measurements. *Phys. Chem. Chem. Phys.* **2000**, *2*, 4740-4742.
(91) Longsworth, L. G. The Mutual Diffusion of Light and Heavy Water. *J. Chem. Phys.* **1960**, *64*, 1914-1917.
(92) Jerschow, A.; Muller, N. Suppression of Convection Artifacts in Stimulated-Echo Diffusion Experiments. Double-Stimulated-Echo Experiments. *J. Magn. Reson.* **1997**, *125*, 372-375.
(93) Barbosa, T. M.; Rittner, R.; Tormena, C. F.; Morris, G. A.; Nilsson, M. Convection in Liquid-State NMR: Expect the Unexpected. *RSC Adv.* **2016**, *6*, 95173-95176.
(94) Findeisen, M.; Brand, T.; Berger, S. A ^{1}H-NMR Thermometer Suitable for Cryoprobes. *Magn. Reson. Chem.* **2007**, *45*, 175-178.
(95) La Mar, G. N.; Horrocks, W. D.; Holm, R. H., *NMR of Paramagnetic Molecules: Principles and Applications*; Academic Press, Inc.: New York. 1973.
(96) Petrov, O.; Furo, I. A Study of Freezing-Melting Hysteresis of Water in Different Porous Materials. Part I: Porous Silica Glasses. *Micropor. Mesopor. Mat.* **2011**, *138*, 221-227.
(97) Aksnes, D. W.; Kimtys, L. ^{1}H NMR Studies of Cyclohexane Confined in Mesoporous Solids. Melting Point Depression and Pore Size Distribution. *Appl. Magn. Reson.* **2002**, *23*, 51-62.
(98) Vargas-Florencia, D.; Petrov, O. V.; Furo, I. NMR Cryoporometry with Octamethylcyclotetrasiloxane as a Probe Liquid. Accessing Large Pores. *J. Colloid. Interf. Sci.* **2007**, *305*, 280-285.
(99) Petrov, O. V.; Furo, I. A Joint Use of Melting and Freezing Data in NMR Cryoporometry. *Micropor. Mesopor. Mat.* **2010**, *136*, 83-91.
(100) Petrov, O. V.; Furo, I. Curvature-Dependent Metastability of the Solid Phase and the Freezing-Melting Hysteresis in Pores. *Phys. Rev. E.* **2006**, *73*, 011608-1-011608-7.
(101) Mazurin, O. V., *Phase Separation in Glass*; Elsevier. 1984.
(102) Vogel, W., *Glass Chemistry*; Springer-Verlag Berlin and Heidelberg GmbH & Co. 1994.
(103) Jackson, C. L.; Mckenna, G. B. The Melting Behavior of Organic Materials Confined in Porous Solids. *J. Chem. Phys.* **1990**, *93*, 9002-9011.
(104) Carr, H. Y.; Purcell, E. M. Effects of Diffusion on Free Precession in Nuclear Magnetic Resonance Experiments. *Phys. Rev.* **1954**, *94*, 630-638.
(105) Meiboom, S.; Gill, D. Modified Spin-Echo Method for Measuring Nuclear Relaxation Times. *Rev. Sci. Instrum.* **1958**, *29*, 688.
(106) Gibbs, J. W., *The Scientific Papers of J. Willard Gibbs, New Dover Edition*; Longmans, Green & Co, . 1906.
(107) Dore, J.; Webber, B.; Strange, J.; Farman, H.; Descamps, M.; Carpentier, L. Phase Transformations for Cyclohexane in Mesoporous Silicas. *Physica. A.* **2004**, *333*, 10-16.
(108) Hansen, E. W.; Schmidt, R.; Stöcker, M. Pore Structure Characterization of Porous Silica by ^{1}H NMR using Water, Benzene, and Cyclohexane as Probe Molecules. *J. Phys. Chem.* **1996**, *100*, 11396-11401.
(109) Indekeu, J. O. Introduction to Wetting Phenomena. *Acta. Phys. Pol. B.* **1995**, *26*, 1065-1100.
(110) Pearson, R. T.; Derbyshire, W. NMR Studies of Water Absorbed on a Number of Silica Surfaces. . *J. Colloid Interf. Sci.* **1974**, *46*, 232-248.
(111) Overloop, K.; Van Gerven, L. Freezing Phenomena in Adsorbed Water as Studied by NMR. *J. Magn. Reson.* **1993**, *101*, 179-187.
(112) Findenegg, G. H.; Jahnert, S.; Akcakayiran, D.; Schreiber, A. Freezing and Melting of Water Confined in Silica Nanopores. *Chem. Phys. Chem.* **2008**, *9*, 2651-2659.

(113) Jahnert, S.; Vaca Chavez, F.; Schaumann, G. E.; Schreiber, A.; Schonhoff, M.; Findenegg, G. H. Melting and Freezing of Water in Cylindrical Silica Nanopores. *Phys. Chem. Chem. Phys.* **2008**, *10*, 6039-6051.

(114) Schreiber, A.; Ketelsen, I.; Findenegg, G. H. Melting and Freezing of Water in Ordered Mesoporous Silica Materials. *Phys. Chem. Chem. Phys.* **2001**, *3*, 1185-1195.

(115) Petrov, O.; Furo, I. A Study of Freezing-Melting Hysteresis of Water in Different Porous Materials. Part II: Surfactant-Templated Silicas. *Phys. Chem. Chem. Phys.* **2011**, *13*, 16358-16365.

(116) Schmidt, R.; Hansen, E. W.; Stocker, M.; Akporiaye, D.; Ellestad, O. H. Pore Size Determination of MCM-41 Mesoporous Materials by Means of ^{1}H NMR Spectroscopy, N_2 Adsorption and HREM. A Preliminary Study. *J. Am. Chem. Soc.* **1995**, *117*, 4049-4056.

(117) Kondrashova, D.; Valiullin, R. Improving Structural Analysis of Disordered Mesoporous Materials using NMR Cryoporometry. *Micropor. Mesopor. Mat.* **2013**, *178*, 15-19.

(118) Faivre, C.; Bellet, D.; Dolino, G. Phase Transitions of Fluids Confined in Porous Silicon: A Differential Calorimetry Investigation. *Eur. Phys. J. B.* **1999**, *7*, 19-36.

(119) Riikonen, J.; Salonen, J.; Lehto, V. P. Utilising Thermoporometry to Obtain New Insights into Nanostructured Materials. *J. Therm. Anal. Calorim.* **2010**, *105*, 811-821.

(120) Barret, E. P.; Joyner, L. G.; Halenda, P. P. The Determination of Pore Volume and Area Distributionsin Porous Substances. Computations from Nitrogen Isotherms. *J. Am. Chem. Soc.* **1951**, *73*, 373-380.

(121) Huirache-Acuna, R.; Nava, R.; Peza-Ledesma, C. L.; Lara-Romero, J.; Alonso-Nunez, G.; Pawelec, B.; Rivera-Munoz, E. M. SBA-15 Mesoporous Silica as Catalytic Support for Hydrodesulfurization Catalysts-Review. *Materials*. **2013**, *6*, 4139-4167.

(122) Mellaerts, R.; Aerts, C. A.; Van Humbeeck, J.; Augustijns, P.; Van den Mooter, G.; Martens, J. A. Enhanced Release of Itraconazole from Ordered Mesoporous SBA-15 Silica Materials. *ChemComm.* **2007**, 1375-1377.

(123) Guillet-Nicolas, R.; Ahmad, R.; Cychosz, K. A.; Kleitz, F.; Thommes, M. Insights Into the Pore Structure of KIT-6 and SBA-15 Ordered Mesoporous Silica - Recent Advances by Combining Physical Adsorption with Mercury Porosimetry. *New J. Chem.* **2016**, *40*, 4351-4360.

(124) Webber, J. B. W.; Anderson, R.; Strange, J. H.; Tohidi, B. Clathrate Formation and Dissociation in Vapour/Water/Ice/Hydrate Systems in SBA-15, Sol-Gel and CPG Porous Media, as Probed by NMR Relaxation, Novel Protocol NMR Cryoporometry, Neutron Scattering and Ab-Initio Quantum Mechanical Dynamics Simulation. *J. Magn. Reson. Imaging.* . **2007**, *25*, 533-536.

(125) Pirez, C.; Caderon, J. M.; Dacquin, J. P.; Lee, A. F.; Wilson, K. Tunable KIT-6 Mesoporous Sulfonic Acid Catalysts for Fatty Acid Esterification. *ACS. Catal.* **2012**, *2*, 1607-1614.

(126) Zhao, D.; Feng, J.; Huo, Q.; Melsoh, N.; Fredrickson, G. H.; Chmelka, B. F.; Stucky, G. D. Triblock Copolymer Synthesis of Mesoporous Silica with Periodic 50 to 300 Angstrom Pores. *Science*. **1998**, *279*, 548-552.

(127) Kleitz, F.; Choi, S. H.; Ryoo, R. Cubic Ia3d Large Mesoporous Silica: Synthesis and Replication to Platinum Nanowires, Carbon Nanorods and Carbon Nanotubes. *ChemComm*. **2003**, 2136.

(128) Rault, J.; Neffati, R.; Judeinstein, P. Melting of Ice in Porous Glass: Why Water and Solvents Confined in Small Pores do not Crystallize? *Eur. Phys. J. B.* **2003**, *36*, 627-637.

(129) Kimtys, L.; Aksnes, D. W. Analysis of Pore Size Distribution by ^{2}H NMR. *Analyst*. **2007**, *132*, 148-152.

(130) Amanuel, S.; Bauer, H.; Bonventre, P.; Lasher, D. Nonfreezing Interfacial Layers of Cyclohexane in Nanoporous Silica. *J. Phys. Chem. C.* **2009**, *113*, 18983-18986.

(131) Zhang, Q.; Dong, Y.; Liu, S.; Elsworth, D.; Zhao, Y. Shale Pore Characterization using NMR Cryoporometry with Octamethylcyclotetrasiloxane as the Probe Liquid. *Energy. Fuels.* **2017**, *31*, 6951-6959.

(132) Riikonen, J.; Salonen, J.; Kemell, M.; Kumar, N.; Murzin, D. Y.; Ritala, M.; Lehto, V. P. A Novel Method of Quantifying the u-Shaped Pores in SBA-15. *J. Phys. Chem. C.* **2009**, *113*, 20349-2034.

(133) Thommes, M.; Cychosz, K. A. Physical Adsorption Characterization of Nanoporous Materials: Progress and Challenges. *Adsorption*. **2014**, *20*, 233-250.

(134) Thommes, M.; Smarsly, B.; Groenewolt, M.; Ravikovitch, P. I.; Neimark, V. Adsorption Hysteresis of Nitrogen and Argon in Pore Networks and Characterization of Novel Micro- and Mesoporous Silica. *Langmuir*. **2006**, *22*, 756-764.

(135) Christenson, H. K. Confinement Effects on Freezing and Melting. *J. Phys. Condens. Matter.* **2001**, *13*, R95-R133.

(136) Qiao, Y.; Christenson, H. K. Direct Observation of Capillary Condensation of a Solid. *Phys. Rev. Lett.* **2001**, *86*, 3807-3810.
(137) Domalski, E. S.; Hearing, E. D. Heat Capacities and Entropies of Organic Compounds in the Condensed Phase. Volume III. *J. Phys. Chem. Ref. Data.* . **1997**, *25*, 1501.
(138) Chickos, J. S.; Braton, C. M.; Hesse, D. G. Estimating Entropies and Enthalpies of Fusion of Organic Compounds. *J. Org. Chem.* **1991**, *56*, 927-938.
(139) Aguilar, J. A.; Nilsson, M.; Bodenhausen, G.; Morris, G. A. Spin Echo NMR Spectra Without J-Modulation. *ChemComm*. **2012**, *48*, 811-813.
(140) Provencher, S. W. CONTIN: A General Purpose Constrained Regularization Program for Inverting Noisy Linear Algebraic and Integral Equations. *Comput. Phys. Commun.* . **1982**, *27*, 229-242.
(141) Serna-Guerrero, R.; Sayari, A. Applications of Pore Expanded Mesoporous Silica. 7. Adsorption of Volatile Organic Compounds. *Environ. Sci. Technol.* **2007**, *41*, 4761-4766.
(142) Rios, N. S.; Pinheiro, M. P.; Lima, M. L. B.; Freire, D. M. G.; da Silva, I. J.; Rodríguez-Castellón, E.; de Sant'Ana, H. B.; Macedo, A. C.; Gonçalves, L. R. B. Pore-Expanded SBA-15 for the Immobilization of a Recombinant Candida Antarctica Lipase B: Application in Esterification and Hydrolysis as Model Reactions. *Chem. Eng. Res. Des.* **2018**, *129*, 12-24.
(143) Vilarrasa-García, E.; Cecilia, J.; Moya, E.; Cavalcante, C.; Azevedo, D.; Rodríguez-Castellón, E. "Low Cost" Pore Expanded SBA-15 Functionalized with Amine Groups Applied to CO2 Adsorption. *Materials*. **2015**, *8*, 2495-2513.
(144) Rottreau, T. J.; Parlett, C. M. A.; Lee, A. F.; Evans, R. NMR Cryoporometric Measurements of Porous Silica: A Method for the Determination of Melting Point Depression Parameters of Probe Liquids. *Micropor. Mesopor. Mat.* **2018**, *264*, 265-271.
(145) Bettotti, P., *Submicron Porous Materials*; Springer. 2017.
(146) Gopinathan, N.; Yang, B.; Lowe, J. P.; Edler, K. J.; Rigby, S. P. NMR Cryoporometry Characterisation Studies of the Relation Between Drug Release Profile and Pore Structural Evolution of Polymeric Nanoparticles. *Int. J. Pharm.* **2014**, *469*, 146-158.
(147) Petrov, O.; Furo, I.; Schuleit, M.; Domanig, R.; Plunkett, M.; Daicic, J. Pore Size Distributions of Biodegradable Polymer Microparticles in Aqueous Environments Measured by NMR Cryoporometry. *Int. J. Pharm.* **2006**, *309*, 157-162.
(148) Oropeza, M. V. C.; Souza, E. F.; Giudici, R. Study of the Porosity of the Microgel of pAA and Co-Polymer Microgel of p(AA-co-NIPAM) Through the Thermoporometry Technique. *Macromol. Symp.* **2016**, *367*, 24-29.
(149) Iza, M.; Woerly, S.; Danumah, C.; LKaliaguine, S.; Bousmina, M. Determination of Pore Size Distribution for Mesoporous Materials and Polymeric Gels by Means of DSC Measurements: Therm. *Polym*. **2000**, *41*, 5885-5893.
(150) Weber, J.; Bergström, L. Impact of Cross-Linking Density and Glassy Chain Dynamics on Pore Stability in Mesoporous Poly(styrene). *Macromolecules*. **2009**, *42*, 8234-8240.
(151) Okay, O. Macroporous Copolymer Networks. *Prog. Polym. Sci.* **2000**, *25*, 711-779.
(152) Buchmeiser, M. R. Polymeric Monolithic Materials: Syntheses, Properties, Functionalization and Applications. *Polymer*. **2007**, *48*, 2187-2198.
(153) Pedley, D. G.; Skelly, P. J.; Tighe, B. J. Hydrogels in Biomedical Applications. *Brit. Polym. J.* . **1980**, *12*.
(154) Hoffman, A. S., *Hydrogels - A Broad Class of Biomaterials*; Springer US: New York. 1975.
(155) Wang, K.; Burban, J.; Cussler, E., *Hydrogels as Separation Agents*; Springer Berlin Heidelberg. 1993.
(156) Wichterle, O.; Lim, D. Hydrophilic Gels for Biologic Use. *Nature*. **1960**, *185*, 117-118.
(157) Chen, J.; Blevins, W. E.; Park, H.; Park, K. Gastric Retention Properties of Superporous Hydrogel Composites. *J. Control. Release.* **2000**, *64*, 39-51.
(158) Schacht, E. H. Polymer Chemistry and Hydrogel Systems. *J. Phys. Conf. Ser.* **2004**, *3*, 22-28.
(159) Nicolson, P. C.; Vogt, J. Soft Contact Lens Polymers: An Evolution. *Biomaterials*. **2001**, *22*, 3273-3283.
(160) Lee, K. Y.; Mooney, D. J. Hydrogels for Tissue Engineering. *Chem. Rev.* **2001**, *101*, 1869-1879.
(161) Drury, J. L.; Mooney, D. J. Hydrogels for Tissue Engineering: Scaffold Design Variables and Applications. *Biomaterials*. **2003**, *24*, 4337-4351.
(162) Hoare, T. R.; Kohane, D. S. Hydrogels in Drug Delivery: Progress and Challenges. *Polymer*. **2008**, *49*, 1993-2007.

(163) Golloch, A., *Handbook of Rare Earth Elements: Analytics*; Walter de Gruyter GmbH & Co KG. 2017.
(164) Granollers, M.; Izquierdo, J. F.; Cunill, F. Effect of Macroreticular Acidic Ion-Exchange Resins on 2-Methyl-1-Butene and 2-Methyl-2-Butene Mixture Oligomerization. *Appl. Catal., A.* **2012**, *435-436*, 163-171.
(165) *Fundamentals of Ion Exchange, Based on a Paper by Wheaton, R. M. and Lefevre, L. J.*; Dow Chemical U.S.A. 2000.
(166) Dardel, F. *Ion Exchange Resin Types*. 2017; Available from: http://dardel.info/IX/resin_types.html.
(167) Lee, A. G.; Arena, C. P.; Beebe, D. J.; Palecek, S. P. Development of Macroporous Poly(ethylene glycol) Hydrogel Arrays within Microfluidic Channels. *Biomacromolecules*. **2010**, *11*, 3316-3324.
(168) Abrams, I. M.; Millar, J. R. A History of the Origin and Development of Macroporous Ion Exchange Resins. *React. Funct. Polym.* **1997**, *35*, 7-22.
(169) Crittenden, J. C.; Trussell, R. R.; Hand, D. W.; Howe, K. J.; Tchobanoglous, G., *Ion Exchange*; John Wiley & Sons, Inc. 2012.
(170) Corain, B.; Zecca, M.; Jerabek, K. Catalysis and Polymer Networks - The Role of Morphology and Molecular Accessibility. *J. Mol. Catal.* **2001**, *177*, 3-20.
(171) Weber, J.; Bergstrom, L. Mesoporous Hydrogels: Revealing Reversible Porosity by Cryoporometry, X-Ray Scattering, and Gas Adsorption. *Langmuir*. **2010**, *26*, 10158-10164.
(172) Ghaderi, A.; Abbasian, M.; Rahmani, S.; Namazi, H.; Baharvand, H.; Entezami, A. A. Preparation of an Anion-Exchange Resin from Styrene-Divinylbenzene Copolymer Obtained by Concetrated Emulsion Polymerization Method. *Iran. Polym. J.* **2006**, *15*, 497-504.
(173) Chiefari, J.; Chong, Y. K.; Ercole, F.; Kristina, J.; Jeffery, J.; Le, T. P. T.; Mayadunne, R. T. A.; Meijs, G. F.; Moad, C. L.; Moad, G. et al. Living Free-Radical Polymerization by Reversible Addition-Fragmentation Chain Transfer: The RAFT Process. *Macromolecules*. **1998**, *31*, 5559-5562.
(174) Savina, I. N.; Gun'ko, V. M.; Turov, V. V.; Dainiak, M.; Phillips, G. J.; Galaev, I. Y.; Mikhalovsky, S. V. Porous Structure and Water State in Cross-Linked Polymer and Protein Cryo-Hydrogels. *Soft Matter*. **2011**, *7*, 4276-4283.
(175) Gane, P. A. C.; Ridgway, C. J.; Lehtinen, E.; Valiullin, R.; Furo, I.; Schoelkopf, J.; Paulapuro, H.; Daicic, J. Comparison of NMR Cryoporometry, Mercury Intrusion Porosimetry and DSC Thermoporosimetry in Characterising Pore Size Distributions of Compressed Finely Ground Calcium Carbonate Structures. *Ind. Eng. Chem. Res.* **2004**, *43*, 7920-7927.
(176) Lee, A. F.; Wilson, K., *Sol-gel Sulfonic Acid Silicas as Catalysts: Handbook of Green Chemistry*; Wiley: U.K., 2009.
(177) BP, *BP Energy Outlook 2030 Conference*. January, 2011: London, U.K.
(178) Montero, J. M.; Gai, P.; Wilson, K.; Lee, A. F. Structure-Sensitive Biodiesel Synthesis over MgO Nanocrystals. *Green. Chem.* **2009**, *11*, 265-268.
(179) Callaghan, P. T., *Principles of Nuclear Magnetic Resonance Microscopy*; Clarendon: Oxford, U.K., 1991.
(180) Mantle, M. D.; Enache, D. I.; Nowicka, E.; Davies, S. P.; Edwards, J. K.; D'Agostino, C.; Mascarenhas, D. P.; Durham, L.; Sankar, M.; Knight, D. W. et al. Pulsed-Field Gradient NMR Spectroscopic Studies of Alcohols in Supported Gold Catalysts. *J. Phys. Chem. C.* **2011**, *115*, 1073-1079.
(181) D'Agostino, C.; Mitchell, J.; Gladden, L. F.; Mantle, M. D. Hydrogen Bonding Network Disruption in Mesoporous Catalyst Supports Probed by PFG-NMR Diffusometry and NMR Relaxometry. *J. Phys. Chem. C.* . **2012**, *116*, 8975-8982.
(182) D'Agostino, C.; Kotionova, T.; Mitchell, J.; Miedziak, P. J.; Knight, D. W.; Taylor, S. H.; Hutchings, G. J.; Gladden, L. F.; Mantle, M. D. Solvent Effect and Reactivity Trend in the Aerobic Oxidation of 1,3-Propanediols over Gold Supported on Titania: NMR Diffusion and Relaxation Studies. *Chem. Eur. J.* **2013**, *19*, 11725-11732.
(183) Gao, X. C.; da Costa, J. C. D.; Bhatia, S. K. Understanding the Diffusional Tortuosity of Porous Materials: An Effective Medium Theory Perspective. *Chem. Eng. Sci.* **2014**, *110*, 55-71.
(184) Epstein, N. On Totuosity and the Totuosity Factor in Flow and Diffusion Through Porous Media. *Chem. Eng. Sci.* **1989**, *44*, 777-779.
(185) Sen, P. N. Time-Dependent Diffusion Coefficient as a Probe of Geometry. *Concept. Magnetic. Res.* **2004**, *23A*, 1-21.
(186) Barrie, P. J. Characterization of Porous Media using NMR Methods. *Annu. Rep. NMR. Spectrosc.* **2000**, *41*, 265-316.

(187) Kärger, J.; Valiullin, R., *Diffusion in Porous Media*; Wiley: Leipzig, Germany. 2011.
(188) Harwood, L. M.; Moody, C. J.; Percy, J. M., *Experimental Organic Chemistry - Standard and Microscale*; Wiley: U.K., 1999.
(189) Nilsson, M. The DOSY Toolbox: A New Tool for Processing PFG NMR Diffusion Data. *J. Magn. Reson.* **2009**, *200*, 296-302.
(190) Huang, L.; Yan, X.; Kruk, M. Synthesis of Ultralarge-Pore FDU-12 Silica with Face-Centered Cubic Structure. *Langmuir*. **2010**, *26*, 14871-14878.
(191) Cox, P. M.; Betts, R. A.; Jones, C. D.; Spall, S. A.; Totterdell, I. J. Acceleration of Global Warming due to Carbon-Cycle Feedbacks in a Coupled Climate Model. *Nature*. **2000**, *408*, 184-187.
(192) Luo, Y.; Li, B.; Wang, W.; Wu, K.; Tan, B. Hypercrosslinked Aromatic Heterocyclic Microporous Polymers: A New Class of Highly Selective CO_2 Capturing Materials. *Adv. Mater.* **2012**, *24*, 5703-5707.
(193) Ding, L.; Gao, H.; Xie, F.; Li, W.; Bai, H.; Li, L. Porosity-Enhanced Polymers from Hyper-Cross-Linked Polymer Precursors. *Macromolecules*. **2017**, *50*, 956-962.
(194) Tan, L.; Tan, B. Hypercrosslinked Porous Polymer Materials: Design, Synthesis, and Applications. *Chem. Soc. Rev.* **2017**, *46*, 3322-3356.
(195) Cowin, S. C. Bone Poroelasticity. *J. Biomech.* **1999**, *32*, 217-238.
(196) Bini, F.; Pica, A.; Marinozzi, A.; Marinozzi, F. 3D Diffusion Model Within the Collagen Apatite Porosity: An Insight to the Nanostructure of Human Trabecular Bone. *PLoS One*. **2017**, *12*, e0189041.
(197) Hoang, V. T. H.; Huang, Q.; Eic, M.; Do, T. O.; Kaliaguine, S. Structure and Diffusion Characterization of SBA-15 Materials. *Langmuir*. **2005**, *21*, 2051-2057.

APPENDIX. 1

Measuring Convection – Standard NMR tube

Appendix 1 contains the analogous graphs to Figure 3.18, Chapter 3, for the remaining solvents at various temperatures. The change in signal intensity with respect to varying delay imbalance time, $\Delta\Delta$, and the fitting of the sinc function (Equation 3.7) is illustrated to obtain a velocity for all solvents used in this work, both in thin-walled and thick-walled NMR tubes.

Deuterated Acetone

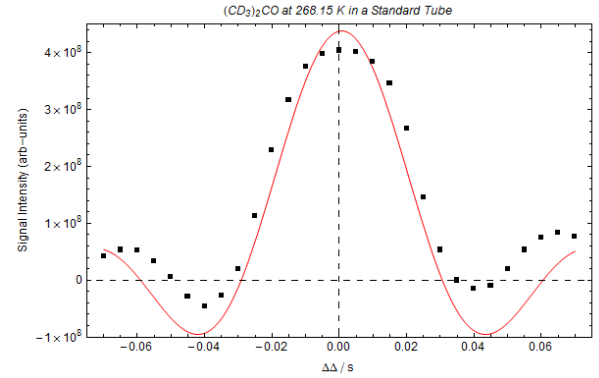

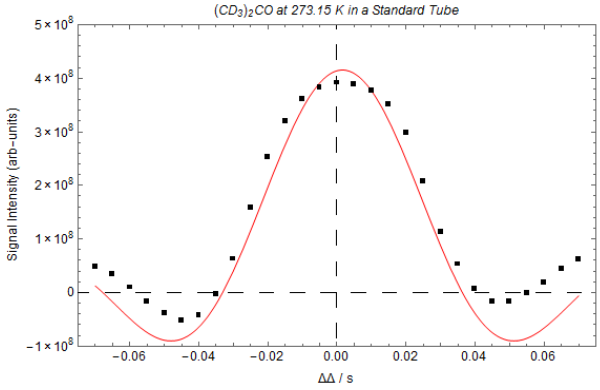

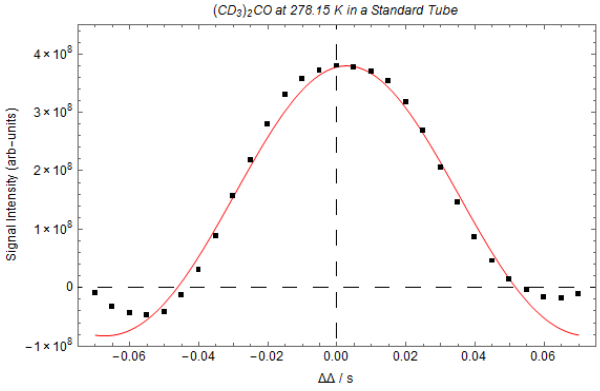

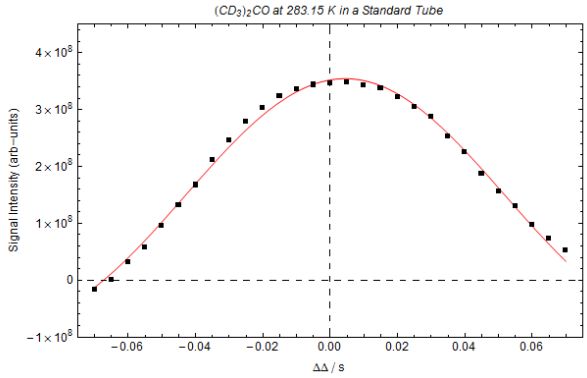
(CD3)2CO at 283.15 K in a Standard Tube
Signal Intensity (arb-units)
ΔΔ / s

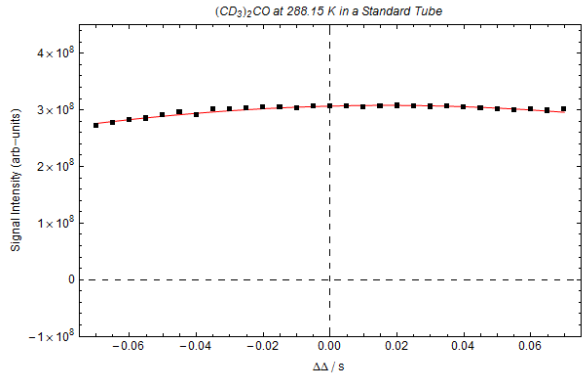
(CD3)2CO at 288.15 K in a Standard Tube
Signal Intensity (arb-units)
ΔΔ / s

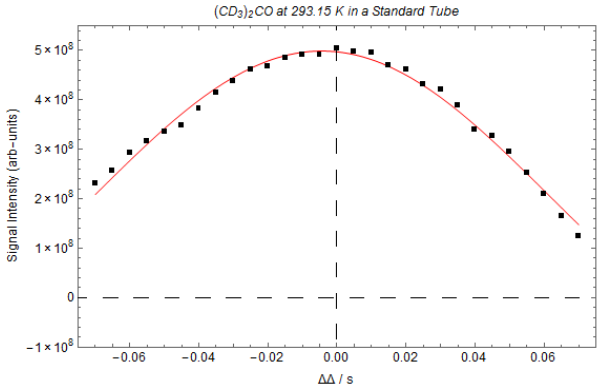
(CD3)2CO at 293.15 K in a Standard Tube
Signal Intensity (arb-units)
ΔΔ / s

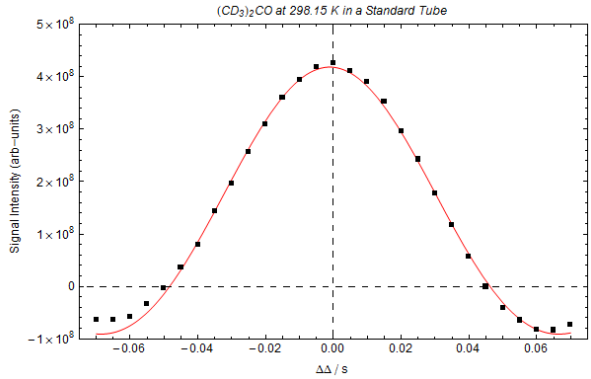
(CD3)2CO at 298.15 K in a Standard Tube
Signal Intensity (arb-units)
ΔΔ / s

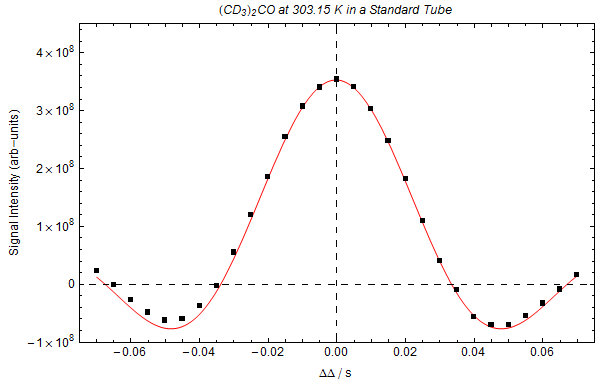

Deuterated Chloroform

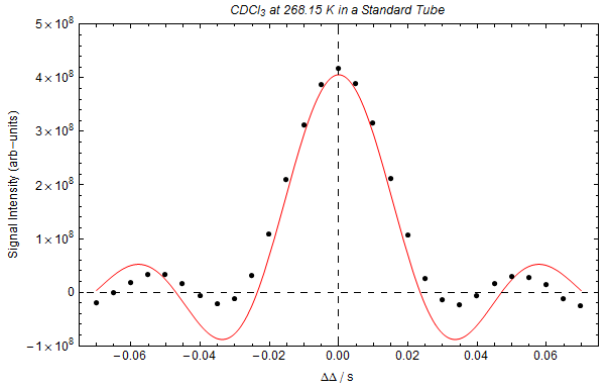

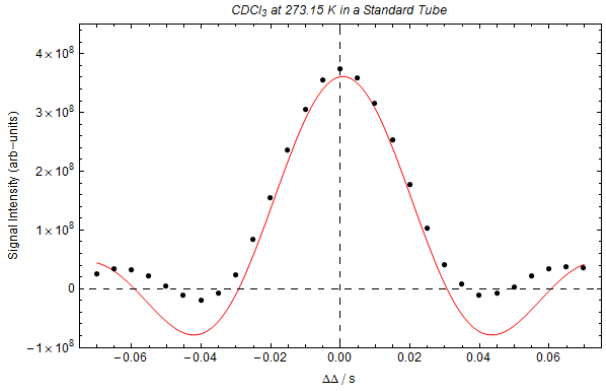

Appendix 1

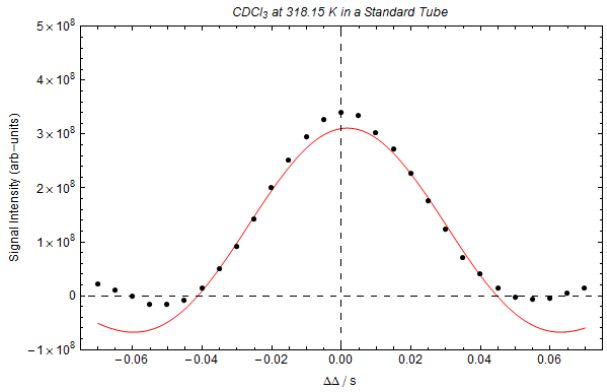
CDCl3 at 318.15 K in a Standard Tube
Signal Intensity (arb−units)
ΔΔ / s

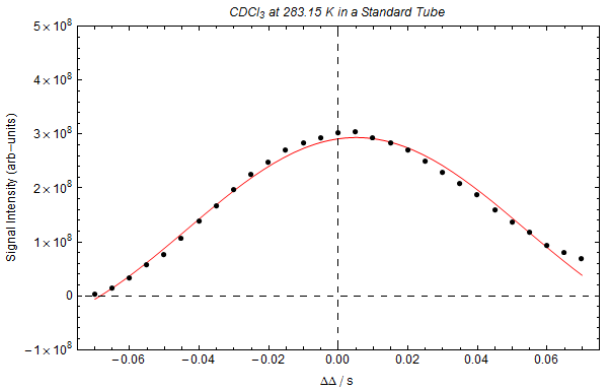
CDCl3 at 283.15 K in a Standard Tube
Signal Intensity (arb−units)
ΔΔ / s

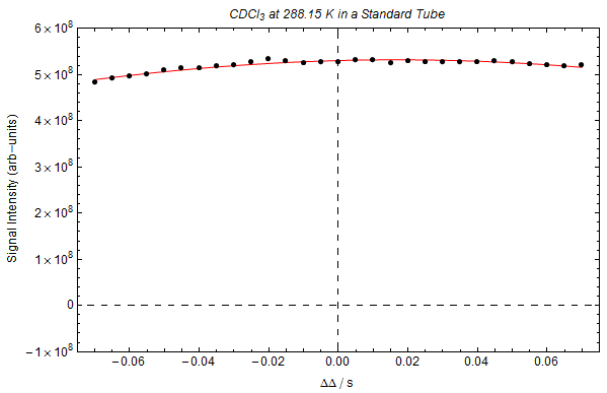
CDCl3 at 288.15 K in a Standard Tube
Signal Intensity (arb−units)
ΔΔ / s

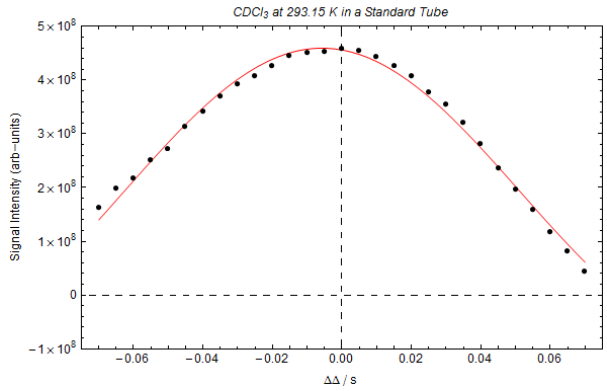
CDCl3 at 293.15 K in a Standard Tube
Signal Intensity (arb−units)
ΔΔ / s

Appendix 1

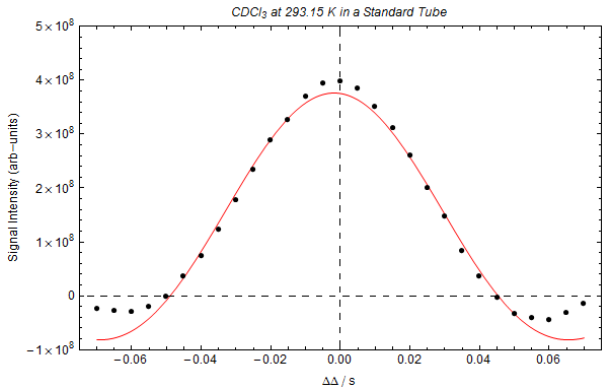
CDCl3 at 293.15 K in a Standard Tube
Signal Intensity (arb–units)
ΔΔ / s

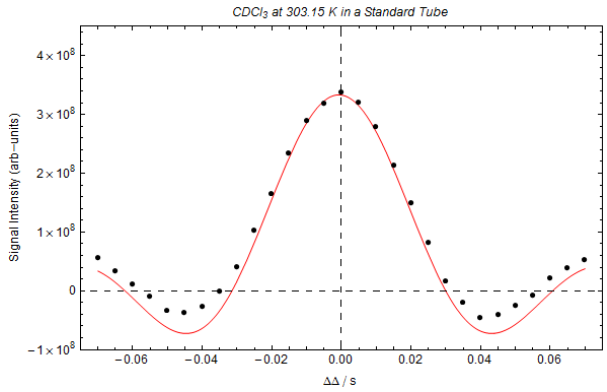
CDCl3 at 303.15 K in a Standard Tube
Signal Intensity (arb–units)
ΔΔ / s

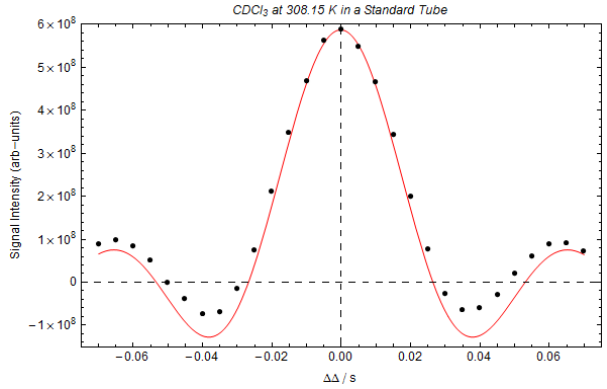
CDCl3 at 308.15 K in a Standard Tube
Signal Intensity (arb–units)
ΔΔ / s

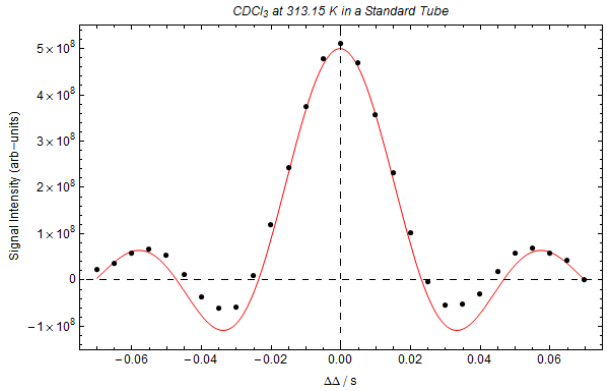
CDCl3 at 313.15 K in a Standard Tube
Signal Intensity (arb–units)
ΔΔ / s

Appendix 1

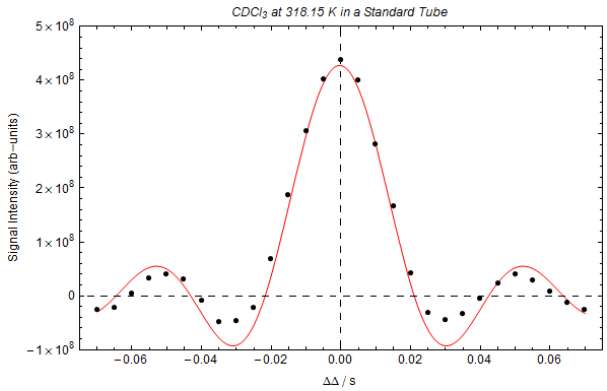

Deuterated Water

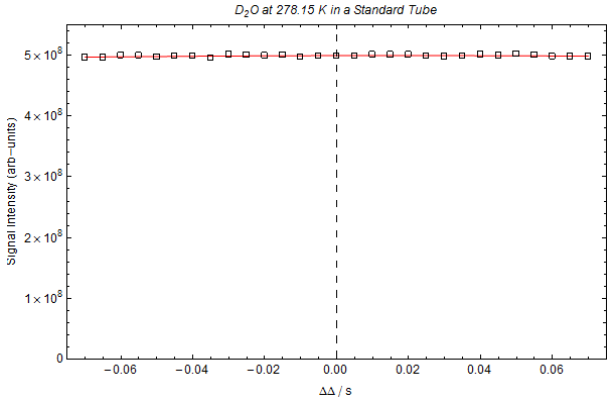

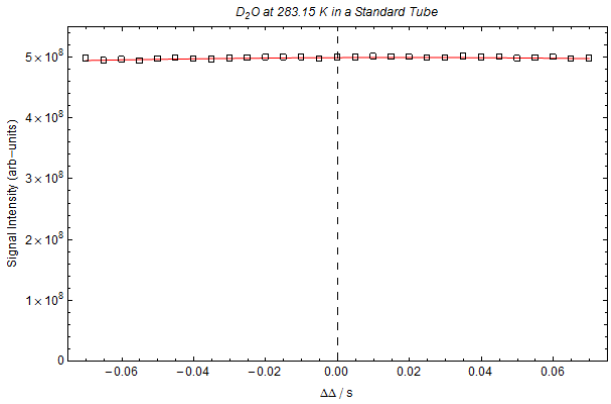

Appendix 1

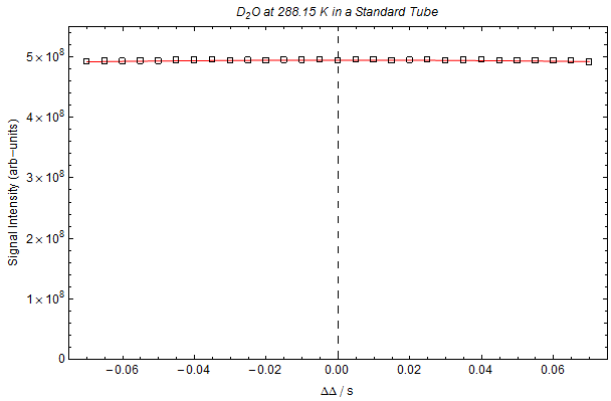
D_2O at 288.15 K in a Standard Tube
Signal Intensity (arb-units)
5×10^8
4×10^8
3×10^8
2×10^8
1×10^8
0
−0.06
−0.04
−0.02
0.00
0.02
0.04
0.06
ΔΔ / s

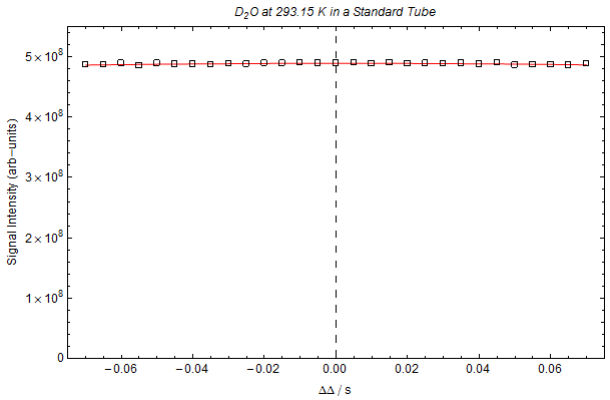
D_2O at 293.15 K in a Standard Tube
Signal Intensity (arb-units)
5×10^8
4×10^8
3×10^8
2×10^8
1×10^8
0
−0.06
−0.04
−0.02
0.00
0.02
0.04
0.06
ΔΔ / s

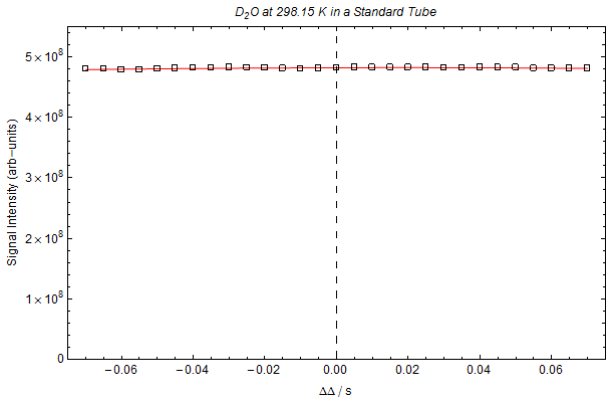
D_2O at 298.15 K in a Standard Tube
Signal Intensity (arb-units)
5×10^8
4×10^8
3×10^8
2×10^8
1×10^8
0
−0.06
−0.04
−0.02
0.00
0.02
0.04
0.06
ΔΔ / s

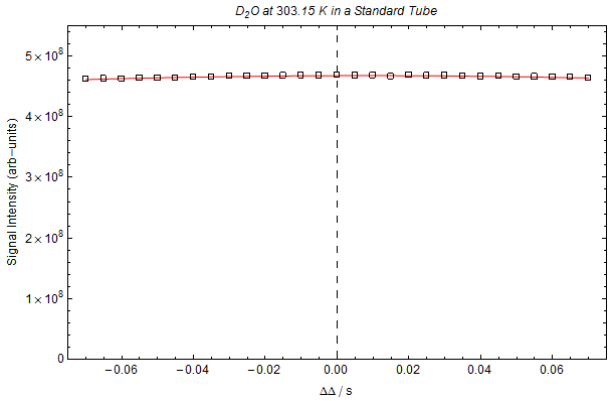
D_2O at 303.15 K in a Standard Tube
Signal Intensity (arb-units)
5×10^8
4×10^8
3×10^8
2×10^8
1×10^8
0
−0.06
−0.04
−0.02
0.00
0.02
0.04
0.06
ΔΔ / s

Appendix 1

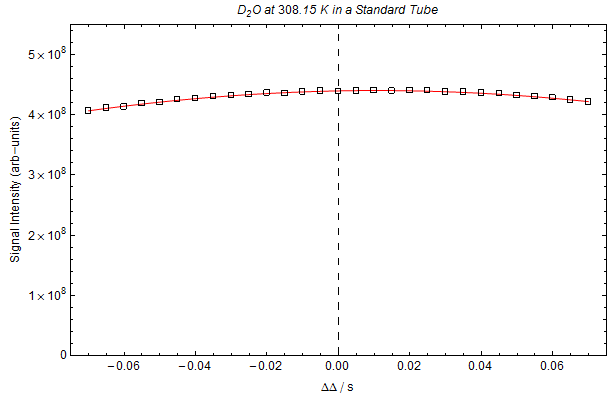
D_2O at 308.15 K in a Standard Tube
Signal Intensity (arb–units)
ΔΔ / s

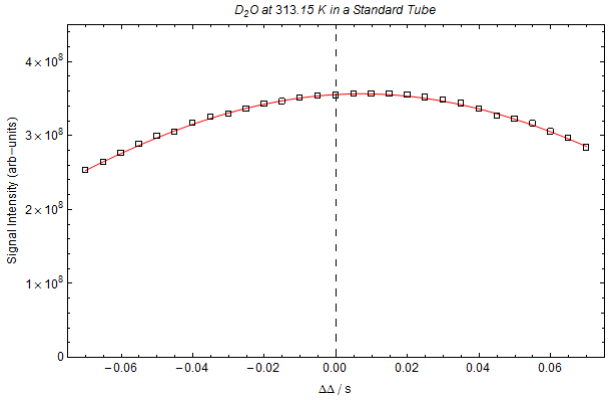
D_2O at 313.15 K in a Standard Tube
Signal Intensity (arb–units)
ΔΔ / s

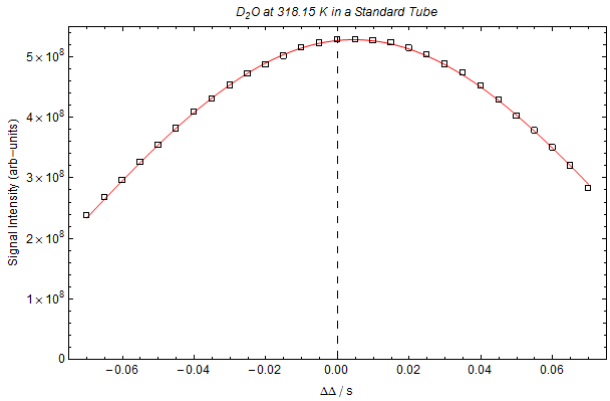
D_2O at 318.15 K in a Standard Tube
Signal Intensity (arb–units)
ΔΔ / s

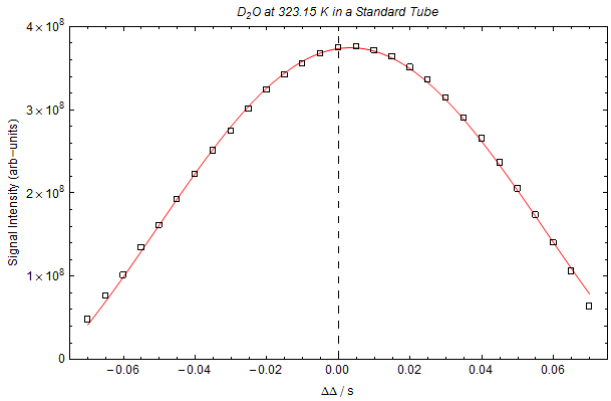
D_2O at 323.15 K in a Standard Tube
Signal Intensity (arb–units)
ΔΔ / s

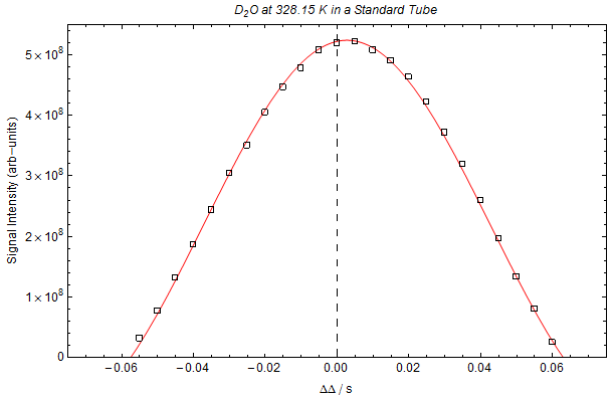

Deuterated Dimethyl Sulfoxide

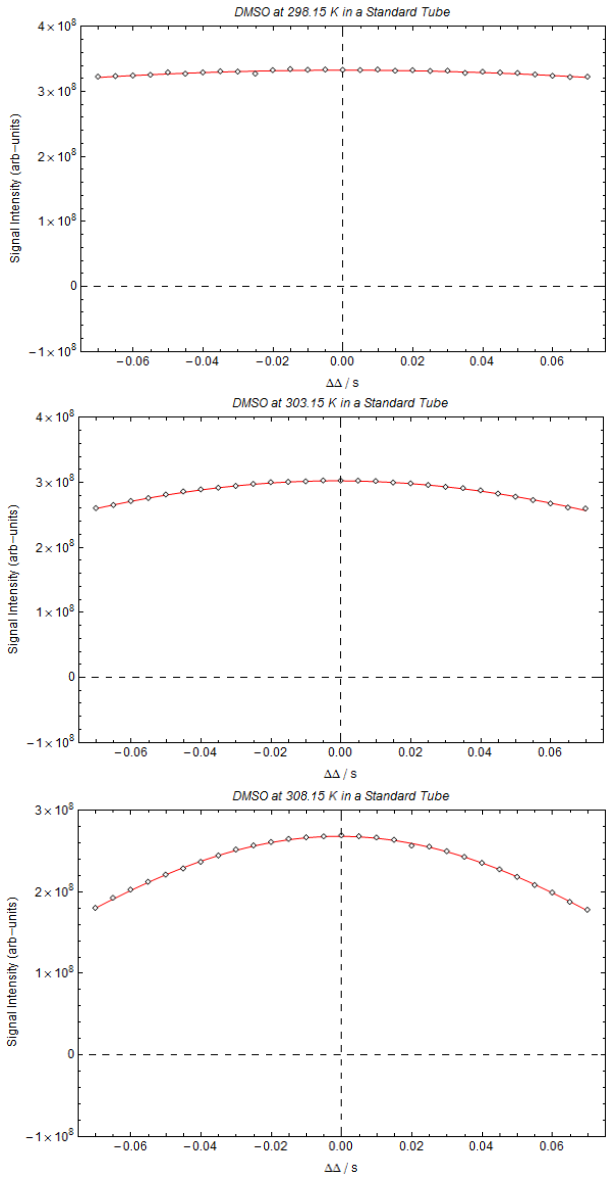

Appendix 1

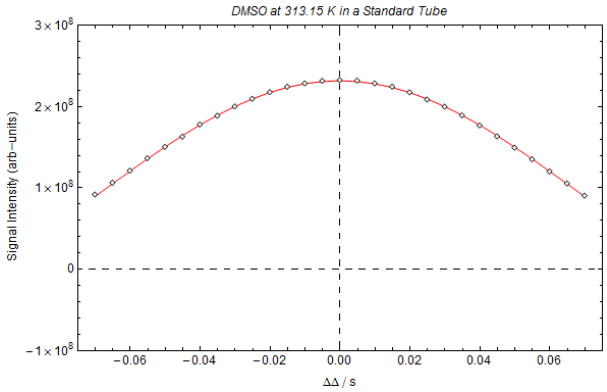
DMSO at 313.15 K in a Standard Tube
Signal Intensity (arb--units)
3×10^8
2×10^8
1×10^8
0
−1×10^8
−0.06
−0.04
−0.02
0.00
0.02
0.04
0.06
ΔΔ / s

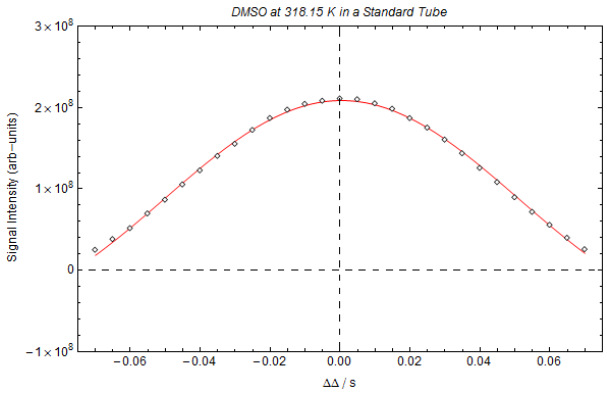
DMSO at 318.15 K in a Standard Tube
Signal Intensity (arb--units)
3×10^8
2×10^8
1×10^8
0
−1×10^8
−0.06
−0.04
−0.02
0.00
0.02
0.04
0.06
ΔΔ / s

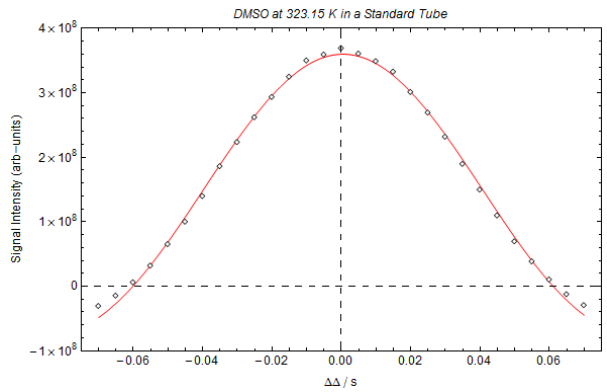
DMSO at 323.15 K in a Standard Tube
Signal Intensity (arb--units)
4×10^8
3×10^8
2×10^8
1×10^8
0
−1×10^8
−0.06
−0.04
−0.02
0.00
0.02
0.04
0.06
ΔΔ / s

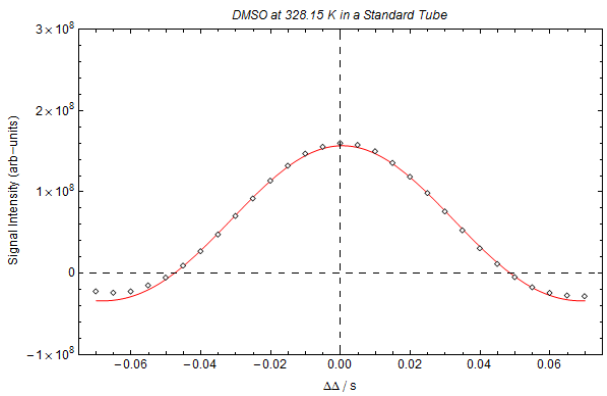
DMSO at 328.15 K in a Standard Tube
Signal Intensity (arb--units)
3×10^8
2×10^8
1×10^8
0
−1×10^8
−0.06
−0.04
−0.02
0.00
0.02
0.04
0.06
ΔΔ / s

Deuterated Methanol

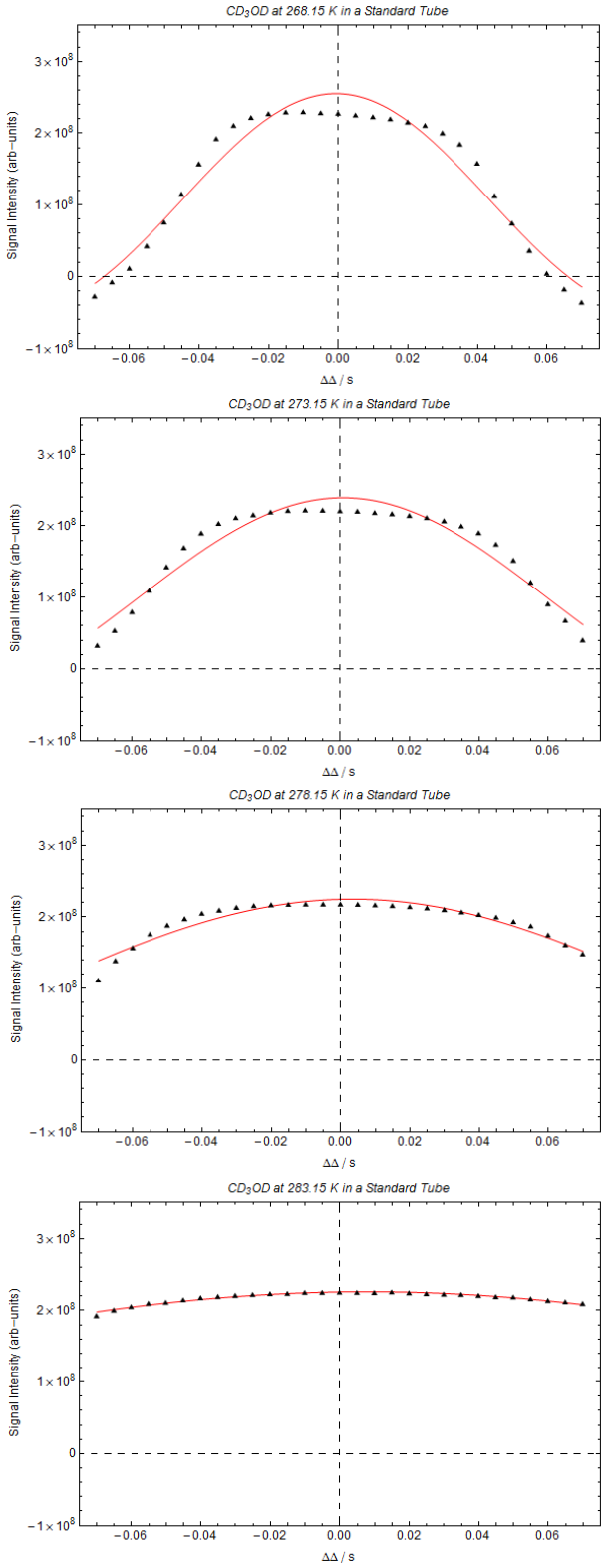

Appendix 1

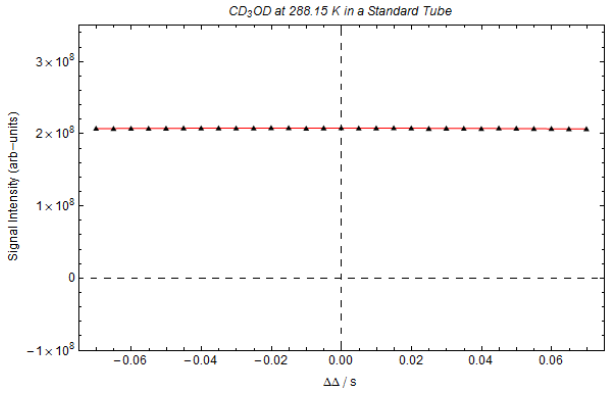
CD3OD at 288.15 K in a Standard Tube
Signal Intensity (arb−units)
3×10^8
2×10^8
1×10^8
0
−1×10^8
−0.06
−0.04
−0.02
0.00
0.02
0.04
0.06
ΔΔ / s

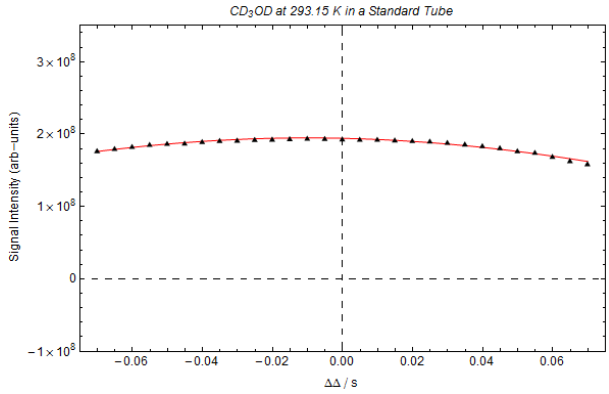
CD3OD at 293.15 K in a Standard Tube
Signal Intensity (arb−units)
3×10^8
2×10^8
1×10^8
0
−1×10^8
−0.06
−0.04
−0.02
0.00
0.02
0.04
0.06
ΔΔ / s

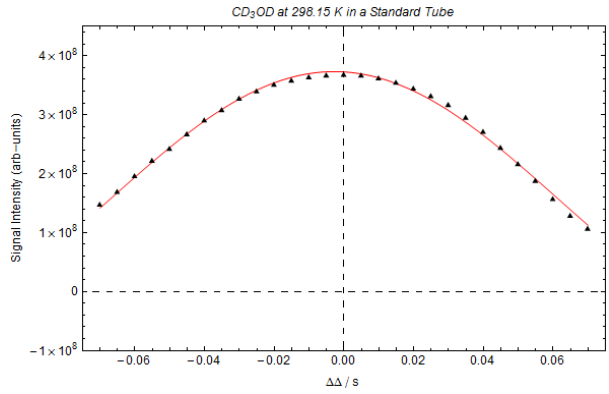
CD3OD at 298.15 K in a Standard Tube
Signal Intensity (arb−units)
4×10^8
3×10^8
2×10^8
1×10^8
0
−1×10^8
−0.06
−0.04
−0.02
0.00
0.02
0.04
0.06
ΔΔ / s

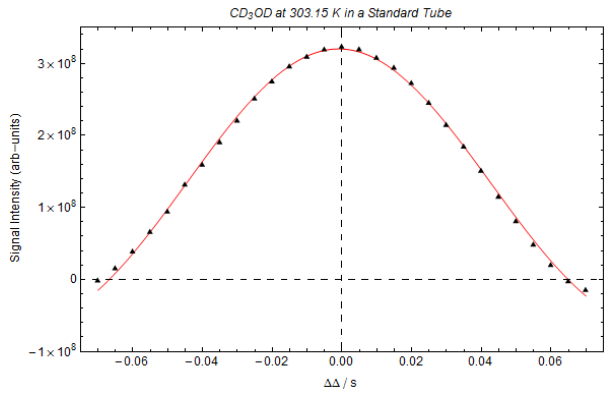
CD3OD at 303.15 K in a Standard Tube
Signal Intensity (arb−units)
3×10^8
2×10^8
1×10^8
0
−1×10^8
−0.06
−0.04
−0.02
0.00
0.02
0.04
0.06
ΔΔ / s

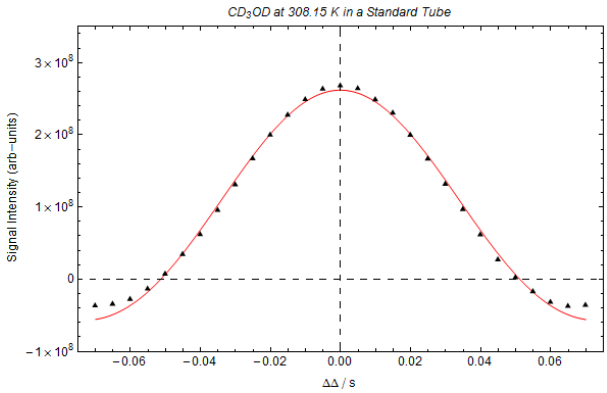

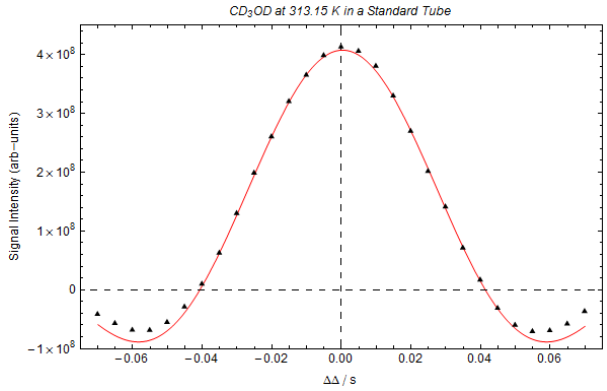

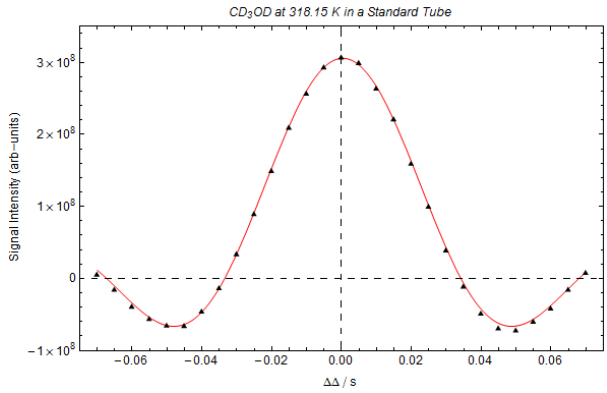

Measuring Convection – Thick Walled NMR tube

Deuterated Acetone

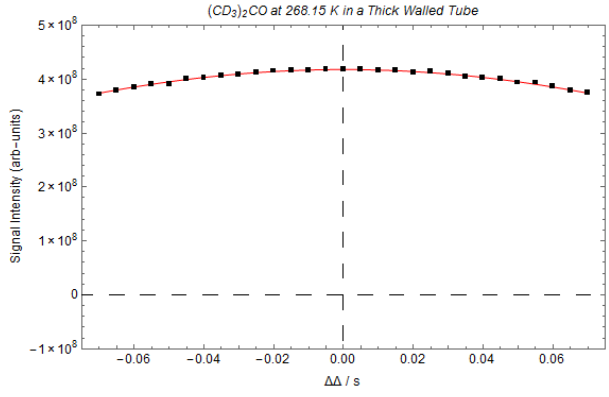

Appendix 1

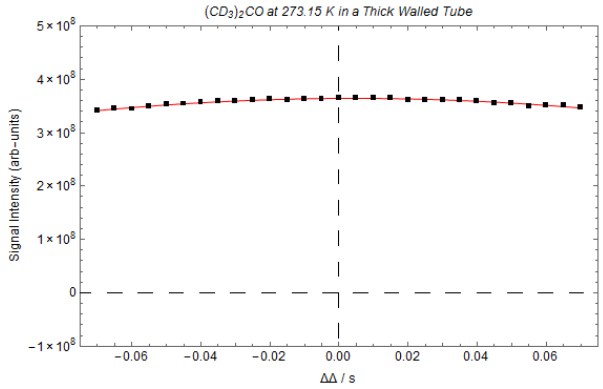
(CD3)2CO at 273.15 K in a Thick Walled Tube
Signal Intensity (arb-units)
ΔΔ / s

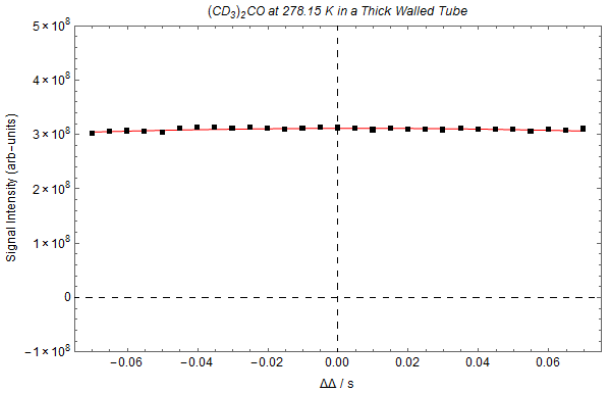
(CD3)2CO at 278.15 K in a Thick Walled Tube
Signal Intensity (arb-units)
ΔΔ / s

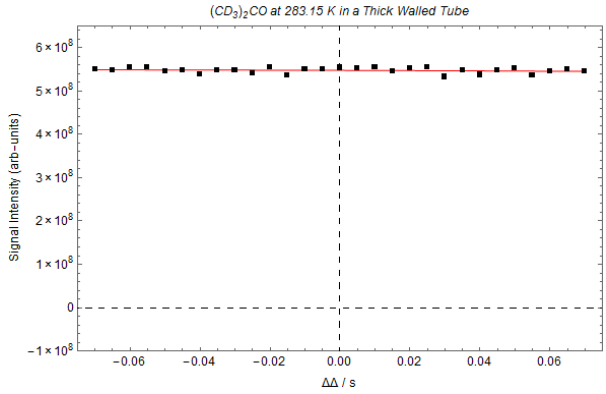
(CD3)2CO at 283.15 K in a Thick Walled Tube
Signal Intensity (arb-units)
ΔΔ / s

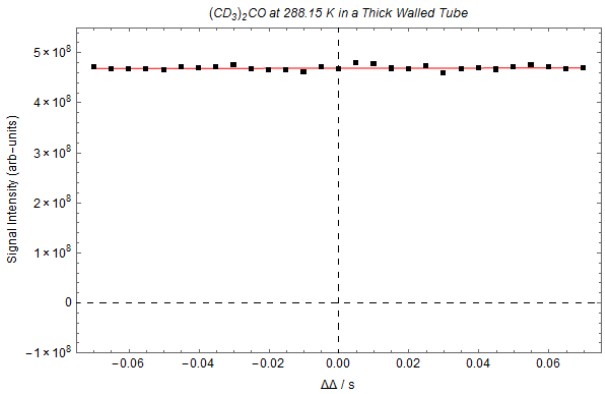
(CD3)2CO at 288.15 K in a Thick Walled Tube
Signal Intensity (arb-units)
ΔΔ / s

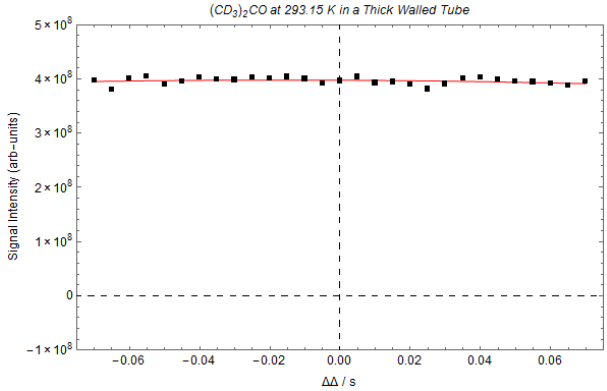

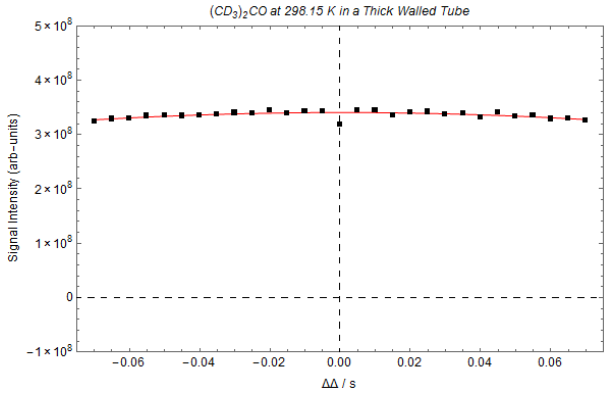

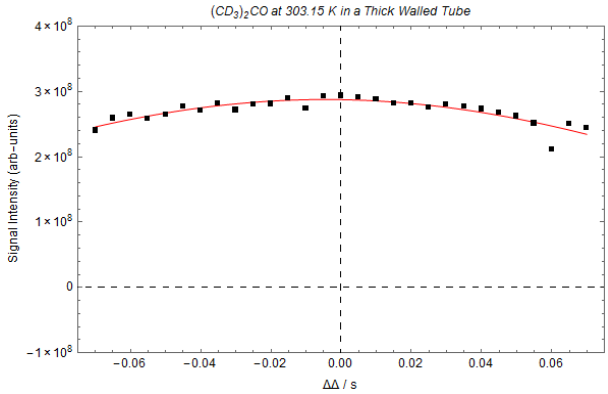

Deuterated Chloroform

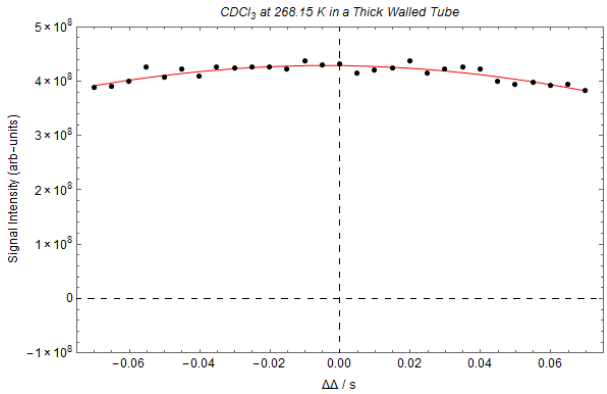

Appendix 1

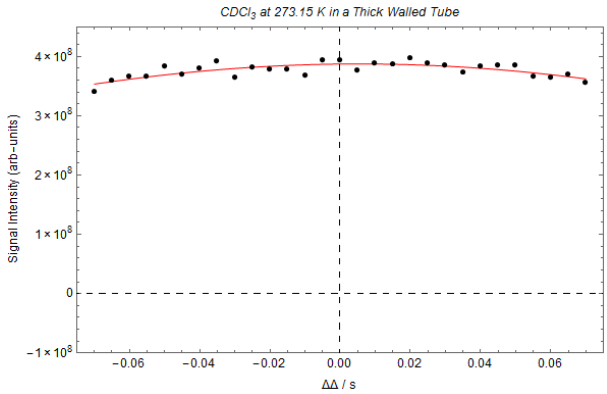
CDCl3 at 273.15 K in a Thick Walled Tube
Signal Intensity (arb-units)
4×10^8
3×10^8
2×10^8
1×10^8
0
−1×10^8
−0.06
−0.04
−0.02
0.00
0.02
0.04
0.06
ΔΔ / s

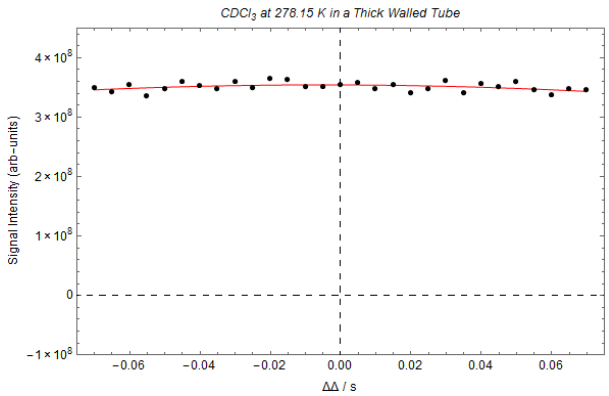
CDCl3 at 278.15 K in a Thick Walled Tube
Signal Intensity (arb-units)
4×10^8
3×10^8
2×10^8
1×10^8
0
−1×10^8
−0.06
−0.04
−0.02
0.00
0.02
0.04
0.06
ΔΔ / s

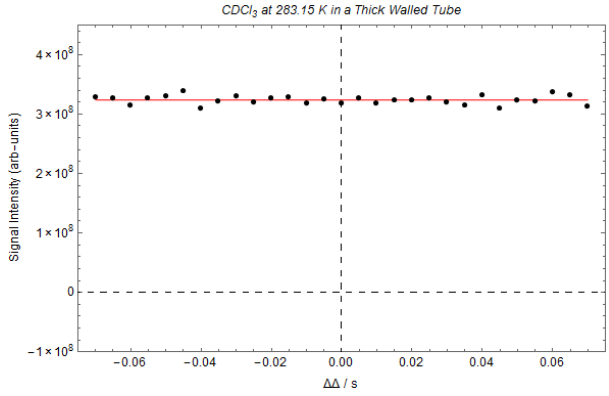
CDCl3 at 283.15 K in a Thick Walled Tube
Signal Intensity (arb-units)
4×10^8
3×10^8
2×10^8
1×10^8
0
−1×10^8
−0.06
−0.04
−0.02
0.00
0.02
0.04
0.06
ΔΔ / s

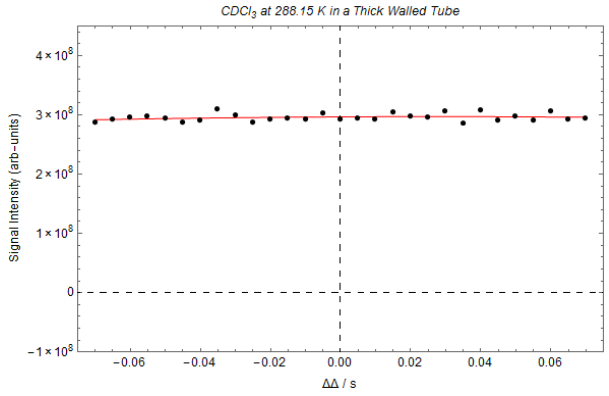
CDCl3 at 288.15 K in a Thick Walled Tube
Signal Intensity (arb-units)
4×10^8
3×10^8
2×10^8
1×10^8
0
−1×10^8
−0.06
−0.04
−0.02
0.00
0.02
0.04
0.06
ΔΔ / s

Appendix 1

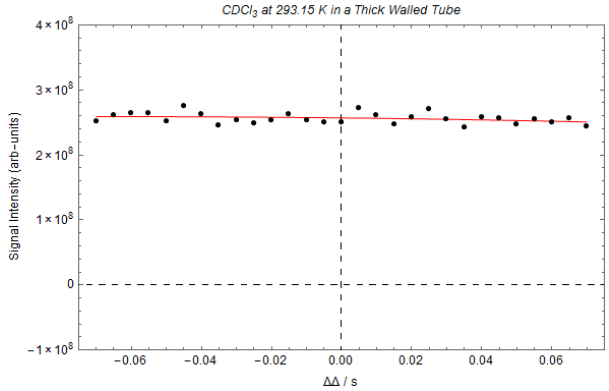
CDCl3 at 293.15 K in a Thick Walled Tube
Signal Intensity (arb-units)
ΔΔ / s

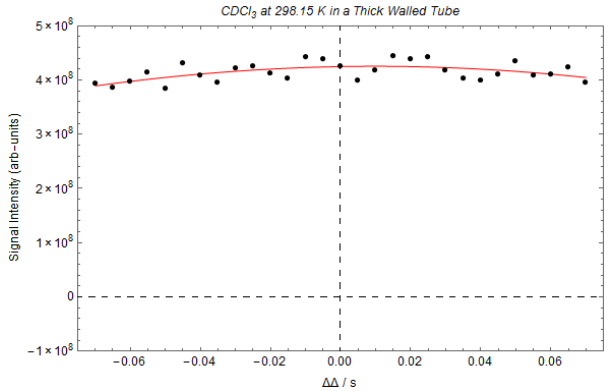
CDCl3 at 298.15 K in a Thick Walled Tube
Signal Intensity (arb-units)
ΔΔ / s

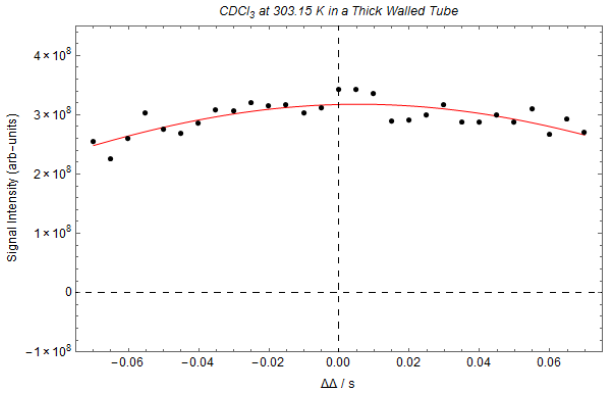
CDCl3 at 303.15 K in a Thick Walled Tube
Signal Intensity (arb-units)
ΔΔ / s

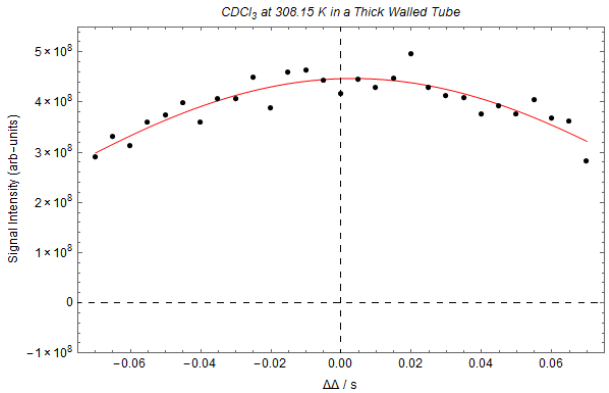
CDCl3 at 308.15 K in a Thick Walled Tube
Signal Intensity (arb-units)
ΔΔ / s

Appendix 1

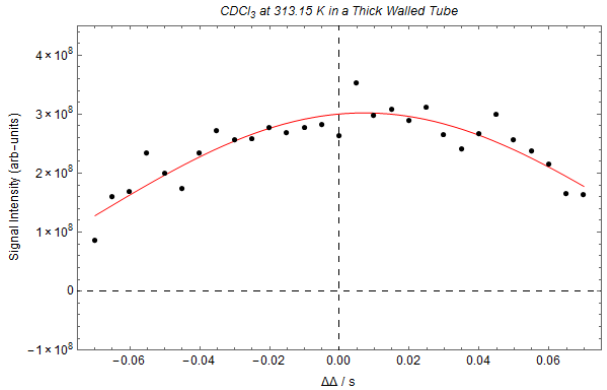

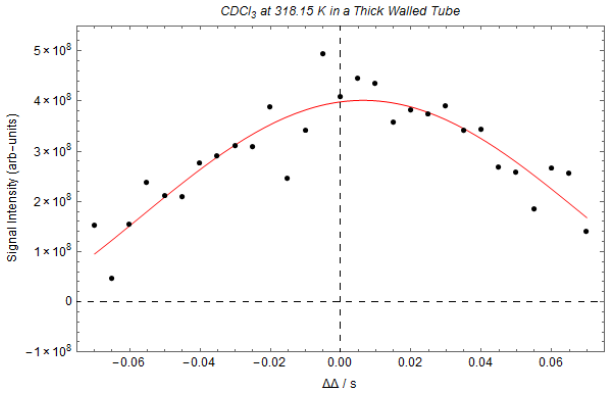

Deuterated Water

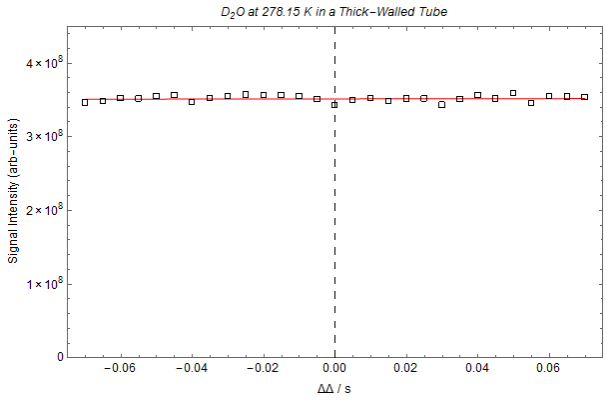

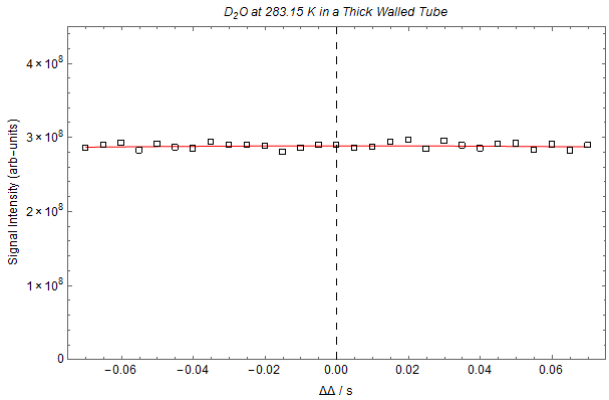

Appendix 1

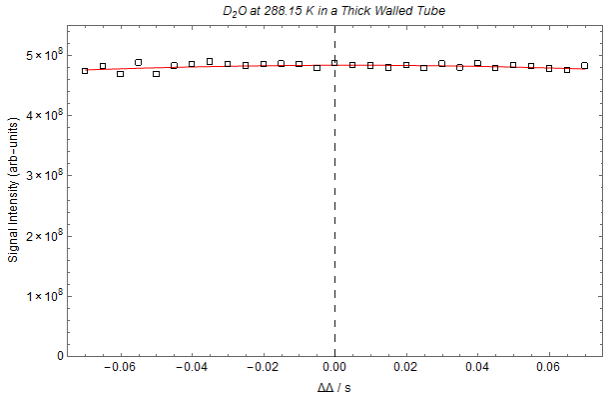
D_2O at 288.15 K in a Thick Walled Tube
Signal Intensity (arb-units)
ΔΔ / s

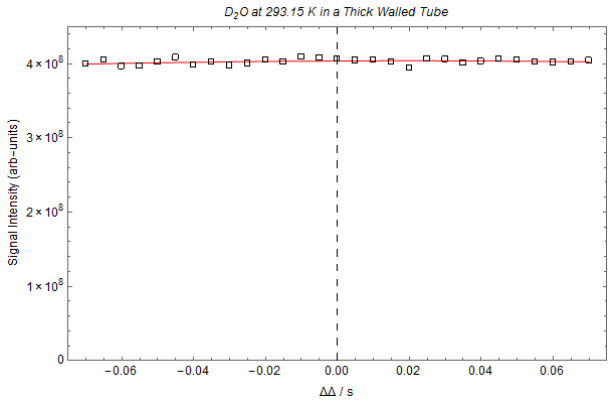
D_2O at 293.15 K in a Thick Walled Tube
Signal Intensity (arb-units)
ΔΔ / s

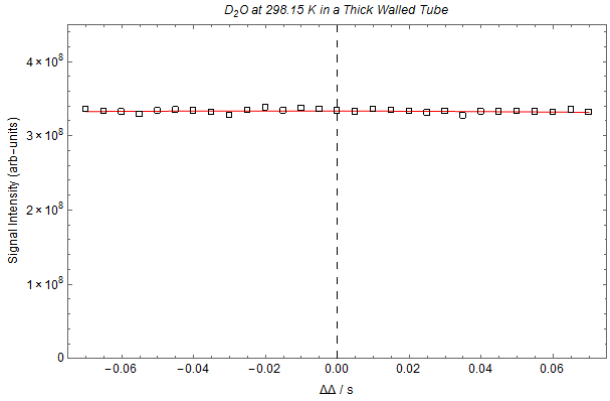
D_2O at 298.15 K in a Thick Walled Tube
Signal Intensity (arb-units)
ΔΔ / s

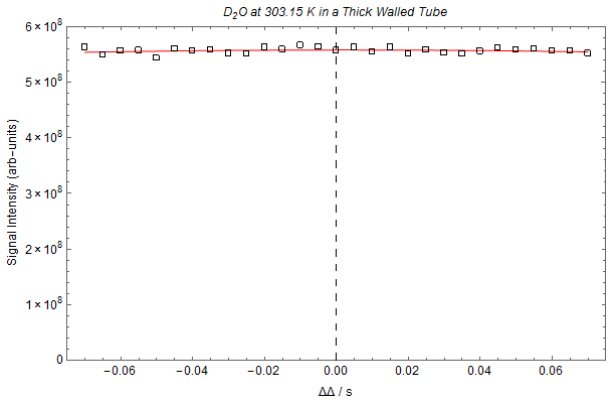
D_2O at 303.15 K in a Thick Walled Tube
Signal Intensity (arb-units)
ΔΔ / s

Appendix 1

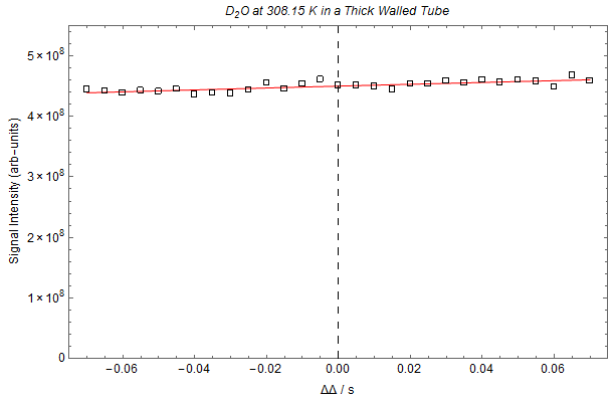
D_2O at 308.15 K in a Thick Walled Tube
Signal Intensity (arb-units)
ΔΔ / s

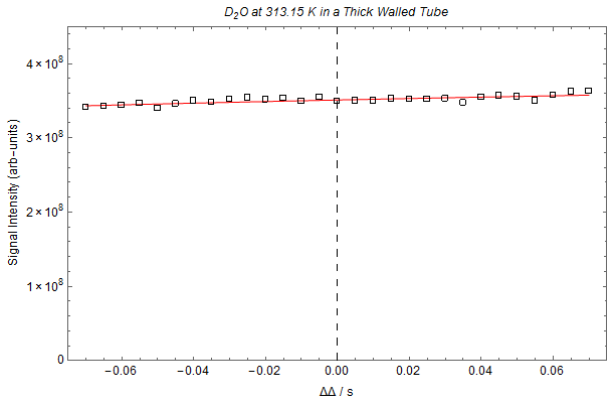
D_2O at 313.15 K in a Thick Walled Tube
Signal Intensity (arb-units)
ΔΔ / s

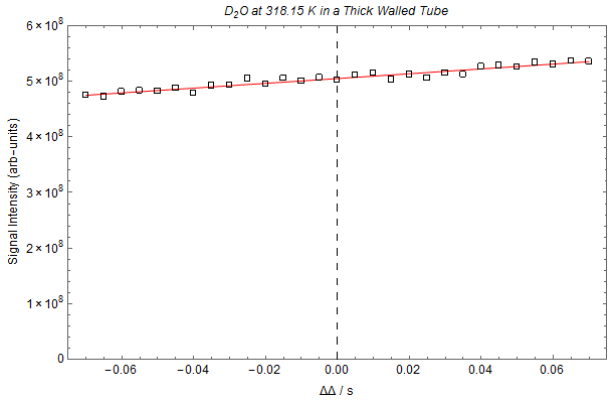
D_2O at 318.15 K in a Thick Walled Tube
Signal Intensity (arb-units)
ΔΔ / s

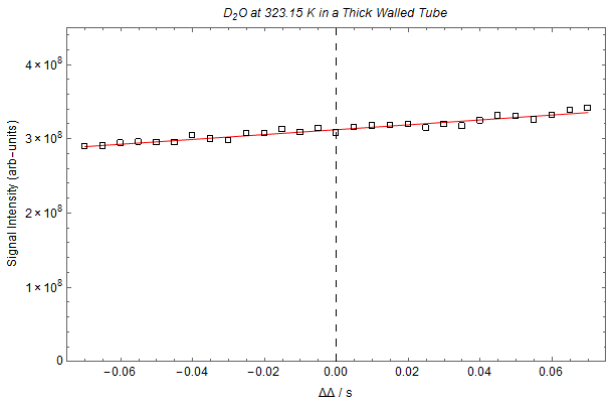
D_2O at 323.15 K in a Thick Walled Tube
Signal Intensity (arb-units)
ΔΔ / s

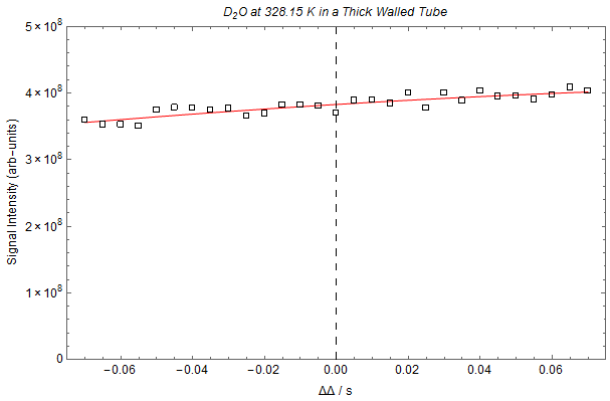

Deuterated Dimethyl Sulfoxide

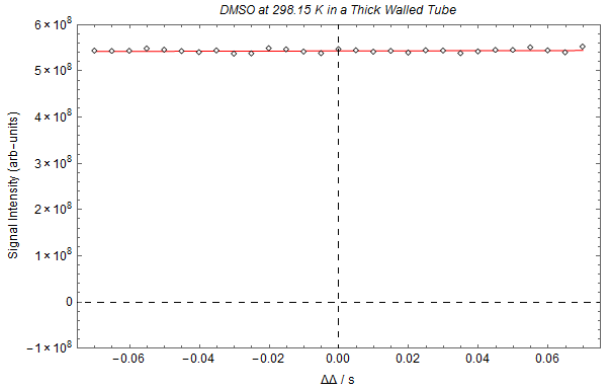

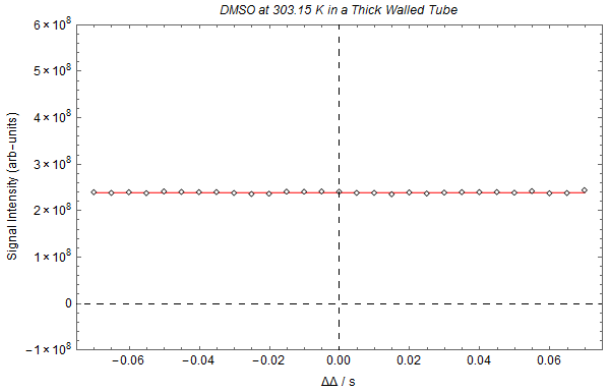

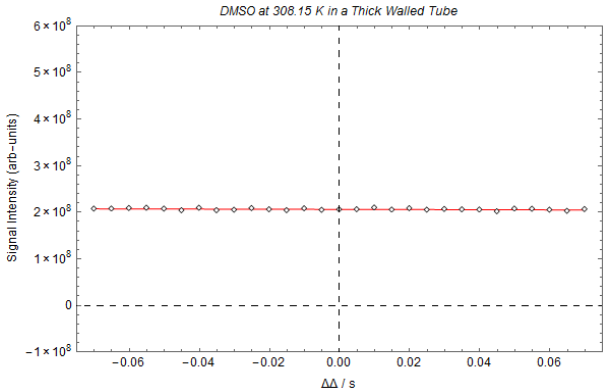

Appendix 1

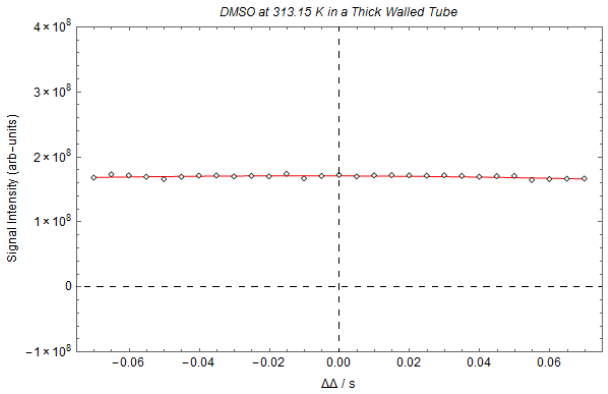
DMSO at 313.15 K in a Thick Walled Tube
Signal Intensity (arb-units)
ΔΔ / s

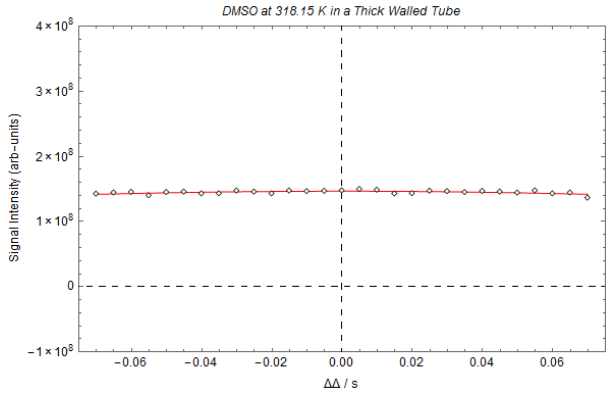
DMSO at 318.15 K in a Thick Walled Tube
Signal Intensity (arb-units)
ΔΔ / s

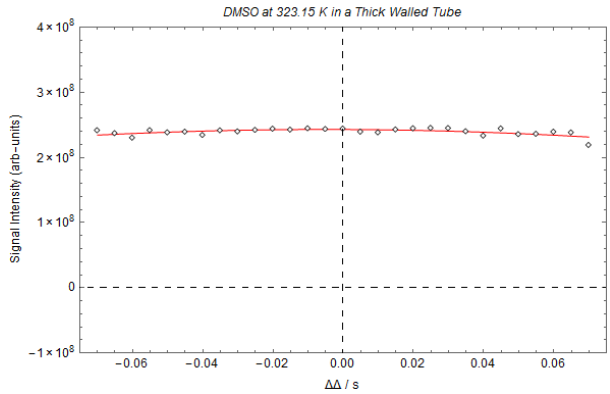
DMSO at 323.15 K in a Thick Walled Tube
Signal Intensity (arb-units)
ΔΔ / s

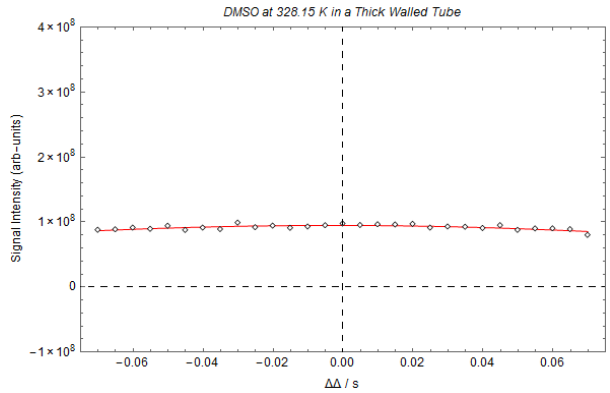
DMSO at 328.15 K in a Thick Walled Tube
Signal Intensity (arb-units)
ΔΔ / s

Appendix 1

Deuterated Methanol

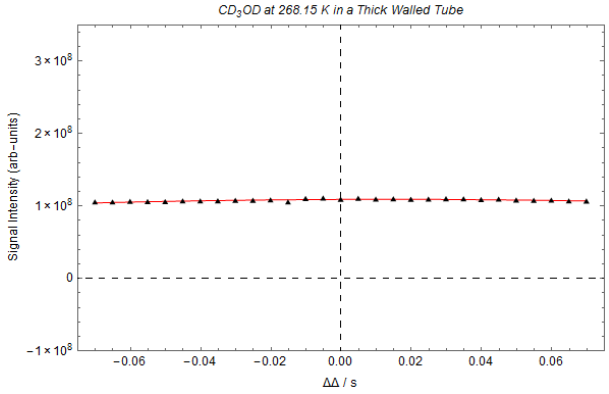

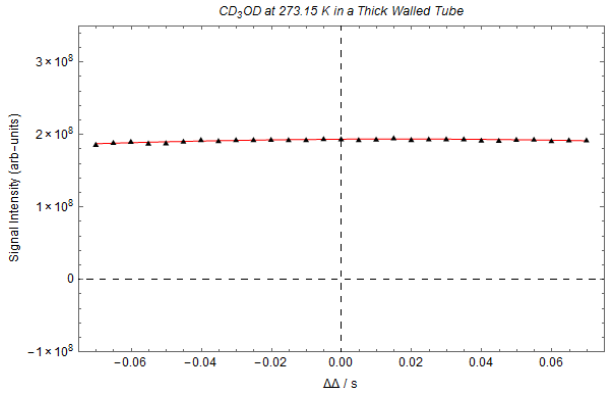

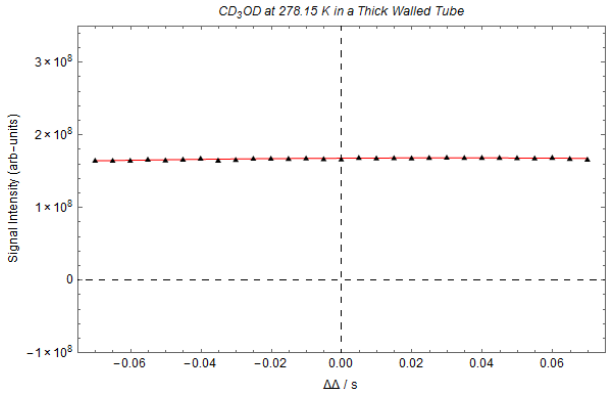

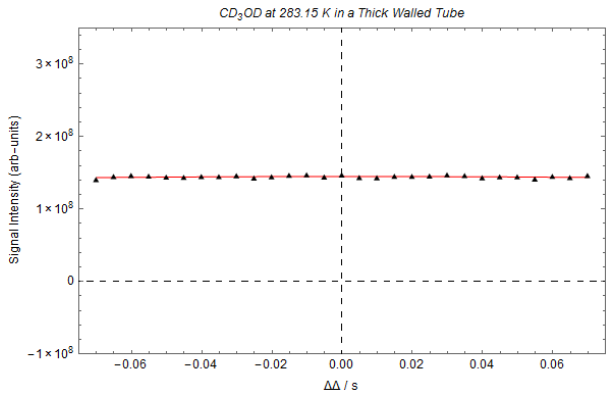

Appendix 1

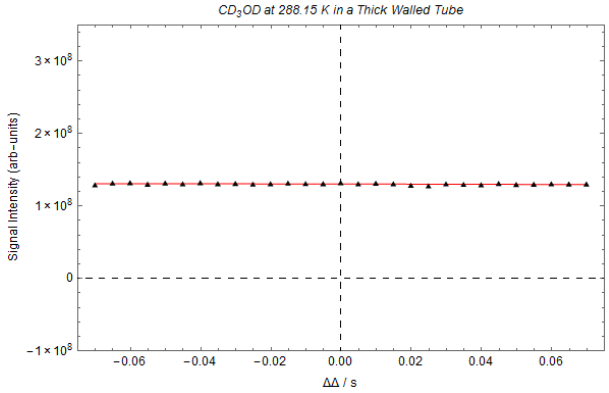
CD3OD at 288.15 K in a Thick Walled Tube
Signal Intensity (arb-units)
3×10^8
2×10^8
1×10^8
0
−1×10^8
−0.06
−0.04
−0.02
0.00
0.02
0.04
0.06
ΔΔ / s

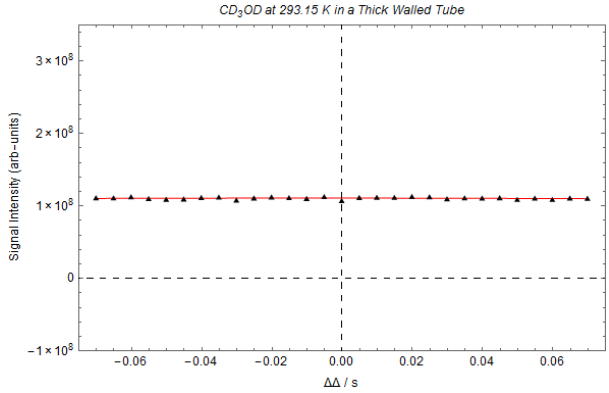
CD3OD at 293.15 K in a Thick Walled Tube
Signal Intensity (arb-units)
3×10^8
2×10^8
1×10^8
0
−1×10^8
−0.06
−0.04
−0.02
0.00
0.02
0.04
0.06
ΔΔ / s

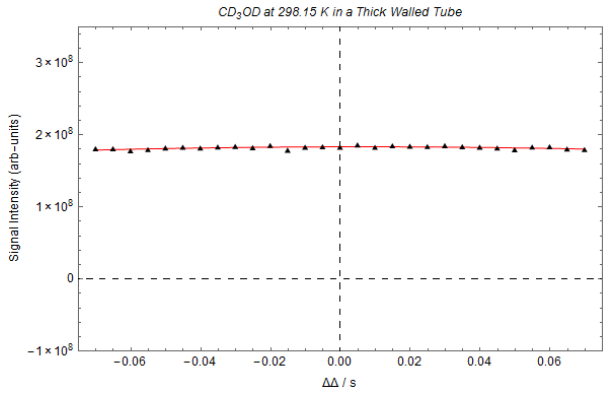
CD3OD at 298.15 K in a Thick Walled Tube
Signal Intensity (arb-units)
3×10^8
2×10^8
1×10^8
0
−1×10^8
−0.06
−0.04
−0.02
0.00
0.02
0.04
0.06
ΔΔ / s

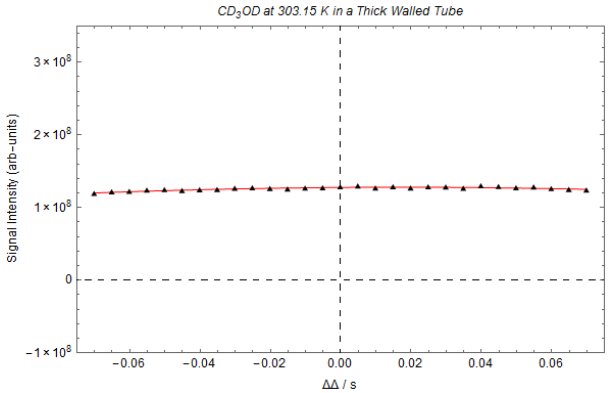
CD3OD at 303.15 K in a Thick Walled Tube
Signal Intensity (arb-units)
3×10^8
2×10^8
1×10^8
0
−1×10^8
−0.06
−0.04
−0.02
0.00
0.02
0.04
0.06
ΔΔ / s

Appendix 1

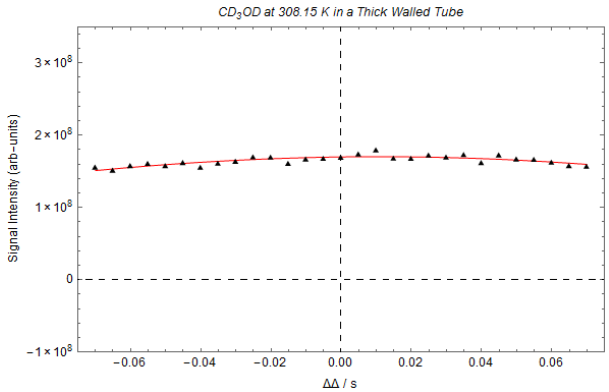
CD3OD at 308.15 K in a Thick Walled Tube
Signal Intensity (arb-units)
3×10^8
2×10^8
1×10^8
0
−1×10^8
−0.06
−0.04
−0.02
0.00
0.02
0.04
0.06
ΔΔ / s

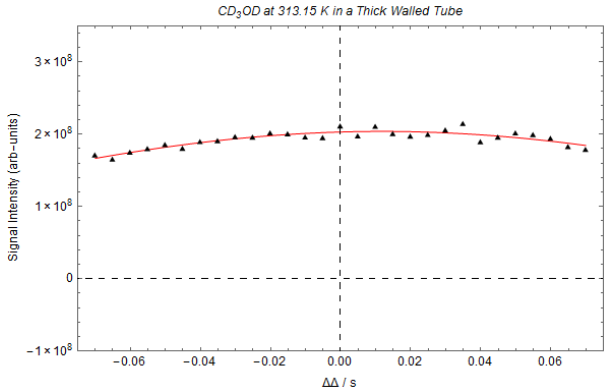
CD3OD at 313.15 K in a Thick Walled Tube
Signal Intensity (arb-units)
3×10^8
2×10^8
1×10^8
0
−1×10^8
−0.06
−0.04
−0.02
0.00
0.02
0.04
0.06
ΔΔ / s

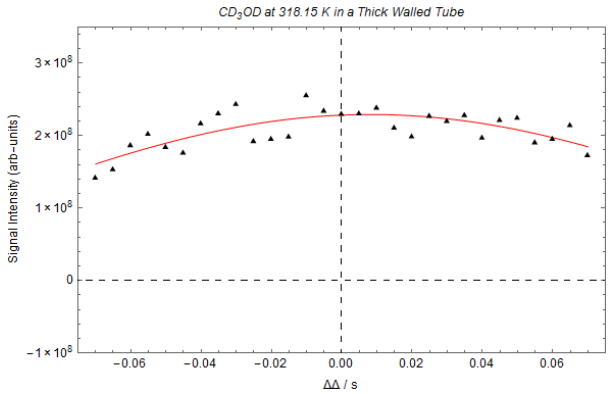
CD3OD at 318.15 K in a Thick Walled Tube
Signal Intensity (arb-units)
3×10^8
2×10^8
1×10^8
0
−1×10^8
−0.06
−0.04
−0.02
0.00
0.02
0.04
0.06
ΔΔ / s

APPENDIX. 2

Differential scanning calorimetry (DSC) thermograms for water confined in the pores of mesoporous silica

Figures A2.1-3 follow the melting of water confined in mesoporous silica using the DSC method. Figures A2.1 and A2.2 clearly show the melting of confined water at approximately 4000 s. Figure A2.3 also demonstrates this behaviour however it is less clear from the figure. In all three cases, the melting of water occurs earliest in the smallest of pore sizes, as expected. A large peak at *ca.* 5500 s is present in all silica and is representative of the bulk water melting.

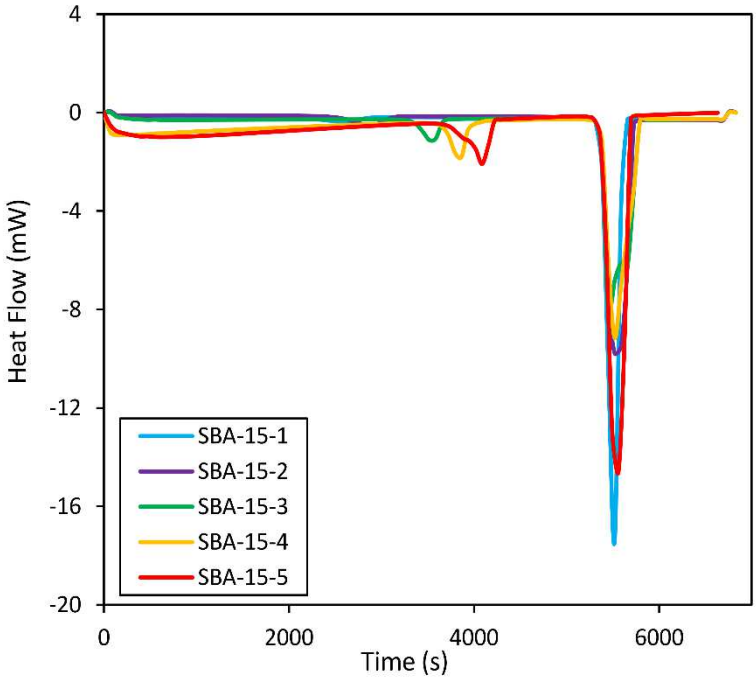

Figure A2.1. *DSC melting data for water confined in the pores of SBA-15 silica of different average pore diameters.*

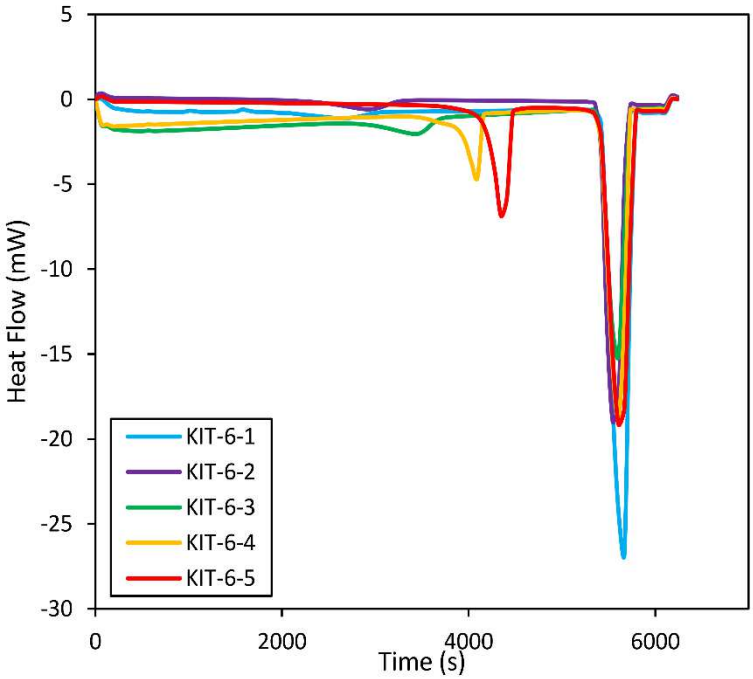

Figure A2.2. *DSC melting data for water confined in the pores of KIT-6 silica of different average pore diameters.*

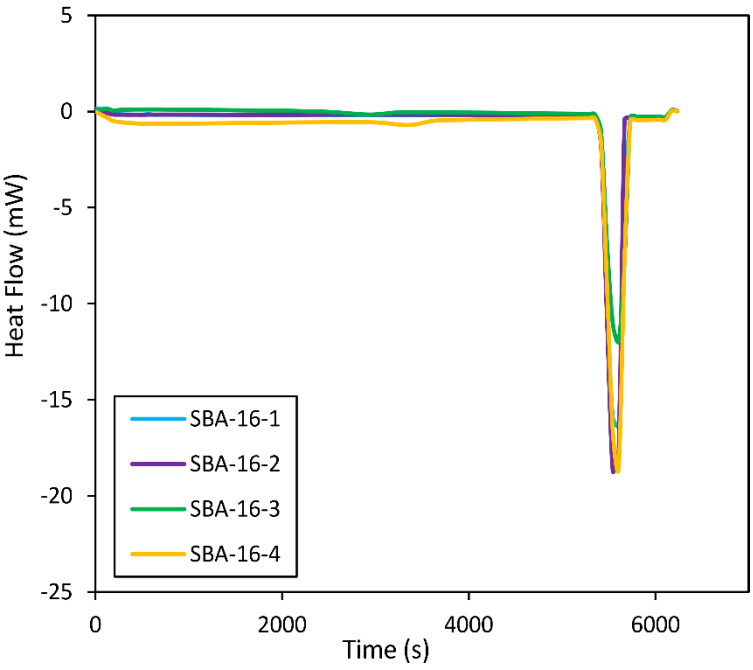

Figure A2.3. *DSC melting data for water confined in the pores of SBA-16 silica of different average pore diameters.*

APPENDIX. 3

Confirming the successful synthesis of methyl hexanoate by ^{1}NMR

Methyl hexanoate was synthesised at Aston and its confirmation of successful systhesis, by NMR, is shown in Figure A3.1, together with the correspinding peak assignment in Table A3.1.

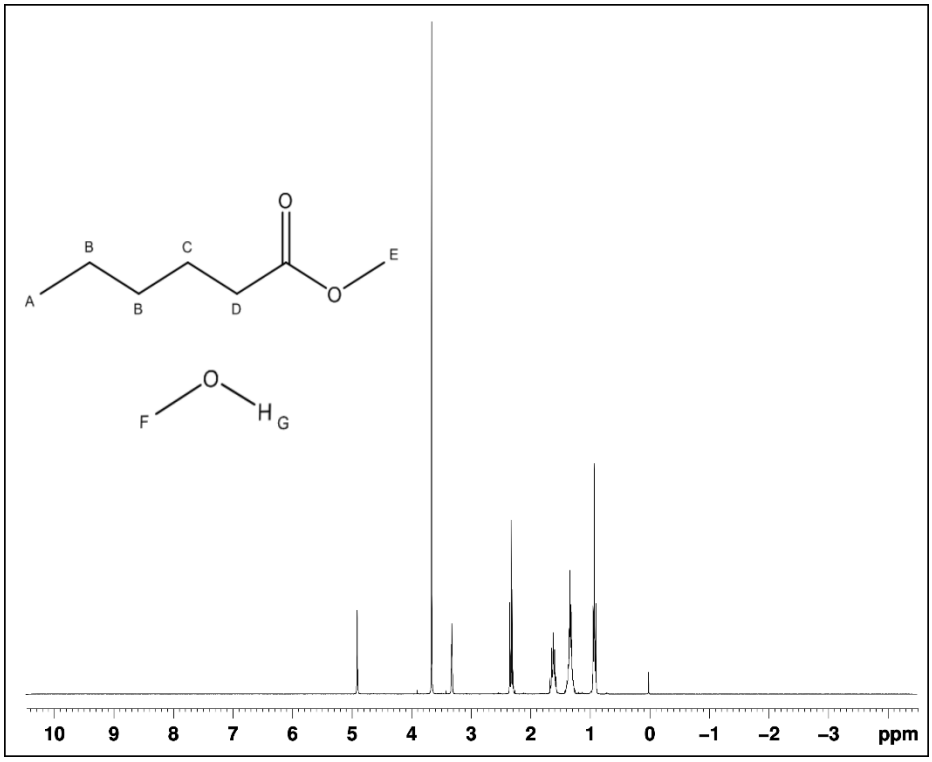

Figure A3.1. *^{1}H NMR spectra for methyl hexanoate used in the tortuosity measurements.*

Table A3.1. ^{1}H NMR Data for methyl hexanoate in solution with deuterated methanol

Peak Assignment	Chemical Shift (ppm)	Multiplet Structure
A	0.90	triplet
B	1.20-1.40	multiplet
C	1.60	quintet
D	2.30	triplet
E	3.65	singlet
F	3.30	quintet
G	4.9	singlet

Confirming the long diffusion delay time limit

Confirmation that all diffusion measurements were conducted in the long diffusion delay time limit. If shorter delay times were used, the diffusion starts to represent that of the bulk liquid as not enough time is allowed for the molecule to interact with the solid system.

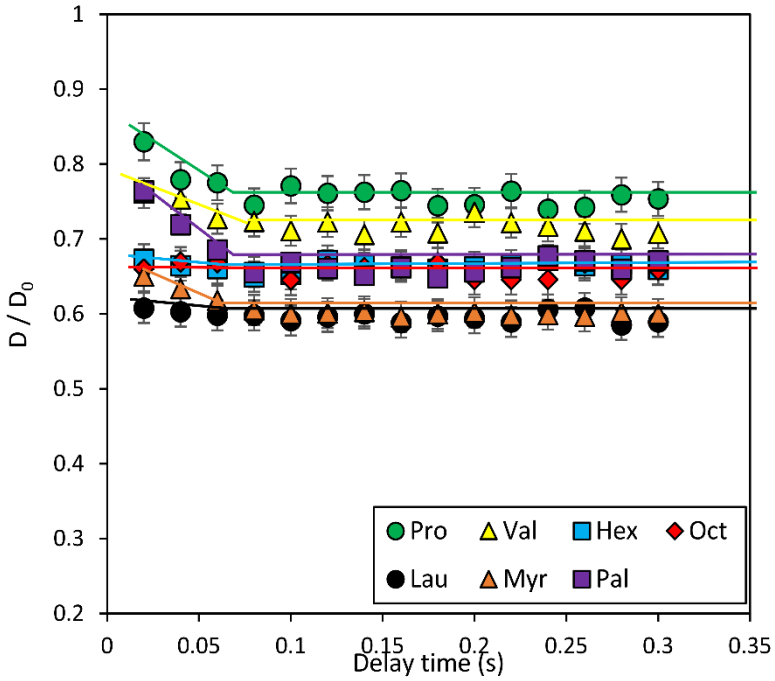

Figure A3.2. *The change in D/D0 with diffusion delay time for the acids confined within the pores of KIT-6 silica. At short diffusion delay times, the diffusion starts to represent that of the bulk liquid.*

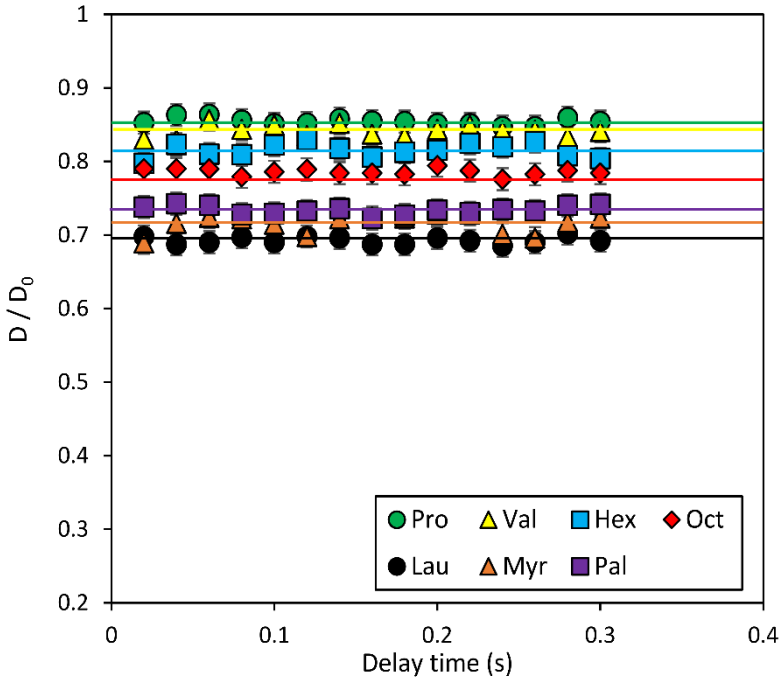

Figure A3.3. *The change in D/D0 with diffusion delay time for the acids confined within the pores of SBA-15 silica. No difference is observed between the diffusion at short and long delay times.*

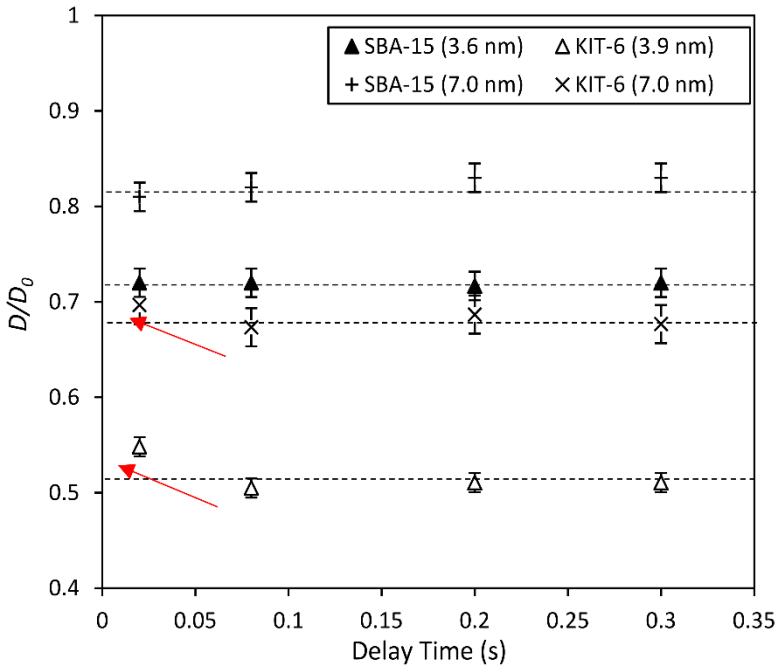

Figure A3.4. *Values of D/D0 acquired with diffusion delay times for heptane and cyclohexane confined in the largest and smallest pore diameters of both KIT-6 and SBA-15. Arrows indicate where species begin to exhibit larger diffusion coefficients. Values for heptane and cyclohexane were indistinguishable.*

APPENDIX. 4

Exploring the systematic discrepancy between thermoporometry and porosimetry pore sizes.

Chapter 5 utilises nitrogen porosimetry as a complementary technique to analyse the accuracy and precision of NMR cryoporometry as a pore size determination technique for mesoporous silica. The results listed use the BJH method of analysis. This appendix introduces other possible methods of porosimetry analysis and offers a discussion on the discrepancy observed between, and within, the different techniques.

The pore sizes obtained within this piece of work has, *via* the gas technique, have predominately been processed using the BJH desorption branch. Illustrated herein are pore size distribution graphs for one example silica of SBA-15, KIT-6 and SBA-16 using the BJH adsorption branch, NLDFT adsorption model using a cylindrical meniscus, NLDFT equilibrium model using a cylindrical meniscus and the NLDFT adsorption model using a hemispherical meniscus. A summary of all pore sizes obtained is included in Table A4.1.

SBA-15-3

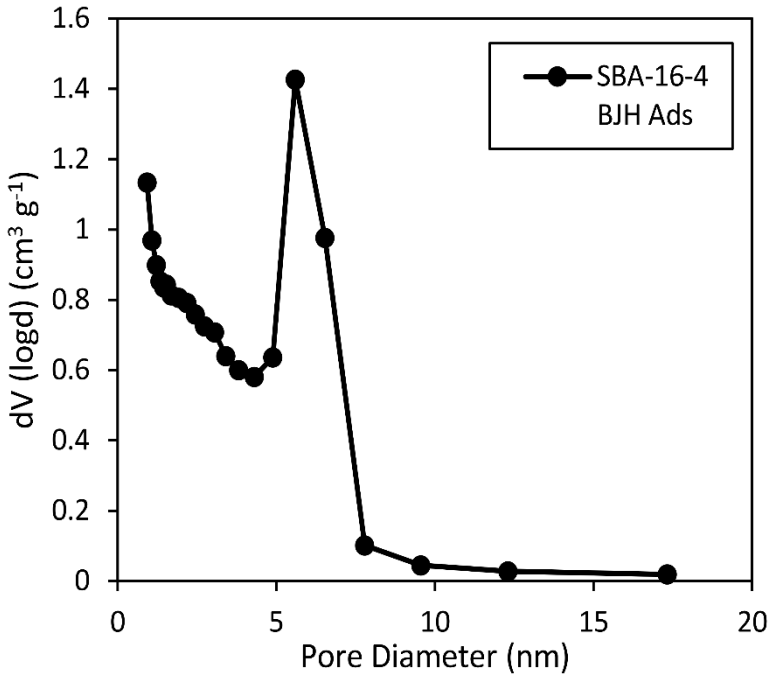

Figure A4.1. *Pore size distribution for SBA-15-3 silica obtained using nitrogen porosimetry processed from the BJH adsorption branch.*

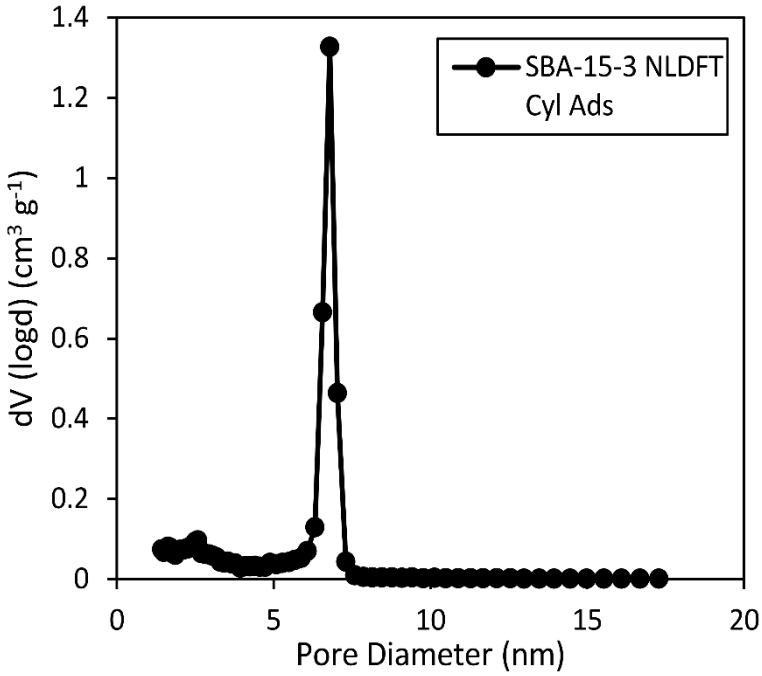

Figure A4.2. *Pore size distribution for SBA-15-3 silica obtained using nitrogen porosimetry processed using the NLDFT adsorption model assuming a cylindrical meniscus.*

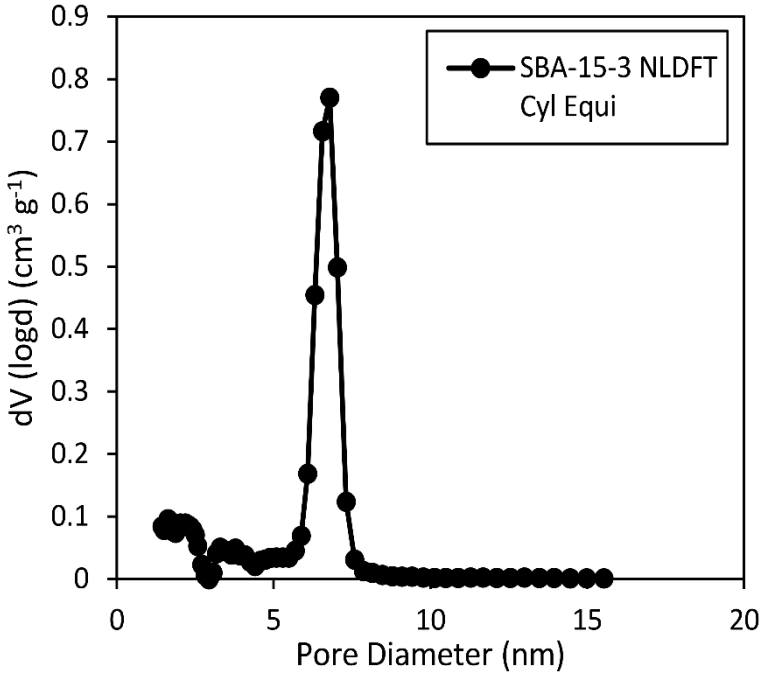

Figure A4.3. *Pore size distribution for SBA-15-3 silica obtained using nitrogen porosimetry processed using the NLDFT equilibrium model assuming a cylindrical meniscus.*

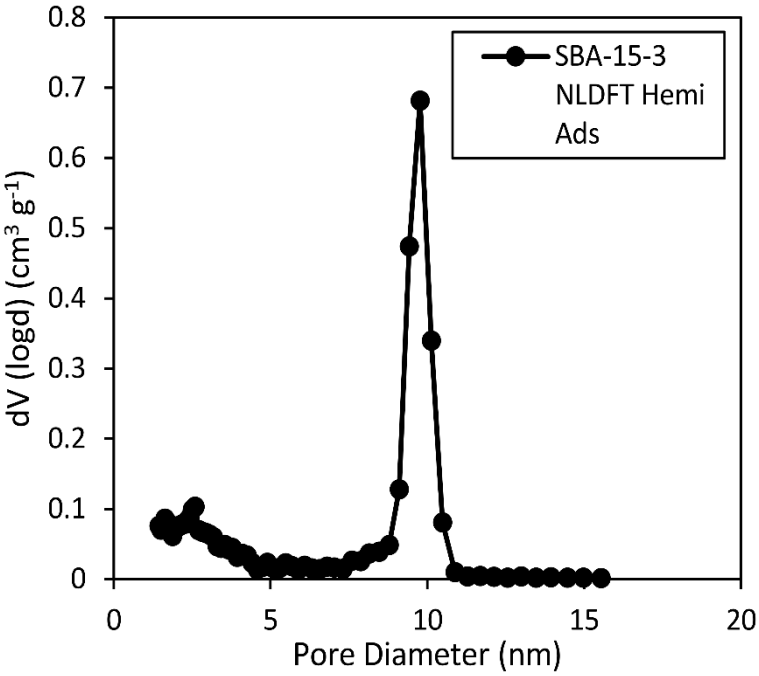

Figure A4.4. *Pore size distribution for SBA-15-3 silica obtained using nitrogen porosimetry processed using the NLDFT adsorption model assuming a hemispherical meniscus.*

KIT-6-3

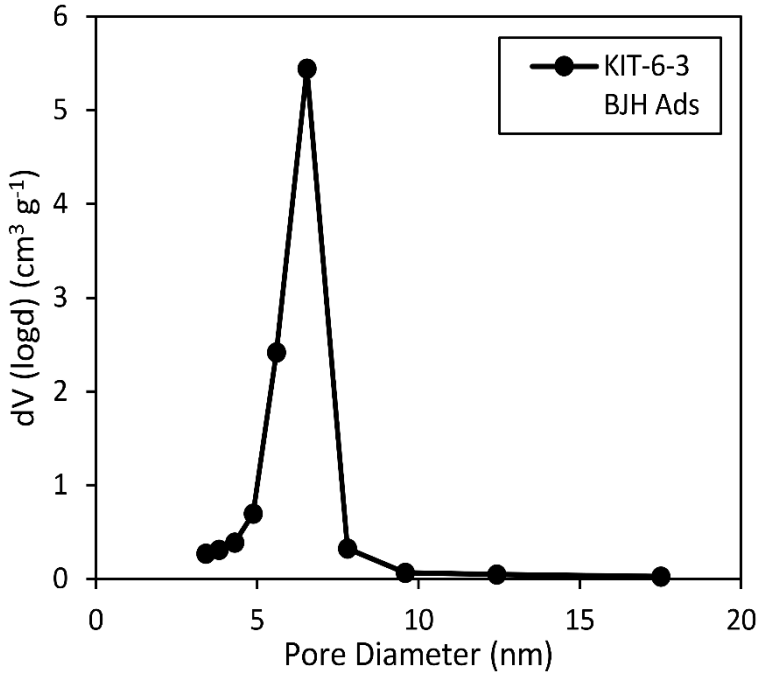

Figure A4.5. *Pore size distribution for KIT-6-3 silica obtained using nitrogen porosimetry processed from the BJH adsorption branch.*

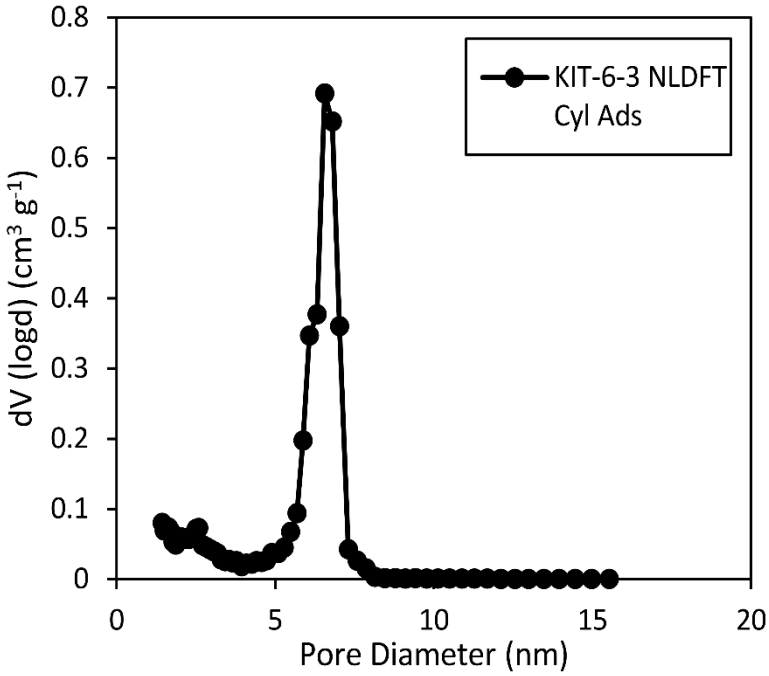

Figure A4.5. *Pore size distribution for KIT-6-3 silica obtained using nitrogen porosimetry processed using the NLDFT adsorption model assuming a cylindrical meniscus.*

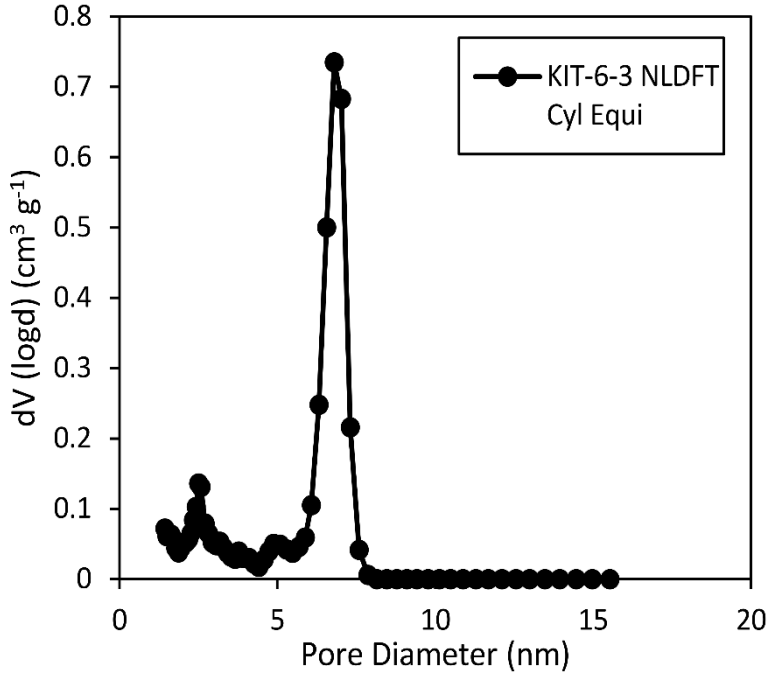

Figure A4.6. *Pore size distribution for KIT-6-3 silica obtained using nitrogen porosimetry processed using the NLDFT equilibrium model assuming a cylindrical meniscus.*

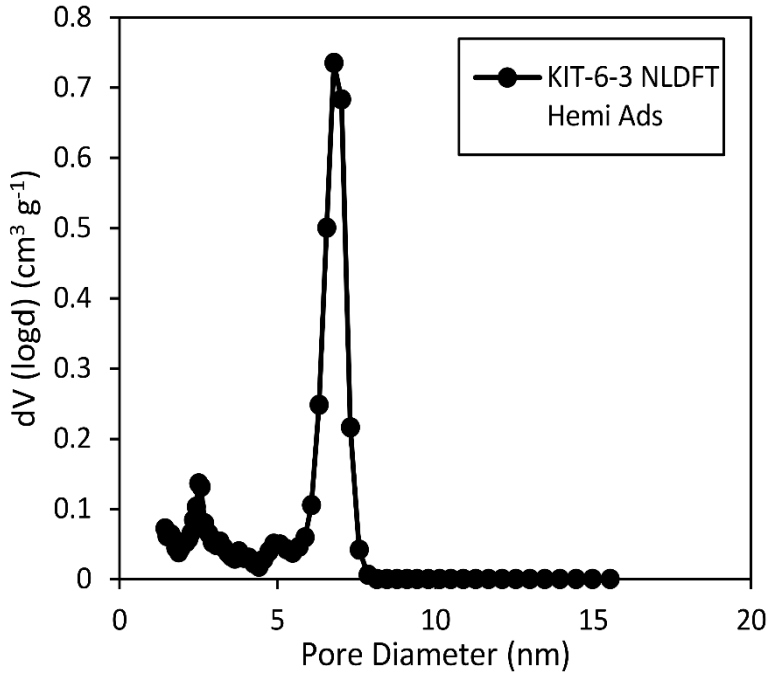

Figure A4.8. *Pore size distribution for KIT-6-3 silica obtained using nitrogen porosimetry processed using the NLDFT adsorption model assuming a hemispherical meniscus.*

SBA-16-4

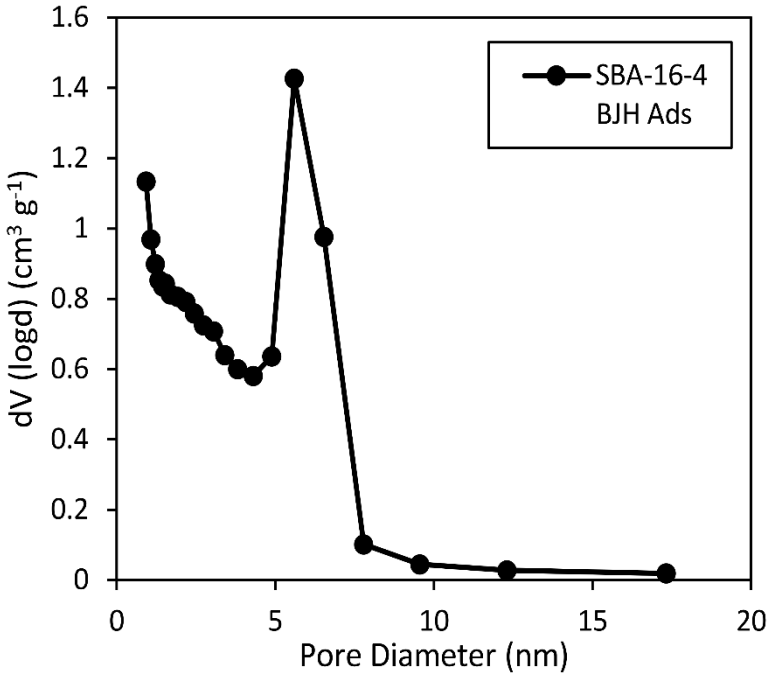

Figure A4.9. *Pore size distribution for SBA-16-4 silica obtained using nitrogen porosimetry processed from the BJH adsorption branch.*

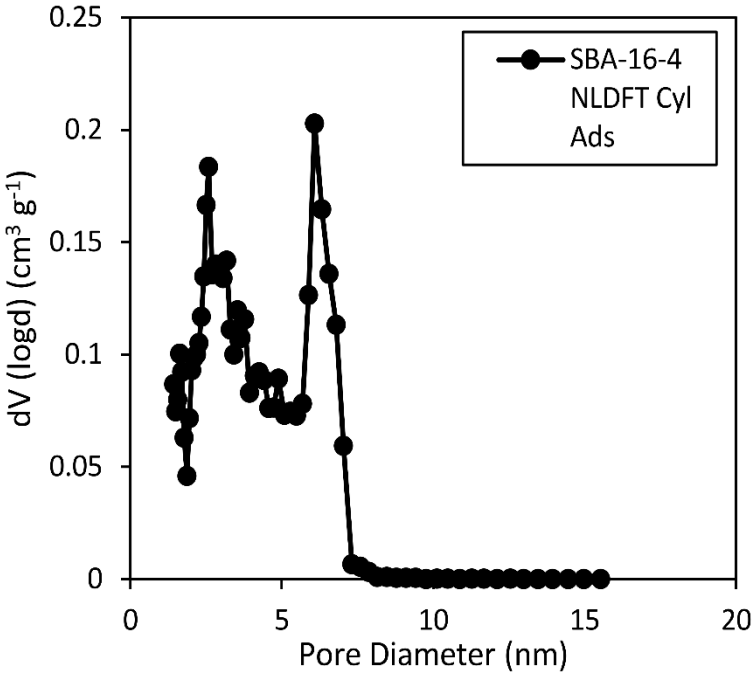

Figure A4.10. *Pore size distribution for SBA-16-4 silica obtained using nitrogen porosimetry processed using the NLDFT adsorption model assuming a cylindrical meniscus.*

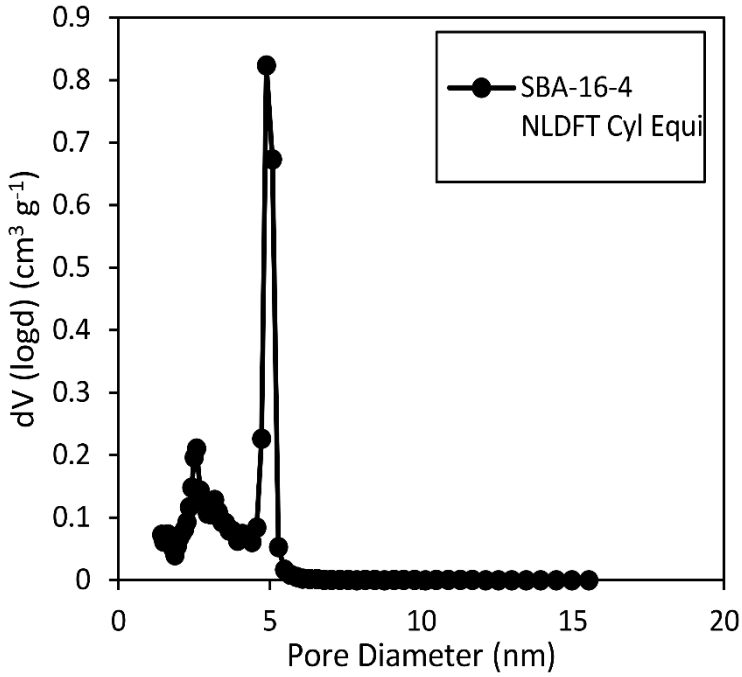

Figure A4.11. *Pore size distribution for SBA-16-4 silica obtained using nitrogen porosimetry processed using the NLDFT equilibrium model assuming a cylindrical meniscus.*

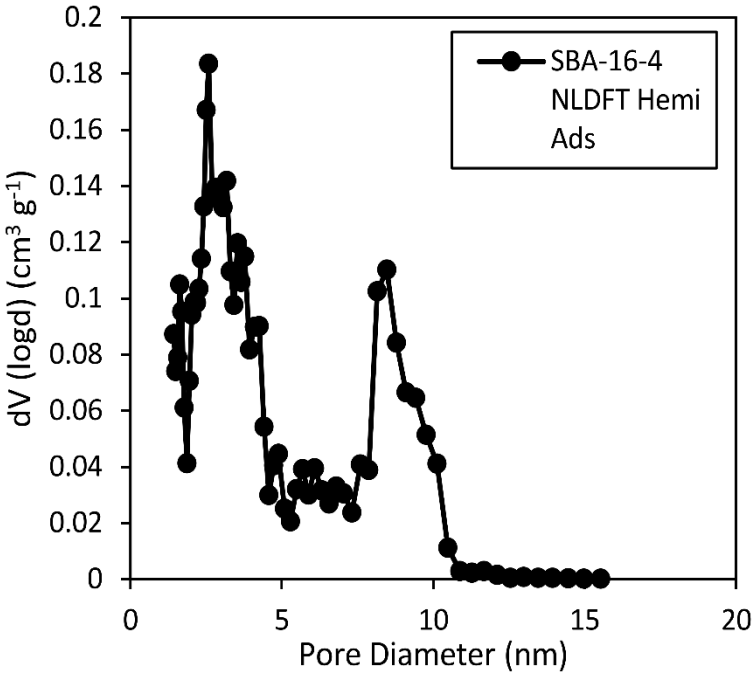

Figure A4.12. *Pore size distribution for SBA-16-4 silica obtained using nitrogen porosimetry processed using the NLDFT adsorption model assuming a hemispherical meniscus.*

The main observation from Chapter 5 was that the porosimetry technique overestimates the pore sizes of cylindrical pore shaped silica compared to both thermoporometry methods. This theme is continued here. In the majority of cases, the extra porosimetry data, obtained in Appendix, 4 also over estimates the pores sizes. The BJH desorption branch and NLDFT equilibrium methods are in closest agreement to NMR and DSC however all measurements taken from the adsorption branch deviate significantly.

The difference between BJH and NLDFT data occur mainly due to assumptions with both techniques. BJH has the inherent assumptions associated with the Kelvin Equation and NLDFT is partially empirical due to the need to calibrate the surface potential from experimental data. Several parameters must also be taken into account for data obtained from the adsorption branch. When a pore fills *via* capillary condensation, a multi-layer film builds up on the wall of the silica. This film layer thickness needs to be taken into account during the processing otherwise the accuracy of pore size determination is significantly affected; a common artefact in pore sizes less than 10 nm and a potential explanation for the differences in pore sized determined here.

Analysis of the spherical shaped pores using the other porosimetry techniques once again demonstrates the advantages of using the thermoporometry techniques. A more accurate analysis of the pore size is obtained using the BJH adsorption branch as the cavitational effect is reduced, but the pore sizes are still underestimated. Analysis by NLDFT also has its drawbacks, despite all techniques observing both pore and throat regions. The equilibrium model does not identify any change in pore size; the cylindrical adsorption only observes a change for the largest of pore sizes and the hemispherical adsorption, arguably the most accurate of the four porosimetry methods, fails to estimate a pore size for SBA-16-2. Even for the narrowest of PSDs, a significant error is apparent.

Table A4.1. Complete list of pore size data obtained throughout this piece of work.

Sample	NMR (nm)	DSC (nm)	STEM (nm)	BJH Cylindrical Desorption (nm)	BJH Cylindrical Adsorption (nm)	NLDFT Cylindrical Adsorption (nm)	NLDFT Hemispherical Adsorption (nm)	NLDFT Cylindrical Equilibrium (nm)
SBA-15-1	3.4	3.4	-	3.6	4.5	5.3	5.5	4.9
SBA-15-2	3.6	3.5	-	3.7	4.9	5.7	7.9	5.1
SBA-15-3	4.3	4.4	5.0	5.2	6.7	6.8	9.8	6.8
SBA-15-4	4.9	5.0	-	6.3	8.3	7.9	11.7	8.1
SBA-15-5	5.9	5.6	-	7.0	9.4	8.5	13.0	9.4
KIT-6-1	3.6	3.8	-	3.9	4.3	5.3	6.8	5.3
KIT-6-2	4.0	4.0	-	4.3	4.9	5.7	7.6	5.7
KIT-6-3	4.9	4.4	5.2	5.4	6.5	6.6	9.4	6.8
KIT-6-4	5.5	5.4	-	7.0	9.5	8.5	13.0	8.8
KIT-6-5	6.4	6.3	-	8.1	12.3	10.1	15.0	9.8
SBA-16-1	3.5	3.6	3.7	3.0	3.1	4.3	4.1	4.3
SBA-16-2	4.0	3.9	4.2	3.3	3.4	4.9	-	4.3
SBA-16-3	5.5	5.6	5.3	3.5	4.9	4.9	7.6	4.9
SBA-16-4	6.5	6.3	6.5	3.6	5.6	6.1	8.5	4.9